Ministero dell'Istruzione dell'Università e Ricerca

Università degli Studi di Palermo

DICGIM

Dipartimento di Ingegneria Chimica, Gestionale,Informatica e Meccanica

POLYMERIC POROUS STRUCTURES VIA PHASE SEPARATION

PhD thesis of **Gianluca A. Mannella**

Dottorato di ricerca in Ingegneria Chimica e dei Materiali

Settore Scientifico Disciplinare: ING-IND 22

Supervisor
Prof. Vincenzo La Carrubba

Head of the PhD board
Prof. Giuseppe Spadaro

Ciclo XXIII: 2009-2011

Thoughts without content are empty,
intuitions without concepts are blind.

— Immanuel Kant, 1781

To my first teacher, *nonno Nino*.

Abstract

Polymer solutions are currently used for the production of porous structures via phase separation for a vaste latitude of applications. Phase separation in polymer solutions is indeed very common to be encountered, owing to the thermodynamic properties of this class of systems.

Many techniques are employed to induce phase separation in polymer solutions: the most widely used are based on temperature or composition effects. As a matter of fact, starting from a homogeneous polymer solution, it is possible to enter the demixing zone by changing the temperature (Thermally Induced Phase Separation, TIPS) or the composition of the system (Diffusion Induced Phase Separation). Despite the apparent simplicity of these methodologies, a great challenge is represented by the possibility to attain a satisfactory final morphology in terms of pore size, porosity, mechanical performance, biodegradation rate and related features.

In this thesis, the attention is focused on the TIPS process, commonly used for the production of membranes for various applications and scaffolds for tissue engineering purposes. Membranes obtained via TIPS are suitable for microfiltration and membrane distillation (MD) operations. On the other hand, scaffolds are utilized in tissue engineering as a support for cell proliferation and growth, with the aim of temporarily substituting and repairing damaged tissues. Polymers to be chosen for this applications must be biocompatible and biodegradable. The target system selected in this work is constituted by poly-L-lactic acid (PLLA), dioxane and water. This ternary solution was adopted for the production of both microfiltration membranes and scaffolds for tissue engineering.

A first approach to the characterization of the system PLLA-dioxane-water was pursued by carrying out turbidity experiments for the determination of cloud point curves. In this purpose, a dedicated experimental apparatus was designed, built and set up. A particular attention was payed to temperature control, as this class of systems presents a high sensitivity on temperature. The basic features of the device are the coupled measurement of temperature and transmitted light, and the possibility to reach cooling rates comparable to common processing conditions (up to $1°C/s$). A set of cloud point curves for the PLLA-dioxane-water system were measured, the results are in line with those available in

literature for similar systems. Moreover, by varying the cooling rate, a cloud point depression was detected. Also in this case, the results were in agreement with other experimental characterizations available in literature.

A second approach to the analysis of polymer solutions behavior is based on models for phase equilibria calculations. Two kinds of lattice fluid modeling approaches were employed: the group contribution model by Oishi and Prausnitz (and successive corrections) and the Sanchez-Lacombe compressible model (and successive integrations). The group contribution model resulted inapplicable to the system considered, owing to high deviations in the calculated water activities. In fact, the peculiar features of water molecule are difficult to be taken into account with this kind of model. On the other hand, the lattice fluid model extended to specific interactions was successfully applied to the PLLA-dioxane-water system for the calculation of the ternary phase diagram.

The two different routes followed in this work, i.e. the experimental investigation of the key features of the phase separation processes and the modeling issues, are complementary. The experimental campaign was mainly dedicated to the individuation of the phase boundaries via turbidity measurements. This information can be used as an input of a thermodynamic model for the derivation of a complete phase diagram of the system (i.e. binodal and spinodal curves). As the experimental derivation of a complete phase diagram is time and cost consuming, the route proposed in this work would overcome the need of many experimental tests, without lacking the link between experiments and theory.

By improving the knowledge about the relations between processing conditions and final morphology, it is possible to better control the membrane microstructure. Depending on the application, a membrane must own specific properties (e.g. pore size and porosity). In this framework, a set of commercial microfiltration membranes were examined in relation to the desalination via membrane distillation process, in order to individuate the key features that are suitable for the considered operation. After defining the most appropriate membrane properties and microstructure, it is then possible to design a dedicated route for their production via phase separation.

Sommario

Le soluzioni polimeriche sono comunemente impiegate per la produzione, tramite processi di separazione di fase, di strutture porose utilizzate in una vasta gamma di applicazioni. La separazione di fase è un fenomeno riscontrato comunemente nelle soluzioni macromolecolari, a causa delle proprietà termodinamiche di questa classe di sistemi.

Per indurre la separazione di fase si impiegano diverse tecniche: le più utilizzate si basano su variazioni di temperatura o di concentrazione del sistema. Infatti, partendo da una soluzione polimerica omogenea, è possibile entrare nella lacuna di miscibilità modificando la temperatura (separazione di fase indotta termicamente, TIPS) o la composizione (separazione di fase indotta da diffusione, DIPS) del sistema. Malgrado l'apparente semplicità di queste metodologie, l'ottenimento di una morfologia soddisfacente, in termini di dimensione dei pori, porosità, proprietà meccaniche, velocità di degradazione e altre caratteristiche correlate, è tuttora un problema aperto.

In questa tesi, l'attenzione è stata focalizzata sul processo di TIPS, tipicamente usato per la produzione di membrane per svariate applicazioni e scaffolds per l'ingegneria tessutale. Le membrane ottenute tramite TIPS sono idonee per l'impiego nei processi di microfiltrazione e distillazione a membrana (MD). Gli scaffolds sono utilizzati nell'ingegneria tessutale come supporti per la proliferazione e crescita cellulare, con lo scopo di sostituire in via temporanea e riparare tessuti danneggiati. I polimeri da utilizzare per questa specifica applicazione devono essere biocompatibili e biodegradabili. Il sistema target selezionato per il presente lavoro è costituito da poliacido-L-lattico (PLLA), diossano (solvente) e acqua (non-solvente). Tale sistema ternario è stato utilizzato sia per la produzione di membrane per microfiltrazione che per la preparazione di scaffolds per l'ingegneria tessutale.

Un primo approccio seguito nella caratterizzazione del sistema PLLA-diossano-acqua è stato volto alla determinazione delle *cloud point curves*, ovvero delle temperature alla quale avviene la separazione di fase, tramite misure di torbidità. A tale scopo, è stato progettato e realizzato un apparato sperimentale dedicato. Una particolare attenzione è stata dedicata al controllo della temperatura, dato che questa classe di sistemi è molto sensibile a piccole variazioni di temperatura. Le caratteristiche principali dello strumento realizzato sono la capacità di misurare contemporaneamente la temperatura e la torbidità del sistema (come

intensità della luce trasmessa), e la possibilità di raggiungere velocità di raffreddamento paragonabili con le comuni condizioni operative (fino a 1°C/s). È stato misurato un set di cloud point curves per il sistema PLLA-diossano-acqua, e i risultati sono comparabili con quelli disponibili in letteratura per sistemi simili. Inoltre, al variare della velocità di raffreddamento imposta al campione, è stata riscontrata una diminuzione della temperatura di cloud point. Anche in questo caso, le evidenze sperimentali sono in accordo con altre caratterizzazioni presenti in letteratura.

Un secondo approccio all'analisi del comportamento delle soluzioni polimeriche è stato basato sull'utilizzo di modelli per il calcolo degli equilibri termodinamici. Sono stati studiati due tipi di modelli, entrambi basati sulla teoria *lattice fluid*: il modello a contributi di gruppo di Oishi e Prausnitz (e le successive correzioni) e il modello comprimibile di Sanchez e Lacombe (e le successive integrazioni). Il modello a contributi di gruppo è risultato inapplicabile al sistema preso in esame, a causa delle considerevoli deviazioni nel calcolo del valore dell'attività dell'acqua. Infatti, in questa tipologia di modello è difficile tenere conto di tutte le caratteristiche peculiari della molecola dell'acqua. D'altro canto, il modello comprimibile, esteso alle interazioni specifiche, si è mostrato invece adeguato per la rappresentazione degli equilibri di fase del sistema PLLA-diossano-acqua.

I due differenti approcci seguiti in questo lavoro, ovvero l'analisi sperimentale e la modellazione, sono complementari. La campagna sperimentale è stata soprattutto dedicata all'individuazione della lacuna di miscibilità tramite misure di torbidità. Questa informazione può essere utilizzata come input di un modello termodinamico, al fine della derivazione di un diagramma di fase completo per il sistema preso in esame (ovvero comprendente la curva binodale e spinodale). Dato che la derivazione sperimentale dei diagrammi di fase è un processo costoso in termini di tempo e di risorse, la metodologia proposta in questo lavoro potrebbe limitare la necessità di numerosi dati sperimentali, senza però trascurare la connessione tra il comportamento reale del sistema e l'interpretazione teorica.

Migliorando la conoscenza riguardo le relazioni tra le condizioni di processo e la morfologia della struttura porosa, è possibile controllare in maniera adeguata la microstruttura della membrana. In base all'applicazione di riferimento, la membrana deve avere caratteristiche specifiche (per esempio, dei valori tipici di dimensione dei pori e porosità). In questa prospettiva, è stato esaminato un set di membrane commerciali nell'ambito del processo di dissalazione tramite distillazione a membrana, al fine individuare le proprietà rilevanti che la struttura porosa deve possedere per questa tecnologia. Solo dopo aver definito quali sono le proprietà e la microstruttura più appropriata per una membrana, è possibile progettare un processo dedicato per la loro produzione tramite separazione di fase.

Publications

Some ideas and figures have appeared previously in the following publications:

ISI Publications

1. G. A. Mannella, V. La Carrubba, V. Brucato, I. C. Sanchez. Lattice fluid model generalized to specific interactions: an application to ternary polymer solutions, *Fluid Phase Equilibria*, 312, 60-65, **2011**

2. G. A. Mannella, V. La Carrubba, V. Brucato. Some features of polymeric membranes for water purification via membrane distillation, *Journal of Applied Polymer Science*, 122, 3557-3563, **2011**

3. G. A. Mannella, V. La Carrubba, V. Brucato. On the calculation of free energy of mixing for aqueous polymer solutions with group-contribution models, *Fluid Phase Equilibria*, 299, 222-228, **2010**

4. G. A. Mannella, V. La Carrubba, V. Brucato. Characterization of hydrophobic polymeric membranes for membrane distillation process, *International Journal of Material Forming*, 3 Suppl. 1, 563-566, **2010**

5. G. A. Mannella, V. La Carrubba, V. Brucato. Evaluation of vapour mass transfer in various membrane distillation configurations. An experimental study, *Heat and Mass Transfer*, **2012** (in press)

International congress presentations

1. G. A. Mannella, V. Brucato, V. La Carrubba. A survey on models for prediction of phase equilibria in polymer solutions. *The Polymer Processing Society 27th Annual Meeting*, Marrakech, **2011**

2. G. A. Mannella, V. Brucato, V. La Carrubba. Characterization of commercial polymeric membranes for membrane distillation processes. *The Polymer Processing Society 27th Annual Meeting*, Marrakech, **2011**

3. G. A. Mannella, V. Brucato, V. La Carrubba. Water Fluxes in Polymeric Membranes for Desalination via Membrane Distillation, *V International Conference on Times of Polymers (TOP) and Composites*, AIP Conf. Proc., Vol. 1255, 243-245, **2010**

4. G. A. Mannella, V. La Carrubba, V. Brucato. Characterization of hydrophobic polymeric membranes for membrane-distillation process, *13th ESAFORM Conference on Material Forming*, Brescia, **2010**

5. M. A. Ben Farh, V. Brucato, A. Cipollina, V. La Carrubba, G. A. Mannella, G. Micale. Membrane Distillation for a solar powered desalination pilot unit, *2nd Maghreb Conference on Water Treatment and Desalination "CMTDE 2009"*, Hammamet, Tunisia, **2009**

National congress presentations

1. G. A. Mannella, V. Brucato, V. La Carrubba. Theoretical prediction and experimental determination of cloud point curves for polymeric solutions: an application to the ternary system PLLA-dioxane-water. *XX Convegno Italiano di Scienza e Tecnologia delle Macromolecole, AIM*, Terni, **2011**

Other works

ISI publications

1. G. A. Mannella, V. La Carrubba, V. Brucato, W. Zoetelief, G. Haagh. No-flow temperature in injection moulding simulation, *Journal of Applied Polymer Science*, 119, 3382-3392, **2011**

International congress presentations

1. G. Mannella, V. La Carrubba, V. Brucato, W. Zoetelief, G. Haagh. Solidification during the filling stage of injection molding: a simulation-oriented study, *The Polymer Processing Society 27th Annual Meeting*, Marrakech, **2011**

2. G. Mannella, V. La Carrubba, V. Brucato, W. Zoetelief, G. Haagh. No-flow temperature and solidification in injection molding simulation, *14th ESAFORM Conference on Material Forming*, Belfast, **2011**

3. G. Mannella, V. La Carrubba, V. Brucato, W. Zoetelief, G. Haagh. A study via simulations of solidification during injection molding, *Advances in Polymer based materials and related Technologies, AIMAT*, Napoli, **2011**

4. G. Mannella, V. La Carrubba, V. Brucato, W. Zoetelief, G. Haagh. The concept and the application of no-flow temperature in injection moulding simulation, *Polymerfest*, Palermo, **2009**

Acknowledgments

A thesis is not only a sum of data and modeling. A thesis is a walk often done together with other people, which must be acknowledged.

Besides the official supervisor, Prof. Vincenzo La Carrubba, this thesis has a "hidden" supervisor, Prof. Valerio Brucato, which guided and supported all my research during these three years. The first thanks go to them, for giving me the chance to "play" with the building of experimental apparatuses and with thermodynamic models, even abroad.

Another co-walker was Dr. Francesco Carfì Pavia, which aside for helping me in SEM imaging and in the preparation of polymer solutions for experimentals, together with long and constructive discussions about phase separation issues, gave me an enjoyable time at the department!

One stop of the journey was at the University of Naples "Federico II", where Prof. Giuseppe Mensitieri with his coworkers Eng. Giuseppe Scherillo and Eng. Gigi Sanguigno, offered to me very stimulant conversations about thermodynamic modeling of polymer solutions and related methods of calculations.

Another long stop of the journey was at the University of Texas at Austin, where Prof. Isaac C. Sanchez gave me the opportunity to spend four months for developing the thermodynamic modeling for PLLA-dioxane-water system. He was an enlightened guide, which changed my approach on modeling, thermodynamics and (less obvious!) writing.

Thanks to Eng. Fedele Di Salvo and Eng. Filippo Paredes for the support in the design and realization of the heat sinks coupled to peltier cells.

All the students which crossed my research road: Salvo Montesanto, Peppe Scaglione, Frankie Guttilla, Alessandro Di Benedetto, Miriam Bartoli, Massimo Giordano, Massimo Giordano 2.0 (!), Piersimone Inguì, Antonio Mulone and Rossana Pendola. All of them shared with me many experimental and modeling issues!

Last but not least, who was here before, and has been during, then will be after this journey: mom and dad, always glad of my work, and Silvia, always with me even when I was engaged in this work.

Contents

List of Figures

List of Tables

Acronyms and notation

A	turbidity, area
D_{ij}	diffusivity
E	energy
F	Helmholtz free energy, volumetric flow rate
$FV\%$	free volume percentage
G	Gibbs free energy
G_i	transfer function
H	enthalpy
I	light intensity, electrical current intensity
K_i	proportional gain
K_t	thermal conductance
L_p	pore length
M	molecular weight
N	number of r-mers, mass flux
N_0	number of empty sites
N_r	total number of lattice sites
N_A	Avogadro's number
P	pressure, power
$\dot{Q}$	heat power
Q_k	area parameter of group
R	gas constant, radius, electrical resistance
R_k	volume parameter of group
S	entropy
T	temperature
U	global heat transfer coefficient
V	volume, voltage
V^*	volume of N r-mers (no-holes)
Z	partition function

a_i	activity
b	proportionality factor
c	parameter of external degree of freedom
c_p	specific heat
d	diameter
f	fraction of occupied sites
f_0	fraction of empty sites
f_{ij}	free energy per number of $i - j$ contact pairs
g	Gibbs free energy per mer
h	heat transfer coefficient
k	Boltzmann's constant
k_C	mass transfer coefficient
k_P	mass transfer coefficient (pressure based)
k_t	thermal conductivity
q	number of ways that nonspecific interactions occur, wavenumber
q_i	area parameter of molecule
r	number of mer per molecule, pore radius
r_i	volume parameter of molecule
t	time
v	molar volume, velocity
w	weight fraction, interaction energy
x	molar fraction
z	coordination number of lattice

Greek letters

Γ_k	parameter of residual contribution
Θ	dimensionless temperature
Ψ_{mn}	interaction parameter between m and n groups
Ω	number of configuration available, weight fraction based activity
α	Seebeck coefficient, thermal diffusivity
γ_i	activity coefficient
$\dot{\gamma}$	shear rate
δ	Hildebrand or Hansen solubility parameter, thickness
$\delta\epsilon^*$	energy difference between specific and nonspecific interactions
ϵ	porosity, interaction energy, error
ϵ_{ij}	pair interaction between components i and j

η	viscosity
λ	light wavelength, mean free path
μ	chemical potential, viscosity, refractive index
$\nu_k^{(i)}$	number of k-type groups in molecule i
ρ	density
σ	interfacial tension, collision diameter
τ	tortuosity factor, characteristic time constant
θ	angle, contact angle, surface fraction
χ	interaction parameter
ϕ, φ	volumetric fraction
ψ	duty cycle
ξ	generic concentration variable, correlation length
ζ	correction factor for interaction energy, damping factor
ω	time contraction/expansion coefficient

Superscripts

a^*	characteristic (or close packed) property
a^0	pure state property
$\tilde{a}$	reduced property $(= a/a^*)$
(i)	pure species property
C	combinatorial
FV	free volume
H	hard-core
R	residual

Dimensionless numbers

Bi	Biot number	$\dfrac{Ud}{k_t}$
Fo	Fourier number	$\dfrac{\alpha t}{d^2}$
Gr	Grashof number	$\dfrac{d^3 g \rho \Delta \rho}{\mu^2}$
Kn	Knudsen number	$\dfrac{\lambda}{d}$
Nu	Nusselt number	$\dfrac{Ud}{k_t}$
Pr	Prandtl number	$\dfrac{c_p \mu}{k_t}$
Re	Reynolds number	$\dfrac{\rho v d}{\mu}$
Sc	Schmidt number	$\dfrac{\mu}{\rho d}$
Sh	Sherwood number	$\dfrac{k_C d}{D_{ij}}$

Introduction

Polymeric porous structures have a wide range of applications in common life. A typical example is represented by membranes for separation and purification of water and beverages. In the design and optimization of a purification process, the role of membrane is crucial. As a matter of fact, the membrane properties, namely pore size and porosity, strongly affect the process efficiency. By varying the pore size of a membrane, it is possible to select the species to be restrained, and thus tuning the quality of purification.

On the other hand, another family of porous polymeric structures is represented by scaffolds employed in tissue engineering as a support for cell proliferation and growth, with the aim of temporarily replacing and steadily repairing damaged tissues [Stamatialis et al., 2008, Jagur-Grodzinski, 2006]. Polymers used in these applications must be biocompatible and biodegradable [Nair and Laurencin, 2007].

Polymer solutions are usually the starting system for the production of porous structures via phase separation, as liquid-liquid (and solid-liquid) phase separation in polymer solutions is very common to be encountered, owing to the thermodynamic properties of this class of systems.

Phase separation techniques for membranes and scaffolds production

Several methodologies are followed to induce liquid-liquid phase separation in a polymer solution, the most widely used are based on the variation of temperature or composition. As a matter of fact, a homogeneous polymer solution can be brought into the miscibility gap by changing the temperature (Thermally Induced Phase Separation, TIPS) or the composition of the system (Diffusion Induced Phase Separation). Despite the apparent simplicity of these techniques, a great challenge is represented by the possibility to attain a satisfactory final morphology in terms of pore size, porosity, mechanical performance, biodegradation rate and related features. Polymer solutions properties, and thus final porous structures, are very sensitive to experimental conditions: for example, in TIPS operations, starting composition and temperature highly influence the resulting morphology. A typical miscibility

gap of a polymer solution is showed in figure 0.1: the binodal curve represents the equilibrium compositions, whereas the spinodal curve delimitates the unstable zone; the critical point is the maximum of both binodal and spinodal curves. The polymer crystallization curve (i.e. solid-liquid phase separation) is also reported. A classification of membrane morphologies in relation to the system composition was proposed by Akki et al. [1999] (see figure 0.1): at a composition close to the critical point, the resulting porous structure is fibrillar and microporous (FMP), owing to the spinodal separation mechanism; otherwise, a polymer concentration slightly higher than critical value gives out a cell-tunnel microporous (CTMP) morphology, whereas a polymer concentration slightly lower than critical value will produce a globular microporous (GMP) structure. At low (or high) polymer concentrations, for which the miscibility gap is not crossed while cooling, a dense membrane will be obtained.

In DIPS operations, the composition pattern, related to the diffusion of nonsolvent into the binary solution polymer-solvent, determines the zone of entrance into the miscibility gap and thus the phase separation mechanism and final morphology (figure 0.2).
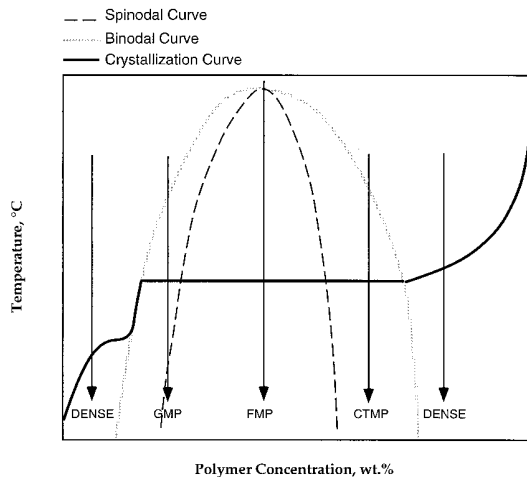
Figure 0.1: Membrane morphology in relation to the position on phase diagram for TIPS processes. Morphologies acronyms are CTMP: cell-tunnel microporous, GMP: globular microporous, FMP: fibrillar microporous, from Akki et al. [1999]

These pictures are obviously a simplified approach for correlating the membrane morphology to the processing conditions. For instance, in TIPS practice, the homogeneous solution is often cooled with a variable cooling rate, thus varying the residence time into the binodal and spinodal regions. Different residence times will influence the separation
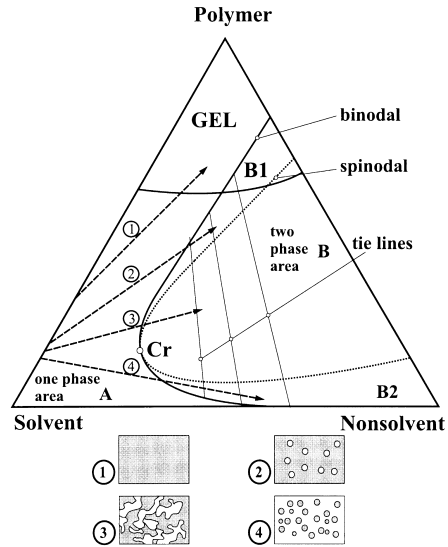
Figure 0.2: Membrane morphology in relation to the position on phase diagram for DIPS processes, from Stropnik et al. [2000]

mechanism and the final membrane microstructure. Moreover, TIPS is often carried out in two stages: firstly the solution is cooled to a temperature within the miscibility gap, then the sample is maintained at that temperature for a certain holding time. Before reaching the target temperature, the phase separation could already have started, thus influencing the resulting microstructure. The holding time can also affect the final structure in terms of domain coarsening. All things considered, the framework schematized in figure 0.1 is mainly referred to the thermodynamic features of polymer solutions: to complete the picture, a third coordinate representing the time must be taken into account, i.e. the kinetic aspects should be carefully examined.

A porous structure with a scarce pore interconnection is not suitable for industrial applications. Membranes for separations must have interconnected pores to allow the diffusion/flow of species through it. Even for scaffolds, pore interconnection is a basic requirement for cell seeding and growth and nutrients/metabolites diffusion. However, the mechanisms of interconnection formation are still unclear and a sound definition of a suitable "degree of interconnection" is not available so far, so that quantitative evaluation and comparison are not easy to be carried out. A possible explanation for the cell-tunnel pore morphology formation was proposed by Akki et al. [1999], by inferring a two step process (figure 0.3):

1. the polymer-lean phase nucleates forming separated cells;

2. the polymer-rich phase, by crystallizing, opens the tunnels between cells.

This supposition is apparently confirmed by electrical conductivity measurements, cited in the same work. However, this measurement technique is only able to discriminate between open and closed pore structures, not to elucidate the mechanism of formation. The domain connection, successive to the separated nucleation and growth, can be related to partial coalescence or secondary phase separation.
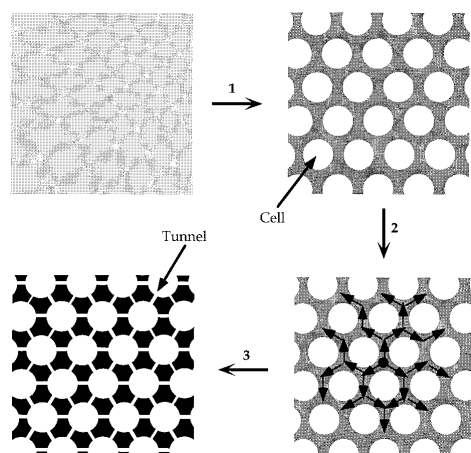
Figure 0.3: Supposed mechanism for the formation of pore interconnection, from Akki et al. [1999]

In this thesis, the attention is focused on the TIPS process, widely used for the production of membranes for various applications (especially microfiltration and membrane distillation) and scaffolds for tissue engineering purposes.

Commonly used polymers for the production of membranes for membrane distillation via phase separation are polypropylene (PP) and polyvinylidene fluoride (PVDF), whereas typical system used (binary and ternary solutions) for TIPS are: isotactic polypropylene (iPP) and diamyl phthalate (DAP) [Lin et al., 2009]; iPP, soybean oil and water [Tang et al., 2010]; polyetherimide (PEI), benzophenone and triethylene glycol [Zhang et al., 2010]; polyvinyl butyral (PVB) and polyethylene glycol [Qiu and Matsuyama, 2010]; PVDF, dibutylphthalate and dioctyl phthalate [Lu and Li, 2009]; poly-L-lactic acid (PLLA), dioxane and water [Tanaka and Lloyd, 2004].

Solutions used for DIPS preparation of microporous membranes are, among the others: PVDF, N-methyl-2-pyrrolidone (NMP) and water [Bottino et al., 2005]; PVDF and

N,N-dimethylacetamide (DMAC) [Khayet and Matsuura, 2001]; PVDF-DMAC, PVDF-DMAC-LiCl and PVDF-DMAC-PEG (polyethylene glycol) [Hou et al., 2009]; PVDF, DMAC and LiCl [Wu et al., 2007]; PLLA, dimethylsulfoxide (DMSO) and water [Moriya et al., 2009].

Examples of synthetic polymers employed for tissue engineering purposes are polylactic acid (PLA), poly(lactic acid-co-glycolic acid) (PLGA) [Hu et al., 2002], polycaprolactone (PCL) [Tanaka et al., 2006], polyurethane (PU). Among those, PLA is of increasing interest in scaffold production technology owing to its peculiar properties, above all the high degree of crystallinity and other significant mechanical performance.

The target system selected in this work is PLLA-dioxane-water, utilized for producing both microfiltration membranes [Tanaka and Lloyd, 2004] and scaffolds for tissue engineering [Carfì Pavia et al., 2008].

Experimental approach

A first approach to the characterization of the system PLLA-dioxane-water was pursued by carrying out turbidity experiments for the determination of cloud point curves. Cloud points represent the threshold between homogeneous and demixed solution, based on which a temperature range for TIPS operations is individuated. In this purpose, a dedicated experimental apparatus was designed, built and set up. A particular attention was payed to temperature control, as this class of systems presents a high sensitivity to temperature.

The cloud point was measured by means of light transmission. Via this method, a more deterministic and quantitative measure of cloud point was gained. Moreover, kinetic information can be derived from the time dependent turbidity.

Modeling approach

A second approach to the characterization of polymer solutions is based on models for phase equilibria calculations. The forefather of thermodynamic models for polymer solutions is the Flory-Huggins (FH) theory [Flory, 1942]. It is a lattice fluid (LF) model, i.e. the total volume is subdivided into elementary units occupied by a solvent molecule or a polymer segment. The entropy of mixing is computed combinatorially, whereas the enthalpy is calculated by assuming a pseudo-chemical reaction of breaking pure components contacts and forming solvent-polymer contacts.

Examples of FH model application for the calculation of phase equilibria in polymer solutions are reported in literature for a variety of polymeric systems: cellulose acetate-

solvent-water and polysulfone-solvent-water [solvents: dioxane, acetone, acetic acid, di-methylformamide (DMF), DMSO, triethyl phosphate (TEP), DMAC] [Altena and Smol-ders, 1982]; nylon, formic acid and water [Bulte et al., 1996]; polyimide, DMSO and water [Kim et al., 2001]; polyethersulfone (PES), NMP (or DMAC) and water [Barzin and Sadatnia, 2007]; PLLA-chloroform-methanol, PLLA-dioxane-water, and PLLA-dioxane-methanol [van de Witte et al., 1996]; polysulfone, NMP (or tetrahydrofuran, THF) and water [Kim et al., 1997].

Among the years, the LF model has been modified and extended to take into account various features of real systems. For example, in the original formulation the volume of a lattice site was fixed and all sites were considered occupied: further improvements were the possibility to vary the lattice site volume and the introduction of vacancies. This latter improvement made it possible the prediction of a Lower Critical Solution Temperature (LCST) in polymer solutions, i.e. a temperature below which the system gets stable and homogeneous at all compositions, not derivable from classical FH theory; in this latter, the Upper Critical Solution Temperature (UCST) is usual, i.e. a temperature above which the solution tends to thermodynamic stability (one phase).

Two kinds of lattice fluid were employed: the group contribution model by Oishi and Prausnitz [1978] (and successive corrections) and the compressible model by Sanchez and Lacombe [1976] (and successive integrations).

In the group contribution model framework, all molecules are assumed as constituted by fundamental "building blocks" (i.e. functional groups). In other words, the properties of a molecule are the "sum" of the properties of its functional groups. The most remarkable aspect of this treatment is the possibility to model whichever molecule without any need for experimental information, except for the chemical structure.

The group contribution model (or UNIQUAC) was successfully utilized for the predic-tion of vapor-liquid and liquid-liquid (binary and ternary) equilibria in molecular mixtures [Anderson and Prausnitz, 1978a,b]. The theory was extended to polymer solutions by tak-ing into account the free volume [Oishi and Prausnitz, 1978]. Examples of application of group contribution model for the prediction of phase equilibria in polymer solution are given in [Wibawa et al., 2005, Liu and Cheng, 2005, Gupte and Danner, 1987].

In our investigation, the group contribution model resulted inapplicable to the system considered, owing to high deviations in the calculated water activities. As a matter of fact, the peculiar features of water molecule are difficult to be taken into account with this kind of model.

The Sanchez-Lacombe model was developed in the statistical thermodynamics frame-work. It introduces the vacancies into the classical Flory-Huggins lattice fluid model, thus

making it possible the prediction of LCST behavior. Moreover, the theory provides an equation of state for the system, which can be used for modeling both pure species and multicomponent mixtures.

A successive improvement of the model was introduced by adding the possibility to take into account specific interactions between species in solutions. In that way, real system can be modeled with more accuracy and adherence to physical properties [Sanchez and Balazs, 1989].

The lattice fluid model extended to specific interactions was successfully applied to the PLLA-dioxane-water system for the calculation of the ternary phase diagram.

Combination of approaches

The two different approaches followed in this work, i.e. the experimental investigation of the key features of the phase separation processes and the modeling issues, are complementary. The experimental campaign was mainly dedicated to the individuation of the phase boundaries via turbidity measurements. This information can be used as an input of a thermodynamic model for the derivation of a complete phase diagram of the system (i.e. binodal and spinodal curves). As the experimental derivation of a phase diagram is time and cost consuming, the route proposed in this work would overcome the need of many experimental tests, without lacking the link between experiments and theory.

In principle, a model able to reproduce the typical features of ternary polymer solutions supported by "easy-to-derive" experimental data is a very useful tool for guiding membrane production. The utopian horizon would be a totally predictive model able to give preliminary information about new promising solvents combination (including "new" and "green" solvents); however, through the proposed route, simple experimental data are the basis for the derivation of complex information regarding phase equilibria.

By improving the knowledge about the relations between processing conditions and final morphology it is thus possible to better control membrane microstructure. Depending on the type of application, a membrane must own specific properties (e.g. pore size and porosity). In this framework, a set of commercial microfiltration membranes were examined in relation to the desalination via membrane distillation process, in order to individuate the key features that are suitable for the considered operation. After defining the most appropriate membrane properties and microstructure, it is finally possible to design a dedicated route for the production via phase separation.

Thesis outline

The first part of this thesis is dedicated to phase separation in polymer solutions. Chapters 1 and 2 present an overview on the TIPS process and on thermodynamic models. The results of phase diagram prediction are commented in Chapter 3. The details of design, construction and operation of the turbidity measurement apparatus are presented in Chapter 4. Results of cloud point measurements are discussed in Chapter 5.

The second part is about the characterization of commercial membranes, particularly for the desalination via membrane distillation. Chapter 6 is an overview on this operation. The experimental apparatuses, built on purpose, are described in Chapter 7. The results obtained are showed in Chapter 8.

The general conclusions of this work are discussed in Chapter 9, followed by a comment about possible and promising future work.

Bibliography

R. Akki, P. Desai, and A. S. Abhiraman. A framework for morphological evolution vis-à-vis phase transitions in polymer solutions. *Journal of Applied Polymer Science*, 73:1343–1355, 1999.

F. W. Altena and C. A. Smolders. Calculation of liquid-liquid phase separation in a ternary system of a polymer in a mixture of a solvent and a nonsolvent. *Macromolecules*, 15(6):1491–1497, 1982.

T. F. Anderson and J. M. Prausnitz. Application of the UNIQUAC equation to calculation of multi-component phase equilibria. 2. Liquid-liquid equilibria. *Industrial Engineering Chemical Process Design Development*, 17(4):561–567, 1978a.

T. F. Anderson and J. M. Prausnitz. Application of the UNIQUAC equation to calculation of multi-component phase equilibria. 1. Vapor-liquid equilibria. *Industrial Engineering Chemical Process Design Development*, 17(4):552–561, 1978b.

J. Barzin and B. Sadatnia. Theoretical phase diagram calculation and membrane morphology evaluation for water/solvent/polyethersulfone systems. *Polymer*, 48:1620–1631, 2007.

A. Bottino, G. Capannelli, and A. Comite. Novel porous poly (vinylidene fluoride) membranes for membrane distillation. *Desalination*, 183:375–382, 2005.

A. M. W. Bulte, E. M. Naafs, F. van Eeten, M. H. V. Mulder, C. A. Smolders, and H. Strathmann. Equilibrium thermodynamics of the ternary membrane-forming system nylon, formic acid and water. *Polymer*, 37(9):1647–1655, 1996.

F. Carfì Pavia, V. La Carrubba, S. Piccarolo, and V. Brucato. Polymeric scaffolds prepared via thermally induced phase separation: Tuning of structure and morphology. *Journal of Biomedical Materials Research Part A*, 86:459–466, 2008.

P. J. Flory. Thermodynamics of high polymer solutions. *Journal of chemical physics*, 10:51–61, 1942.

P. A. Gupte and R. P. Danner. Prediction of liquid-liquid equilibria with UNIFAC: A critical evaluation. *Industrial Engineering Chemical Research*, 26:2036–2042, 1987.

D. Hou, J. Wang, D. Qu, Z. Luan, and X. Ren. Fabrication and characterization of hydrophobic PVDF hollow fiber membranes for desalination through direct contact membrane distillation. *Separation and Purification Technology*, 69:78–86, 2009.

Y. Hu, D. W. Grainger, S. R. Winn, and J. O. Hollinger. Fabrication of poly(α-hydroxy acid) foam scaffolds using multiple solvent systems. *Journal of Biomedical Materials Research*, 59:563–572, 2002.

J. Jagur-Grodzinski. Polymers for tissue engineering, medical devices, and regenerative medicine. Concise general review of recent studies. *Polymers for Advanced Technologies*, 17:395–418, 2006.

M. Khayet and T. Matsuura. Preparation and characterization of polyvinylidene fluoride membranes for membrane distillation. *Industrial Engineering Chemical Research*, 40:5710–5718, 2001.

J. H. Kim, B. R. Min, J. Won, H. C. Park, and Y. S. Kang. Phase behavior and mechanism of membrane formation for polyimide/DMSO/water system. *Journal of Membrane Science*, 187: 47–55, 2001.

J. Y. Kim, H. K. Lee, K. J. Baik, and S. C. Kim. Liquid-liquid phase separation in polysulfone/solvent/water systems. *Journal of Applied Polymer Science*, 65:2643–2653, 1997.

Y. K. Lin, G. Chen, J. Yang, and X. L. Wang. Formation of isotactic polypropylene membranes with bicontinuous structure and good strength via thermally induced phase separation method. *Desalination*, 236:8–15, 2009.

Q. L. Liu and Z. F. Cheng. A modified UNIFAC model for the prediction of phase equilibrium for polymer solutions. *Journal of Polymer Science: Part B: Polymer Physics*, 43:2541–2547, 2005.

X. Lu and X. Li. Preparation of polyvinylidene fluoride membrane via a thermally induced phase separation using a mixed diluent. *Journal of Applied Polymer Science*, 114:1213–1219, 2009.

A. Moriya, T. Maruyama, Y. Ohmukai, T. Sotani, and H. Matsuyama. Preparation of poly(lactic acid) hollow fiber membranes via phase separation methods. *Journal of Membrane Science*, 342: 307–312, 2009.

L. S. Nair and C. T. Laurencin. Biodegradable polymers as biomaterials. *Progress in Polymer Science*, 32:762–798, 2007.

T. Oishi and J. M. Prausnitz. Estimation of solvent activities in polymer solutions using a group-contribution method. *Industrial Engineering Chemical Process Design Development*, 17(3):333–339, 1978.

Y.-R. Qiu and H. Matsuyama. Preparation and characterization of poly(vinyl butyral) hollow fiber membrane via thermally induced phase separation with diluent polyethylene glycol 200. *Desalination*, 257:117–123, 2010.

I. C. Sanchez and A. C. Balazs. Generalization of the lattice-fluid model for specific interactions. *Macromolecules*, 22:2325–2331, 1989.

I. C. Sanchez and R. H. Lacombe. An elementary molecular theory of classical fluids. Pure fluids. *Journal of Physical Chemistry*, 80(21):2352–2362, 1976.

D. F. Stamatialis, B. J. Papenburg, M. Girones, S. Saiful, S. N. M. Bettahalli, S. Schmitmeier, and M. Wessling. Medical applications of membranes: Drug delivery, artificial organs and tissue engineering. *Journal of Membrane Science*, 308:1–34, 2008.

C. Stropnik, V. Musil, and M. Brumen. Polymeric membrane formation by wet-phase separation; turbidity and shrinkage phenomena as evidence for the elementary processes. *Polymer*, 41:9227–9237, 2000.

T. Tanaka and D. R. Lloyd. Formation of poly(L-lactic acid) microfiltration membranes via thermally induced phase separation. *Journal of Membrane Science*, 238:65–73, 2004.

T. Tanaka, T. Tsuchiya, H. Takahashi, M. Taniguchi, H. Ohara, and D. R. Lloyd. Formation of biodegradable polyesters membranes via thermally induced phase separation. *Journal of Chemical Engineering of Japan*, 39(2):144–153, 2006.

N. Tang, Q. Jia, H. Zhang, J. Li, and S. Cao. Preparation and morphological characterization of narrow pore size distributed polypropylene hydrophobic membranes for vacuum membrane distillation via thermally induced phase separation. *Desalination*, 256:27–36, 2010.

P. van de Witte, P. J. Dijkstra, J. W. A. van den Berg, and J. Feijen. Phase behavior of polylactides in solvent-nonsolvent mixtures. *Journal of Polymer Science: Part B: Polymer Physics*, 34:2553–2568, 1996.

G. Wibawa, S. Takishima, Y. Sato, and H. Masuoka. An improved prediction result of entropic-FV model for vapor-liquid equilibria of solvent-polymer systems. *Journal of Applied Polymer Science*, 97:1145–1153, 2005.

B. Wu, K. Li, and W. K. Teo. Preparation and characterization of poly(vinylidene fluoride) hollow fiber membranes for vacuum membrane distillation. *Journal of Applied Polymer Science*, 106:1482–1495, 2007.

H. Zhang, Y. Zhao, H. Wang, W. Zhong, Q. Du, and X. Zhu. Phase behavior of polyetherimide/benzophenone/triethylene glycol ternary system and its application for the preparation of microporous membranes. *Journal of Membrane Science*, 354:101–107, 2010.

Part I

Phase separation in polymer solutions

The first part of the thesis pertains to the study of phase separation in polymer solutions. Since the development of Flory-Huggins model in the Forties, great advances were achieved in the field of polymer solutions, for both modeling and experimental point of view.

As regards to modeling, a great scientific effort produced many frameworks for the prediction and/or interpretation of phase behavior in polymer solutions. A general model valid for all kinds of polymer solutions is still lacking, thus a vaste latitude of thermodynamic models are available in literature, and everyone has its peculiarities and limits of applications. If the modeling takes into account the peculiar features of a real polymer solution (e.g. non-specific and specific interactions between species, influence of free volume, and their temperature and concentration dependence), a successful reproduction of the actual behavior of a given system can be achieved.

From an experimental point of view, phase separation processes for the production of polymer porous structures are still under development. The main issue encountered when preparing a polymeric foam is the high dependence of final morphology (i.e. pore size, porosity, pore interconnection) on the processing conditions (e.g. temperature and system composition, in terms of components and concentrations). At present, an exhaustive interpretation and correlation of all the process variables with the output is still missing, owing to the high complexity of the involved phenomenologies.

The studies presented in the first part of the thesis concern both the modeling and the experimental characterization of ternary polymer solutions, in relation to the Thermally Induced Phase Separation (TIPS) process. By coupling these two approaches, a representation of the system properties more adherent to the real behavior can be achieved.

1 Thermally induced phase separation (TIPS)

Thermally induced phase separation (TIPS) is a protocol currently used to prepare membranes and scaffolds. It consists in cooling a homogeneous polymeric solution to a temperature where the single phase system becomes thermodynamically unstable and spontaneously separates into a polymer-rich and a polymer-lean phase.

Generally, the system is a ternary solution of a polymer, a solvent and a nonsolvent. The nonsolvent is added to increase the free energy of mixing, thus promoting the phase separation [Schugens et al., 1996]. If one choose the appropriate system composition, the polymer-lean phase will nucleate into a continuous polymer-rich phase. The polymer-lean phase, after the solvent removal, will constitute the pores (voids), whereas the polymer-rich phase will form the "skeleton" of the scaffold.

Ease of operation, versatility and vaste latitude of achievable morphologies are the main advantages of this technique.

In this chapter, the main thermodynamic and kinetic features of TIPS process are presented, together with the related experimental methods. Moreover, the system polylactide-dioxane-water is described, reviewing the TIPS protocols proposed in literature to produce porous scaffolds.

1.1 Thermodynamic features

In the classical thermodynamics framework, a solution is stable if $\Delta G < 0$; otherwise, if $\Delta G > 0$, the pure components will constitute two separated and distinct phases. Considering a generic composition variable ξ (e.g. volume or mole fraction), an *intensive* free energy can be defined:

$$G_\xi = \frac{G}{X} \tag{1.1}$$

where X can represent the total volume or mole number. A typical $\Delta G_\xi - \xi$ diagram for a totally miscible binary system is showed in figure 1.1a. A completely miscible system at

constant temperature and pressure will fulfill the following condition:

$$\frac{\partial^2 \Delta G_\xi}{\partial \xi^2} > 0 \tag{1.2}$$

Even in the case of partially miscible systems, the condition $\Delta G < 0$ is satisfied: however, the shape of $\Delta G_\xi - \xi$ curve shows two inflection points (figure 1.1b). The condition for partial miscibility is:

$$\frac{\partial^2 \Delta G_\xi}{\partial \xi^2} < 0 \tag{1.3}$$

(a) Totally miscible system

(b) Partially miscible system
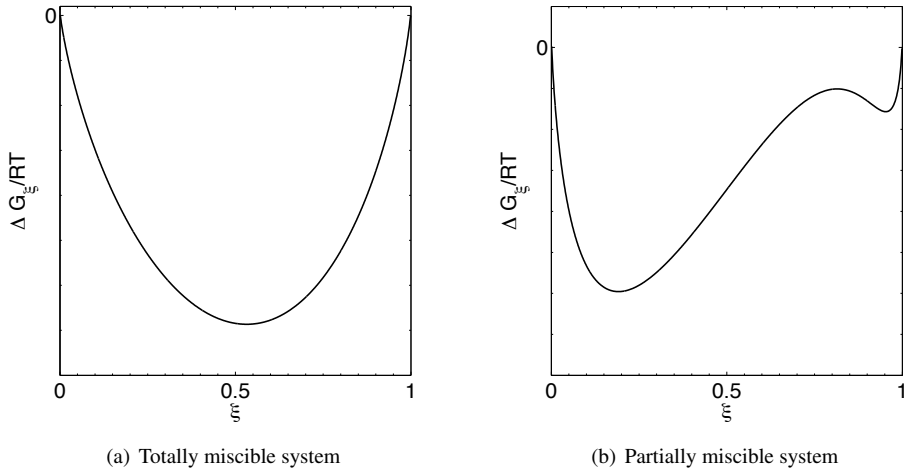
Figure 1.1: $\Delta G_\xi - \xi$ diagrams for binary systems

The limit compositions for stability are the inflection points, defined by:

$$\frac{\partial^2 \Delta G_\xi}{\partial \xi^2} = 0 \tag{1.4}$$

and the corresponding point locus is called *spinodal*. If a solution belongs to a composition inside the spinodal locus, it will spontaneously separate into two equilibrium phases. The condition of coexistence of two distinct phases with different composition is the chemical potential equality in both phases:

$$\Delta \mu_i^\alpha = \Delta \mu_i^\beta \tag{1.5}$$

where $\Delta\mu_i$ is the chemical potential variation of species i from pure to mixed state; α and β are the separated phases. The corresponding locus is called *binodal* and represents the equilibrium compositions. The chemical potential is related to free energy as:

$$\Delta\mu_i = \left.\frac{\partial\Delta G}{\partial n_i}\right|_{T,P,n_j} \tag{1.6}$$

where n_i is the mole number of component i and $j \neq i$. Referring to the intensive free energy, by means of a coordinates transformation the following relation can be obtained:

$$\left.\frac{\partial\Delta G}{\partial n_i}\right|_{T,P,n_j} = X_i \left[\Delta G_\xi + \frac{\partial\Delta G_\xi}{\partial\xi_i} - \sum_{i=1}^{c-1}\xi_j\frac{\partial\Delta G_\xi}{\partial\xi_j}\right] \tag{1.7}$$

where $X_i = \partial X/\partial n_i$ and c is the number of species in mixture. For a binary system the chemical potential of species 1 and 2 are:

$$\Delta\mu_1 = X_1\left[\Delta G_\xi + (1-\xi_1)\frac{\partial\Delta G_\xi}{\partial\xi_1}\right] = X_1\left[\Delta G_\xi - \xi_2\frac{\partial\Delta G_\xi}{\partial\xi_2}\right] \tag{1.8}$$

$$\Delta\mu_2 = X_2\left[\Delta G_\xi + (1-\xi_2)\frac{\partial\Delta G_\xi}{\partial\xi_2}\right] \tag{1.9}$$

Combining equations 1.5, 1.8 and 1.9, and by assigning $\xi \equiv \xi_1 = 1 - \xi_2$, the following equilibrium condition is derived:

$$\left.\frac{\partial\Delta G_\xi}{\partial\xi}\right|_{\xi^\alpha} = \left.\frac{\partial\Delta G_\xi}{\partial\xi}\right|_{\xi^\beta} \tag{1.10}$$

which implies that equilibrium coexisting phases have a common tangent in a $\Delta G_\xi - \xi$ diagram. Thus, when using the molar free energy ΔG_m, the independent variable is the mole fraction x; otherwise, when the volumetric free energy ΔG_v is employed, the independent variable is the volume fraction ϕ. The variable X_i in equation 1.7 is equal to 1 when referring to mole fraction; conversely, if volume fraction are employed, X_i is the partial molar volume of species i.

The considerations made above do not refer to the system energy. As a matter of fact, a spontaneous transformation is always related to a reduction in total free energy. In figure 1.2 is reported the $\Delta G_\xi - \xi$ curve for a partially miscible system, together with the tangent to the two binodal points of coordinates $(\xi^\alpha, \Delta G_\xi^\alpha)$ and $(\xi^\beta, \Delta G_\xi^\beta)$. Let us consider a point inside the unstable interval, with a free energy ΔG_ξ^I. The point which represents the system with two coexisting phases (at the same global composition) has a free energy ΔG_ξ^*, expressed as:

$$\Delta G_\xi^* = \xi^\alpha \Delta G_\xi^\alpha + \xi^\beta \Delta G_\xi^\beta \tag{1.11}$$

From the picture, it is easy to infer that the free energy of the two phase system is lower than the monophasic configuration.
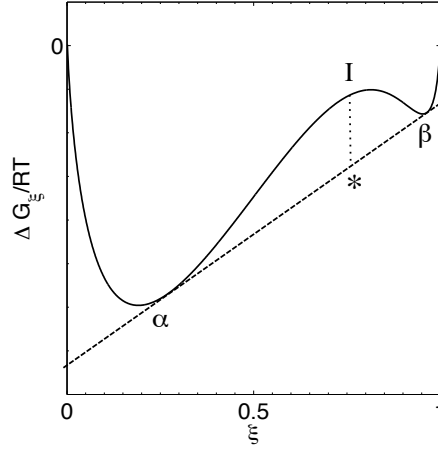
Figure 1.2: $\Delta G_\xi - \xi$ diagram for a partially miscible system. α and β are the two equilibrium phases, individuated by the tangent line

The $\Delta G_\xi - \xi$ diagrams showed above are drawn at constant temperature and pressure. From $\Delta G_\xi - \xi$ data at various temperatures (or pressures), it is possible to construct a $T - \xi$ phase diagram, according to the scheme presented in figure 1.3.

The maximum of binodal and spinodal curves is the *critical point* (or temperature, T_c), which represents the threshold temperature for phase separation. Referring to figure 1.3, the critical point is also called "Upper Critical Solution Temperature" (UCST): if the system is at a temperature $T > T_c$, the solution is homogeneous at all compositions. The critical temperature can be derived by solving the equations:

$$\begin{cases} \dfrac{\partial^2 \Delta G_\xi}{\partial \xi^2} = 0 \\[3mm] \dfrac{\partial^3 \Delta G_\xi}{\partial \xi^3} = 0 \end{cases} \tag{1.12}$$

A typical phase diagram for a binary mixture composed by a molecular solvent and a macromolecular solute is showed in figure 1.4. The miscibility lack is asymmetric: the
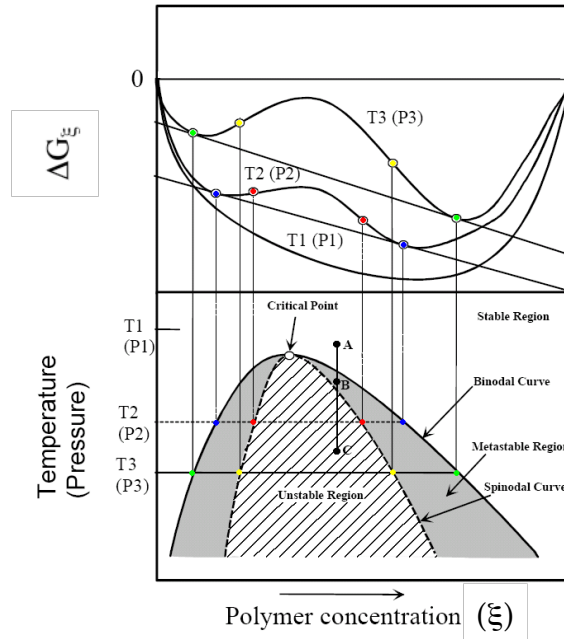
Figure 1.3: Transposition of points from $\Delta G_\xi - \xi$ diagram to $T - \xi$ plane; green and blue points are binodals, yellow and red are spinodal, adapted from Zhang [2005]

two branches of the miscibility gap are usually referred to a polymer-lean phase (left side) and a polymer-rich phase (right side). The asymmetry is due to the high difference in molecule size: by increasing the dimension of one solution component, the critical point shifts towards lower concentrations and higher temperatures. Thus, as a general rule, polymer solutions are less stable than molecular solutions (as the critical point increases) and a relatively low amount of macromolecular component can induce phase separation (as the critical point concentration is $\phi_c < 0.5$). Both these effects are directly related to the lower entropy of macromolecular systems with respect to molecular ones.

When cooling a homogeneous polymer solution, depending on the position of the starting point (i.e. composition) with respect to the critical point, different morphologies can be obtained. The proportion between polymer-lean and polymer-rich phases are determined by the lever rule, i.e. the nucleating phase belongs to the branch farther to the composition point. For example, in a solution with polymer concentration $\phi_P < \phi_C$, a polymer-rich phase will nucleate, which usually precipitates (dense phase). Otherwise, if the polymer concentration is $\phi_P > \phi_C$, a polymer-lean phase will nucleate: in this case, the polymer-rich phase will constitute a porous network, after solvent removal.
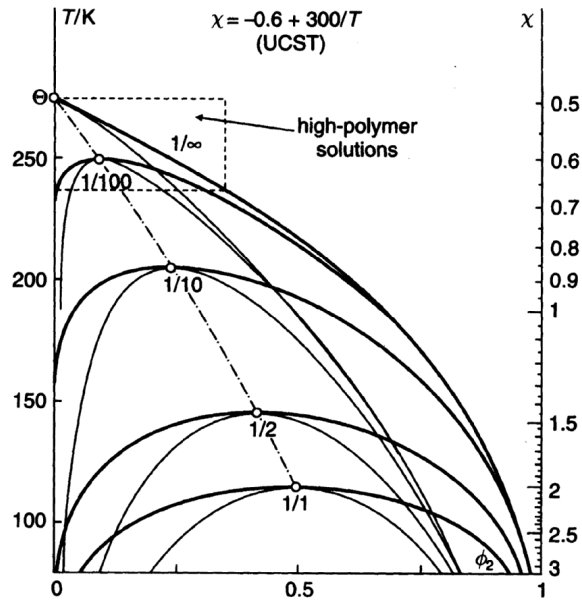
Figure 1.4: Miscibility gap for binary polymer solutions calculated with Flory-Huggins theory. The ratios are between the length of solvent and polymer, from Koningsveld et al. [2001]

For ternary systems, the concepts discussed above are still applicable with some complication. With the addition of a third variable, the $\Delta G_\xi - \xi$ diagram gets three dimensional and the binodal line is represented by the intersection of ΔG_ξ curve with the tangent plane (figure 1.5). The ternary phase diagrams are usually represented at constant temperature and pressure in a triangular diagram, where each vertex represents a pure component. The binodal and spinodal are still distinct; however, the temperature influence is less intuitive with this representation.

The phase diagram of a polymer solution can be derived experimentally. In common practice, a solution at known composition is brought to a temperature where phase separation occurs, and maintained for a long time (12-24 hours) [Tanaka and Lloyd, 2004], to allow phase separation and segregation. Later, the two phases are weighted for the determination of compositions. This procedure is quite simple for binary systems, whereas for ternary some assumptions are usually made, e.g. the polymer-lean phase is practically polymer *free*.

A more straightforward way to get experimental information about phase separation is the determination of cloud point curves. According to that procedure, a homogeneous solution is slowly cooled: when phase separation starts, it becomes cloudy. However, the cloud
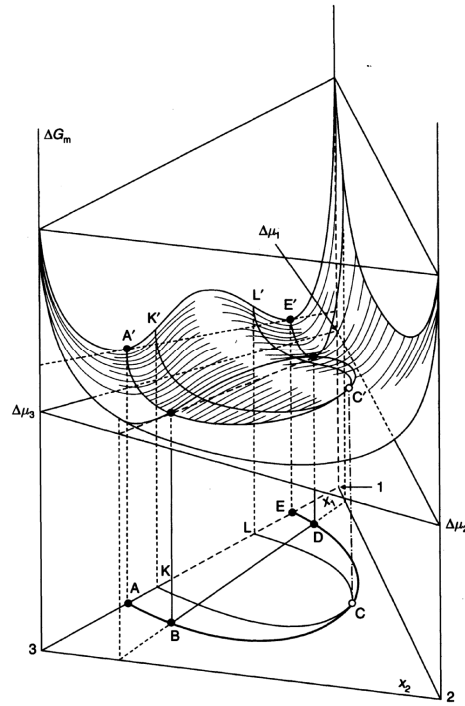
Figure 1.5: Typical shape of ΔG_m for partially miscible ternary solutions. On the bottom, the projection of binodal and spinodal, from Koningsveld et al. [2001]

point does not necessarily coincide with binodal curve, as the kinetics of demixing can influence the cloud point detection. For example, for a system in incipient phase separation, the domain size can be as small as undetectable with common methods.

For ternary polymer solutions, usually the cloud point curves are represented in a $T - \xi_P$ plane, where ξ_P is the polymer concentration (figure 1.6). The solvent/nonsolvent ratio is taken as a constant parameter. This kind of representation recalls a binary phase diagram: however, some important differences must be noticed:

- the cloud point curve does not show a maximum (i.e. a critical point);

- the composition of separated phases are not directly derivable;

- there is not a spinodal locus.

The composition of separated phases are derived by tracing tie lines on the ternary phase diagram, whereas the cloud point curve roughly represents (even if not rigorously) one of
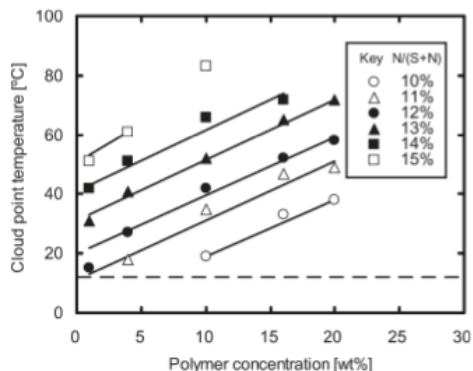
Figure 1.6: Cloud point curves for the system PCL-dioxane-water, from Tanaka et al. [2006]

the two branches of the binodal curve. To overcome this limitation, the cloud point curve can be coupled with a *shadow curve*, which represents the compositions in equilibrium with cloud points (figure 1.7). Obviously, it cannot be directly derived from cloud points: the complete ternary phase diagram is needed (figure 1.8).
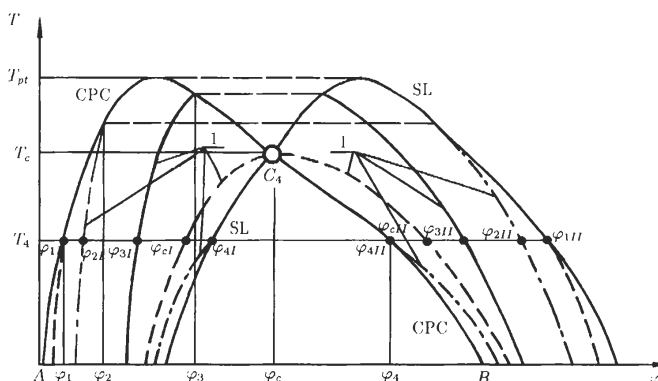
Figure 1.7: Schematic of the quasibinary section of a ternary (multicomponent) system, from Klenin [2000]

Although cloud point curves present several limitations in the description of phase equilibria in multicomponent systems, they are still useful for the characterization of ternary polymer solutions. The phase boundaries detected are those interesting in membrane production, and a simple map of homogeneous/demixed state is useful for guiding an experimental campaign on porous structure preparation.

Thermodynamic diagrams give information about a possible phase separation process, depending on temperature, pressure and composition. Moreover, composition of separated
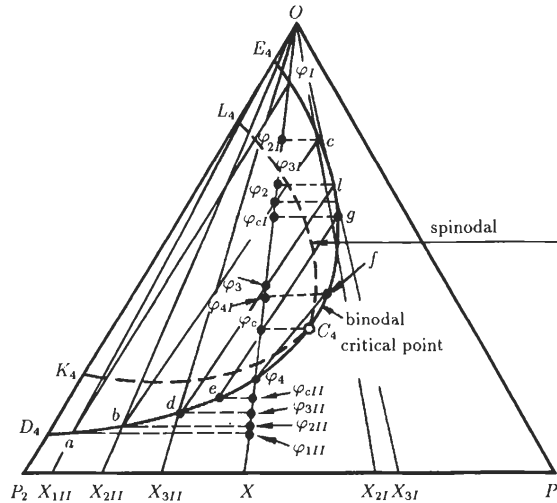
Figure 1.8: State diagram of the ternary system composed of one solvent (0) and two polymers (P1 and P2), from Klenin [2000]

phases and nucleating phase are determined by thermodynamics. The dense, microporous, macroporous nucleating phase in its turn determines the type of microstructure obtained [Akki et al., 1999]. Therefore, knowing the phase diagram of a system helps to choose the best processing parameters in order to obtain the desired microstructure.

Nevertheless, the construction of a phase diagram for a ternary polymeric system is not straightforward. Experiments for the determination of tie lines are time-consuming. Moreover, as commercial polymers are polydisperse, phase diagrams loose physical meaning.

Besides the liquid-liquid phase separation, other transitions can occur during TIPS, as crystallization and vitrification (see figure 1.9) [van de Witte et al., 1996c].

1.1.1 Flory-Huggins model

Flory-Huggins model (FH) is based on lattice fluid theory: the system is supposed as a lattice with each site occupied by a solvent molecule or a polymer monomer (see figure 1.10). The free energy of the system is calculated as the sum of two distinct contributions:

1. the random mixing of polymer chains with the solvent molecules, neglecting all possible energetic interactions (i.e. the combinatorial entropy);

2. the interaction energy between species in mixture (i.e. enthalpy), which, in its turn, can affect entropy.
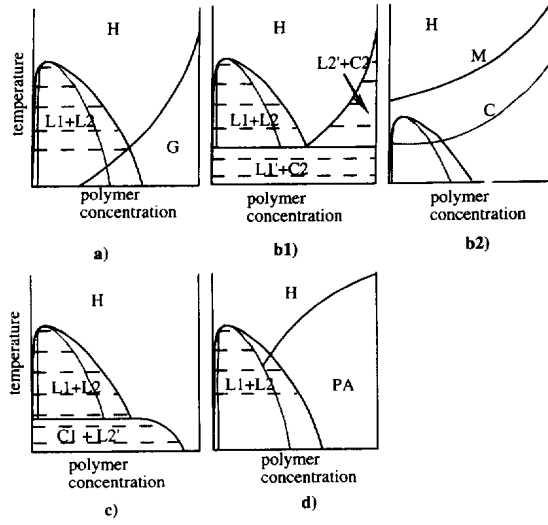
Figure 1.9: Phase diagrams of binary polymer solutions. H: homogeneous solutions; L1 and L2: liquid phases; G: glassy state; C2: polymer crystallites; PA: polymer association; M: melting point; C: crystallization. From [van de Witte et al., 1996c]

To compute the entropy, the lattice is assumed empty: firstly, the polymer chains are disposed into the lattice; note that a polymer chain will occupy only adjacent lattice sites. The monomer and solvent volume are assumed to be equal to the lattice site volume. The resulting combinatorial entropy is:

$$\Delta S = -k \left(N_1 \ln \phi_1 + N_2 \ln \phi_2 \right) \tag{1.13}$$

where k is the Boltzmann constant, N_i is the number of molecules or polymer chains and ϕ_i is the volume fraction, defined as:

$$\phi_i = \frac{r_i N_i}{r_1 N_1 + r_2 N_2} \tag{1.14}$$

where r_i is the number of sites occupied by the species i. For a molecular species $r = 1$, whereas for a polymer chain r coincides with the (average) degree of polymerization. At fixed polymer volume fraction ϕ_2, the number of polymer chains in solution decreases with increasing the chain length. As a matter of fact, by rearranging equation 1.14 one gets:

$$N_2 = \frac{\phi_2}{1 - \phi_2} N_1 r_1 \frac{1}{r_2} \tag{1.15}$$

Figure 1.10: Example of lattice with solvent (white sites) and polymer (grey sites), from Teraoka [2002]

Therefore, by increasing the polymer chain length (r_2), the system entropy decreases in absolute value (see equation 1.13).

For the computation of mixing enthalpy, a quasi chemical reaction is assumed, and the contact interaction energy is expressed as:

$$\Delta w = w_{12} - \frac{1}{2}(w_{11} + w_{22}) \tag{1.16}$$

where w_{ij} is the interaction energy between species i and j. Thus, the mixing enthalpy is calculated multiplying Δw times the number of contacts between species 1 and 2:

$$\Delta H = zN_1\phi_2\Delta w \tag{1.17}$$

where z is the lattice correlation number. Defining an interaction parameter:

$$\chi_{12} = \frac{z\Delta w}{kT} \tag{1.18}$$

the free energy of mixing is expressed as:

$$\Delta G = \Delta H - T\Delta S = kT(N_1 \ln \phi_2 + N_2 \ln \phi_2 + \chi_{12}N_1\phi_2) \tag{1.19}$$

From this expression, chemical potential, binodal and spinodal curves can be derived. If the solution has a miscibility gap, the critical point coordinate is:

$$\phi^C = \frac{1}{1 + \sqrt{r}} \tag{1.20}$$

where the volume fraction and the occupied sites refer to polymer. This expression shows that increasing the polymer chain length, the critical point moves towards lower polymer concentrations (see figure 1.4). Also the interaction parameters depends on r; at the critical point:

$$\chi^C = \frac{1}{2} + \frac{1}{2r} + \frac{1}{\sqrt{r}} \tag{1.21}$$

As χ^C decreases by increasing r, and $\chi \propto 1/T$ (see equation 1.18), the critical temperature increases by increasing r (as shown in figure 1.4).

For high polymer solutions, $r \to \infty$: the threshold between homogeneous and demixed solution is thus $\chi = 1/2$ (also called *theta condition*). If $\chi < 1/2$ (even for negative values), the solution will be homogeneous; conversely, if $\chi > 1/2$, the molecular component is a nonsolvent for the polymer.

The free energy of mixing (at constant volume) for a multicomponent system can be expressed as:

$$\Delta g = \frac{\Delta G}{V} = kT \left[\sum_{i<j} \sum_j \phi_i \phi_j \chi_{ij} + \sum_i \frac{\phi_i}{v_i} \ln \phi_i \right] \tag{1.22}$$

where v_i is the molar volume. It is worth noticing that in this expression the molar volume is used instead of the r parameter, thus making it more easily applicable to real systems. As a matter of fact, with this formulation different sizes of lattice sites are taken into account. The volume fraction is defined as:

$$\phi_i = \frac{N_i v_i}{\sum N_i v_i} \tag{1.23}$$

The interaction parameter between molecular species can be derived from excess free energy data. A correlation was provided by Flory [1953]:

$$\chi_{12} = \frac{1}{x_1 v_2} \left[x_1 \ln \frac{x_1}{v_1} + x_2 \ln \frac{x_2}{v_2} + \frac{\Delta G^E}{RT} \right] \tag{1.24}$$

The FH interaction parameters can be also derived from solubility (or Hildebrand) parameters [Sanchez, 1987]:

$$\chi_{ij} = \frac{(\delta_i - \delta_j)^2}{RT} \tag{1.25}$$

The chemical potential is given by:

$$\frac{\Delta\mu_i}{kT} = \ln\phi_i + \left(1 - \frac{v_i}{v}\right) - v_i\left[\sum_j \phi_j\chi_{ij} - \sum_{i<j}\sum_j \phi_i\phi_j\chi_{ij}\right] \qquad (1.26)$$

where v is the averaged molar volume:

$$\frac{1}{v} \equiv \sum_i \frac{\phi_i}{v_i} \qquad (1.27)$$

The spinodal equation for a n components system is the determinant of the matrix:

$$\begin{vmatrix} g_{11} & g_{12} & \cdots & g_{1n} \\ g_{21} & g_{22} & \cdots & g_{2n} \\ \vdots & \vdots & \ddots & \vdots \\ g_{n1} & g_{n2} & \cdots & g_{nn} \end{vmatrix} = 0$$

where $g_{ij} = \partial^2 g/\partial\phi_i\phi_j$.

The spinodal equation for a ternary system is then:

$$g_{22}g_{33} - g_{23}^2 = 0 \qquad (1.28)$$

where the subscripts refer to the partial derivative with respect to ϕ_2 and ϕ_3.

The second derivatives are computed as:

$$g_{22} = \frac{1}{v_1\phi_1} + \frac{1}{v_2\phi_2} - 2\chi_{12} \qquad (1.29)$$

$$g_{33} = \frac{1}{v_1\phi_1} + \frac{1}{v_3\phi_2} - 2\chi_{13} \qquad (1.30)$$

$$g_{23} = g_{32} = \frac{1}{v_1\phi_1} - \chi_{13} - \chi_{12} + \chi_{23} \qquad (1.31)$$

Substituting these expressions in equation 1.28 one gets:

$$\sum_{i<j}\sum_j \frac{1}{v_iv_j\phi_i\phi_j} - 2\sum_i \frac{\chi_{jk}}{v_i\phi_i} + Q = 0 \qquad (1.32)$$

where Q is defined as [Tompa, 1956]:

$$Q = 2\sum \chi_{ij}\chi_{ik} - \sum \chi_{ij}^2 \qquad (1.33)$$

Equation 1.32 can be rewritten in a more convenient form:

$$\sum v_i\phi_i - 2\sum \phi_i\phi_j v_i v_j \chi_{ij} + Q\prod v_i\phi_i = 0 \qquad (1.34)$$

The Flory-Huggins theory for ternary solutions was used by van de Witte et al. [1996b] to study the influence of thermodynamic parameters on the phase diagrams. Binary interaction parameters were drawn from experiments and are reported in the same reference. No ternary interaction parameter was used, owing to the difficulty of measure. Nevertheless, a sensitivity analysis showed a large influence of the ternary interaction parameter on the amplitude of the miscibility gap.

1.2 Kinetic features

Kinetic features influence the process rate, and therefore the morphology obtained. Kinetics of phase separation depends on temperature, composition, cooling rate and demixing time. Each parameter affects the final morphology of porous structure. The pore structure can be fixed by a rapid decrease of polymer chain mobility, which can be caused by polymer crystallization or vitrification, and has been also related to changes in the polymer/solvent interaction. In this way, the phase separation is kinetically inhibited, although it should go on by pure thermodynamic considerations [Nunes and Inoue, 1996].

Nucleation and growth (NG) is the expected mechanism when a system slowly crosses the binodal line and enters the metastable region of the phase diagram. If the activation energy for the formation of nuclei is higher than their surface energy, dispersed nuclei can form and become stable, usually in a slow process. Spinodal decomposition (SD) occurs when a fast quench brings the system into the two phase region limited by the spinodal curve, or even in a slow crossing of the metastable region close to the critical point. In this case, the phase separation occurs with concentration fluctuations of increasing amplitude, producing two continuous phase [Nunes and Inoue, 1996].

In the classical nucleation theory, the free energy variation for the formation of a spherical domain with radius R is:

$$\Delta F = -\frac{4}{3}\pi R^3 \Delta G + 4\pi R^2 \sigma \qquad (1.35)$$

where ΔG is the Gibbs free energy variation referred to the supersaturation and σ is the interfacial tension between the forming domains and the continuous phase. The first term is proportional to the domain volume, whereas the second one is proportional to the surface. Figure 1.11 represents these two contribution to total free energy as a function of domain radius. The value R^* is the so called *critical radius*: if a domain has $R < R^*$, it is unstable

and will redissolve in the continuous phase; on the other hand, if $R > R^*$, the domain is stable and it will spontaneously grow. When the system is inside the spinodal region, the critical radius value tends to zero ($R^* \rightarrow 0$): the phase separation and growth occur spontaneously for any domain size.
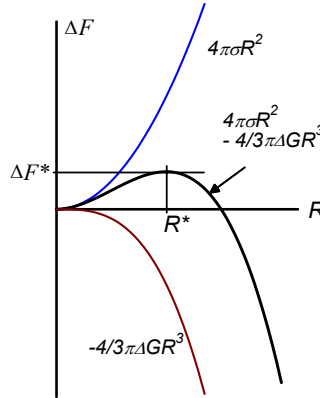
Figure 1.11: Free energy variation for the formation of a spherical nucleus, from Zhang [2005]

A simple model for pore diameter estimate in TIPS of binary solutions is reported in [Barton and McHugh, 2000]. The droplet volume increases linearly with time, and the kinetic data can be derived from light scattering measurements or spinodal calculations. The heat transfer is considered as one-dimensional. The solution gives a distribution of pore diameter, which increase from surface to bulk, reaching a limit value.

A simulation of pore growth rate showed that firstly it increases and then it decreases with undercooling [Barton et al., 1998]. The thermodynamic and kinetic aspects were decoupled denoting an opposite influence: higher undercooling will enhance the thermodynamic driving force, but will also slow down the diffusion process. A confirmation of this qualitative behavior was measured via light scattering by the same research group (see figure 1.12).

Besides NG and SD mechanisms, the microstructure evolution can be affected by the domain coarsening. Different coarsening mechanisms can take place during phase separation, and they are not necessarily mutually exclusive:

- coalescence

- Ostwald ripening

- hydrodynamic flow
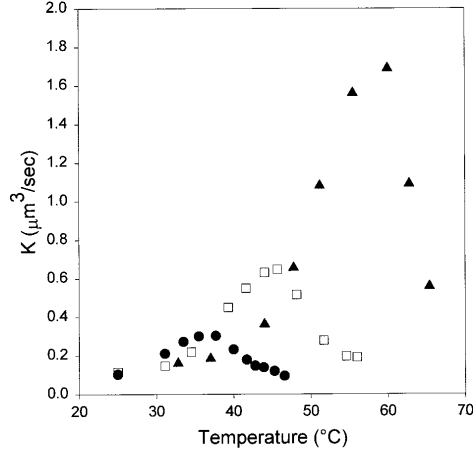
Figure 1.12: Temperature dependence of the growth rate for the system PMMA, NMP and glycerin at various nonsolvent concentrations (20% wt PMMA), from Graham et al. [1999]

Coalescence is the merging of growing domain droplets due to diffusion driven impingements. The average droplet radius growing by coalescence is described by a power law:

$$R \propto \left(\frac{kT}{\eta}\right)^{1/3} t^{1/3} \tag{1.36}$$

where k is the Boltzmann's constant, T is the temperature and η is the viscosity of the continuous phase.

Ostwald ripening is related to the surface area of separating domains: droplets with a radius below the critical value (see equation 1.35) are unstable and will be solved into the continuous phase. Also in this case, the kinetics of growth is expressed by a power law:

$$R \propto (D\xi)^{1/3} t^{1/3} \tag{1.37}$$

where D is the diffusion coefficient and ξ is the correlation length in polymer solutions.

The hydrodynamic flow is generated by the different size of droplets, which induce a flow of the solution. The drop size increases linearly with time:

$$R \propto \left(\frac{\sigma}{\eta}\right) t \tag{1.38}$$

where σ is the droplet interfacial tension.

These mechanisms can overlap, generating a mixed coarsening process.

Another possible mechanism is the coalescence-induced-coalescence process [Martula et al., 2000]. It postulates that the droplets diffusion and impingement induces a flow field in the near region, which causes the motion and thus the impingement of other close droplets. Also in this case the kinetics of growth is described by a power law:

$$R \propto t^\lambda \tag{1.39}$$

where the scaling exponent λ was found $0.22 < \lambda < 0.47$ for the system iPP and diphenyl ether.

The growth mechanism can be determined experimentally [Matsuyama et al., 1999]. From d vs t data it is possible to calculate a kinetic constant, which can be also estimated theoretically for Ostwald ripening and coalescence. Comparison of theoretical and experimental values gives an indication of the predominant growth mechanism. A morphological analysis via SEM is needed to validate this characterization.

Song and Torkelson [1994] measured the growth rate in quenched polystyrene-diethyl malonate via SEM imaging. The power law exponent (see equation 1.39) was found to be proportional to the quenching depth: at the lowest investigated temperature $\lambda = 0.33$, whereas at a temperature close to cloud point $\lambda = 0.09$. The λ exponent was empirically correlated to the separation temperature as:

$$\lambda^2 \propto \frac{1}{T} \tag{1.40}$$

although no physical explanation was provided.

From light scattering measurement it is possible to quantify the kinetics of phase separation [Graham and McHugh, 1998]. In this paper, measurement were carried out by varying the quench temperature and the polymer concentration. Beyond the polymer crystallization temperature, the kinetics was enhanced at lower temperatures and lower polymer concentration. Below the polymer crystallization temperature, the kinetics was enhanced at higher temperatures and lower polymer concentration.

1.3 Methods of investigation

Various experimental methods are adopted to measure thermodynamic and kinetic features of TIPS. The cloud point curve is usually derived by means of turbidity measurements or differential scanning calorimetry (DSC). Light scattering techniques allow the determination of separation mechanisms (i.e. nucleation and growth or spinodal) and growth rate.

1.3.1 Turbidity

The simplest technique for cloud point detection is based on turbidity measurement. Turbidity (A) is defined as:

$$A = \frac{1}{\delta} \ln \left(\frac{I_0}{I} \right) \tag{1.41}$$

where δ is the sample thickness, I_0 is the incident light intensity and I is the light intensity exiting the sample. When phase separation starts, the growing domains scatter a fraction of incident light, thus resulting in a decreasing I detected.

For a system of nonabsorbing spherical particles with equal radius R, the turbidity can be estimated as [Melik and Fogler, 1983]:

$$A = \pi N R^2 Q(R, \lambda, m) \tag{1.42}$$

where N is the particle concentration and Q the scattering coefficient, dependent of particle radius R, light wavelength λ and ratio between the refractive index of particle and suspending medium m:

$$m = \frac{\mu_p}{\mu_m} \tag{1.43}$$

where μ_p and μ_m are the refractive index of particle and suspending medium, respectively.

The cloud point detection is a common method to determine phase boundaries [van de Witte et al., 1996b]. A homogeneous solution is cooled down slowly: when phase separation starts, the suspension will start to appear cloudy. Often the cloud point detection is made out visually [Chen et al., 2010, Tanaka et al., 2006, Tanaka and Lloyd, 2004, Hua et al., 2002, Graham et al., 1999, van de Witte et al., 1996b]. However, this method is not deterministic and quantitative. A more precise way to carry out turbidity measurement is to adopt light transmission detection [Bulte et al., 1996, Bae et al., 1991]. This technique was also successfully employed for the characterization of immersion precipitation [Kim et al., 2001, Stropnik et al., 2000, Matsuyama et al., 1999]. In this case, the turbidity evolution with time is measured at constant temperature (figure 1.13), thus giving information about the rate of phase separation and nonsolvent/solvent diffusion.

An example of a typical light transmission pattern for TIPS is showed in figure 1.14. The cloud point is individuated by a sudden decrease in transmitted light with decreasing temperature. When heating a demixed solution, usually it will become clear at a temperature higher than the cloud point temperature. However, there is in literature an example of turbidity measured by heating a demixed sample [Bulte et al., 1996]. From a thermodynamic point of view, the liquid-liquid demixing and re-mixing should occur at the same

(a) From Kim et al. [2001]

(b) From Stropnik et al. [2000]
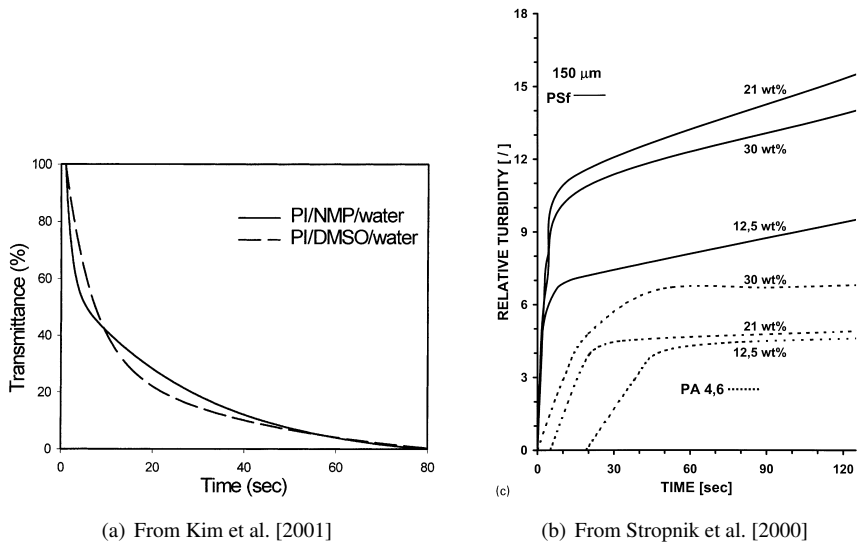
Figure 1.13: Turbidity patterns in immersion precipitation
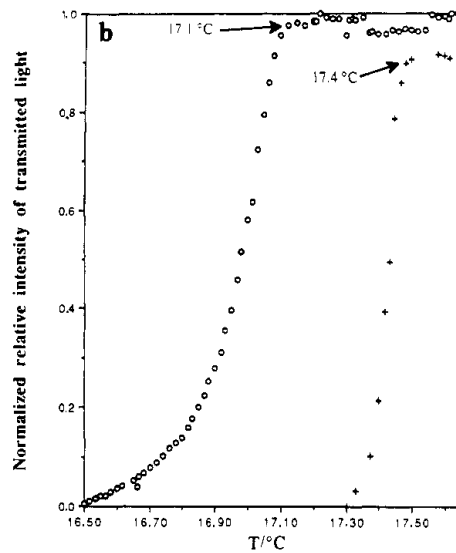
Figure 1.14: Example of turbidity pattern. Circles: cooling, crosses: heating, from [Bae et al., 1991]
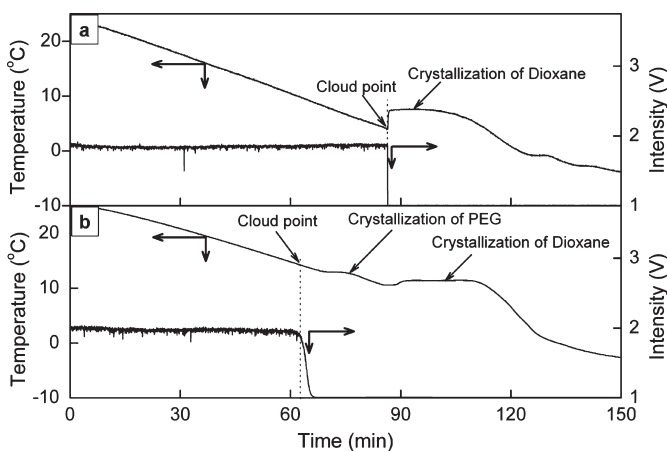
Figure 1.15: Turbidity in a PEG-dioxane system. (a) PEG600/dioxane solution with 10% wt PEG concentration; (b) PEG2000/dioxane solution with 30% wt PEG concentration, from Kim et al. [2009]

temperature; however, the re-dissolution of the separated phases can be a slow process, thus "reverse" cloud point measurements should be performed with sufficiently long holding times.

Figure 1.15 shows both thermal history and light transmission pattern for a PEG-dioxane system. Also in this case, the transmitted light decreases rapidly to zero in a relatively short time. Moreover, the solidification of solvents can be detected easily.

If the kinetics of demixing is sufficiently fast, the cloud point curve reasonably coincides with the binodal curve. van de Witte et al. [1996b] assumed that liquid-liquid phase separation produces an instantaneous turbidity increase of the solutions; on the other hand, crystallization results in a slow whitening of the solution sample. The thermal history plays an important role in the determination of the cloud point. Figure 1.16 shows the influence of cooling rate on the measured cloud point. The first example (figure 1.16a) refers to the binary systems iPP-dialkyl phthalates, which show an UCST type of miscibility gap: the cloud point shifts towards lower temperatures when increasing the cooling rate. Conversely, in the second example (figure 1.16b), the system considered is the poly(N-isopropylacrylamide)-water solution, which shows a LCST: the cloud point shifts towards higher temperatures with increasing the heating rate. To determine a "thermodynamic" cloud point, the cooling rate must be as low as possible. In experimental practice, however, it is only possible to determine a "critical" cooling rate below which the measured cloud point is not affected by the cooling rate. In figure 1.17 are showed the light transmis-
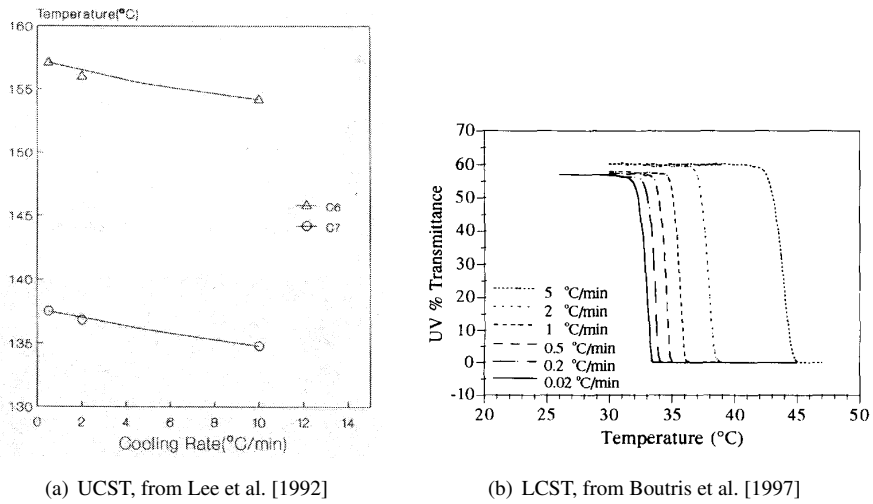
(a) UCST, from Lee et al. [1992]   (b) LCST, from Boutris et al. [1997]

Figure 1.16: Influence of cooling rate on cloud point recorded
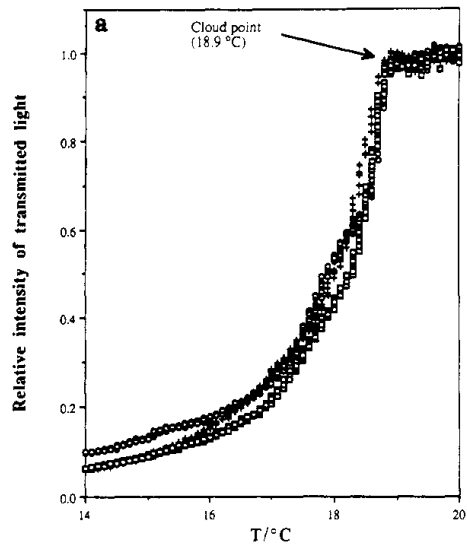
Figure 1.17: Light transmission pattern in polystyrene-cyclohexane, from [Bae et al., 1991]

37

sion patterns for the polystyrene-cyclohexane system at various cooling rates: in all cases considered (0.1, 0.3 and 0.5°C/min), the cloud point is not affected by the cooling rate.

The onset of turbidity increase is when the domain size is comparable with the incident light wavelength; after, if the domain size increases, the turbidity will continue to increase accordingly. The rate of change of turbidity is a measure of the domain growth, as turbidity is the result of light scattering upon the division surfaces of the two liquid phases. In the early stages of phase separation, the turbidity should increase linearly with time [Matsuyama et al., 1999], since the turbidity is proportional to the domain size:

$$A \propto d^3 \tag{1.44}$$

because the domain size is proportional to time. During intermediate and late stages of phase separation, the linear relation between turbidity and light does not hold, owing to the complex scattering patterns associated to relatively large particles.

1.3.2 Light scattering

Light scattering is the result of light redirection due to inhomogeneity into the enlightened sample. The non-homogeneity of the sample can be related for example to suspended solid particles, or to liquid droplets dispersed into the fluid phase. In this latter case, the boundary surfaces between the separated phases are responsible for light scattering.

Depending on the incident light wavelength and the particle size, different scattering regimes can be experienced. It is convenient to define a dimensionless particle size:

$$\alpha = \frac{2\pi R}{\lambda} \tag{1.45}$$

where R is the particle radius and λ is the incident light wavelength. If $\alpha < 0.16$, i.e. the particles radius is $R < \lambda/20$, Rayleigh scattering occurs. Otherwise, if $\alpha > 0.16$, the light scattering is more complex, highly dependent on the particle dimension: in this case, the system can be modeled by means of Mie scattering theory.

Light scattering can be used for the detection of phase separation mechanism. The NG mechanism will give out a monotonic decrease of scattered light intensity (see figure 1.18a), which can be fitted to a power law:

$$I = K(t - \tau)^n \tag{1.46}$$

where K is the kinetic constant (growth factor), τ is the onset time for phase separation and n is the power law index related to the nucleation mechanism: for $n = 3$, the nucleation

is heterogeneous, whereas if $n = 4$, homogeneous nucleation occurs [Nunes and Inoue, 1996].

As regards to SD investigation, time-resolvable light scattering measurements with angle dependence can be employed. Results are usually in accord with the Cahn theory [Nunes and Inoue, 1996]. In the early stage of SD the shape of scattered light intensity vs. angle passes through a maximum (see figure 1.18b), corresponding to a typical diffraction halo pattern; in the intermediate or late stage of SD, the I peaks shift towards smaller angle with time and increase in intensity. In this latter case, the phase separated structure is assumed to grow in the time scale of the peaks shifting [Matsuyama et al., 2000].

(a) Nucleation and growth

(b) Spinodal decomposition
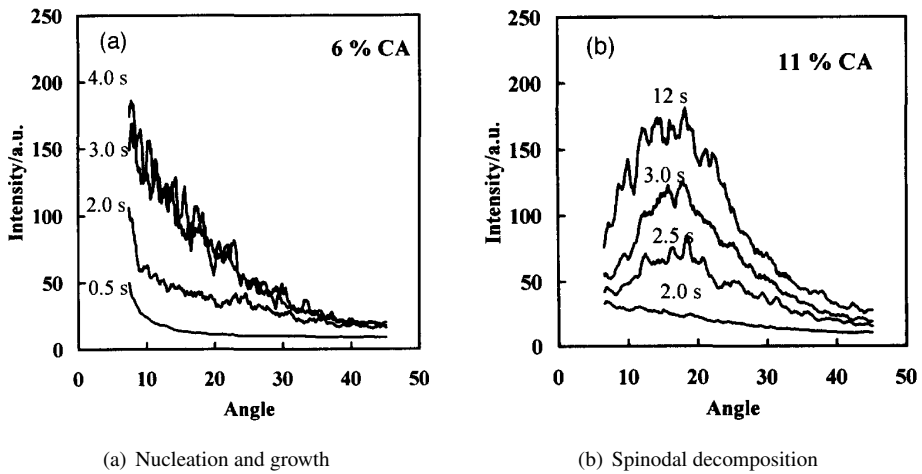
Figure 1.18: Light scattering patterns for the system cellulose acetate, acetone and water, from Nunes and Inoue [1996]

At the early stage of SD, the linear Cahn theory describes the relation between scattered intensity I_s and time:

$$I_s(q, t) \propto \exp\left[2R(q)t\right] \qquad (1.47)$$

where $R(q)$ represents the growth rate of the concentration fluctuation and q is the so called *wavenumber*:

$$q = \frac{4\pi\mu}{\lambda_0} \sin\left(\frac{\theta}{2}\right) \qquad (1.48)$$

where μ is the refractive index of the solution and λ_0 is the light wavelength in vacuum. The growth rate $R(q)$ can be expressed as:

$$R(q) = D_{app} \cdot q^2 \left(1 - \frac{q^2}{2q_m^2} \right) \tag{1.49}$$

where D_{app} is the apparent diffusion coefficient and q_m is the wavenumber of the I_s peaks (note that q_m is constant in early stage of SD). The values of parameters D_{app} and q_m are easily derivable by fitting experimental results with a straight line in a $R(q)/q^2$ vs q^2 plot. From these parameters, a characteristic time for phase separation can be drawn [Matsuyama et al., 2000]:

$$\tau_s = (D_{app} \cdot q_m^2)^{-1} \tag{1.50}$$

1.3.3 Differential scanning calorimetry

If the liquid-liquid phase separation exhibits heat effects, they could be measured via differential scanning calorimetry (DSC).

An example of DSC characterization of phase boundaries was presented by van Emmerik and Smolders [1973], who analyzed the binary solution poly-(2,6 dimethyl-1,4 phenylene-oxide) (PPO) and toluene. The resulting DSC thermograms for cooling and heating are reported in figure 1.19. Authors stated that with a sufficiently high cooling rate (in this case 16°C/min), the onset of liquid-liquid phase separation via nucleation and growth is inhibited: the exothermic heat effect is thus related to spinodal decomposition and the temperature T_1 is assumed to be the spinodal temperature for the considered system. Conversely, when the sample is reheated, the endothermic heat effect is related to the remixing of separated phases: the temperature T_2 is thus assumed to be the cloud point; further heating above T_2 did not show any heat effect.

The presented framework presents two important weaknesses:

1. from the phase diagram reported in the same paper, constructed with the as derived DSC results, the temperature difference between cloud point and spinodal for a solution with 30% wt of polymer is $\approx 30 \div 35°C$; this means that cooling at 16°C/min, the sample is in the metastable zone for 2 minutes: the assumption that in this time no nucleation occurs is too "strong" to be reasonably accepted;

2. the cloud point is defined as *the temperature at which a homogeneous solution becomes cloudy upon slowly cooling*; in this case, the cloud point is derived by heating a sample which experienced phase separation. As stated before (see section 1.3.1), usually the remelting of phase separated system occurs at a temperature higher than
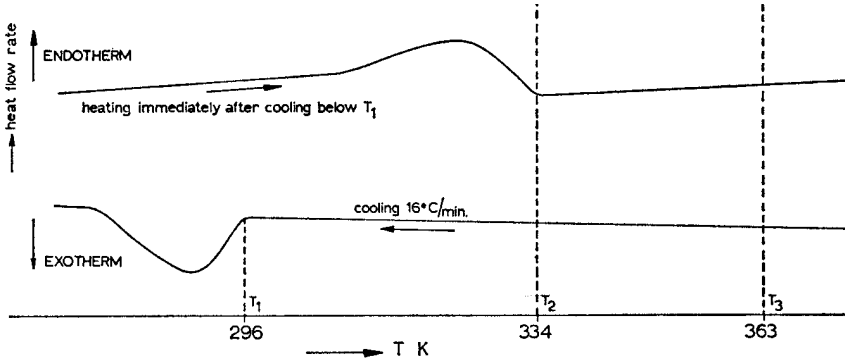
Figure 1.19: Schematic of DSC thermograms for a PPO-toluene solution (30% wt of polymer), from van Emmerik and Smolders [1973]

cloud point temperature: this means that cloud point measured during heating are always overestimated.

The same method was used for the determination of spinodal points in the system PMMA-sulfolane [Tsai and Torkelson, 1990]. The critical weaknesses discussed above are also present in this work. The cloud point curve was measured via light transmission (see figure 1.20), whereas the spinodal points were measured via DSC at a cooling rate of $40°C/min$ (see figure 1.21). Even in this case, at a cooling rate of $40°C/min$, the solution spent at least 5 seconds into the metastable zone, thus making it possible the formation of nuclei belonging to the separating phase. These nuclei will obviously influence the phase separation and therefore the detected spinodal temperature.

Different results were drawn from DSC measurements in a PLLA-chloroform-methanol solution [van de Witte et al., 1996a]. An exothermic transition related to liquid-liquid demixing, often distinguishable from crystallization, was recorded by cooling a solution. The liquid-liquid phase separation was associated to an exothermic step in DSC traces; the magnitude of the step was influenced by the polymer concentration. The as obtained demixing temperatures were comparable with those derived from turbidimetry. Moreover, by changing the cooling rate (from 2 to $10°C/min$), no shift of the demixing temperature was recorded. Conversely, the cooling rate influenced the magnitude of the exothermic step.

The DSC characterizations showed are highly conflicting as far as methods and results are concerned. In the former case, only the spinodal can be recorded at high cooling rates; at low and mild cooling rates, no traces of liquid-liquid phase separation were detected. In the latter case, the cloud point is detected with mild cooling rates. In conclusion, DSC
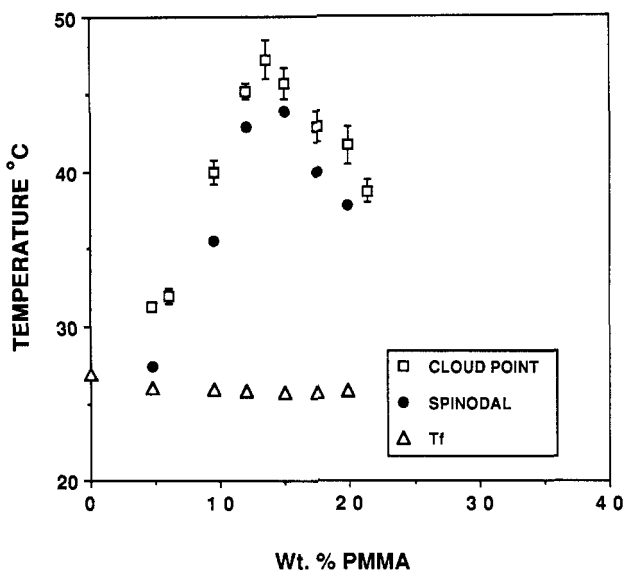
Figure 1.20: Phase diagram for the system PMMA-sulfolane, from Tsai and Torkelson [1990]
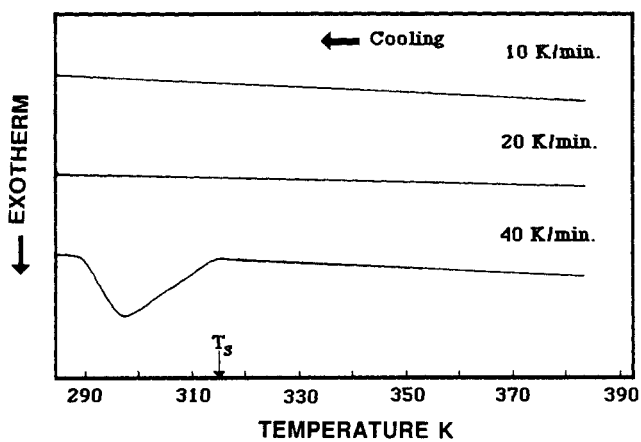
Figure 1.21: DSC curves at various cooling rate for the system PMMA-sulfolane (12.5% wt of PMMA), from Tsai and Torkelson [1990]

measurements for phase boundaries detection in this class of system, to become a useful, quantitative and deterministic method of investigation, need a deeper investigation and discussion, in order to define proper protocols and to correctly interpret the results.

1.4 The polylactide-dioxane-water system

The polylactide-dioxane-water system has been widely used for the production of porous structures via phase separation. Owing to the chiral nature of the monomer (lactic acid), three different kinds of PLA can be produced, with different properties: PLLA and PDLA are composed by only stereoisomer D or L, respectively; PDLLA is a copolymer composed by both stereoisomers. The most widely used for scaffold fabrication is the PLLA, as it is a semicrystalline polymer and a porous structure with good mechanical properties can be produced; on the other hand, PDLA and PDLLA are amorphous, thus their pristine application is of small interest. However, blends of PLLA and amorphous PLA can be used for tuning peculiar properties of scaffolds, e.g. degradation rate.

Table 1.1: Summary of PLLA and PDLLA solubility in some common organic solvents, from Sodegard and Stolt [2002]

Solvent	P(LLA)	P(rac-LA)
ISOPROPYL ETHER	NON-SOLUBLE	NON-SOLUBLE
CYCLOHEXANE	NON-SOLUBLE	NON-SOLUBLE
XYLENE	SWELLING	SOLUBLE
ETHYL ACETATE	SWELLING	SOLUBLE
TETRAHYDROFURAN	SWELLING	SOLUBLE
CHLOROFORM	SOLUBLE	SOLUBLE
METHYL ETHYL KETONE	SWELLING	SOLUBLE
FURAN	SOLUBLE	SOLUBLE
ACETONE	SWELLING	SOLUBLE
1,4-DIOXANE	SOLUBLE	SOLUBLE
ETHYL LACTATE		SOLUBLE
1,3-DIOXOLANE	SOLUBLE	SOLUBLE
PYRIDINE	SOLUBLE	SOLUBLE
DIMETHYLSULFOXIDE	SWELLING	SOLUBLE
N,N-DIMETHYLFORMAMIDE		SOLUBLE
ETHANOL	NON-SOLUBLE	NON-SOLUBLE

SOLUBLE ■
SWELLING ▨
NON-SOLUBLE ☐

For the production of PLLA scaffolds, usually a ternary system composed by polymer, solvent and nonsolvent is employed. Good solvents are e.g. dioxane and chloroform, whereas as nonsolvents, usually water and ethanol are employed, being PLLA hydropho-

bic. A summary of organic solvents/nonsolvents for PLLA and PDLLA is provided in tables 1.1 and 1.2.

The solubility of PDLLA is strongly dependent on the content of L and D monomers in chains: increasing the D monomer content, the solubility will increase. Rissanen et al. [2008] performed a set of solubility experiments of PDLLA with different L/D ratios (from 96/4 to 50/50) in various solvents and nonsolvents. The results are resumed in table 1.3. The physical reasons to this behavior can be related to the disorder induced in the polymer chains by the D stereoisomer, which reduces the polymer crystallinity and thus the positive interactions between chains (e.g. hydrogen bonding). In this way, the polymer results less compatible with itself and therefore more soluble.

The binary solution dioxane-water has peculiar features. The solvents are completely miscible in all proportions, the vapor-liquid equilibrium shows an azeotrope [Nayak et al., 2004] and the freezing points of mixtures are below the freezing points of pure components [Goates and Sullivan, 1958] (see figure 1.22).

Table 1.2: List of solvents and nonsolvents of PLLA and Hansen solubility parameters, from Agrawal et al. [2004]

Solvents	HSP $(J/cc)^{0.5}$ at 25 °C			
	$\delta_d{}^a$	$\delta_p{}^a$	$\delta_h{}^a$	δ_t
Acetone	15.0	10.4	7	19.6
Acetonitrile	15.3	18.0	6.1	24.4
Benzene	18.4	0.0	2.0	18.5
Chloroform	17.8	3.1	5.5	18.9
m-Cresol	18	5.1	12.9	22.7
Dimethyl formamide	17.4	13.7	11.3	24.9
Dimethyl sulphoxide	18.4	16.4	10.0	26.6
1-4 Dioxane	19.0	1.8	7.4	20.5
1-3 Dioxolane	18.1	6.6	9.3	21.4
Ethyl acetate	15.8	5.3	7.2	18.2
Furan	17.8	1.8	5.3	18.7
Hexafluoro isopropanol	17.2	4.5	14.7	23.1
Isoamyl alcohol	15.8	5.2	13.3	21.3
Methylene dichloride	18.2	6.3	6.1	20.2
Methyl ethyl ketone	16.0	9.0	5.1	19.1
n-Methyl pyrolidone	18.0	12.3	7.2	23.0
Pyridine	19.0	8.8	5.9	21.8
Tetrahydrofuran	16.8	5.7	8.0	19.5
Toluene	18.0	1.4	2.0	18.2
Xylene	17.6	1.0	3.1	17.9
Nonsolvents				
Isopropyl ether	13.7	3.9	2.3	14.4
Cyclohexane	16.5	0.0	0.2	16.5
Hexane	14.9	0.0	0.0	14.9
Ethanol	15.8	8.8	19.4	26.5
Methanol	15.1	12.3	22.3	29.6
Water	15.5	16.0	42.3	47.8
Diethyl ether	14.5	2.9	5.1	15.6

Table 1.3: Solubility of PDLLA in various organic solvents. (1) clear solution; (2) gel-like, thread-shaped struc-
tures; (3) gelatinous solid; (4) very swollen; (5) slightly swollen; (6) insoluble. From Rissanen et al.
[2008]

	Polymer			
	P(L,D)LA 96/4, IV = 2.2 dL/g	P(L,D)LA 96/4, IV = 4.8 dL/g	P(L,DL)LA 70/30	P(L,D)LA 50/50
Solvent				
Dichloromethane	1	1	1	1
1,4-Dioxane	3	4	3	1
Propylene carbonate	6	5	4	1
Acetone	5	5	3	1
Methyl acetate	5	5	3	1
Tetrahydrofuran	4	5	3	1
Pyridine	3	5	3	1
Formic acid (98%)	5	5	2	1
Nonsolvent				
n-Hexane	6	6	6	6
Methanol	6	6	6	5
Ethanol	6	6	6	5
Isopropyl alcohol	6	6	6	6
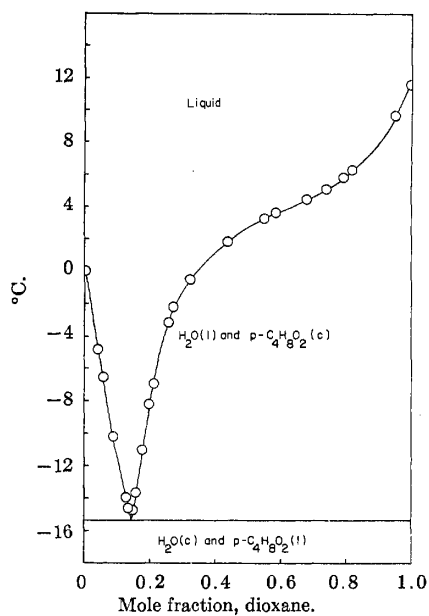
Figure 1.22: Phase diagram of dioxane-water system, from Goates and Sullivan [1958]. The melting point of the
mixture is lower than the pure component value
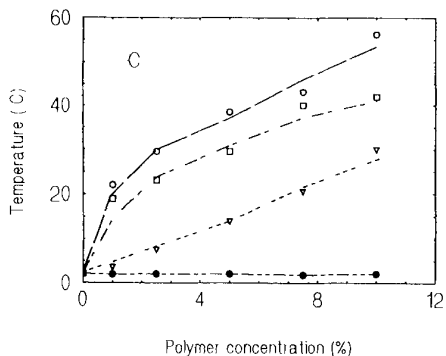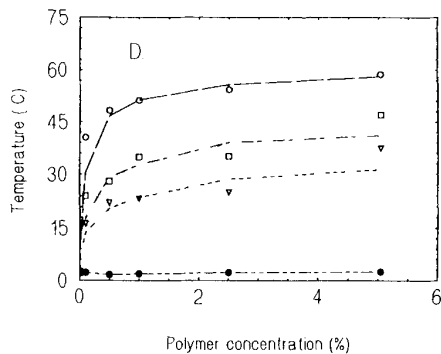
Figure 1.23: Cloud point curves of semicrystalline PLLA. The dioxane/water ratio in solution are: circles, 86/14; squares, 88/12; triangles, 90/10. Filled circles are crystallization points, from Schugens et al. [1996]. As a general rule, by increasing the dioxane content in the mixture the cloud point temperature decreases. Moreover, the cloud point increases substantially with the molecular weight
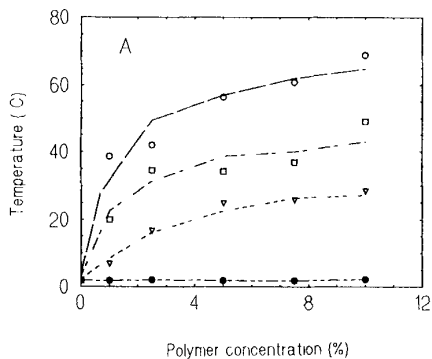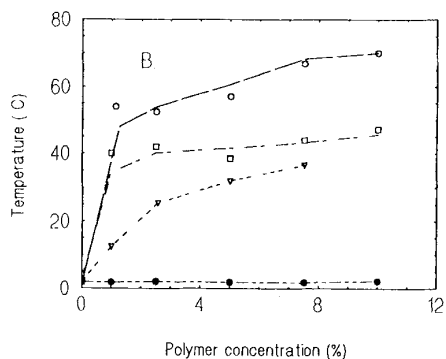
Figure 1.24: Cloud point curves of amorphous PDLLA. The dioxane/water ratio in solution are: circles, 83/17; squares, 85/15; triangles, 87/13. Filled circles are crystallization points, from Schugens et al. [1996]. As a general rule, by increasing the dioxane content in the mixture the cloud point temperature decreases. The influence of polymer molecular weight is low

Cloud point curves available in literature are reported in figures 1.23, 1.24, 1.25 and 1.26. The locations of cloud point curves for PLLA and PDLLA in dioxane and water are close [van de Witte et al., 1996b]. The influence of molecular weight (MW) is clear from comparing figures 1.23a and 1.24a (lower MW) with figures 1.23b and 1.24b (higher MW). Higher MW gave out a higher cloud point temperature, i.e. the phase separation is more probable. Moreover, the cloud point temperatures are highly sensitive to dioxane/water ratio: by reducing the dioxane content of 2%, the cloud point increase is at least of 10°C.
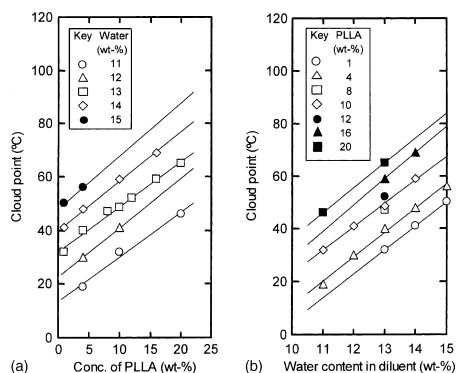
(a) From Tanaka and Lloyd [2004]
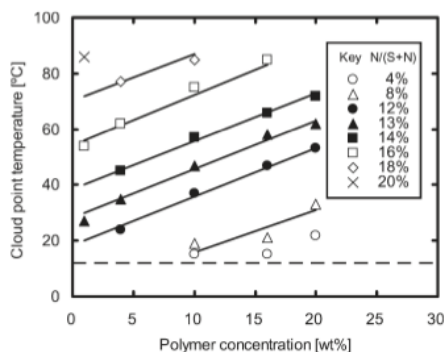
(b) From Tanaka et al. [2006]
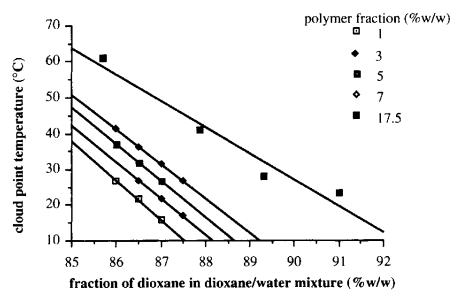
(c) From van de Witte et al. [1996b]
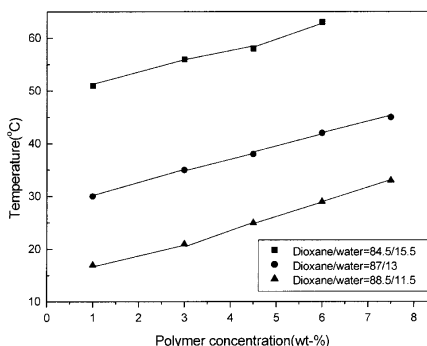
(d) From Hua et al. [2002]

Figure 1.25: Cloud point curves of semicrystalline PLLA. The global trends are similar: the peculiar differences are related to the molecular weight and the polydispersity of the PLLA tested

A phase diagram of PLLA-dioxane-water system was reported by Tanaka and Lloyd [2004] (see figure 1.27).

The following two sections report the typical TIPS protocols adopted for the production of porous structures with the PLA-dioxane-water system. A synoptic scheme resuming all
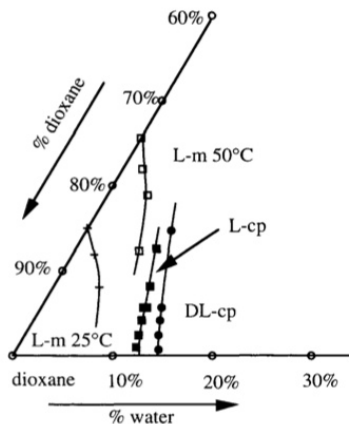
Figure 1.26: Cloud point (cp) and melting (m) curves of semicrystalline (L) and amorphous (LD) polylactide at 25°C, from van de Witte et al. [1996b]. Phase separation occurs at lower polymer concentrations when using a semicrystalline polymer
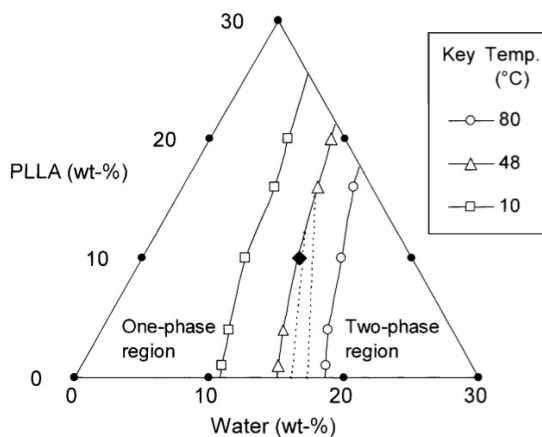
Figure 1.27: Phase diagrams of PLLA-dioxane-water system, from Tanaka and Lloyd [2004]. The two tie lines were obtained at $T = 48°C$

the data available in literature is provided at the end of this chapter (table 1.4).

1.5 Direct quenching TIPS

A simple way to produce porous structures via TIPS consists in quenching a homogeneous polymer solution at low temperatures (usually $-196 < T_q < 0°$C). The solution passes through the miscibility gap and then enters the solidification zone. The experimental parameters which allow the structure control are:

- quenching temperature (T_q);

- sample dimension (thickness);

- polymer concentration;

- solvent/nonsolvent ratio.

The quenching temperature is the temperature at which the sample is exposed. Depending on the sample size, a temperature gradient is experienced by the solution, giving out different morphologies at different distances from the cooled wall. The core zone has usually larger pores than the skin layer, as the time spent in the liquid-liquid miscibility gap and/or available to coarsening is higher [Nam and Park, 1999].

Polymer concentration and solvent/nonsolvent ratio influence the system thermodynamics (critical solution point, relative amount of polymer-rich and polymer-lean phases, polymer-diluent energy interactions) and kinetics (solution viscosity).

Schugens et al. [1996] prepared PLLA and PDLLA scaffolds with solutions in dioxane/water of different proportions. In this study two different molecular weights for each polymer were used. Solutions were directly quenched in liquid nitrogen ($-196°$C) for 2 hours. Low polymer concentrations gave out irregular and discontinuous structures, while scaffolds obtained with intermediate concentrations exhibited small and large pores (about 10 and 100 μm). Relatively high polymer concentration gave out regular porous foams with pore diameter of about 10 μm.

Comparing the resulting morphologies from high and low molecular weight polymers, the key role of viscosity comes out. At the same polymer concentration, the porous structure appears more regular and suitable for scaffolding purposes for the higher molecular weight polymer (see figures 1.28 and 1.29). Solutions of lower molecular weight polymers (figure 1.28a) are expected to form during phase separation a polymer-rich phase less viscous and of a smaller volume. The lower viscosity can also affect the stability of the structure formed, which can, in its turn, coalesce into dispersed phases.

Another interesting comparison worked out by the same research group is between the morphologies obtained via solid-liquid and liquid-liquid phase separation processes. A binary PLLA-dioxane and a ternary PLLA-dioxane-water solutions, with the same polymer concentration, were exposed to the same thermal history (direct quench in liquid nitrogen). The resulting morphologies are very different (figure 1.30): the solid-liquid phase separation generates large and closed pores (figure 1.30a), whereas the liquid-liquid demixing results in an open pore structure (figure 1.30b). Authors supposed that the isotropic morphology of the foam obtained via liquid-liquid phase separation can be related to a spinodal decomposition mechanism.

(a) Lower molecular weight　　　　　　　　(b) Higher molecular weight
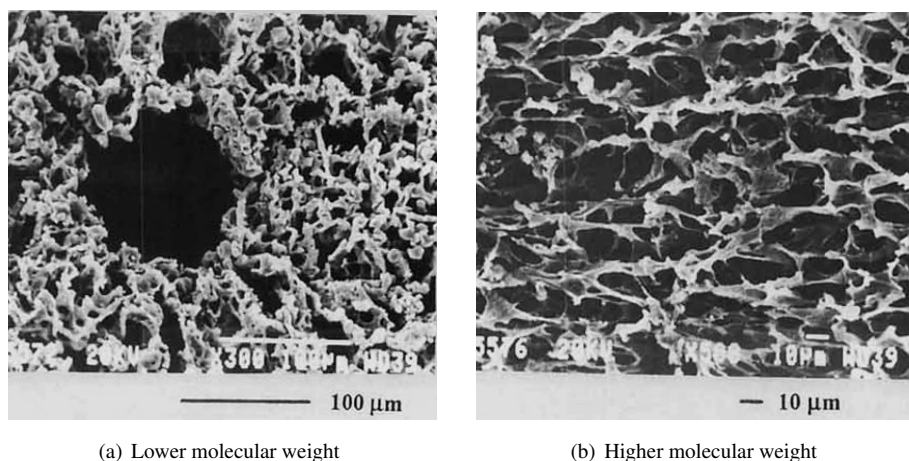
Figure 1.28: SEM micrographs of amorphous PDLLA foams obtained by direct quenching in liquid nitrogen a ternary solution with 5% wt polymer and dioxane/water=87/13, from Schugens et al. [1996]. The higher molecular weight polymer produces a more regular structure, owing to the stabilizing effect of the higher viscosity

Nam and Park [1999] prepared scaffolds with solution of PLLA and PDLLA in dioxane/water at $-15°$C, $-40°$C and in liquid nitrogen. At low polymer concentrations (1% wt/v), the structure obtained via TIPS with a dioxane/water ratio of 87/13 v/v was beady, resulting from the nucleation and growth of a polymer-rich phase.

At high polymer concentrations (10% wt/v) and various dioxane/water ratios (84/16, 87/13 and 90/10), porous structures were obtained. For all polymers used, increasing the water fraction the pore dimension increases, while lowering the quench temperature the pore interconnection increases. Pore sizes obtained are in the range of $1-100\ \mu m$.

Lower quenching temperatures and lower solvent/nonsolvent ratio promote coarsening of polymer-lean domains, giving out closed and large pores (up to $1000\ \mu m$). A higher
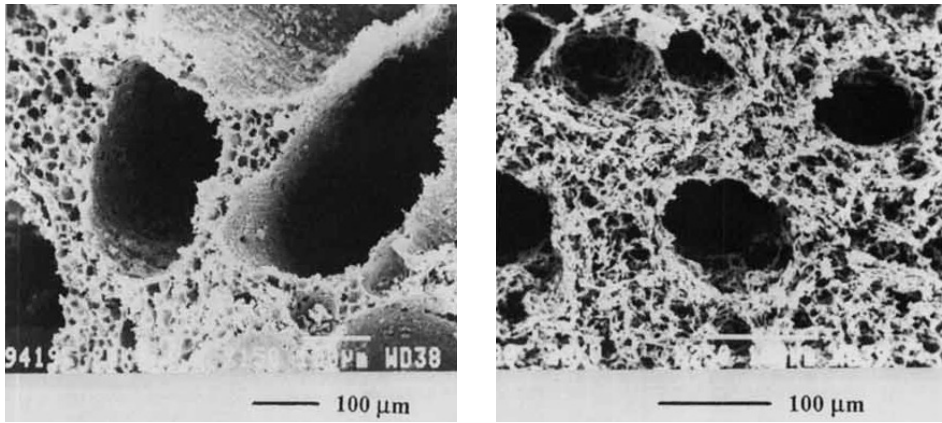
(a) Lower molecular weight, 10% wt

(b) Higher molecular weight, 2.5% wt

Figure 1.29: SEM micrographs of semicrystalline PLLA foams obtained by direct quenching in liquid nitrogen a ternary solution with dioxane/water=87/13, from Schugens et al. [1996]. The differences in viscosity are mitigated by varying the polymer concentration, thus more similar morphologies were obtained
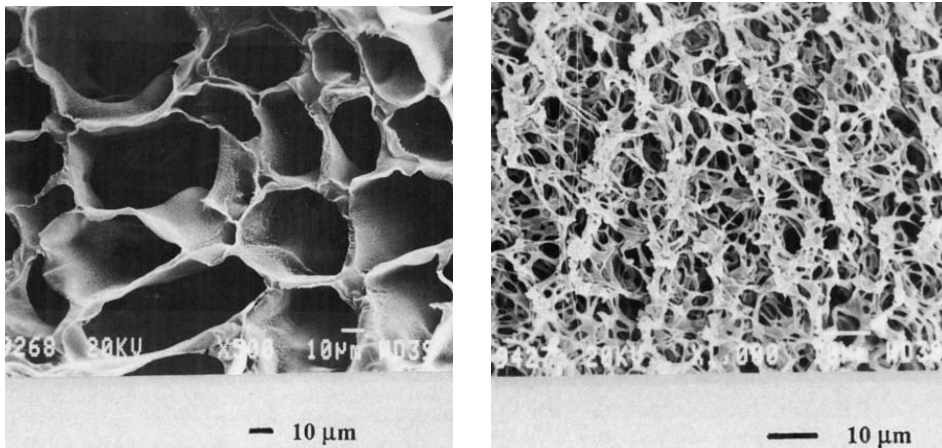
(a) Binary solution PLLA-dioxane: solid-liquid phase separation

(b) Ternary solution PLLA-dioxane-water: liquid-liquid phase separation

Figure 1.30: SEM micrographs of semicrystalline PLLA foams obtained by direct quenching in liquid nitrogen binary and ternary solution with 5% wt of polymer, from Schugens et al. [1996]. Note that the solid-liquid phase separation produces closed pores, whereas liquid-liquid demixing generates an open pore structure with good interconnection

51

water content weaken the polymer-diluent interaction and probably inhibit the interconnection, whereas a lower quenching temperature reduces the mobility, freezing the structure early formed. Moreover, increasing the water content in the solution, the quenching depth is higher and the viscosity is lower.

Li et al. [2004] quenched PLLA-dioxane-THF solutions with 2% wt/v polymer and different solvent/nonsolvent ratio at -70°C, leading to different residence time in the binodal region. Pore size and interconnection obtained were not proportional to solvent/nonsolvent ratio, but a maximum of interconnection (coupled with a minimum in pore size) was obtained at dioxane/THF=70/30. The 90/10 sample resulted in a closed-cell morphology, while other samples led to an interconnected structure.

An investigation of PDLLA scaffold preparation with dioxane/water from 91/9 to 98/2 (v/v) is provided by Hu et al. [2002]. Solution of PDLLA (1% wt/v) were quenched to -24°C, giving out open-cell morphologies (except for the 98/2 sample, which resulted with closed pores). Pore dimension exhibit a maximum of $100-350$ μm (95% dioxane solution), while for 98% solution is $100-250$ μm and for 91% solution is lower than 100 μm.

Budyanto et al. [2009] quenched a PLLA-dioxane-water (87/13 wt/wt) solution at -80°C and in liquid nitrogen. For a solution with 5% wt of PLLA, pore size and interconnection are higher when the solution is quenched at -80°C. For both quenching temperatures, an uniform pore size distribution was obtained, with average dimension of 47 μm (-80°C) and 22 μm (-196°C). Solution with 3% wt of PLLA gave out a powder-like solid, as the composition is below the critical solution point. Average pore size of scaffold prepared with a 7% wt PLLA solution was 38 μm, a value lower than 5% wt solution, and the foam exhibited a closed-cell morphology.

1.6 Stepwise TIPS

In stepwise techniques, a homogeneous ternary solution is cooled to an appropriate demixing temperature and maintained for a suitable demixing time. After that, the system is quenched to to a suitably low temperature so as to freeze the structure obtained. Pore dimension, shape and interconnection can be controlled by varying the experimental conditions:

- demixing temperature (T_d);

- demixing time (t_d);

- polymer concentration;

- solvent/nonsolvent ratio.

Usually, in scaffold preparation, the influence of parameters is deduced with offline characterization of porous structures obtained. Scaffold morphology (i.e. pore dimension and interconnection) is highly sensitive to all the aforementioned parameters, and their correlation is often complex.

Hua et al. [2002] prepared scaffolds via TIPS with the PLLA-dioxane-water system. Results denoted a faster phase separation lowering the weight fraction of PLLA in solution. For a 3% wt solution of PLLA in dioxane and water (87/13), the phase separation appeared faster at $T_d = 25°C$ than at 30°C, while pore size increased with t_d (see figure 1.31). The rapid growth of pores can be due to coalescence. For this system, sedimentation of polymer-rich domains was observed, due to the low concentration of polymer in solution. Sedimentation does not allow one to obtain scaffolds, as the porous structure resulting is highly irregular and the morphology cannot be controlled.

(a) 25°C, 2 min	(b) 25°C, 10 min
(c) 30°C, 2 min	(d) 30°C, 30 min
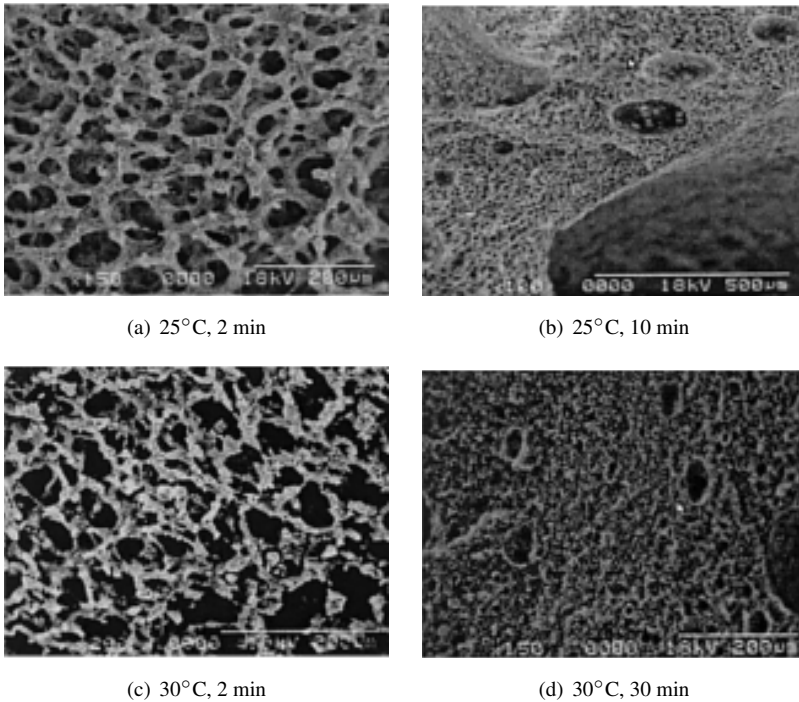
Figure 1.31: SEM micrographs of PLLA foams, obtained from a solution with 3% wt of polymer and dioxane/water 87/13, from Hua et al. [2002]. At $T = 25°C$ the phase separation seems to be faster than at $T = 30°C$. By increasing the holding time, the pore size increases

Regular porous structures were obtained with higher PLLA concentration (4.5 and 6% wt) for $T_d = 20$ and 30°C (figure 1.32). Although at constant T_d the quenching depth is higher for higher polymer concentration, and therefore the driving force to phase separation is higher, the average pore size obtained from 4.5% wt solution is higher than from 6% wt solution for all t_d. Authors ascribe this result to the higher viscosity of the 6% wt solution, i.e. to a kinetic control. Viscosity increase is due to both higher concentration and higher crystallinity (which induces gelation), as confirmed by DSC measurements. Lowering T_d the pore size decreased, thus denoting a kinetically controlled process.

Average pore sizes of scaffolds produced from 4.5% wt solution of PLLA are 150 μm ($T_d = 30$°C, $t_d = 30$ min), 90 μm ($T_d = 20$°C, $t_d = 60$ min) and 130 μm ($T_d = 20$ °C, $t_d = 120$ min).

Increasing the water content in the solution (dioxane/water=85.5/14.5), polymer sedimentation was observed. In this case, the higher water content strongly reduces the solubility of polymer. A higher dioxane/water ratio (88.5/11.5) gave out smaller pores than the 87/13 solution. Authors explain this result by means of higher viscosity and lower driving force (i.e. quenching depth) of 88.5/11.5 solution. However, the coarsening can be inhibited by the higher concentration of solvent, thus reducing the interfacial tension.

Carfì Pavia et al. [2008] prepared scaffolds via TIPS with the PLLA-dioxane-water system (4% wt of polymer, 87/13 wt/wt). For $T_d = 25$°C, average pore size was fairly independent of t_d (10 to 15 μm for t_d from 5 to 40 min) and a good interconnection was noticed. For $T_d = 30$ and 35°C, pore size has a sigmoidal dependence of t_d (see figure 1.33), with a short times plateau (related to nucleation) and a long times plateau (connected to the domain impingements).

Pore size resulted low at short t_d, due to the predominance of nucleation with respect to the growth process. However, when raising temperature, the short times plateau level gets higher due to the more sporadic nucleation. For higher T_d, long demixing time ($t_d > 30$ min) gave out closed-cell structures.

Budyanto et al. [2009] prepared scaffolds from a PLLA-dioxane-water (87/13 wt/wt) solution with a demixing step at $T_d = 25$°C and $t_d = 5$ min, and then quenching to -80°C or in liquid nitrogen. For a solution with 5% wt of PLLA, a porous structure with low interconnection and a combination of large and small pores was obtained. Authors ascribe this result to the time spent by the solution into the metastable region, which induces phase separation via nucleation and growth, without promoting interconnection.

A way to prepare scaffolds with large pores by means of controlled coarsening is reported by Gong et al. [2006]. The proposed method consists in a two step demixing: firstly, the porous structure is produced, and then at lower temperature is promoted a further phase

(a) 4.5% wt, 20°C, 2 min

(b) 4.5% wt, 20°C, 30 min

(c) 4.5% wt, 30°C, 2 min

(d) 4.5% wt, 30°C, 30 min

(e) 6% wt, 20°C, 2 min

(f) 6% wt, 20°C, 30 min

(g) 6% wt, 30°C, 2 min

(h) 6% wt, 30°C, 30 min
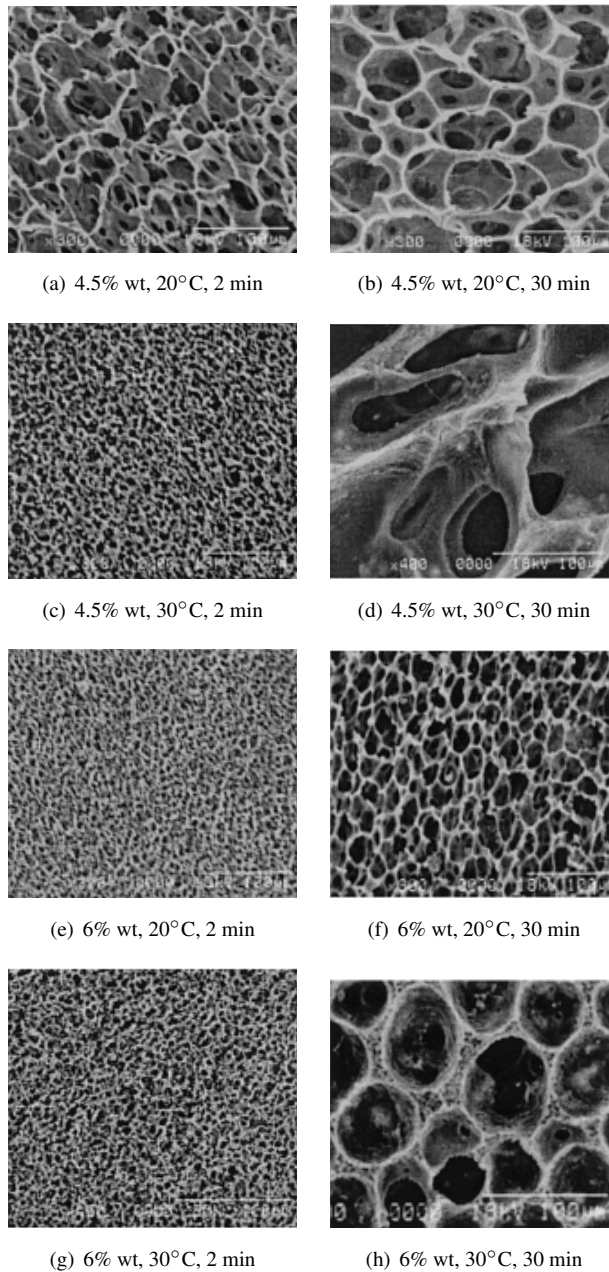
Figure 1.32: SEM micrographs of PLLA foams, obtained from a solution with dioxane/water 87/13, from Hua et al. [2002]. At fixed temperature and holding time, the lower polymer concentration gave out a higher pore size, probably due to viscosity effects. For long holding time (b), lower concentration and temperature produced an open porous structure, whereas at higher concentration and temperature (h), closed pores were obtained
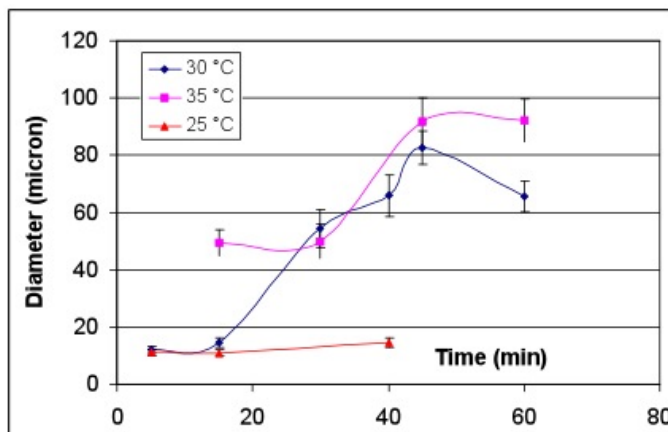
Figure 1.33: Average pore diameter of scaffolds as a function of t_d, from Carfì Pavia et al. [2008]. At low temperature the holding time does not affect the pore size, whereas at higher temperatures a sigmoidal dependence was recorded

separation coupled to coarsening, resulting in a larger pore dimension without loss of interconnectivity.

The system studied was a solution of 5% wt PLLA in dioxane/water (87/13 v/v). Pore growth in the second step was observed after 1 h, as firstly new polymer-lean domains nucleate and grow, and after they will coalesce with previously-formed polymer-lean domains. After 3 h, the average pore size reached about 320 μm, whereas at the end of first step the average pore dimension was about 140 μm. Pore interconnection appears high, and authors ascribe the interconnection formation to the coarsening process.

Table 1.4: Synoptic table of TIPS data on PLA-dioxane-water solutions

Reference	Method	Polymer	Pol wt%	D/W	T_d, °C	Pore size, μm	Notes
Schugens et al. [1996]	DQ	DL	0.5	87/13	−196		B
			5			10 − 100	OP, GI
			10			10	OP, GI
		L	1	87/13	−196		B
			2.5			10 − 100	OP, GI
			5			10	OP, GI
Nam and Park [1999]	DQ	L, DL	1	87/13	−15, −196		B
		L	9	90/10	−15	10 − 30	OP, GI
					−40	10 − 30	OP, GI
					−196	<10	OP, GI
				87/13	−15	80	CP
					−40	50	CP
					−196	5	CP
				84/16	−15	> 100	CP
					−40	> 100	CP
					−196	25	CP
		DL	9	90/10	−15	< 10	OP, GI
					−40	< 40	OP, GI
					−196	< 50	CP
				87/13	−15	10	OP, GI
					−40	> 100	CP
					−196	> 100	CP

Reference	Method	Polymer	Pol wt%	D/W	T_d, °C	Pore size, μm	Notes
Hu et al. [2002]	DQ	DL	1	98/2	−24	100 − 250	CP
				97/3		100 − 300	OP, GI
				95/5		100 − 350	OP, GI
				93/7		50 − 200	F
				91/9		< 100	F
Budyanto et al. [2009]	DQ	L	5		−80	47 ± 8	OP, LI
					−196	22 ± 4	CP
			7		−80		CP
	S		5		25	14 − 40 (5 min)	OP, LI
Hua et al. [2002]	S	L	3	87/13	25		S (10 min)
					30		S (30 min)
			4.5	88.5/11.5	20	<50 (10 min)	OP, GI
						<100 (30 min)	OP, GI
				87/13	20	90 (60 min)	OP, GI
						130 (120 min)	OP, GI
					30	>150 (30 min)	OP, GI
				85.5/14.5	30		S (2 min)
			6	87/13	30	<50 (10 min)	OP, GI
						<100 (30 min)	CP
Gong et al. [2006]	S	L	5	87/13	25	150 (8 h)	OP, GI
					37	150 (8 h)	OP, LI
					25 → 20	320 (3 h)	OP, GI

Reference	Method	Polymer	Pol wt%	D/W	T_d, °C	Pore size, μm	Notes
Carfi Pavia et al. [2008]	S	L	4	87/13	25	$10 - 15$ ($5 - 40$ min)	OP, GI
					30	$12 - 15$ ($5 - 15$ min)	OP, GI
						80 (45 min)	CP
					35	50 ($15 - 30$ min)	CP
						90 ($45 - 60$ min)	CP
He et al. [2009]	S	L	5	88/12	20	50 (2 h)	OP, LI
					16	25	OP, GI
					12	$10 - 50$	CP
					8	40	LI
					4	$25 - 50$	CP
					0	$20 - 50$	LI

Notes: B: beady. CP, closed pores. OP, open pores. LI, low interconnection. GI, good interconnection. S: sedimentation.

Bibliography

A. Agrawal, A. D. Saran, S. S. Rath, and A. Khanna. Constrained nonlinear optimization for solubility parameters of poly(lactic acid) and poly(glycolic acid) - Validation and comparison. *Polymer*, 45:8603–8612, 2004.

R. Akki, P. Desai, and A. S. Abhiraman. A framework for morphological evolution vis-à-vis phase transitions in polymer solutions. *Journal of Applied Polymer Science*, 73:1343–1355, 1999.

Y. C. Bae, S. M. Lambert, D. S. Soane, and J. M. Prausnitz. Cloud-point curves of polymer solutions from thermooptical measurements. *Macromolecules*, 24:4403–4407, 1991.

B. F. Barton and A. J. McHugh. Modeling the dynamics of membrane structure formation in quenched polymer solutions. *Journal of Membrane Science*, 166:119–125, 2000.

B. F. Barton, P. D. Graham, and A. J. McHugh. Dynamics of spinodal decomposition in polymer solutions near a glass transition. *Macromolecules*, 31:1672–1679, 1998.

C. Boutris, E. G. Chatzi, and C. Kiparissides. Characterization of the LCST behaviour of aqueous poly(N-isopropylacrylamide) solutions by thermal and cloud point techniques. *Polymer*, 38(10): 2567–2570, 1997.

L. Budyanto, Y. Q. Goh, and C. P. Ooi. Fabrication of porous poly(L-lactide) (PLLA) scaffolds for tissue engineering using liquid-liquid phase separation and freeze extraction. *Journal of Materials Science: Materials in Medicine*, 20:105–111, 2009.

A. M. W. Bulte, E. M. Naafs, F. van Eeten, M. H. V. Mulder, C. A. Smolders, and H. Strathmann. Equilibrium thermodynamics of the ternary membrane-forming system nylon, formic acid and water. *Polymer*, 37(9):1647–1655, 1996.

F. Carfì Pavia, V. La Carrubba, S. Piccarolo, and V. Brucato. Polymeric scaffolds prepared via thermally induced phase separation: Tuning of structure and morphology. *Journal of Biomedical Materials Research Part A*, 86:459–466, 2008.

J.-S. Chen, S.-L. Tu, and R.-Y. Tsay. A morphological study of porous polylactide scaffolds prepared by thermally induced phase separation. *Journal of the Taiwan Institute of Chemical Engineers*, 41: 229–238, 2010.

P. J. Flory. *Principles of Polymer Chemistry*. Cornell University Press, 1953.

J. R. Goates and R. J. Sullivan. Thermodynamic properties of the system water-p-dioxane. *Journal of Physical Chemistry*, 62(2):188–190, 1958.

Y. Gong, Z. Ma, C. Gao, W. Wang, and J. Shen. Specially elaborated thermally induced phase separation to fabricate poly(L-lactic acid) scaffolds with ultra large pores and good interconnectivity. *Journal of Applied Polymer Science*, 101:3336–3342, 2006.

P. D. Graham and A. J. McHugh. Kinetics of thermally induced phase separation in a crystallizable polymer solution. *Macromolecules*, 31(8):2565–2568, 1998.

P. D. Graham, B. F. Barton, and A. J. McHugh. Kinetics of thermally induced phase separation in ternary polymer solutions. II. Comparison of theory and experiment. *Journal of Polymer Science: Part B: Polymer Physics*, 37:1461–1467, 1999.

L. He, Y. Zhang, X. Zeng, D. Quan, S. Liao, Y. Zeng, J. Lu, and S. Ramakrishna. Fabrication and characterization of poly(L-lactic acid) 3D nanofibrous scaffolds with controlled architecture by liquidÐliquid phase separation from a ternary polymerÐsolvent system. *Polymer*, 50:4128–4138, 2009.

Y. Hu, D. W. Grainger, S. R. Winn, and J. O. Hollinger. Fabrication of poly(α-hydroxy acid) foam scaffolds using multiple solvent systems. *Journal of Biomedical Materials Research*, 59:563–572, 2002.

F. J. Hua, G. E. Kim, J. D. Lee, Y. K. Son, and D. S. Lee. Macroporous poly(L-lactide) scaffold 1. Preparation of a macroporous scaffold by liquid-liquid phase separation of a PLLA-dioxane-water system. *Journal of Biomedical Materials Research (Appl Biomater)*, 63:161–167, 2002.

J. H. Kim, B. R. Min, J. Won, H. C. Park, and Y. S. Kang. Phase behavior and mechanism of membrane formation for polyimide/DMSO/water system. *Journal of Membrane Science*, 187: 47–55, 2001.

J.-W. Kim, K. Taki, S. Nagamine, and M. Ohshima. Preparation of porous poly(L-lactic acid) honeycomb monolith structure by phase separation and unidirectional freezing. *Langmuir*, 25(9): 5304–5312, 2009.

V. J. Klenin. *Thermodynamics of systems containing flexible-chain polymers*. Elsevier, 2000.

R. Koningsveld, W. H. Stockmayer, and E. Nies. *Polymer phase diagrams. A textbook*. Oxford University Press, 2001.

H. K. Lee, A. S. Myerson, and K. Levon. Nonequilibrium liquid-liquid phase separation in crystallizable polymer solutions. *Macromolecules*, 25:4002–4010, 1992.

S. Li, V. La Carrubba, S. Piccarolo, D. Sannino, and V. Brucato. Preparation and properties of poly(L-lactic acid) scaffolds by thermally induced phase separation from a ternary polymer-solvent system. *Polymer International*, 53:2079–2085, 2004.

D. S. Martula, T. Hasegawa, D. R. Lloyd, and R. T. Bonnecaze. Coalescence-induced coalescence of inviscid droplets in a viscous fluid. *Journal of Colloid and Interface Science*, 232:241–253, 2000.

H. Matsuyama, M. Teramoto, T. Uesaka, M. Goto, and F. Nakashio. Kinetics of droplet growth in the metastable region in cellulose acetate/acetone/nonsolvent system. *Journal of Membrane Science*, 152:227–234, 1999.

H. Matsuyama, S. Kudari, H. Kiyofuji, and Y. Kitamura. Kinetic studies of thermally induced phase separation in polymer-diluent system. *Journal of Applied Polymer Science*, 76:1028–1036, 2000.

D. H. Melik and H. S. Fogler. Turbidimetric determination of particle size distributions of colloidal systems. *Journal of Colloid and Interface Science*, 92(1):161–180, 1983.

Y. S. Nam and T. G. Park. Porous biodegradable polymeric scaffolds prepared by thermally induced phase separation. *Journal of Biomedical Materials Research*, 47:8–17, 1999.

J. N. Nayak, M. I. Aralaguppi, B. V. Kumar Naidu, and T. M. Aminabhavi. Thermodynamic properties of water+tetrahydrofuran and water+1,4-dioxane mixtures at (303.15, 313.15, and 323.15) K. *Journal of Chemical Engineering Data*, 49:468–474, 2004.

S. P. Nunes and T. Inoue. Evidence for spinodal decomposition and nucleation and growth mechanisms during membrane formation. *Journal of Membrane Science*, 111:93–103, 1996.

M. Rissanen, A. Puolakka, P. Nousiainen, M. Kellomaki, and V. Ella. Solubility and phase separation of poly(L,D-lactide) copolymers. *Journal of Applied Polymer Science*, 110:2399–2404, 2008.

I. C. Sanchez. *Encyclopedia of Physical Science and Technology*, volume 11, chapter Polymer Phase Separation. Academic Press, 1987.

C. Schugens, V. Maquet, C. Grandfils, R. Jerome, and P. Teyssie. Polylactide macroporous biodegradable implants for cell transplantation. II. Preparation of polylactide foams by liquid-liquid phase separation. *Journal of Biomedical Materials Research*, 30:449–461, 1996.

A. Sodegard and M. Stolt. Properties of lactic acid based polymers and their correlation with composition. *Progress in Polymer Science*, 27:1123–1163, 2002.

S.-W. Song and J. M. Torkelson. Coarsening effects on microstructure formation in isopycnic polymer solutions and membranes produced via thermally induced phase separation. *Macromolecules*, 27 (22):6389–6397, 1994.

C. Stropnik, V. Musil, and M. Brumen. Polymeric membrane formation by wet-phase separation; turbidity and shrinkage phenomena as evidence for the elementary processes. *Polymer*, 41:9227–9237, 2000.

T. Tanaka and D. R. Lloyd. Formation of poly(L-lactic acid) microfiltration membranes via thermally induced phase separation. *Journal of Membrane Science*, 238:65–73, 2004.

T. Tanaka, T. Tsuchiya, H. Takahashi, M. Taniguchi, H. Ohara, and D. R. Lloyd. Formation of biodegradable polyesters membranes via thermally induced phase separation. *Journal of Chemical Engineering of Japan*, 39(2):144–153, 2006.

I. Teraoka. *Polymer Solutions: An Introduction to Physical Properties*. Wiley, 2002.

H. Tompa. *Polymer solutions*. Butterworths, London, 1956.

F.-J. Tsai and J. M. Torkelson. Roles of phase separation mechanism and coarsening in the formation of poly(methyl methacrylate) asymmetric membranes. *Macromolecules*, 23:775–784, 1990.

P. van de Witte, A. Boorsma, H. Esselbrugge, P. J. Dijkstra, J. W. A. van den Berg, and J. Feijen. Differential scanning calorimetry study of phase transitions in poly(lactide)-chloroform-methanol systems. *Macromolecules*, 29:212–219, 1996a.

P. van de Witte, P. J. Dijkstra, J. W. A. van den Berg, and J. Feijen. Phase behavior of polylactides in solvent-nonsolvent mixtures. *Journal of Polymer Science: Part B: Polymer Physics*, 34:2553–2568, 1996b.

P. van de Witte, P. J. Dijkstra, J. W. A. van den Berg, and J. Feijen. Phase separation processes in polymer solutions in relation to membrane formation. *Journal of Membrane Science*, 117:1–31, 1996c.

P. T. van Emmerik and C. A. Smolders. Differential scanning calorimetry of poly-(2,6 dimethyl-1,4 phenylene-oxide)-toluene solutions. *European Polymer Journal*, 9:293–300, 1973.

W. Zhang. *Phase Behavior and Phase Separation Kinetics in Polymer Solutions under High Pressure*. PhD thesis, Virginia Polytechnic Institute and State University, 2005.

2 Modeling approach: thermodynamics

Lattice fluid (LF) models have been successfully used to predict properties of binary polymer solutions. In this study, two different typologies of LF models were tested for the prediction of phase equilibria in ternary polymer solutions: the group-contribution model by Oishi and Prausnitz [1978] and the compressible LF model by Sanchez and Lacombe [1978]. The former allows one to calculate the activity coefficient of solvents (but not of the polymer), whereas the latter provides an expression for the chemical potential of each species in a mixture (including also the macromolecular component).

The group-contribution model, in principle, is versatile and fully predictive: a molecule is treated as composed by a number of functional groups with determined properties, reported in the UNIFAC table [Bondi, 1968]; with the appropriate mixing rules, the properties of a molecule are derived from its "building blocks". Nevertheless, the Oishi-Prausnitz model gives out unreliable results when calculating the activity of water. To overcome this issue, different formulations and corrections of the model were considered. On the other hand, the compressible LF model contains a number of adjustable parameters related to the interaction energy between molecules. Specific interactions can be taken into account, e.g. hydrogen bonding, to improve the system description.

In this chapter, these two approaches for the modeling of polymer solution thermodynamics are presented and comparatively discussed.

2.1 Compressible lattice fluid model

The lattice fluid model by Flory-Huggins does not allow the prediction of LCST (Lower Critical Solution Temperature) behavior, common in polymer solutions. This lack was overcome by taking into account the *compressibility* of the solution, i.e. the volumetric effects occurring upon mixing, by adding a fictitious component to the mixture representing the free volume.

The model was initially formulated for a pure fluid [Sanchez and Lacombe, 1976], and then extended to fluid mixtures [Lacombe and Sanchez, 1976]. During years, the model was slightly modified by changing some internal formulations (e.g. mixing rules), without

modifying the basic framework of the theory.

2.1.1 Pure fluid

In statistical mechanics framework, the key point is to determine the partition function of the system considered:

$$Z(T, P) = \sum_{V} \sum_{E} \Omega(E, V, N) \exp[-\beta(E + PV)] \tag{2.1}$$

where $\Omega(E, V, N)$ is the number of configurations available to a system composed of N molecules, whose configurational energy and volume are E and V, respectively. The temperature T ($\beta \equiv 1/kT$) and pressure are fixed.

After an expression for the partition function Z is determined, all thermodynamic properties of the system can be derived from the Gibbs free energy G:

$$G = -kT \ln Z(T, P) \tag{2.2}$$

In order to determine Ω, a number of assumptions about the spatial distribution of the molecules and their interactions are needed. The first assumption made in the modeling is the presence of vacancies in the lattice, thus the system is treated as composed by two components: N r-mers and N_0 empty sites. Therefore, the *total number of lattice sites* is:

$$N_r = N_0 + rN \tag{2.3}$$

The *close packed state* is defined as the configuration of a system without holes. The close packed volume of a mer is v^*, and it is assumed equal to the volume of a lattice site. The close packed volume of the N r-mers is:

$$V^* = N(rv^*) \tag{2.4}$$

The close packed molecular volume can be estimated by means of the close packed *mass density* (ρ^*, which is close but not equal to the crystal density) and molecular weight M:

$$rv^* = \frac{M}{\rho^*} \tag{2.5}$$

The volume of an empty lattice site (a hole) is assumed to be equal to v^*; the volume of the system is therefore:

$$V = (N_0 + rN)v^* = N_r v^* \tag{2.6}$$

As regards to energy, it is assumed to depend only on nearest neighbor interactions. In general, the lattice energy (only attractive) can be expressed as:

$$E = -(z/2)N_r \sum_i \sum_j p(\mathrm{i},\mathrm{j})\epsilon_{ij} \qquad (2.7)$$

where ϵ_{ij} is the pair interaction energy between components i and j, $p(i,j)$ is the pair probability of an (i,j) contact in the system and z is the lattice coordination number. The only pair interaction energy considered is the one associated with nonbonded mer-mer interactions; hole-hole, hole-mer, and bonded mer-mer pairs are assigned a zero energy.

The lattice energy is therefore:

$$E = -\frac{z\epsilon}{2} \frac{(rN)^2}{N_r} \qquad (2.8)$$

or by using equations 2.4 and 2.6:

$$\frac{E}{rN} = -\epsilon^* \frac{V^*}{V} \qquad (2.9)$$

where ϵ is the nonbonded, mer-mer interaction energy and

$$\epsilon^* \equiv \frac{z\epsilon}{2} \qquad (2.10)$$

is the total interaction energy per mer. The quantity $r\epsilon^*$ is the characteristic interaction energy per molecule in the absence of holes; ϵ^* is also the energy required to create a hole into the lattice.

With all these assumptions, both E and Ω are functions only of the number of holes in the lattice; the mathematical form of Ω is thoroughly discussed in [Sanchez and Lacombe, 1976]. The partition function (equation 2.1) can be therefore expressed as:

$$Z(T,P) = \sum_{N_0=0}^{\infty} \Omega \exp[-\beta(E + PV)] \qquad (2.11)$$

The corresponding free energy is:

$$G = E + PV - kT \ln \Omega \qquad (2.12)$$

which can be expressed in dimensionless variables as:

$$\frac{G}{Nr\epsilon^*} \equiv \tilde{G} = -\tilde{\rho} + \tilde{P}\tilde{v} + \tilde{T}\left[(\tilde{v}-1)\ln(1-\tilde{\rho}) + \frac{1}{r}\ln\tilde{\rho} \right] \qquad (2.13)$$

The dimensionless variables $\tilde{T}$, $\tilde{P}$, $\tilde{v}$ and $\tilde{\rho}$ are the reduced temperature, pressure, volume and density:

$$\tilde{T} \equiv \frac{T}{T^*} \qquad T^* \equiv \frac{\epsilon^*}{k} \tag{2.14}$$

$$\tilde{P} \equiv \frac{P}{P^*} \qquad P^* \equiv \frac{\epsilon^*}{v^*} \tag{2.15}$$

$$\tilde{v} \equiv \frac{V}{V^*} \qquad \tilde{v} \equiv \frac{1}{\tilde{\rho}} \tag{2.16}$$

The minimum value of the free energy is:

$$\left. \frac{\partial \tilde{G}}{\partial \tilde{v}} \right|_{\tilde{T}, \tilde{P}} = 0 \tag{2.17}$$

from which the *equation of state* of the system is defined:

$$\tilde{\rho}^2 + \tilde{P} + \tilde{T} \left[\ln(1 - \tilde{\rho}) + \left(1 - \frac{1}{r} \right) \tilde{\rho} \right] = 0 \tag{2.18}$$

In this framework, a pure fluid is completely characterized by three molecular parameters:

ϵ^* (total interaction energy per mer)

v^* (close packed volume of a mer)

r (number of mer of a molecule)

or equivalently by the scale factors T^*, P^* and ρ^*. The number of sites r occupied by the molecule and its molecular weight M are related to the scale factors by

$$\frac{RT^*}{P^*} \rho^* = v^* \rho^* = \frac{M}{r} \tag{2.19}$$

and

$$\frac{P^* v^*}{RT^*} = 1 \tag{2.20}$$

For a polymer liquid in which $r \to \infty$, the equation of state (2.18) becomes

$$\tilde{\rho}^2 + \tilde{P} + \tilde{T}[\ln(1 - \tilde{\rho}) + \tilde{\rho}] = 0 \tag{2.21}$$

To sum up, the assumptions made within the model are:

- lattice fluid made by mers and holes;

- closed packed mer volume and hole volume are equal (v^*);

- only nonbonded mer-mer interactions energy is considered;

- mean field approximation (single ϵ^* value);

- Ω is function of the single parameter N_0 (number of lattice holes).

2.1.2 Fluid mixtures

To extend the theory to fluid mixtures, a set of mixing rules were defined, on the basis of modeling assumptions. As stated in the pure fluid treatment, only the nearest neighbor interactions determine the total lattice energy, whereas hole-mer and hole-hole interactions have zero energy.

The lattice energy in the large z limit is defined as:

$$E = -N_r \sum_i \sum_j f_i f_j \epsilon_{ij}^* \tag{2.22}$$

$$\epsilon_{ij}^* \equiv \frac{z}{2} \epsilon_{ij} \tag{2.23}$$

where ϵ_{ij}^* is the interaction energy of a mer belonging to component i when it is surrounded by z mers belonging to component j.

The total volume of the mixture is obtained multiplying the total mer number by the *average close packed volume of a mer* in the mixture (v^*):

$$V = N_r v^* \tag{2.24}$$

The total mer number is:

$$N_r \equiv N_0 + \sum_i r_i N_i \tag{2.25}$$

where N_0 is the number of holes, r_i is the mer number of molecule i and N_i is the number of i molecules.

The close packed volume of the mixture is:

$$V^* = v^* \sum r_i N_i \equiv r N v^* \tag{2.26}$$

It is worth noticing that the *reduced volume* of the mixture $\tilde{v}$ is independent of v^*:

$$\tilde{v} \equiv \frac{V}{V^*} = \frac{N_0 + rN}{rN} \tag{2.27}$$

The unknown value of v^* was determined by enunciating two more mixing rules, related to the close packed mixture:

1. The pure component (denoted by the 0 superscript) and mixture volume and mer number are related by:

$$r_i = r_i^0 \frac{v_i^*}{v^*} \tag{2.28}$$

   i.e., the close packed molecular volume of each component is conserved.

2. Considering the close packed condition, the total number of pair interactions in mixture and the sum of the pair interactions of the components in pure states are equal:

$$(z/2) \sum r_i^0 N_i = (z/2) \sum r_i N_i = (z/2)rN \tag{2.29}$$

From equations 2.28 and 2.29, a relationship for the average close packed mer volume can be drawn:

$$v^* = \sum \phi_i^0 v_i^* \tag{2.30}$$

where

$$\phi_i^0 = \frac{r_i^0 N_i}{\sum r_i^0 N_i} \equiv \frac{r_i^0 N_i}{rN} \tag{2.31}$$

These combining rules introduce a surface area effect. A component with a larger mer volume can establish more interactions per mer in the mixture than in the pure state. For example, if $v_1^* > v_2^*$, the pair interactions of component 1 in the mixture are more than in the pure state, as $r_1 > r_1^0$. Conversely, the component 2 will establish a number of interactions lower than in the pure state, as the total number of interactions is conserved.

The free energy can be expressed in dimensionless variables:

$$\frac{G}{Nr\epsilon^*} \equiv \tilde{G} = -\tilde{\rho} + \tilde{P}\tilde{v} + \tilde{T}\left[(\tilde{v} - 1)\ln(1 - \tilde{\rho}) + \frac{1}{r}\ln\tilde{\rho} + \sum \frac{\phi_i}{r_i}\ln\phi_i\right] \tag{2.32}$$

where

$$\tilde{T} \equiv \frac{T}{T^*} \qquad T^* \equiv \frac{\epsilon^*}{k} \tag{2.33}$$

$$\tilde{P} \equiv \frac{P}{P^*} \qquad P^* \equiv \frac{\epsilon^*}{v^*} \tag{2.34}$$

$$\tilde{v} \equiv \frac{1}{\tilde{\rho}} \equiv \frac{V}{V^*} \tag{2.35}$$

$$\epsilon^* = \sum\sum \phi_i \phi_j \epsilon_{ij}^* = \sum \phi_i \epsilon_{ii}^* - kT \sum\sum \phi_i \phi_j \chi_{ij} \tag{2.36}$$

$$\chi_{ij} = \frac{\epsilon_{ii}^* + \epsilon_{jj}^* - 2\epsilon_{ij}^*}{kT} \tag{2.37}$$

$$\phi_i = \frac{r_i N_i}{\sum r_i N_i} = \frac{r_i N_i}{rN} \tag{2.38}$$

The resulting equation of state is

$$\tilde{\rho}^2 + \tilde{P} + \tilde{T}\left[\ln(1-\tilde{\rho}) + \left(1 - \frac{1}{r}\right)\tilde{\rho}\right] = 0 \tag{2.39}$$

or, rearranged

$$\frac{PV}{NkT} = \frac{r\tilde{P}\tilde{v}}{\tilde{T}} = 1 - r\left[1 + \frac{\ln(1-\tilde{\rho})}{\tilde{\rho}} + \frac{\tilde{\rho}}{\tilde{T}}\right] \tag{2.40}$$

Equation 2.39 is formally identical with the EOS of a pure fluid (equation 2.18).

The chemical potential is defined as:

$$\mu_i \equiv \left.\frac{\partial G}{\partial N_i}\right|_{T,P,N_j} \tag{2.41}$$

where N_j are the other components of the system. It is useful to transform the derivative in terms of volume fraction, as the model equation are not directly related to the number of molecules:

$$\frac{\partial G}{\partial N_i} = r_i g + \frac{rN}{r_i}\sum_{i,j}\left(\frac{\partial g}{\partial \phi_k}\frac{\partial \phi_k}{\partial N_i}\right) \tag{2.42}$$

where g is the free energy per mer ($g = G/rN$) and N is the total number of molecules.

Recalling the relation 2.38, the derivatives of volume fraction with respect to the mole number are:

$$\frac{\partial \phi_i}{\partial N_i} = \frac{\phi_i(1-\phi_i)}{N_i} \tag{2.43}$$

71

$$\frac{\partial \phi_j}{\partial N_i} = -\frac{\phi_i \phi_j}{N_i} \tag{2.44}$$

Therefore, the chemical potential can be calculated as:

$$\mu_i = r_i \left[g + (1 - \phi_i)\frac{\partial g}{\partial \phi_i} - \sum_j \left(\phi_j \frac{\partial g}{\partial \phi_j} \right) \right] \tag{2.45}$$

For a binary mixture can be derived

$$\mu_1 = kT \left\{ \ln \phi_1 + \left(1 - \frac{r_1}{r_2} \right) \phi_2 + r_1^0 \tilde{\rho} \left[\chi_{12} + \left(1 - \frac{v_1^*}{v_2^*} \right) \lambda_{12} \right] \phi_2^2 \right\} +$$
$$+ r_1^0 \epsilon_{11}^* \left\{ -\tilde{\rho} + \tilde{P}_1 \tilde{v} + \tilde{T}_1 \left[(\tilde{v} - 1) \ln(1 - \tilde{\rho}) + \frac{1}{r_1^0} \ln \tilde{\rho} \right] \right\} \tag{2.46}$$

where

$$\lambda_{12} = \frac{\partial (\epsilon^*/kT)}{\partial \phi_1} = \frac{1}{\tilde{T}_1} - \frac{1}{\tilde{T}_2} + (\phi_1 - \phi_2)\chi = -\lambda_{21} \tag{2.47}$$

$$\tilde{T}_i \equiv \frac{T}{T_i^*} \qquad \tilde{P}_i \equiv \frac{P}{P_i^*} \tag{2.48}$$

The expression for μ_2 is easily obtained by interchanging the indices 1 and 2.

Only the ϵ_{12}^* parameter is needed to characterize a binary mixture, whereas all other parameters can be obtained from pure component properties. Authors assumed that ϵ_{12}^* can be estimated by means of Berthelot formula with a dimensionless corrective parameter:

$$\epsilon_{12}^* = \zeta_{12}(\epsilon_{11}^* \epsilon_{22}^*)^{1/2} \tag{2.49}$$

A slightly different formulation of the model assumes that characteristic pressures are pairwise additive in the close packed mixtures [Sanchez and Lacombe, 1978]:

$$P^* = \phi_1 P_1^* + \phi_2 P_2^* - \phi_1 \phi_2 \Delta P^* \tag{2.50}$$

$$\Delta P^* = P_1^* + P_2^* - 2P_{12}^* \tag{2.51}$$

This consideration stems from the observation that P^* can be directly correlated to the Cohesive Energy Density (CED), quantifiable by means of Hildebrand solubility parameters:

$$P_i^* = \delta_i^2 \tag{2.52}$$

The two combining rules yield the following relationship for the average close packed mer volume:

$$v^* = \phi_1^0 v_1^* + \phi_2^0 v_2^* \tag{2.53}$$

where

$$\phi_1^0 = \frac{r_1^0 N_1}{rN} = 1 - \phi_2^0 \tag{2.54}$$

The concentrations ϕ_1 and ϕ_1^0 are related by

$$\phi_1^0 = \frac{\phi_1}{\phi_1 + \nu\phi_2}; \quad \phi_1 = \frac{\nu\phi_1^0}{\nu\phi_1^0 + \phi_2^0} \tag{2.55}$$

$$\nu = \frac{v_1^*}{v_2^*} \tag{2.56}$$

The mer-mer interaction energy of the mixture is given by

$$\epsilon^* = P^* v^* = (\phi_1 P_1^* + \phi_2 P_2^* - \phi_1\phi_2\Delta P^*)(\phi_1^0 v_1^* + \phi_2^0 v_2^*) \tag{2.57}$$

T^* can be expressed as

$$\frac{T^*}{T} \equiv \frac{1}{\tilde{T}} = \frac{\dfrac{\phi_1}{\tilde{T_1}} + \dfrac{\nu\phi_2}{\tilde{T_2}}}{\phi_1 + \nu\phi_2} - \phi_1\phi_2 X \tag{2.58}$$

where

$$X \equiv \frac{\Delta P^* v^*}{kT} \tag{2.59}$$

A third model formulation introduces explicitly the free volume, by means of the hole volume v_0 [Sanchez, 1987]. In this case, the hole volume and the close packed volume are defined as:

$$\frac{1}{v_0} \equiv \sum \phi_i \frac{P_i^*}{kT_i^*} \tag{2.60}$$

$$\frac{1}{rv^*} \equiv \sum \frac{\phi_i}{r_i v_i^*} \tag{2.61}$$

73

The mixtures characteristic properties are defined as:

$$T^* = \frac{P^* v_0}{k} \tag{2.62}$$

$$P^* = \sum \phi_i P_i^* - \sum_{i<j} \sum_j \phi_i \phi_j \chi_{ij} \tag{2.63}$$

where the interaction parameter χ_{ij} is calculated as:

$$kT\chi_{ij} = \frac{\epsilon_{ii}^*}{v_i^*} + \frac{\epsilon_{jj}^*}{v_j^*} - \frac{2\epsilon_{ij}^*}{(v_i^* v_j^*)^{0.5}} \tag{2.64}$$

For determining the size parameter r of mixture, the following relation can be used:

$$r = \frac{(rv^*)}{v_0} = \frac{P^*(rv^*)}{kT^*} \tag{2.65}$$

The Gibbs free energy per mer can be expressed as:

$$g = kT \sum_i \frac{\phi_i \ln \phi_i}{r_i v_i^*} - \tilde{\rho}P^* + P\tilde{v} + kT\tilde{v}\left[\frac{(1-\tilde{\rho})\ln(1-\tilde{\rho})}{v_0} + \frac{\tilde{\rho}\ln\tilde{\rho}}{rv^*}\right] \tag{2.66}$$

2.1.3 Spinodal calculation

For a binary system, the spinodal equation is:

$$g_{11}g_{vv} - g_{1v}^2 = 0 \tag{2.67}$$

where the subscripts refer to the partial derivatives with respect to ϕ_1 and $\tilde{v}$.

The derivative terms, referring to the model formulation given in [Sanchez, 1987], are reported in appendix A.

The spinodal equation must be coupled with the equation of state:

$$g_v = \tilde{\rho}^2 + \tilde{P} + \tilde{T}\left[\ln(1-\tilde{\rho}) + \left(1 - \frac{1}{r}\right)\tilde{\rho}\right] = 0 \tag{2.68}$$

The spinodal equation for a ternary compressible system is:

$$\Delta \begin{vmatrix} g_{11} & g_{12} & g_{1v} \\ g_{21} & g_{22} & g_{2v} \\ g_{v1} & g_{v2} & g_{vv} \end{vmatrix} = 0 \tag{2.69}$$

where the mixed derivative are equal ($g_{ij} = g_{ji}$). This relation can be expressed as:

$$\prod g_{ii} + 2 \prod g_{ij} - \sum g_{ii} g_{jk}^2 = 0 \tag{2.70}$$

The derivative terms, referring to the model formulation given in [Sanchez, 1987], are reported in appendix A.

2.2 Compressible LF model with specific interactions

A consistent improvement of the Sanchez-Lacombe model was attained with the incorporation of a specific interaction term [Sanchez and Balazs, 1989]. Specific interactions between molecules are often encountered in real systems (e.g. hydrogen bonding), and can substantially influence both the entropic and energetic contents of the mixture. Thus, taking into account specific interactions can improve the predictions with a higher adherence to the physical properties of a solution.

Within this framework, the expression of free energy is the same as derived in the case without specific interactions:

$$g = -\tilde{\rho}\epsilon_T^* + \frac{Pv^*}{\tilde{\rho}} + kT \left[\frac{1 - \tilde{\rho}}{\tilde{\rho}} \ln(1 - \tilde{\rho}) + \frac{\ln \tilde{\rho}}{r} + \sum \frac{\phi_i}{r_i} \ln \phi_i \right] \tag{2.71}$$

where the only different parameter is ϵ_T^*, i.e. the mixing interaction energy, which is expressed as:

$$\epsilon_T^*(\phi, T) = \phi_1^2 \epsilon_{11}^* + \phi_2^2 \epsilon_{22}^* + 2\phi_1 \phi_2 f_{12}^* \tag{2.72}$$

where the f_{12}^* temperature dependent parameter is related to specific interactions between components 1 and 2.

An expression for f_{12}^* was derived by assuming that a fraction θ of interactions are "strong" with energy $\epsilon_{12}^* + \delta\epsilon^*$, and the remaining $1 - \theta$ are nonspecific and equal to ϵ_{12}^* (the same value encountered in the previous model statement):

$$f_{12}^* = \epsilon_{12}^* + \theta\delta\epsilon^* - \frac{z}{2}RT \left[\theta \ln \theta + (1 - \theta) \ln \frac{1 - \theta}{q} + \ln(1 + q) \right] \tag{2.73}$$

where z is the lattice coordination number (usually $z = 12$) and q is the number of ways that the nonspecific 1-2 interaction occurs. Minimizing the free energy related to the 1-2 interactions, the θ dependence can be eliminated obtaining:

$$f_{12}^* = \epsilon_{12}^* + \delta\epsilon^* - \frac{z}{2}RT \left[\frac{1 + q}{1 + q \exp(-\delta\epsilon^*/6RT)} \right] \tag{2.74}$$

The model, in its original formulation, is applicable only on binary mixtures. An extension can be derived, based on the following mixing rule for the $\epsilon_T^*(\phi, T)$ interaction parameter:

$$\epsilon_T^*(\phi, T) = \sum_i \sum_j \phi_i \phi_j f_{ij}^* \tag{2.75}$$

where $f_{ii}^* = \epsilon_{ii}^*$.

Also in this case, the spinodal locus is determined by the determinant of the 3×3 matrix:

$$\Delta \begin{vmatrix} g_{11} & g_{12} & g_{1\tilde{\rho}} \\ g_{21} & g_{22} & g_{2\tilde{\rho}} \\ g_{\tilde{\rho}1} & g_{\tilde{\rho}2} & g_{\tilde{\rho}\tilde{\rho}} \end{vmatrix} = 0 \tag{2.76}$$

where the mixed derivatives are equal ($g_{ij} = g_{ji}$). See appendix A for the terms of the matrix.

For the compressible LF model extended to specific interactions, the chemical potential of a species i in a mixture with j components becomes:

$$\mu_i = r_i \tilde{\rho} \left[\epsilon_T^* - 2 \left(\phi_i \epsilon_{ii}^* + \sum \phi_j f_{ij}^* \right) + \frac{P v_i^*}{\tilde{\rho}} \right]$$
$$+ kT \left[\ln \phi_i + \sum_j \left(1 - \frac{r_i}{r_j} \right) \phi_j + r_i \left(\frac{1 - \tilde{\rho}}{\tilde{\rho}} \ln(1 - \tilde{\rho}) + \frac{\ln \tilde{\rho}}{r_i} \right) \right] \tag{2.77}$$

2.2.1 Critical point

The critical point represents the state of incipient phase separation in a mixture, where the compositions of the coexisting phases are equal. In the case of a UCST (Upper Critical Solution temperature) phase diagram, at temperatures above the critical point, phase separation do not occur. Conversely, when the solution exhibits a LCST (Lower Critical Solution Temperature) behavior, at temperatures below the critical point the system is completely miscible. In some cases, a mixture can have both critical points.

The critical point can be defined mathematically in different ways: for example, if $\Psi(\phi, T, \tilde{\rho})$ is the spinodal equation, the critical point is expressed as:

$$\left. \frac{\partial \Psi}{\partial T} \right|_{\phi, \tilde{\rho}} = 0 \tag{2.78}$$

Another way, more precise, to define the critical point is referred to the free energy:

$$\frac{d^3 g}{d\phi^3} = 0 \tag{2.79}$$

At low pressure, the phase equilibria in polymer solutions are practically independent of pressure. To simplify the model equations, the intensive free energy at zero pressure (f) can be considered, and the total derivative is then computed as:

$$\frac{d^3 f}{d\phi^3} = \frac{\partial^3 f}{\partial \phi^3} + 3 \frac{\partial^3 f}{\partial^2 \phi \partial \tilde{\rho}} \left(\frac{d\tilde{\rho}}{d\phi} \right) + 3 \frac{\partial^3 f}{\partial \phi \partial^2 \tilde{\rho}} \left(\frac{d\tilde{\rho}}{d\phi} \right)^2 + \frac{\partial^3 f}{\partial \tilde{\rho}^3} \left(\frac{d\tilde{\rho}}{d\phi} \right)^3 \tag{2.80}$$

where

$$\frac{d\tilde{\rho}}{d\phi} = -\frac{f_{\phi\tilde{\rho}}}{f_{\tilde{\rho}\tilde{\rho}}} \tag{2.81}$$

The critical point equation can be therefore expressed as:

$$f_{\phi\phi\phi} - 3 f_{\phi\phi\tilde{\rho}} \frac{f_{\phi\tilde{\rho}}}{f_{\tilde{\rho}\tilde{\rho}}} + 3 f_{\phi\tilde{\rho}\tilde{\rho}} \left(\frac{f_{\phi\tilde{\rho}}}{f_{\tilde{\rho}\tilde{\rho}}} \right)^2 - f_{\tilde{\rho}\tilde{\rho}\tilde{\rho}} \left(\frac{f_{\phi\tilde{\rho}}}{f_{\tilde{\rho}\tilde{\rho}}} \right)^3 = 0 \tag{2.82}$$

where the single terms are computed in the following ways:

$$f_{\phi\phi\phi} = -\frac{1}{r_1 \phi_1} + \frac{1}{r_2 \phi_2} \tag{2.83}$$

$$f_{\phi\phi\tilde{\rho}} = -\frac{2}{RT}(\epsilon_{11}^* + \epsilon_{22}^* - 2f_{12}^*) \tag{2.84}$$

$$f_{\phi\tilde{\rho}\tilde{\rho}} = \frac{1}{\tilde{\rho}} \left\{ \frac{1}{\tilde{\rho}} \left(\frac{1}{r_1} - \frac{1}{r_2} \right) - \frac{4}{RT} \left[\phi_1 \epsilon_{11}^* - \phi_2 \epsilon_{22}^* + (\phi_2 - \phi_1) f_{12}^* \right] \right\} \tag{2.85}$$

$$f_{\tilde{\rho}\tilde{\rho}\tilde{\rho}} = -\frac{1}{\tilde{\rho}^2} \left[\frac{2\tilde{\rho} - 3}{(1 - \tilde{\rho})^2} - \frac{1}{r\tilde{\rho}^2} + \frac{6\epsilon_T^*}{RT} \right] \tag{2.86}$$

Equation 2.82 must be coupled with the spinodal equation and the equation of state for the solution finding.

2.3 Oishi-Prausnitz model

The Oishi-Prausnitz (OP) model [Oishi and Prausnitz, 1978] derives from the Flory-Huggins theory. The solvent activity is calculated as:

$$\ln a_i = \ln a_i^C + \ln a_i^R + \ln a_i^{FV} \tag{2.87}$$

The activity is expressed as a sum of three contributions: the combinatorial term, which considers only the possible microscopic conformations of the system; the residual term,

related to the energy interactions between solute and solvent molecules; the free volume term, which must always be added in case of polymer solutions.

The OP formulation is not entirely applicable to ternary systems, as it is valid for binary solutions and the expression was not extended to multicomponent mixtures [Oishi and Prausnitz, 1978]. The free-volume expression was taken, whereas the combinatorial and residual terms were computed as reported in [Reid et al., 1987].

In principle, input parameters to calculate the activity of the solvent are few and simple: temperature, composition and chemical formula of the components.

The combinatorial term assumes the form:

$$\ln a_i^C = \ln x_i + \ln \frac{\varphi_i}{x_i} + 5Q_i \ln \frac{\theta_i}{\varphi_i} + l_i - \frac{\varphi_i}{x_i} \sum_j x_j l_j \tag{2.88}$$

where x_i is the molar fraction, φ_i is the segment fraction, θ_i is the surface fraction and l_i is a function of volume and surface parameters (R_k and Q_k, respectively).

The segment fraction is defined as:

$$\varphi_i = \frac{r_i x_i}{\sum_j r_j x_j} \tag{2.89}$$

where the volume parameter r_i is:

$$r_i = \sum_k \nu_k^{(i)} R_k \tag{2.90}$$

where $\nu_k^{(i)}$ is the number of k type functional groups in molecule i. The surface fraction is:

$$\theta_i = \frac{q_i x_i}{\sum_j q_j x_j} \tag{2.91}$$

where the surface parameter q_i is:

$$q_i = \sum_k \nu_k^{(i)} Q_k \tag{2.92}$$

The remaining parameter l_i is calculated as:

$$l_i = 5(r_i - q_i) - (r_i - 1) \tag{2.93}$$

The residual term is expressed by the following:

$$\ln a_i^R = \sum_k \nu_k^{(i)} \left[\ln \Gamma_k - \ln \Gamma_k^{(i)} \right] \tag{2.94}$$

where Γ_k is the activity coefficient of k functional group in the solution at the system temperature; $\Gamma_k^{(i)}$ is the activity coefficient of k functional group in the pure component i. These two parameters are calculated as:

$$\ln \Gamma_k = Q_k \left[1 - \ln \left(\sum_k \theta_m' \Psi_{mk} \right) - \sum_m \left(\frac{\theta_m' \Psi_{km}}{\sum_n \theta_n' \Psi_{nm}} \right) \right] \qquad (2.95)$$

where Ψ_{nm} is the interaction parameter between molecule n and m and M is the molecular weight. The interaction parameter is:

$$\Psi_{nm} = \exp \left(-\frac{a_{mn}}{T} \right) \qquad (2.96)$$

where a_{mn} are tabulated values for group pairs. The quantity θ_m' is the surface fraction of the m group calculated on a mass fraction basis:

$$\theta_m' = \frac{Q_m W_m}{\sum_n Q_n W_n} \qquad (2.97)$$

The mass fraction of the k group is defined as:

$$W_k = w_i \frac{M_k \nu_k^{(i)}}{M_i} \qquad (2.98)$$

where w_i is the mass fraction of species i.

For the calculation of $\Gamma_k^{(i)}$ all summations are referred to the only molecule i and its own functional groups.

The free-volume contribution is computed as follows:

$$\ln a_i^{FV} = 3c \ln \left[\frac{\bar{v}_i^{1/3} - 1}{\bar{v}_M^{1/3} - 1} \right] - c \left[\left(\frac{\bar{v}_i}{\bar{v}_M} - 1 \right) \left(1 - \frac{1}{\bar{v}_M^{1/3}} \right)^{-1} \right] \qquad (2.99)$$

where

$$\bar{v}_i = \frac{v_i}{15.17 b \frac{r_i}{M_i}} \qquad (2.100)$$

is the reduced volume of the solvent i; v_i, r_i and M_i are the specific volume, the volume parameter (defined by the model) and the molecular weight of the ith component, respectively; furthermore

$$\bar{v}_M = \frac{\sum_i v_i w_i}{15.17 b \sum_i \frac{r_i w_i}{M_i}} \qquad (2.101)$$

is the reduced volume of solution; w_i is the weight fraction of the ith component.

The c coefficient (equation 2.99) is an external degree of freedom parameter equal to 1.1; b (equations 2.100 and 2.101) is a proportionality factor equal to 1.28.

The calculation of polymer activity is not intrinsically possible via this model. In all these cases, the Gibbs-Duhem equation must be recalled and applied:

$$\sum_i x_i d \ln \gamma_i = 0 \tag{2.102}$$

For a ternary system ($i = 3$), equation 2.102 becomes:

$$x_1 d \ln \gamma_1 + x_2 d \ln \gamma_2 + x_3 d \ln \gamma_3 = 0 \tag{2.103}$$

which rearranged for γ_3 (polymer activity coefficient) gives out:

$$d \ln \gamma_3 = -\frac{x_1}{x_3} d \ln \gamma_1 - \frac{x_2}{x_3} d \ln \gamma_2 \tag{2.104}$$

The activity coefficient of polymer is therefore:

$$\ln \gamma_3 = -\int_1^{x_3'} \frac{x_1}{x_3} d \ln \gamma_1 - \int_1^{x_3'} \frac{x_2}{x_3} d \ln \gamma_2 \tag{2.105}$$

where the reference state ($\ln \gamma_3 = 0$) is the pure polymer ($x_3 = 1$). Although the reference state for polymers is usually taken at infinite dilution, in this case was taken coherently with the solvents' reference state.

The integral equation derived for polymer activity coefficient can be computed with numerical methods. The x_i/x_3 ratios are only functions of x_3, as the solvent ratio x_1/x_2 was fixed in calculations. By fixing a value for the solvent ratio ($\alpha = x_1/x_2$), the solvents' composition can be expressed as:

$$\begin{cases} x_1 = \alpha \dfrac{1 - x_3}{1 + \alpha} \\[2ex] x_2 = \dfrac{1 - x_3}{1 + \alpha} \end{cases} \tag{2.106}$$

After calculation of components' activity, the molar free energy of mixing may be computed as follows:

$$\Delta G_m = RT \sum_{i=1}^{3} x_i \ln a_i \tag{2.107}$$

When applying the Oishi-Prausnitz model to the ternary system consisting of PLLA-dioxane-water system, very high values ($15 < \ln a^{FV} < 65$) of free-volume contribution for water were obtained, which lead to results physically unacceptable.

Therefore, the attempt to correct the modeling of Oishi-Prausnitz by Elbro et al. [1990] was explored.

2.4 Corrections to the free volume contribution: model by Elbro et al., [1990]

Elbro et al. [1990] pointed out that free-volume influences activity coefficient only if free-volumes of solution components are significantly different; in other words, the existence of free-volume on its own does not necessary imply a deviation from ideal conditions. As a matter of fact, multicomponent systems with solute, solvent and antisolvent exhibiting similar free volume might behave as ideal mixtures. This statement derives from the analysis of a different form for combinatorial and free-volume terms calculation, incorporated into a single term:

$$\ln \gamma_i^{FV+C} = \ln \left(\frac{\varphi_i^{FV}}{x_i} \right) + 1 - \frac{\varphi_i^{FV}}{x_i} \tag{2.108}$$

where φ_i^{FV} is

$$\varphi_i^{FV} = \frac{x_i(v_i - v_i^*)}{\sum_j x_j \left(v_j - v_j^* \right)} \tag{2.109}$$

where v and v^* are the effective specific volume and the van der Waals specific volume of component. The latter can be estimated based on the volume parameter R_k [Abrams and Prausnitz, 1975]:

$$v^* = 15.17 R_k \tag{2.110}$$

Dimensions of v^* are cm^3/mol and the coefficient 15.17 is derived from a reference volume. If one subtracts to equation 2.108 the combinatorial term (equation 2.88), a different expression of free-volume contribution can be drawn:

$$\ln \gamma_i^{FV} = \ln \frac{(FV\%)_i}{(FV\%)_{mix}} + \frac{v_i}{v_{mix}} \left(1 - \frac{(FV\%)_i}{(FV\%)_{mix}} \right) \tag{2.111}$$

where

$$(FV\%)_i = \frac{v_i - v_i^*}{v_i} \cdot 100 \tag{2.112}$$

$$(FV\%)_{mix} = \frac{v_{mix} - v_{mix}^*}{v_{mix}} \cdot 100 \tag{2.113}$$

Equation 2.111 shows that there is a free-volume contribution on solvent activity if and only if free-volume bears different amounts for the various species in solution. On the other hand, when $(FV\%)_i = (FV\%)_{mix}$:

$$\ln \gamma^{FV+C} - \ln \gamma^C = 0 \tag{2.114}$$

and, therefore,

$$\ln \gamma^{FV} = 0 \tag{2.115}$$

Based on equation 2.111, the activity of the ith component can be defined as:

$$\ln a_i = \ln a_i^{FV+C} + \ln a_i^R \tag{2.116}$$

The residual term, $\ln a^R$, maintains the same expression of Oishi-Prausnitz model.

Bibliography

D. S. Abrams and J. M. Prausnitz. Statistical thermodynamics of liquid mixtures: A new expression fo the excess gibbs energy of partly or completely miscible systems. *AIChE Journal*, 21(1):116–128, 1975.

A. Bondi. *Physical Properties of Molecular Crystals, Liquids and Glasses*. Wiley, New York, N.Y., 1968.

H. S. Elbro, Aa. Fredenslund, and P. Rasmussen. A new simple equation for the prediction of solvent activities in polymer solutions. *Macromolecules*, 23:4707–4714, 1990.

R. H. Lacombe and I. C. Sanchez. Statistical thermodynamics of fluid mixtures. *Journal of Physical Chemistry*, 80(23):2568–2580, 1976.

T. Oishi and J. M. Prausnitz. Estimation of solvent activities in polymer solutions using a group-contribution method. *Industrial Engineering Chemical Process Design Development*, 17(3):333–339, 1978.

R. C. Reid, J. M. Prausnitz, and B. E. Poling. *The properties of gases and liquids*. McGraw-Hill, 1987.

I. C. Sanchez. *Encyclopedia of Physical Science and Technology*, volume 11, chapter Polymer Phase Separation. Academic Press, 1987.

I. C. Sanchez and A. C. Balazs. Generalization of the lattice-fluid model for specific interactions. *Macromolecules*, 22:2325–2331, 1989.

I. C. Sanchez and R. H. Lacombe. An elementary molecular theory of classical fluids. Pure fluids. *Journal of Physical Chemistry*, 80(21):2352–2362, 1976.

I. C. Sanchez and R. H. Lacombe. Statistical thermodynamics of polymer solutions. *Macromolecules*, 11(6):1145–1156, 1978.

3 Phase diagram prediction: results

The thermodynamic models presented in the previous chapter were applied to calculate the phase diagram of the PLLA-dioxane-water system.

The Sanchez-Lacombe model, with the extension to specific interactions, provided a very good accord with experimental data. The influence of specific interactions on the predicted phase diagrams is thereafter discussed. A simple framework based on Hansen solubility parameters was adopted to select the appropriate couple of species with specific interactions. Then, the results accomplished are presented.

On the other hand, the Oishi-Prausnitz model, and its successive modifications were not capable to reproduce results even qualitatively comparable to experimental data. The main reason was argued to be correlated to the water behavior: as a matter of fact, some model parameters for water generated a set of results with no sound physical justification and therefore not reliable. In this case, a digression on the possible arguments, together with a set of trials performed with various aqueous solutions, are dibated.

3.1 Compressible LF with specific interactions

In order to apply the compressible LF model, three characteristic parameters (usually P^*, T^* and ρ^*) for each species are needed. Tables of parameters for molecular solvents and polymers are reported in literature [Sanchez and Lacombe, 1976, 1978]. However, no data referring to PLLA were available. To overcome this lack, the characteristic parameters were estimated by fitting the equation of state with experimental PVT data on polylactide (reported by Sato et al. [2000]). In this procedure, the r parameter was assumed to be infinite, as it is related to the chain lenght [Sanchez and Lacombe, 1977]: the values of calculated parameters are resumed in table 3.1. The r parameter, i.e. the number of lattice sites occupied by the macromolecule, is a linear function of the molecular weight:

$$r = M \frac{P^*}{kT^*\rho^*} \tag{3.1}$$

In common practice, a polymeric material is characterized by a distribution of molecular weights instead of a unique value. For high r values, i.e. for polymer liquids, the equation of state is poorly sensitive to r, and therefore the r value can be estimated via the (average) molecular weight. All things considered, although polydispersity affects the chemical potential, and therefore influences phase equilibria [Tompa, 1956], in the following analysis a unique value of r is adopted.

Table 3.1: Characteristic parameters for PLLA

ρ^* [g/cm^3]	T^* [K]	P^* [atm]
1.357	609	6462.1

The lattice fluid model accounting for specific interactions, when dealing with a ternary solution, incorporates six adjustable parameters: three are related to the nonspecific pair interaction energies (ζ), and the other three are the specific interaction energies between the mixture components ($\delta\epsilon_{ij}^*$).

It is reasonable to asser that not all of these are necessary for a complete description of the system. A qualitative analysis, based on Hansen solubility parameters, allows one to select the appropriate interaction parameters. As a matter of fact, Hansen solubility parameters have been already used successfully for the calculation of interaction parameters in the lattice-fluid model [Rodgers and Sanchez, 1993]. The Hansen parameters give a measure of nonpolar or dispersion interactions (δ_d), polar interactions (δ_p) and specific association interactions (δ_h), e.g. hydrogen bonding. The value of the total (or Hildebrand) solubility parameter (δ_t) is computed as following:

$$\delta_t^2 = \delta_d^2 + \delta_p^2 + \delta_h^2 \tag{3.2}$$

The values for PLLA, dioxane and water are reported in table 3.2.

Table 3.2: Hansen solubility parameters [MPa$^{0.5}$]

	δ_d	δ_p	δ_h	δ_t
PLLA	18.6	9.9	6.0	21.9
dioxane	19.0	1.8	7.4	20.5
water	15.5	16.0	42.3	47.8

In principle, specific interactions can occur between all pairs of the PLLA-dioxane-water system, and water is able to form hydrogen bonds both with the polymer and the dioxane.

Nevertheless, due to the polymer hydrophobicity, hydrogen bonds can play a relevant role only in the adsorption of water by the polymer, i.e. in the region of high polymer contents, that is aside from liquid-liquid equilibrium region. Moreover, the values of δ_h terms result very different: as the δ_h value is directly related to the hydrogen bond energy, this would suggest that PLLA-water specific interactions are not favored as much as the water-water hydrogen bonds (which are stronger). For that reason, the specific interaction parameter between PLLA and water was neglected in calculations. Moreover, as PLLA is a hydrophobic polymer, a negative nonspecific interaction is expected, i.e. $\zeta < 1$.

On the other hand, although it has been shown the presence of hydrogen bonds between water and dioxane [Chaudhari, 2010], the model predicted total miscibility for the binary solution dioxane-water without the use of any adjustable parameter (i.e. $\zeta = 1$ and $\delta\epsilon^*_{ij} = 0$). The addition of a specific interaction parameter for the dioxane-water pair would increase the number of adjustable parameters, thus augmenting the model complexity, without a substantial improvement of the system description. Furthermore, the value of this specific interaction parameter, due to its negligible effect, could trigger large instabilities in the numeric evaluation of the other adjustable parameters. Moreover, more complex arrangements of polymer and solvents in solution may be hypothesized, e.g. ternary complexes (and consequent ternary interaction parameters); however, here the ternary phase behavior is completely deducted from binary properties, making this procedure more easily generalizable and applicable to other ternary system.

PLLA and dioxane show very similar value of all parameters, indicating a very good affinity of the polymer with the solvent. Additionally, the values of the δ_h terms are close (6.0 and 7.4, respectively), suggesting that specific interactions possibly occurs between these two species. Therefore, the $\delta\epsilon^*_{ij}$ term was considered in computations, together with ζ (as they are not independent).

To sum up, among the 6 adjustable parameters, only 3 are needed to suitably depict the solution phase behavior: one for PLLA-water nonspecific interactions and two for PLLA-dioxane specific interactions.

Figure 3.1 shows the phase diagrams obtained with and without the specific interactions parameter. For the PLLA-water pair was set $\zeta_{wp} = 0.88$, i.e. highly negative interactions. In one case (dash-dot line), all other interaction parameters were set to ideal values: the binodal is approximately a straight line. This means the binodal can be expressed mathematically with a linear relation between ϕ_p and ϕ_w, i.e. the phase equilibria are poorly influenced by dioxane.

Introducing specific interactions between PLLA and dioxane (e.g. $\zeta_{dp} = 0.98$ and $\delta\epsilon^*_{dp} = 7500$ J), different features can be noticed (bold line, figure 3.1). At high diox-

ane concentration, the system becomes completely miscible, reflecting the experimental experience. The slope of tie lines is higher with respect to previous case: the polymer rich phase has a dioxane content higher than polymer lean phase. In both cases presented, one of the separated phases is polymer free, thus, accounting for specific interactions between PLLA and dioxane, a more realistic description of the system behavior is obtained.

The temperature effects on the coexistence curve are presented in figure 3.2, where two temperatures are showed (30 and 60°C). The main influence is in the high dioxane concentration region, enlarging the stable zone.

To have a complete picture of the phase diagram, the spinodal was calculated (see figure 3.3). The unstable region is denoted by a "critical" water content in the mixture, which in this case is $\phi_w = 0.15$. Therefore, if employing a solution with a $\phi_w > 0.15$ to prepare scaffold via TIPS, setting a demixing temperature $T_d < 30°C$ will determine a foam microstructure controlled by spinodal decomposition. Otherwise, a multistep cooling protocol can be designed and set-up with the aim to firstly creating a basic architecture via nucleation and growth, and then modifying it via spinodal decomposition.
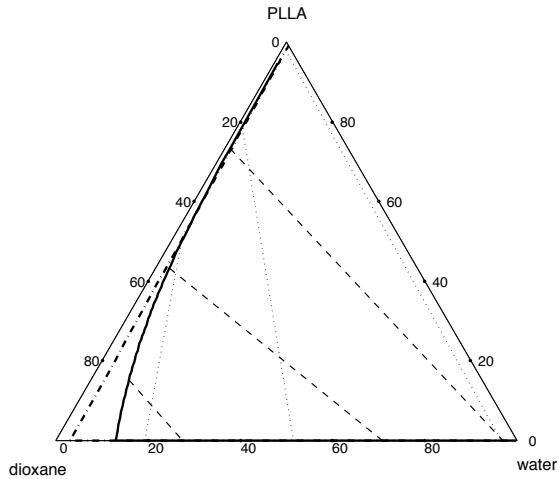
Figure 3.1: Calculated binodal with $\zeta_{wp} = 0.88$, 30°C, $M = 338000$, PLLA-dioxane-water system. Bold line: $\zeta_{dp} = 0.98$, $\delta\epsilon^*_{dp} = 7500$ J. Dash-dot line: ideal parameters. Tie lines are the dashed (specific interactions) and point (ideal parameters) lines

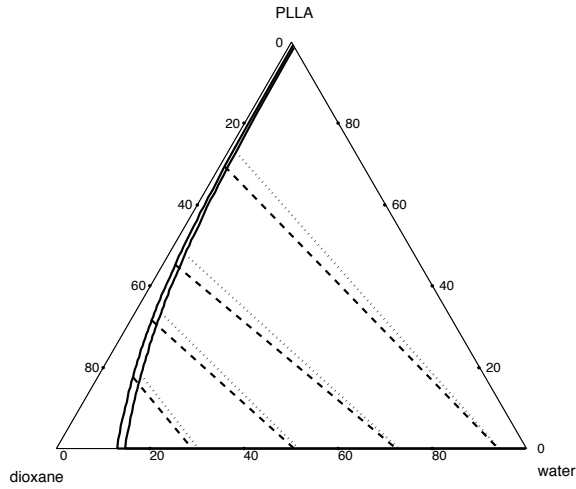**Figure 3.2:** Calculated binodal with $\zeta_{wp} = 0.88$, $\zeta_{dp} = 0.98$, $\delta\epsilon_{dp}^* = 7500$ J, 30 and 60°C, $M = 338000$, PLLA-dioxane-water system. Tie lines are the dashed (30°C) and point (60°C) lines

Figure 3.3: Calculated binodal and spinodal with $\zeta_{wp} = 0.88$, $\zeta_{dp} = 0.98$, $\delta\epsilon_{dp}^* = 7500$ J, 30°C, $M = 338000$, PLLA-dioxane-water system

3.1.1 Correlation with experimental cloud point curves

The lack of data on phase equilibria in ternary polymer solutions is overcome in practice by the experimental derivation of cloud point curves. These are determined by cooling slowly a solution sample: when phase separation starts, the homogeneous solution becomes visually cloudy. The cloud point curves then represent the temperature under which phase separation occurs, and in general are derived at constant solvent/nonsolvent ratio, i.e. treating the system as pseudobinary. However, as a result of this process, they do not show a critical point (typical of binary solutions).

The justification of this behavior is deducible by analyzing the phase diagram at different temperatures. For example, let us consider a solution composed of 13% v/v of PLLA with a dioxane/water ratio of 88.5/11.5. Its location in the phase diagram is shown in figure 3.4. At $T = 70°C$, the solution is homogeneous. To carry out a cloud point measurement for this solution, the sample is cooled, resulting into an enlargement of the immiscible region; at a certain temperature, the binodal intersects the experimental point: the solution will start the demixing process and the cloud point is detected. If the kinetics of phase separation is sufficiently fast, and this is the case of liquid-liquid demixing [van de Witte et al., 1996], the cloud point belongs to binodal line. As can be noticed in figure 3.4, the intersection with the straight line moves toward higher PLLA content with increasing temperature, i.e. the cloud point increases with polymer concentration. From this point of view, at constant solvent/nonsolvent ratio, the cloud point is not expected to show a critical point as binary solutions.

The cloud point curves are then strictly related to coexistence curves, and can be used to depict phase boundaries [van de Witte et al., 1996]. Two sets of experimental cloud point data for the PLLA-dioxane-water system, reported in literature by Hua et al. [2002] and Tanaka and Lloyd [2004], were compared with calculated binodal curves. The interaction parameters were set to equal values in the two cases: only r was modified, as the molecular weights of the polymers investigated were different. The weight average molecular weights were 338000 and 187000, respectively.

As discussed above, three parameters were used to reproduce the phase behavior: the nonspecific interaction parameters for the pairs water-PLLA ($\zeta_{wp} = 0.985$) and dioxane-PLLA ($\zeta_{dp} = 0.815$), and the specific interaction energy for the dioxane-PLLA pair ($\delta\epsilon_{dp}^* = 18600$ J). The parameters were derived on the basis of the data reported by Hua et al. [2002]: the two points at $T = 30°C$ (1% PLLA at d/w=87/13 and 6% PLLA at d/w 88.5/11.5) were chosen as reference. The fitting procedure consisted as following:

- at fixed ζ_{wp}, the two interaction parameters of the PLLA-dioxane pair were changed
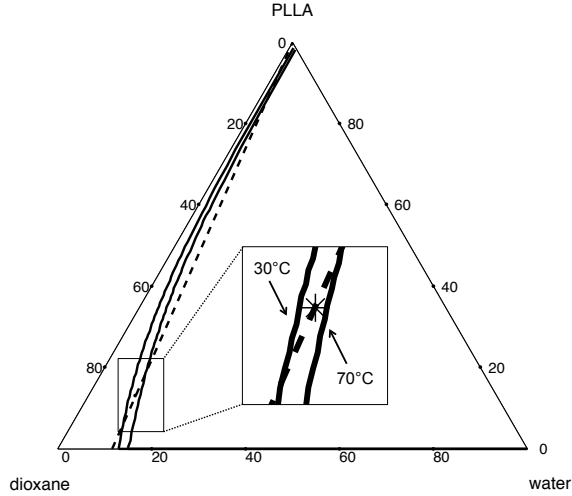
Figure 3.4: Phase diagram at 30 and 70°C, PLLA-dioxane-water system. The dashed line represents the points at which the dioxane/water ratio is 88.5/11.5. The point is $\phi_{diox} = 0.77$

to obtain a satisfactory distance (i.e. composition difference) between the two reference points;

- subsequently, ζ_{wp} was tuned to shift the compositions close to experimental values.

The calculated cloud point curve, reported in figure 3.5, is in a good agreement with experimental data. The corresponding phase diagram is reported in figure 3.6. It is worth noticing that the calculation of equilibrium concentrations at low dioxane content was not possible. This numerical issue does not affect the consistency and usefulness of the as derived phase diagram: as a matter of fact, the relevant information regarding this system are related to the region of high dioxane concentrations (above 80%). Low dioxane concentrations have not yet been experimentally explored, as they do not give out a membrane forming system. Therefore, although having a complete phase diagram, the low dioxane concentration zone cannot be easily validated owing to the lack of experimental data.

The as-derived interaction parameters were used to calculate the cloud point curves reported by Tanaka and Lloyd [2004]. Results are displayed in figure 3.7. In this case, a quantitative agreement was not obtained; however, the main qualitative features of the system are reproduced correctly:

- temperatures and compositions are close to experimental for low polymer weight fraction;

91

- the slope is nearly independent of dioxane/water ratio;

- the cloud point increases with water content in the mixture.
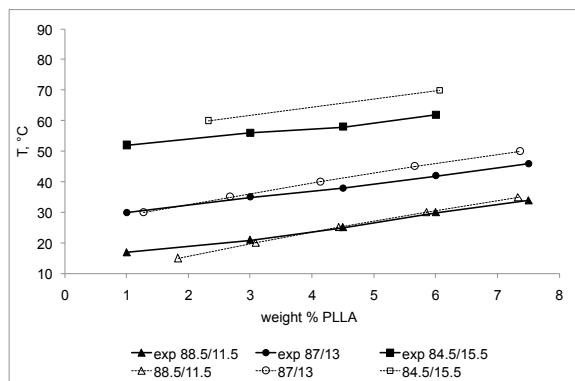
Figure 3.5: Comparison between experimental (filled symbols) and calculated (open symbols) cloud points, PLLA-dioxane-water system, data from Hua et al. [2002]
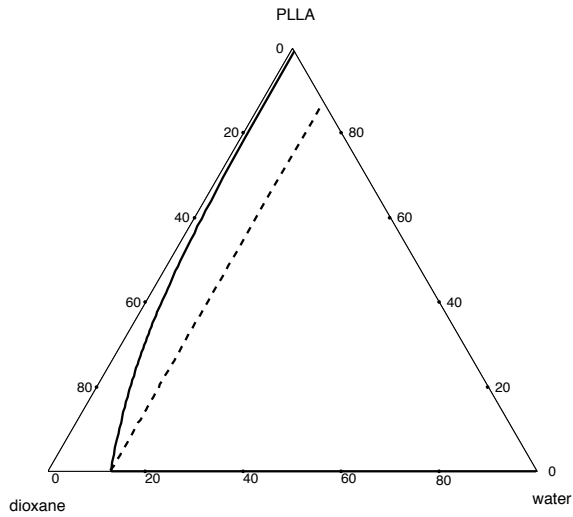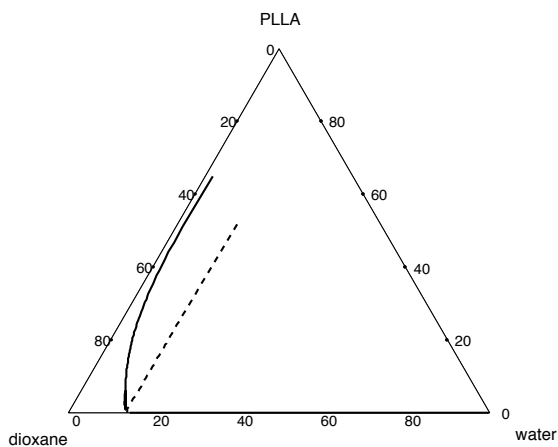

Figure 3.6: Calculated binodal and spinodal with $\zeta_{wp} = 0.985$, $\zeta_{dp} = 0.815$, $\delta\epsilon^*_{dp} = 18600$ J, 30 °C, $M = 338000$, PLLA-dioxane-water system

The quantitative disagreement can be explained by inferring the effects of polydispersity. As a matter of fact, the PLLA sample studied by Hua et al. [2002] had a polydispersity of 1.55, whereas the other one had a polydispersity of 2.4. As discussed above, the molecular weight distribution is highly influencing phase equilibria: the larger polydispersity suggests
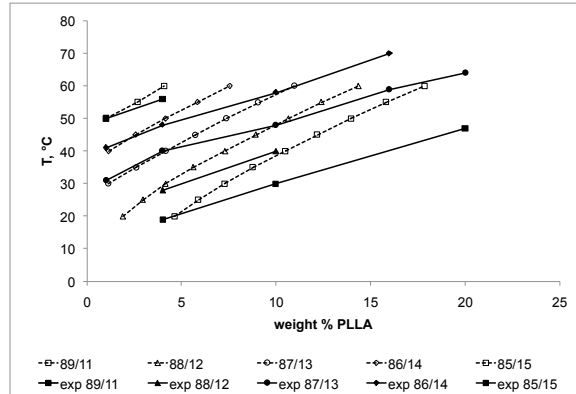
Figure 3.7: Comparison between experimental (filled symbols) and calculated (open symbols) cloud points, PLLA-dioxane-water system, data from Tanaka and Lloyd [2004]

that a consistent fraction of the polymer sample has a molecular weight lower than the average, and therefore it is more miscible with solvents, thus lowering the cloud point temperature.

3.2 Oishi-Prausnitz model

The computation of all parameters of Oishi-Prausnitz model involves the scrutinization of the chemical formula of solution components. The molecular structures of PLLA, dioxane and water are represented in figure 3.8.

(a) PLLA   (b) dioxane   (c) water
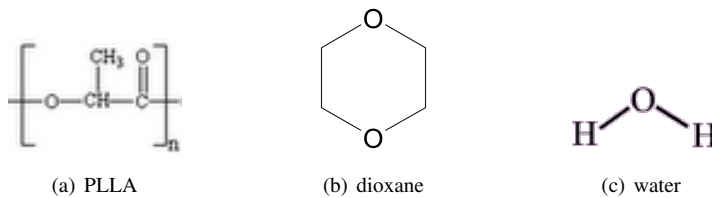
Figure 3.8: Molecular structure of PLLA, dioxane and water

The mixture components were then subdivided into their characteristic functional groups available in the UNIFAC table. The PLLA monomer was subdivided into one COO, one CH and one CH_3 group. The dioxane was composed by two CH_2O and two CH_2 groups. The water was not split, as the H_2O group is already defined in the UNIFAC table. The characteristic R_k, Q_k and a_{mn} parameters are reported in tables 3.3 and 3.4, respectively.

Table 3.3: Species, chemical formula, group division and characteristic parameters for the PLLA-dioxane-water system

Species	Formula	Groups	ID 1	ID 2	$\nu_k^{(i)}$	M	R_k	Q_k
Dioxane	$C_4H_8O_2$							
		CH_2O	13	26	2	30.03	0.9183	0.78
		CH_2	1	2	2	14.03	0.6744	0.54
Water	H_2O							
		H_2O	7	17	1	18.02	0.92	1.4
PLLA	$(C_3H_4O_2)_n$							
		COO	41	77	n	44.01	1.38	1.2
		CH	1	3	n	13.02	0.4469	0.228
		CH_3	1	1	n	15.03	0.9011	0.848

Table 3.4: Interaction parameters a_{mn} between pairs of functional groups. The number within parentheses is the ID 1.

$m \downarrow n \rightarrow$	CH_3 (1)	CH_2 (1)	CH (1)	H_2O (7)	CH_2O (13)	COO (41)
CH_3 (1)	0	0	0	1318	251.5	387.1
CH_2 (1)	0	0	0	1318	251.5	387.1
CH (1)	0	0	0	1318	251.5	387.1
H_2O (7)	300	300	300	0	540.5	-197.5
CH_2O (13)	83.36	83.36	83.36	-314.7	0	417
COO (41)	529	529	529	284.4	-247.8	0

By choosing a solution temperature and composition, the system is univocally determined and the solvents' activities were calculated. As regards to the chain length, it is possible to work out estimations by varying the degree of polymerization n. The calculations were carried out at different temperature and composition, in order to derive the influence of polymer weight fraction on solvents' activities.

Figure 3.9 reports the free energy of mixing as a function of polymer molar fraction for the dioxane/water/PLLA system, calculated at 300 and 320 K, where the dioxane to water ratio was assumed to be 87/13 (which experimentally produces a two-phase system) and the numerical degree of polymerization $x_n = 100$. As it can be easily observed by looking to figure 3.9 in the examined conditions, curvature changes on ΔG_m are found. However, the polymer composition of the polymer-lean phase is very high with respect to the experimental evidence.
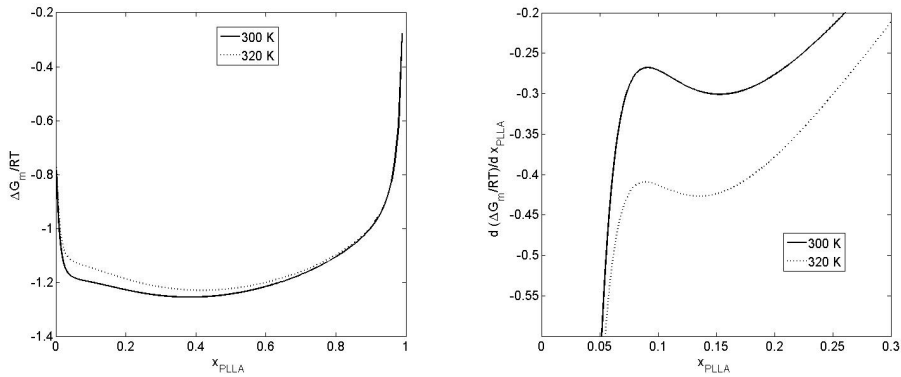
Figure 3.9: $\Delta G_m/RT - x_{PLLA}$ plot calculated with Elbro's free volume

3.2.1 The free volume issue

Focusing on water free volume contribution, a simple double-check on the model can be carried out by calculating the free volume fraction via equations 2.110 and 2.112. The experimental value of water free volume reported in Elbro et al. [1990], 36% (although the authors do not supply precise information about the origin of this value), is larger than the one computed, 22%. As a matter of fact, when equation 2.110 is used to calculate the percentage of free-volume for species as acetone, n-pentane and diethyl-ether, values obtained fall into the measured range for commons organic solvents.

Calculations of free-volume percentage for species which involves hydrogen bonds as glycerine, ethylene glycol, water and ethanol, provide instead underestimated values. Relevant results are resumed in table 3.5.

Table 3.5: Free-volume percentage calculated via equations 2.110 and 2.112

	M [g/mol]	v [cm^3/mol]	v^* [cm^3/mol]	%FV
glycerine	92	72.96	72.75	0.28
ethylene glycol	62	55.66	50.80	8.72
water	18	18.02	13.96	22.54
ethanol	46	58.30	39.07	32.99
acetone	58	73.42	39.04	46.82
n-pentane	72	115.02	58.03	49.55
diethyl-ether	74	103.79	51.50	50.38

Kannan et al. [2005a] pointed out that volume and surface parameters R_k and Q_k of H_2O group used in UNIFAC are different from the corresponding van der Waals values (see table 3.6). This difference exerts a great influence on activity contributions.

Table 3.6: Group parameter of H_2O group

	UNIFAC	van der Waals
R_k	0.92	0.8154
Q_k	1.4	0.904

When using these parameters, the free-volume amount for water results 31.4% (calculated via equations 2.110 and 2.112).

Moreover, a different expression for the free-volume contribution (weight-fraction based) was provided by the authors [Kannan et al., 2005a]:

$$\ln \Omega_i^{FV} = \ln \left[\frac{\varphi_i^{FV}}{\varphi_i^H} \right] + \left[\frac{\varphi_i^{FV} - \varphi_i^H}{x_i} \right] \tag{3.3}$$

where the subscript H indicates the hard-core volume.

The three different expressions for free-volume contribution (OP, eq. 2.99; Elbro, eq. 2.111; Kannan, eq. 3.3) were compared for both dioxane and water, in a ternary solution with PLLA, at $T = 300$ K and with a dioxane to water ratio of 87/13. In OP model the coefficient 15.17 of equations 2.100 and 2.101 was changed to 12.5 only for water, to obtain a free-volume value corresponding to the data reported by Elbro et al. [1990]. Results are displayed in figures 3.10 and 3.11 respectively.

Curves obtained with different models show different shapes, thus denoting a remarkable influence of mixing effects due to free-volume differences among the solution components.

The correction of coefficient of equations 2.100 and 2.101 was applied to Oishi-Prausnitz model. A plot of $\Delta G_m/RT - w_{PLLA}$ was drawn at $T = 300$ K. Figure 3.12 compares ΔG_m curves calculated without FV contribution, with the correction of equations 2.100 and 2.101 (i.e. OP model with the coefficient 15.17 reduced to 12.5) and with the van der Waals parameters for water. Although the last two corrections appear similar, differences in results are ascribable to different Q_k values. Nevertheless, results are scarcely sensitive to temperature changes.
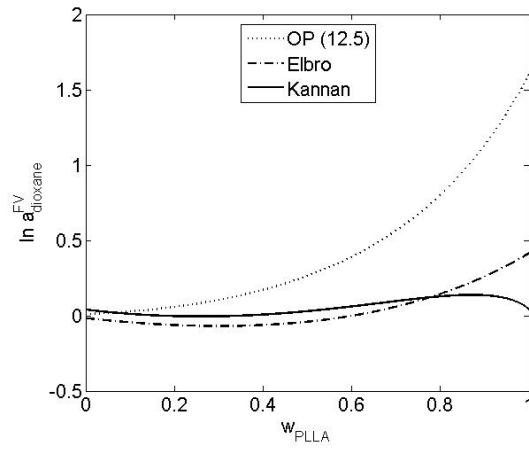
Figure 3.10: $\ln a^{FV} - w_{PLLA}$ plot of dioxane, calculated with OP model (eq. 2.99), Elbro's (eq. 2.111) and Kannan's (eq. 3.3) formulations
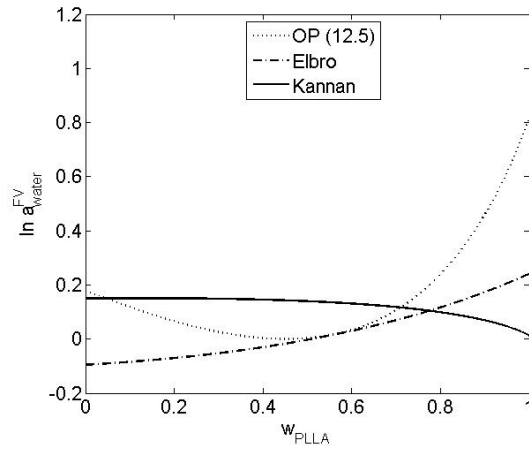
Figure 3.11: $\ln a^{FV} - w_{PLLA}$ plot of water, calculated with OP model (eq. 2.99), Elbro's (eq. 2.111) and Kannan's (eq. 3.3) formulations
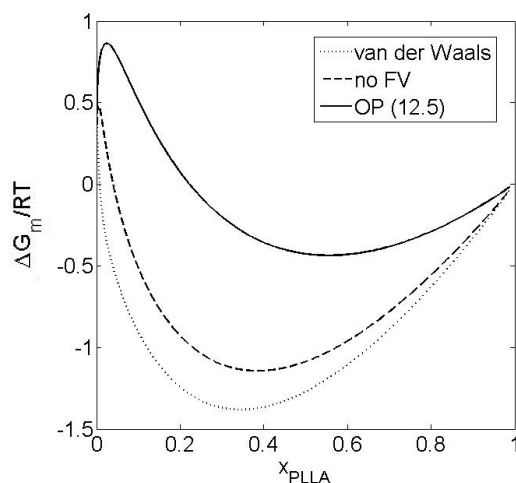
Figure 3.12: $\Delta G_m/RT - x_{PLLA}$ plot, calculated with van der Waals parameters, without the FV contribution and with the correction of equations 2.100 and 2.101 (OP 12.5)

3.2.2 Model validation with other binary and ternary systems

In order to deeply understand the influence of water and its model parameters on the quality of predictions of activity coefficients, two different binary and one ternary aqueous solutions were studied.

This need comes from the particularity of water molecule, which forms hydrogen bonds and shows anomalies with respect to other substances, as outlined in the previous paragraph.

3.2.2.1 The water-dioxane system

The water-dioxane system does not exhibit experimentally a partial miscibility, therefore, a $\Delta G_m - x_{PLLA}$ diagram with a positive curvature is expected.

The calculations were carried out with four versions of OP model: standard formulation (eq. 2.87), neglecting the free-volume contribution (eq. 2.99), using the van der Waals volume and surface parameters of water (table 3.6) and modifying the coefficient of equations 2.100 and 2.101 (so called *OP 12.5*).

The curves obtained for $T = 300$ K (except for standard OP) are reported in figure 3.13.

It is easy to notice that curves calculated with different formulation do not overlap on each other. The ΔG_m obtained via standard model denotes a completely immiscible sys-

tem, owing to the high difference among the free-volume percentage calculated (22% for water and 43% for dioxane), which, in their turn, provide large values of free-volume contribution.

Other curves are similar in shape and the common tangent points (related to the coexisting phases) are close. Particularly, the curve obtained with van der Waals parameters is close to correction of coefficient of equations 2.100 and 2.101. In any case, whichever the model form chosen, the experimental behaviour (total miscibility) is not reproduced at all.
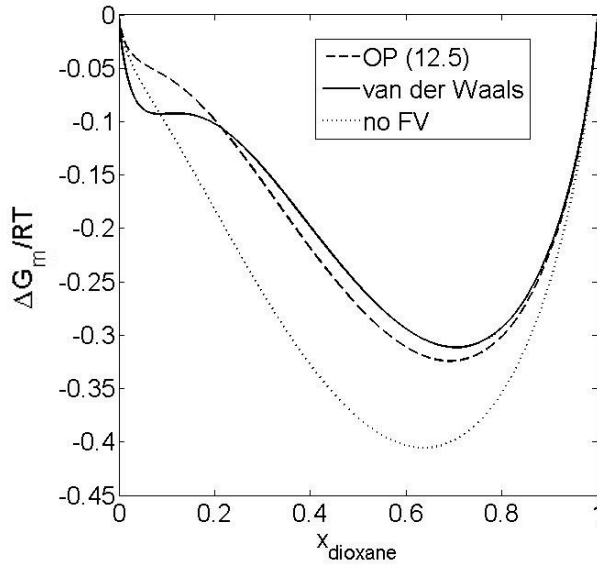
Figure 3.13: $\Delta G_m/RT - x_{dioxane}$ plot at $T = 300$ K, water-dioxane system

Furthermore, all the curves do not modify appreciably with temperature, in evident contradiction to the experimental evidence.

3.2.2.2 The water-aniline system

To extend the characterization of aqueous solutions, the water-aniline system was studied, which shows a miscibility gap.

Calculations were carried out with four versions of OP model, as in the previous case. Results obtained at $T = 300$ K and a curve calculated with *OP 12.5* at 320 K are reported in figure 3.14.

As observed for the water-dioxane system, the ΔG_m obtained from standard model de-

notes a completely immiscible system, owing to high difference among free-volume percentage calculated (22% for water and 38% for aniline), which provides therefore high values for the free-volume term.

Curves obtained by neglecting the free-volume contribution and with modification of equation 2.110 are quite similar, showing the inflection points typical of partially miscible systems. As both corrections are related only to water and to its free-volume contribution, this is the reason of the observed similarity.

Results obtained with van der Waals parameters also denote a partially miscible system, but the compositions of the coexisting phases are different. Unlike the water-dioxane solution, the water-aniline system is slightly sensitive to temperature changes. However, phase separation was predicted also in the temperature region where the solution is stable, thus confirming the inadequateness of the model to predict phase behavior of aqueous solutions.
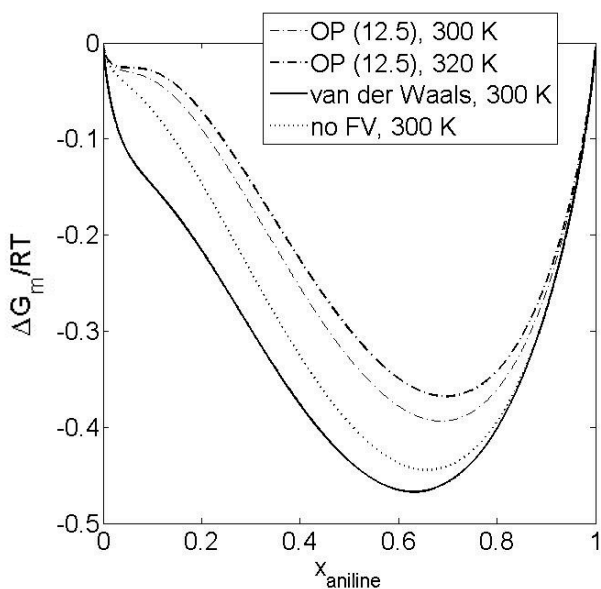
Figure 3.14: $\Delta G_m/RT - x_{aniline}$ plot at $T = 300$ K, water-aniline system

3.2.2.3 The water-acetone-chloroform system

To verify the applicability of OP model to ternary systems, the water-acetone-chloroform system was selected, which shows a partial miscibility due to the water-chloroform pair; acetone is completely miscible with water and chloroform in all proportions. For this sys-

tem, equilibria composition of two phases are known as experimentally measured. In this case, calculations were carried out by using the compositions of a tie line: therefore, a ΔG_m diagram with two inflection points is expected.

Four pairs of equilibrium points were double-checked, adopting the four versions of OP model here examined.

With the stantard OP model and without the free-volume term, a change in curvature was not recorded: only with the van der Waals parameters a partial miscibility curve was obtained (figure 3.15). Nevertheless, also in this case, results do not reproduce experimental data.
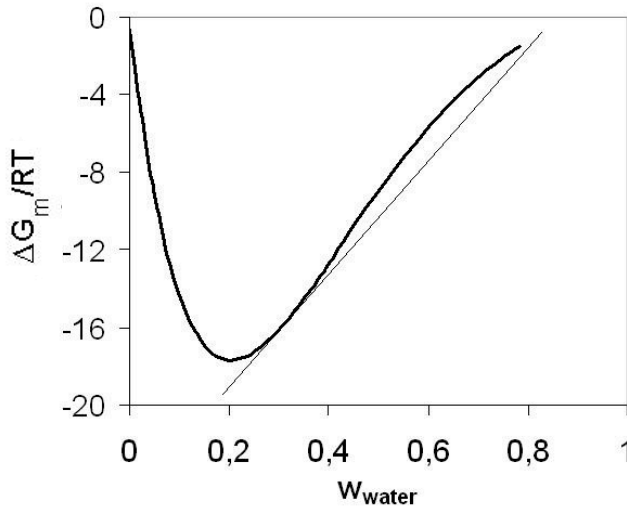
Figure 3.15: $\Delta G_m/RT - w_{water}$ plot, calculated with van der Waals parameters, water-acetone-chloroform system

3.2.3 Discussion

Oishi-Prausnitz model, in its standard formulation, does not provide acceptable results in the simulation of liquid-liquid equilibria involving a polymeric component, as shown throughout the past exposition. High values of water activity, due to a high contribution of the free-volume term, can be attributed to the particularity of H_2O molecule. Moreover, UNIFAC parameters were calculated for the model without the free-volume contribution [Abrams and Prausnitz, 1975], while this last was proposed some years later [Oishi and Prausnitz, 1978]. It is then possible that these values do not fit adequately the free-volume

term.

Polymers have generally a free-volume percentage lower than common small-molecule solutes. To take into account this issue, the $\ln a^{FV}$ term formulated by Oishi and Prausnitz adds a positive contribution to the solvent activity. However, in the case of a solvent with a free-volume content lower than a polymer (that is the case of water), a negative correction of $\ln a$ is necessary, which, according to the term expression of Oishi and Prausnitz is not introducible [Kannan et al., 2005b].

On the other hand, changing the expression of free-volume term as a function of molar volume and free-volume content could be a very strong approximation. In this case, a coefficient to take into account system morphology (i.e. linear or branched chain, conformation in solution) is lacking, whereas it is accounted for in OP model (equation 2.99). This coefficient was determined for a certain group of solvents; for other species, and for macromolecular solutions, a different value of c could be possible (in particular, it should be higher [Oishi and Prausnitz, 1978]).

The corrections made by Elbro et al. [1990] were verified for liquid-vapor equilibria in binary polymer solutions: for some systems there are weak interactions between species, and for others strong interactions exist between molecules. However, in that paper, validation on liquid-liquid equilibria was not carried out, being beyond the scope of the work, therefore a term of comparison is lacking.

As far as the expression of $\ln a^{FV}$ proposed by Kannan et al. [2005a] is concerned, the scarce matching with experimental data can be due to the kind of correction introduced. Kannan's corrections were proposed for binary solutions water-polymer: it is then likely that this modification is inadequate for ternary polymer solutions or for binary solutions without polymers where water is not included. Moreover, the PLLA was not considered in the validation of this correction. Another possibility of improvement in the parameters' estimate consists in new group definition, which are lacking in the UNIFAC parameters table. To accomplish this, estimates of interaction, volume and surface parameters are needed [Kannan et al., 2005a].

Modification of coefficient of equations 2.100 and 2.101 represents a correction similar to the use of van der Waals parameters; in that case, the free-volume of water as-obtained is closer to experimental, but whether other components need a correction is a matter of speculation.

All the formulations here used do not include a term accounting for the contributions dependent on the shape of polymer chains (random-coil or extended), on ramifications, on solution mobility, on chain flexibility. The only parameter considered is the molecular weight of polymer, multiplying all molecular properties for the number of chain units. In

this way, all the peculiar properties of polymer related to macromolecularity are neglected; those properties being the key point to characterize this kind of solution equilibria, the model is intrinsically limited, especially when LLE are considered.

3.3 Conclusion

The lattice fluid model extended to specific interactions was applied to the PLLA-dioxane-water system. The main aim was to predict a phase diagram, limiting the need for experimental information, and trying to develop a tool able to easily describe the phase behavior of scaffold forming systems.

The use of a specific interactions parameter resulted adequate for reaching a satisfactory agreement with experimental data. The appropriated interaction parameters were selected by scrutinizing Hansen solubility parameters values and with the help of empirical observations, thus reducing the number of adjustable parameters.

A qualitative and quantitative picture of the phase behavior of a ternary polymer solution was derived. The main features of the system were well depicted, suggesting a possible application of the model to this class of systems. The comparison with experimental cloud point curves suggests a route to derive the complete phase diagram by means of simple measurements. In this perspective, cloud point data can be utilized for fitting interaction parameters, then deducing the complete phase diagram of the system. The calculation of the spinodal will improve the selection of processing parameters on the basis of the desired microstructure. The discrepancies in quantitative values can be attributed to the polymer polydispersity, which strongly affects phase equilibria.

On the other hand, by using group contribution models, calculations of phase diagram for the PLLA-dioxane-water denoting a phase separation were not successful. Checks were extensively carried out on simpler binary and ternary systems (water-dioxane, water-aniline and water-acetone-chloroform), with simple molecules and polymers, with OP model and its variations and corrections, with unsatisfactory and disappointing results.

The Oishi-Prausnitz model resulted inadequate for phase separation prediction. The other models explored gave out phase diagrams denoting phase separation, although equilibrium compositions were different from experimental. Moreover, for the water-dioxane system, a phase separation was predicted, whereas experimentally it is a homogeneous system in the whole composition range. Purely predictive models for solution thermodynamics have limited application in phase equilibria prediction, as some parameters are usually adjusted to fit experimental data. This represents a strong limitation to the potential capability of a predictive model.

The development of a predictive model for LLE in polymer solutions is needed, due to the scarcity of experimental data for all possible solutions. The fast growing of membrane and scaffold technology can take many advantages from this tool: potential new systems can be studied before the experimental campaign, thus reducing research costs and time; moreover, a better understanding of LLE phenomenology can be reached, as information on thermodynamics are, until now, derived from cloud-point curves and from morphology obtained.

Other possibilities for group-contribution models improvement are the modification of the interaction parameters with a set of experimental data, and, if necessary, also of the parameters of UNIFAC table. This table was constructed by using liquid-vapor equilibrium data, where results are barely sensible to errors in activity estimation. It is possible also to define new functional groups which allow to consider structural isomers or cyclic structure of molecule (e.g. dioxane).

Finally, a deep study on free-volume effects of mixing in polymer solutions would be proper to find out a general expression for the free-volume contribution. At present, there are many expression optimized for certain groups of binary or ternary systems, but a general expression widely consistent is not available. Moreover, the open issues on water parameters should be overcome through a dedicated experimental campaign in order to determine if they are universal or system dependent.

Bibliography

D. S. Abrams and J. M. Prausnitz. Statistical thermodynamics of liquid mixtures: A new expression fo the excess gibbs energy of partly or completely miscible systems. *AIChE Journal*, 21(1):116–128, 1975.

A. Chaudhari. Hydrogen bonding interaction between 1,4-dioxane and water. *International Journal of Quantum Chemistry*, 110:1092–1099, 2010.

H. S. Elbro, Aa. Fredenslund, and P. Rasmussen. A new simple equation for the prediction of solvent activities in polymer solutions. *Macromolecules*, 23:4707–4714, 1990.

F. J. Hua, G. E. Kim, J. D. Lee, Y. K. Son, and D. S. Lee. Macroporous poly(L-lactide) scaffold 1. Preparation of a macroporous scaffold by liquid-liquid phase separation of a PLLA-dioxane-water system. *Journal of Biomedical Materials Research (Appl Biomater)*, 63:161–167, 2002.

D. C. Kannan, J. L. Duda, and R. P. Danner. A free-volume term based on the van der Waals partition function for the UNIFAC model. *Fluid Phase Equilibria*, 228-229:321–328, 2005a.

D. C. Kannan, J. L. Duda, and R. P. Danner. Application of UNIFAC-vdW-FV model to water-PEO systems. *Fluid Phase Equilibria*, 237:86–88, 2005b.

T. Oishi and J. M. Prausnitz. Estimation of solvent activities in polymer solutions using a group-contribution method. *Industrial Engineering Chemical Process Design Development*, 17(3):333–339, 1978.

P. A. Rodgers and I. C. Sanchez. Improvement to the lattice-fluid prediction of gas solubilities in polymer liquids. *Journal of Polymer Science: Part B: Polymer Physics*, 31:273–277, 1993.

I. C. Sanchez and R. H. Lacombe. An elementary molecular theory of classical fluids. Pure fluids. *Journal of Physical Chemistry*, 80(21):2352–2362, 1976.

I. C. Sanchez and R. H. Lacombe. An elementary equation of state for polymer liquids. *Journal of Polymer Science: Polymer Letters Edition*, 15(2):71–75, 1977.

I. C. Sanchez and R. H. Lacombe. Statistical thermodynamics of polymer solutions. *Macromolecules*, 11(6):1145–1156, 1978.

Y. Sato, K. Inohara, S. Takishima, H. Masuoka, M. Imazumi, H. Yamamoto, and M. Takasugi. Pressure-volume-temperature behavior of polylactide, poly(butylene succinate), and poly(butylene succinate-co-adipate). *Polymer Engineering and Science*, 40(12):2602–2609, 2000.

T. Tanaka and D. R. Lloyd. Formation of poly(L-lactic acid) microfiltration membranes via thermally induced phase separation. *Journal of Membrane Science*, 238:65–73, 2004.

H. Tompa. *Polymer solutions*. Butterworths, London, 1956.

P. van de Witte, P. J. Dijkstra, J. W. A. van den Berg, and J. Feijen. Phase behavior of polylactides in solvent-nonsolvent mixtures. *Journal of Polymer Science: Part B: Polymer Physics*, 34:2553–2568, 1996.

4 Experimental approach: design of a turbidity measurement apparatus

The most widely used method for measuring cloud point curves is the turbidity detection. Turbidity can be detected visually or with light transmission measurements. The visual approach is more easy to be implemented, but scarcely quantitative. On the other hand, with light transmission it is possible to measure and record a quantitative turbidity value, so that comparison at different compositions and temperatures can be made.

To derive the cloud point curve of ternary polymer solutions, a turbidity measurement apparatus was designed and realized. The basic features of the device are the coupled measurement of temperature and transmitted light, and the possibility to reach cooling rates comparable with common processing conditions (up to 1 °C/s).

With a relatively wide range of cooling rates explorable, a solution can be characterized from both thermodynamic and kinetic point of view. As a matter of fact, thermodynamic information are determined with slow cooling rates, and the cloud point is defined as the temperature at which the turbidity starts to increase. Kinetic features are determined by varying the cooling rate: for example, by increasing the cooling rate the cloud point will shift towards lower temperatures. This is an important aspect to take into account in membrane production via TIPS. Moreover, the rate of turbidity change can be related to the speed of phase separation processes: for example, different mechanisms as nucleation and growth or spinodal decomposition could be deducted.

In polymer processing, it has been widely showed that the thermal history experienced by the polymer affects the final microstructure obtained. For example, in the case of crystallization from the melt, the cooling rate influences the crystallinity value and the crystals morphology obtained [Brucato et al., 2009, 2002]. It is reasonable to assume that also the phase behavior of polymer solutions could be influenced by the thermal history, and not only by its thermodynamic properties. Many features of polymer solutions are temperature dependent (e.g. driving force for phase separation, demixing mechanism, system viscosity, polymer mobility and conformation in solution): therefore, a thermal history influence on the phase separation processes could be hypothesized.

The data obtained with a deterministic measurement of cloud points can be employed for tuning model parameters. As showed in Chapter 3, cloud point data are useful for the derivation of interaction parameters in lattice fluid model. A relatively simple measurement technique coupled with a consistent model can give out functional information on phase behavior of polymer solutions.

The turbidity measurement device designed and realized in this work consists (figure 4.1) of a laser diode for light emission, a sample cell and a photodiode for light detection. The sample cell temperature was monitored by a thermocouple and controlled via peltier cells. All components are connected to a I/O device remotely controlled via PC. This chapter provides a description of the whole apparatus, starting from its elements and analyzing the temperature control capabilities by a heat transfer analysis.
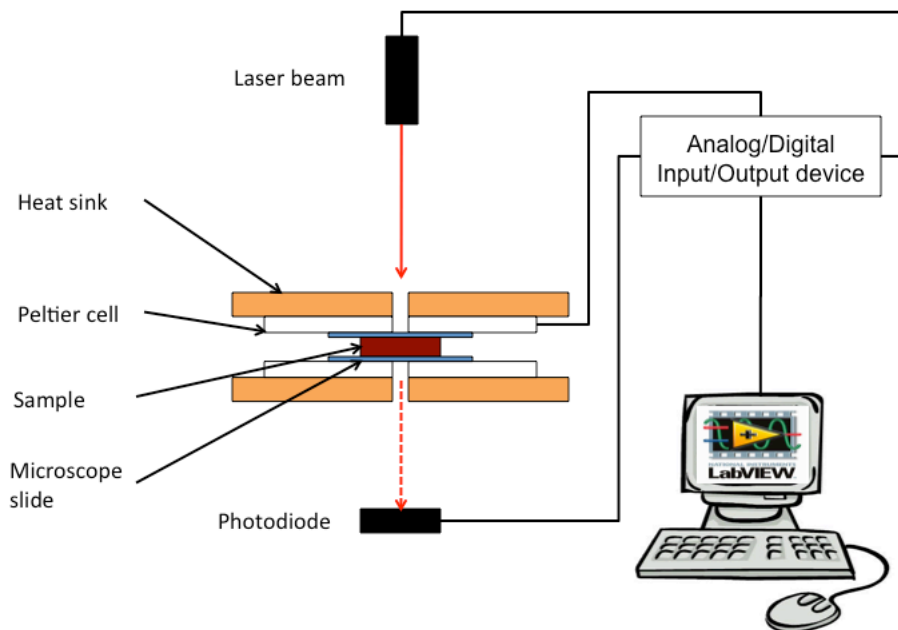
Figure 4.1: Schematic of the turbidity measurement apparatus

4.1 Light emission and detection

A laser diode (HLM1845, HlaserOpto CO) of $P_{max}=$ 100 mW and wavelength $\lambda = 655$ nm was used for light emission. The power was remote controlled via "Pulse Width Modulation" (PWM) method. The minimum radius of the light beam is around 1 mm.

A photodiode (OSD15-5T, Centronic) was used in reverse bias mode (figure 4.2). The load resistance was chosen by selecting the value which gives out a linear dependence between optical power and output voltage (see line c on figure 4.2a), with an appreciable slope. Values of R_L from 10 Ω to 100 kΩ were tested. Also the laser frequency was tuned, from 10 Hz to 10 kHz. The value used in all measurements is 100 Hz. The load resistance (R_L) selected was 217 Ω (figure 4.3), with a bias voltage of 5 V. In this case, the correlation was linear with a slope of 18.8 V/W.

(a) Photocurrent vs bias voltage	(b) Operative circuit
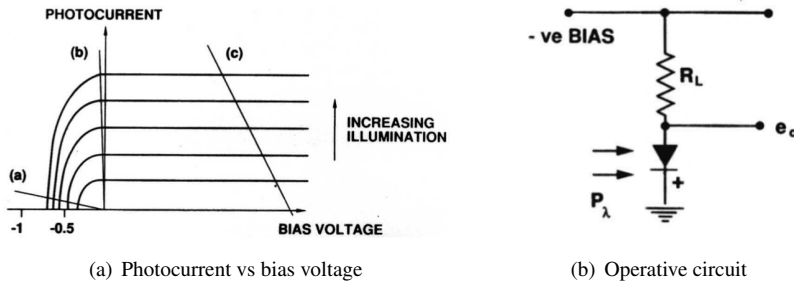
Figure 4.2: Reverse bias operation characteristics
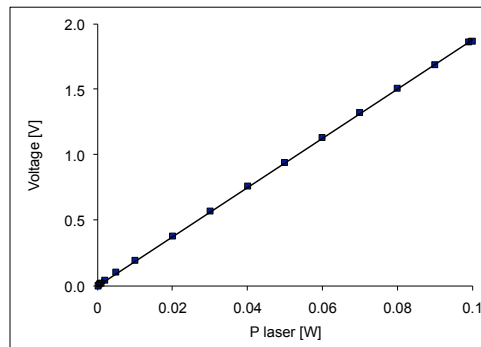
Figure 4.3: Output voltage vs laser beam power (frequency 100 Hz). The load resistance is $R_L = 217$ Ω

4.2 Temperature measurement

Temperature measurement and control is a key feature when investigating ternary polymer solutions.

T-type thermocouples were used to measure temperature. A thermistor (LM35-DT, National Semiconductor) was used to measure the cold junction temperature. The thermistor was connected to a power supply of 5 V, stabilized with a zener diode and a 100 Ω resistance.

The thermistor was calibrated by measuring the output voltage and the "actual" temperature by a separated thermocouple (figure 4.4). A wide range of temperatures was explored, owing to the possible high variations of ambient temperature during the year.
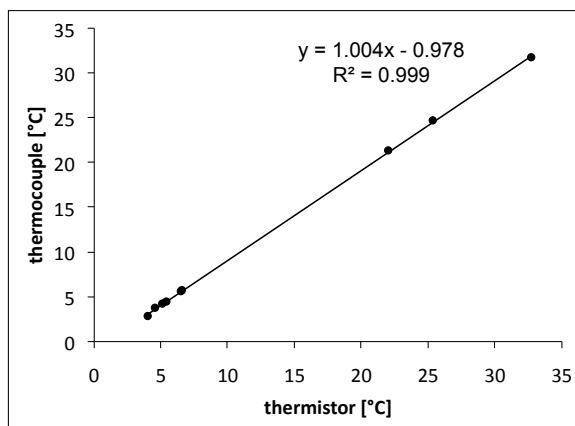
Figure 4.4: Calibration curve of the temperature measured by the thermistor with the "actual" temperature measured by a thermocouple

4.3 Peltier cells

Peltier cells are thermoelectric devices allowing both heating and cooling. They are constituted of pairs of semiconductors which, imposing a direct current, will generate an heat flow and consequently a temperature difference on the two sides (see figures 4.5 and 4.6). This phenomenon (named *Peltier effect*) is expressed by the relation [Kraftmakher, 2005, Martorana, 1975]:

$$\dot{Q} = \alpha T I \tag{4.1}$$

where $\dot{Q}$ is the heat power, α is the Seebeck coefficient, T is the temperature and I is the current. This phenomenon is opposite to the *Seebeck effect*, which consists in the generation of a voltage from a temperature difference:

$$V = \alpha \Delta T \qquad (4.2)$$

and is commonly encountered e.g. in thermocouple operations.

The heat flow is related to the energy variation of electrons when flowing through oppositely doped semiconductors. For example, let consider the scheme in figure 4.5, where two pellets of oppositely doped semiconductors are connected in series: the applied voltage drives electrons flow from the P type to the N type semiconductor. In this case, at the P-N junction the electrons must jump over a energy barrier, thus absorbing energy from the environment. This energy absorption produces a heat flow from the environment to the P-N junction. On the opposite side, the energy barriers are negatives, so that the electrons release heat. Opposite phenomena occur when inverting the current direction (figure 4.6): at the N-P junction, the electrons release energy.
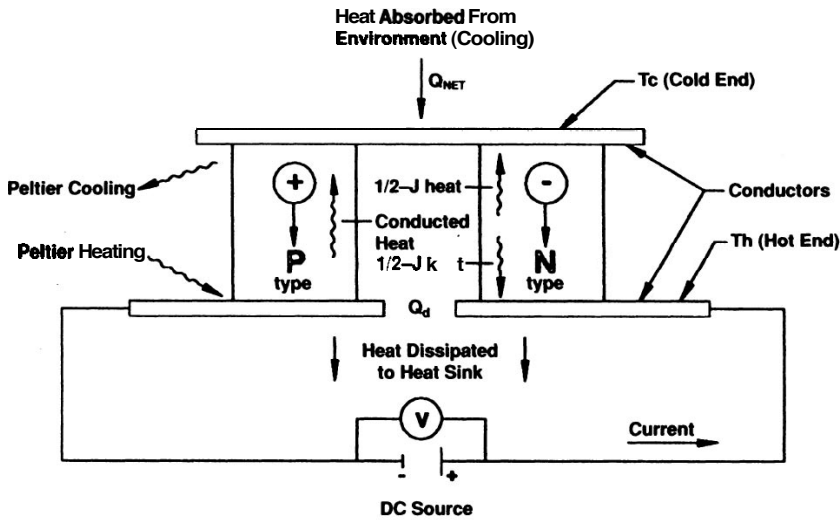
Figure 4.5: Thermoelectric pair of semiconductors employed in cooling operation, from Rowe [1995]

A single P-N junction does not offer a heat flow employable for practical application. Commercial devices are composed of a number of semiconductor pairs connected in series configuration (see figure 4.7), in order to enhance the thermal energy exchangeable. The connections between pellets are usually made by copper tabs, with all P-N junctions located

Heat **dissipated To**
Environment (Heating)

Th (Hot End)

14

Peltier Heating

type
P

1/2-J heat

type
N

Conductors

Conducted
Heat

Peltier Cooling

1/2-J heat

Tc (Cold End)

+

-

Q_{NET}

Heat Absorbed
From Heat Sink

Current

V

DC Source

+   -
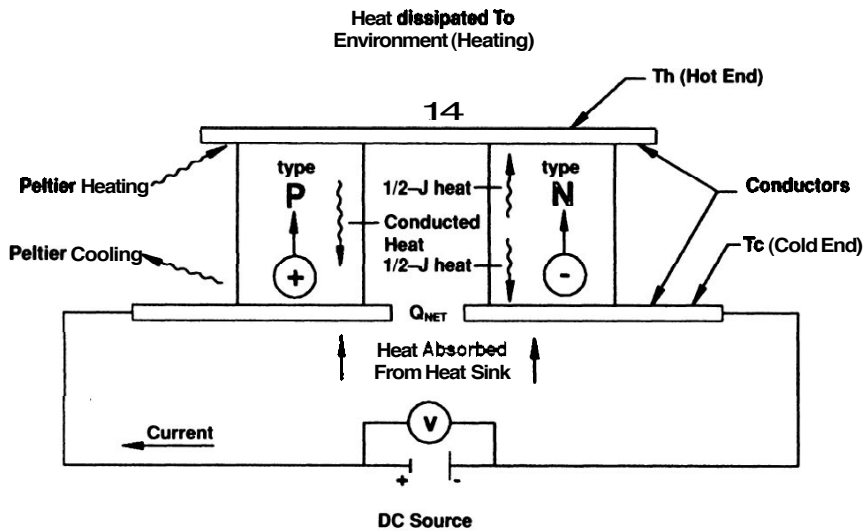
Figure 4.6: Thermoelectric pair of semiconductors employed in heating operation, from Rowe [1995]

Heat Absorbed (Cold Side)   Positive(+)

Negative(-)

n   p   n

p   n

P-Type Semiconductor

N-Type Semiconductor

Ceramic Plates
(Electrical Insulator)

Copper Tabs
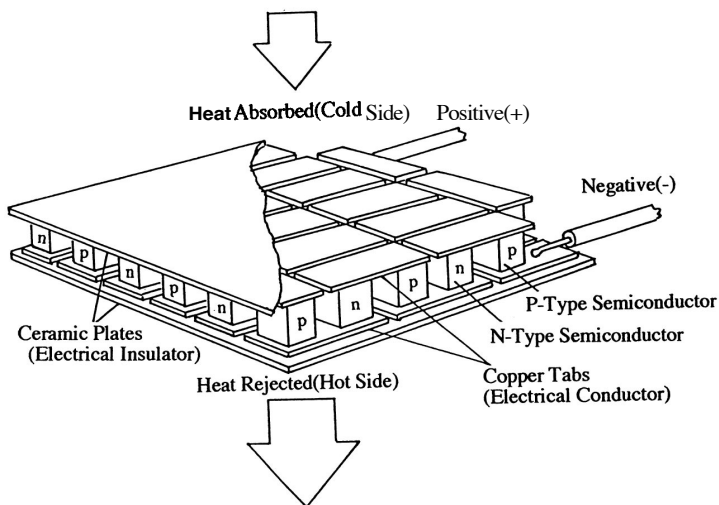(Electrical Conductor)

Heat Rejected (Hot Side)

Figure 4.7: Schematic of a commercial peltier cell device, from Rowe [1995]

112

in the opposite side of N-P junction. The external surfaces are usually covered by a high thermal conductivity ceramic material, to ensure electrical insulation and providing a good thermal transport. The cooling capacity can be tuned by changing the module dimension and the number of pellets.

Usually, peltier cells are employed as cooling devices. As a general rule, peltier cells must be coupled with a heat sink, to dissipate the heat pumped to the hot side. Following the heat flow directions schematized in figures 4.5 and 4.6, the total heat flow removed at the cold side and pumped to the hot side are respectively [Perez-Aparicio et al., 2012, Martorana, 1975]:

$$\dot{Q}_c = \alpha T_c I - \frac{1}{2} I^2 R - K_t (T_h - T_c) \tag{4.3}$$

$$\dot{Q}_h = \alpha T_h I + \frac{1}{2} I^2 R - K_t (T_h - T_c) \tag{4.4}$$

where K_t and R are the thermal conductance and electrical resistance of the module, respectively. The heat generated by Joule's effect is assumed to be equally distributed in both sides of the device (it reduces the heat removed and increases the heat pumped); on the other hand, the heat conduction influences negatively both cooling and heating operations.

The total power transferred is obtained by subtracting equation 4.3 to 4.4 [Mitrani et al., 2003]:

$$P = \dot{Q}_h - \dot{Q}_c = \alpha (T_h - T_c) I + I^2 R \tag{4.5}$$

which is equal to the electrical power needed to drive the device, $P = VI$. The power supplied is then converted into two different heat sources: the thermoelectric heat flow, proportional to the electrical current, and the heat generation by Joule's effect, proportional to the square of the current.

In cooling operations, the heat pumped to the hot side must be dissipated by a heat sink. If not, the hot side temperature will increase and the cooling performance will reduce. This fact is easily deduced from equation 4.5: at fixed electrical power, the temperature difference $T_h - T_c$ is constant; by increasing T_h, the cold side temperature T_c will obviously increase.

The performances of a peltier cell (e.g. ΔT or $\dot{Q}_c$) can be controlled with the imposed current and voltage. The maximum of $\dot{Q}_c$ (called $\dot{Q}_{max}$) is reached for $\Delta T = 0$, whereas the maximum ΔT (called ΔT_{max}) is attained when $\dot{Q}_c = 0$. The current and voltage required for reaching ΔT_{max} are defined as I_{max} and V_{max}, respectively. Note that even

though $\dot{Q}_{max}$ is attained at I_{max}, the voltage required is $V < V_{max}$. From equations 4.3 and 4.5, the following relations can be derived:

$$(\alpha I_{max} + K_t)\Delta T_{max} = \alpha I_{max} T_h - \frac{1}{2} I_{max}^2 R \tag{4.6}$$

$$\dot{Q}_{max} = \alpha I_{max} T_h - \frac{1}{2} I_{max}^2 R \tag{4.7}$$

$$V_{max} = \alpha \Delta T_{max} + I_{max} R \tag{4.8}$$

It is worth noticing that both I_{max} and V_{max} are not the maximum values allowable for the thermoelectric module, but the values related to the maximum performance. These four maximum performance values can be used to draw the behavior of a peltier cell for any operating condition: a universal dimensionless chart for peltier cells can be inferred from equations 4.3 and 4.5, showed in figure 4.8.
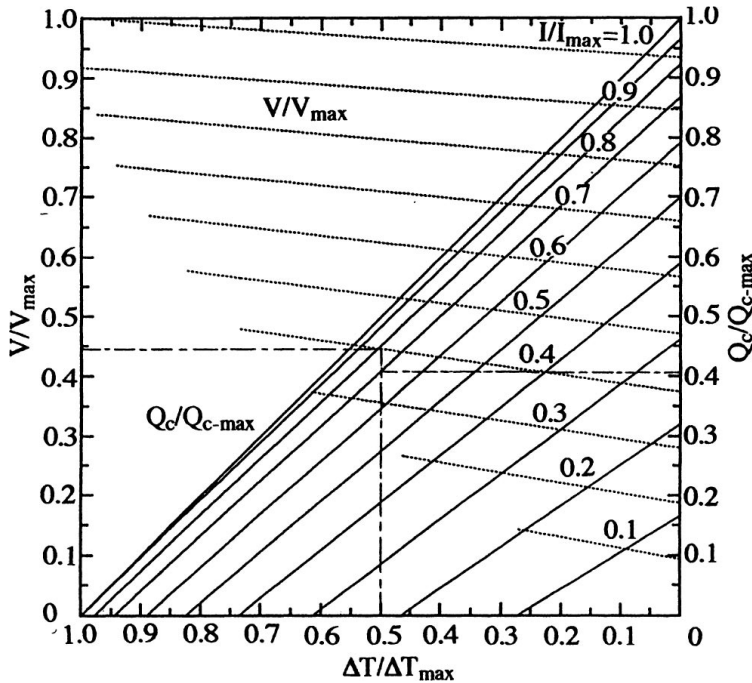

Figure 4.8: Universal chart of peltier cells, from Rowe [1995]

The technical specifications (i.e. nominal data) provided with commercial devices are the four maximum performance parameters at a fixed hot side temperature T_h. Additional

information are reported in a graphical form, by means of charts similar to that showed in figure 4.8, expressed with dimensional quantities. Palacios et al. [2009] reported a graphical method to extrapolate the thermoelectric module parameters from the nominal data charts. Nevertheless, the Seebeck coefficient, electrical resistance and thermal conductance of the module can be directly calculated by solving equations 4.6, 4.7 and 4.8:

$$\alpha = \frac{V_{max}I_{max} + 2\dot{Q}_{max}}{I_{max}(\Delta T_{max} + 2T_h)} \tag{4.9}$$

$$R = 2\frac{V_{max}I_{max}T_h - \dot{Q}_{max}\Delta T_{max}}{I_{max}^2(\Delta T_{max} + 2T_h)} \tag{4.10}$$

$$K_t = \frac{2\dot{Q}_{max}T_h - \Delta T_{max}(\dot{Q}_{max} + V_{max}I_{max})}{\Delta T_{max}(\Delta T_{max} + 2T_h)} \tag{4.11}$$

At a first approximation, α, R and K_t can be considered as constant values [Palacios et al., 2009]. Indeed, they are temperature-dependent, as T_h is a variable in equations 4.9, 4.10 and 4.11. By increasing temperature, the electrical resistance and the Seebeck coefficient will increase, whereas the thermal conductance will decrease.

These three parameters are directly related to the module performances. A figure-of-merit of the module can be defined:

$$Z = \frac{\alpha^2}{RK_t} \tag{4.12}$$

and can be expressed by means of maximum performance parameters:

$$Z = \frac{\Delta T_{max}(V_{max}I_{max} + 2\dot{Q}_{max})^2}{2(V_{max}I_{max}T_h - \dot{Q}_{max}\Delta T_{max})[2\dot{Q}_{max}T_h - \Delta T_{max}(\dot{Q}_{max} + V_{max}I_{max})]} \tag{4.13}$$

The ΔT_{max} achievable is related to the figure-of-merit with the relation:

$$\Delta T_{max} = \frac{1}{2}ZT_c^2 \tag{4.14}$$

As Z is dependent of T_h, it is convenient to rearrange equation 4.14 to eliminate T_c:

$$\Delta T_{max} = T_h + \frac{1}{Z} - \sqrt{\frac{1}{Z}\left(2T_h + \frac{1}{Z}\right)} \tag{4.15}$$

A valuable thermoelectric material should have a high Seebeck coefficient together with a low thermal conductivity and electrical resistance, to minimize the heat loss by conduction and dissipation. These requirements are well fitted by semiconductors. Example of

thermoelectric materials employed in commercial devices are bismuth telluride, antimony telluride and lead telluride.

Considering the peltier cell as a heat engine, the efficiency can be calculated, commonly called Coefficient Of Performance (COP):

$$COP = \frac{\dot{Q}_c}{P} = \frac{\alpha T_c I - \frac{1}{2} I^2 R - K_t(T_h - T_c)}{\alpha(T_h - T_c)I + I^2 R} \tag{4.16}$$

Even in this case, a universal chart for single stage peltier modules can be drawn, correlating the operational conditions with the COP value (figure 4.9). At a fixed ΔT value, by increasing the electrical current the COP will firstly increase and then decrease.
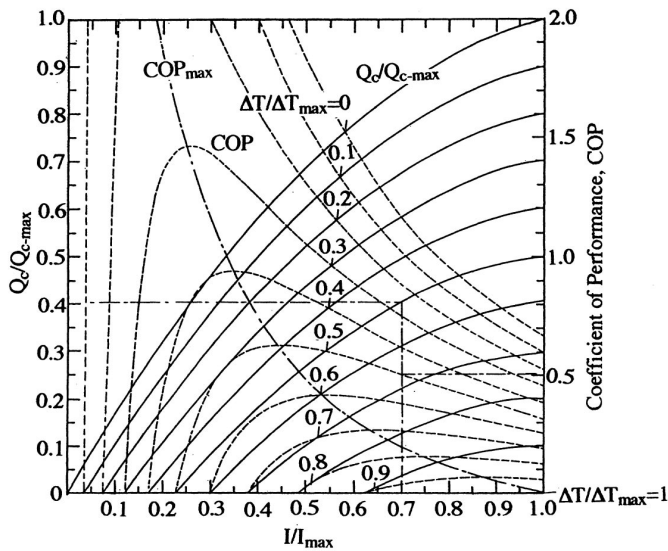
Figure 4.9: Universal chart of COP, from Rowe [1995]

The cooling/heating mode, i.e. the heat flow direction, is selected by the current direction. The current direction was controlled by using an "H bridge" (figure 4.10). Four solid stare relay (A to D) composed the H bridge, whereas the E one is used to control the current on the load by PWM. By closing the pairs A-D or B-C, it is possible to choose the current direction through the peltier cell. The global system is composed by 20 relays, 5 for each peltier cell. A power supply (15 V, 20 A) was equipped to the system, connecting each H bridge in parallel configuration.

The peltier cells used in this work were purchased from Global Component Sourcing (item ET-127-14-15-RS).

(a) General configuration   (b) Direct current   (c) Inverse current
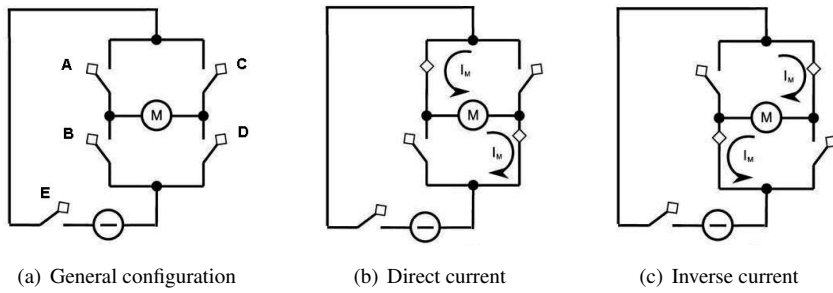
Figure 4.10: H bridge

4.3.1 Heat sink

A heat sink was used to maintain constant the temperature on one side of the peltier cells. At a first sight, fan coolers were adopted: however, they resulted poorly efficient at high cooling power. To overcome this issue, two copper plates were designed and realized, to be in contact with both sides of the sample. Each plate has a casing for two peltier cells (depth 1/10 mm), and a hydraulic circuit is provided. Each channel can be fed independently, thus offering the possibility to test asymmetric cooling configurations.

The plates are sketched in figures 4.11, 4.12 and 4.13. The dimensions are 120 mm long, 50 mm width and 10 mm height. The inner channels equivalent diameter is 6 mm.
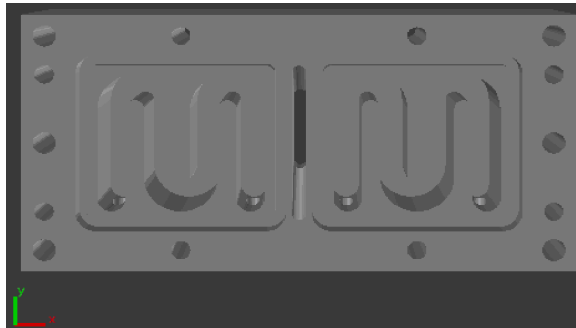
Figure 4.11: Heat sink: top view

To avoid the condensation of water vapor when operating below room temperature, a hole directed to the sample was provided, to flux a nitrogen cleaning stream.

The heat power absorbable by the considered heat sink can be calculated by analyzing the flow conditions inside the channels. The fluid velocity inside the channels can be calculated as:
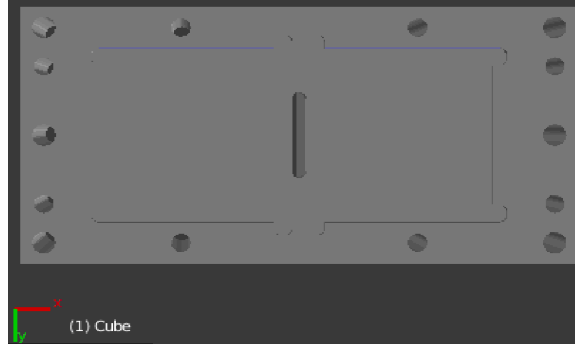
Figure 4.12: Heat sink: bottom view
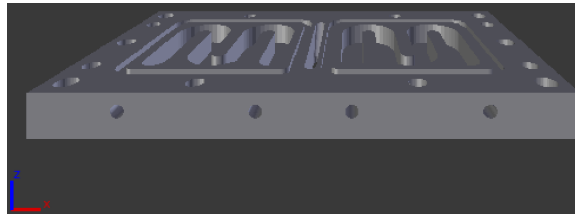
Figure 4.13: Heat sink: 3D view

$$v = \frac{F}{S} \tag{4.17}$$

where F is the volumetric flow rate and S is the channel section. The total flow rate fed by the thermostatic bath is 2.4 l/min, thus $v = 0.35$ m/s. The Reynolds number indicates the flow regime (laminar or turbulent):

$$\mathrm{Re} = \frac{\rho v d_{eq}}{\mu} \tag{4.18}$$

where d_{eq} is the equivalent diameter of the channel (it is not circular), ρ and μ are the fluid density and viscosity, respectively. In this case, $\mathrm{Re} = 2123$, so that the flow regime can be considered laminar.

The Nusselt number for laminar flow in circular channels is a constant which depends on boundary conditions. For constant heat flow at the wall:

$$\mathrm{Nu} = \frac{h_{int}d}{k_t} = \frac{48}{11} \tag{4.19}$$

where h_{int} is the internal heat transfer coefficient (i.e. of the fluid) and k_t is the fluid thermal conductivity.

The global heat transfer coefficient is:

$$U = \left(\frac{1}{h_{int}} + \frac{1}{h_{ext}} \right)^{-1} \tag{4.20}$$

where h_{ext} is the external heat transfer coefficient, referred to the copper wall of the heat sink:

$$h_{ext} = \frac{k_{Cu}}{\delta_{Cu}} \tag{4.21}$$

where the thickness of copper wall, δ_{Cu}, was assumed to be the distance between the bottom layer of channels and the external surface.

The total heat flow can be determined as:

$$\dot{Q} = U A \Delta T \tag{4.22}$$

4.4 Sample vial

The sample vial should satisfy two conditions:

1. transparency, to allow the laser beam pass through

2. possibility to measure the sample temperature

Two transparent materials were selected for the present study: glass and sapphire. The glass is a relatively low cost material and easy to handle; on the other hand, the sapphire has excellent heat transfer properties (as thermal conductivity and diffusivity), but it is more fragile.

The sample vial utilized in this study was composed by an O-ring inserted between two glass slides and sealed with tongs. Thermocouple wires were inserted into the O-ring to allow the direct measurement of sample temperature.

The solution is introduced into the sealed vial with a syringe; during the filling, a needle is inserted in the O-ring to allow the release of the air entrapped inside. To avoid the phase separation during filling operations and to lower the solution viscosity, the syringe and the sample vial were preheated.

In present work, only the glass was actually employed as sample vial: an effective use of sapphire windows, to take advantage of its heat transfer performances, requires a very small sample thickness (in the order of 10 μm, see the heat transfer analysis in Section 4.7). Therefore, the use of sapphire will be considered in future improvement and upgrade of the experimental apparatus.

4.5 Interfacing with PC

The whole system was connected to a personal computer via a NI DAQPad-6015 (National Instruments), an input/output analog/digital device. This device is equipped with 8 differential analog input (AI) and 8 digital output (DO) channels. The maximum sampling rate is 200 kS/s. The device is connected to the PC via an USB cable.

The connection scheme of AI channels is schematized in figure 4.14. All channels except two were equipped for thermocouple temperature measurement (TC from 1 to 6). A resistance of 1 kΩ for each channel was connected to the analog ground (AG) to reduce the signal oscillations. The remaining two AI channels were dedicated to the cold junction temperature and photodiode response measurement. The thermistor is connected to a 5 V voltage source (and the corresponding digital ground, DG); a 100 Ω resistance and a zener diode were employed for the sake of protection of the element. The photodiode, as stated above, was utilized in reverse bias mode, applying a 5 V bias and by using a 217 Ω resistance.

Three digital output channels were employed for controlling peltier cells. Two channels were used to drive the H bridges, i.e. for choosing the current direction across peltier cells. The remaining one is dedicated to manipulate the duty cycle, with an internal counter of the device. Another counter channel was employed for the control of laser power.
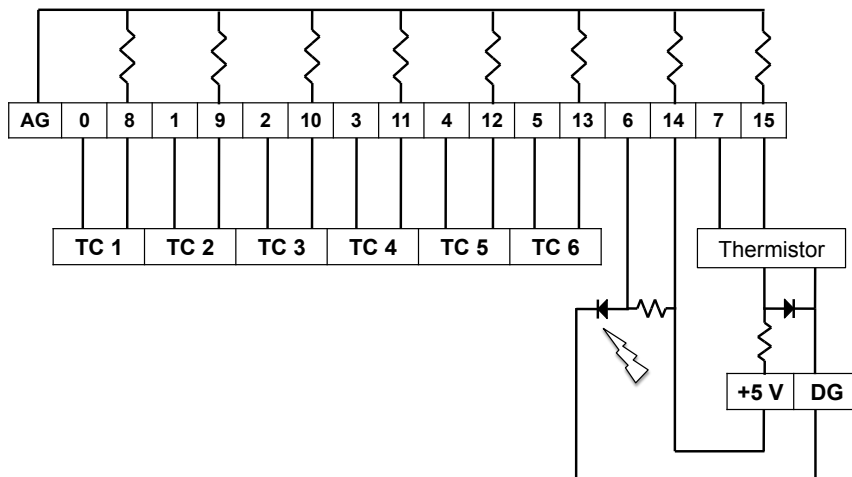
Figure 4.14: Connection scheme of the analog input channels

Both measurement and manipulation related to the single components were achieved by means of LabVIEW software package. With this package it is possible to build Virtual
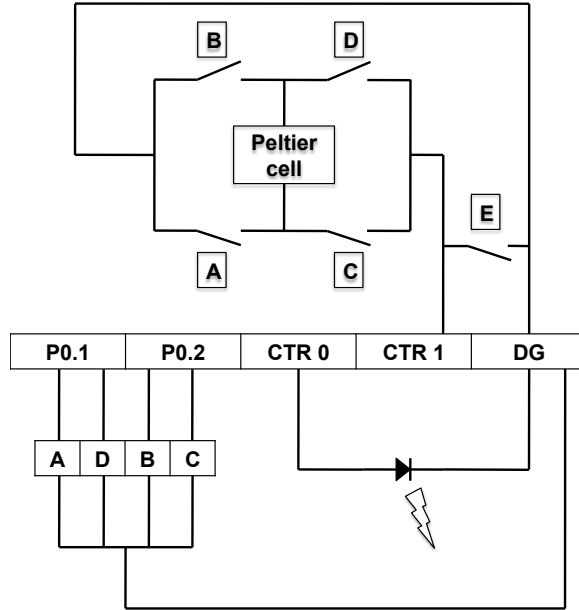
Figure 4.15: Connection scheme of the digital output channels

Instruments (VI) similar to common laboratory devices. As a matter of fact, a VI is constituted by a block diagram, which represents the data flow from/to the PC and the device, and by a front panel, where it is possible to see measured values and to manipulate directly the device.

4.6 Experimental characterization

The electrical current supplied to peltier cells was manipulated via Pulse Width Modulation (PWM). Giving a constant voltage from a power supply, by fixing a duty cycle value, a change on the temperature difference was recorded (at steady state). Assuming a constant temperature at the hot side (T_h), the temperature difference is:

$$\Delta T = T_h - T_c = \frac{\alpha I T_h - \frac{1}{2} I^2 R}{\alpha I + K_t} \tag{4.23}$$

The duty cycle (ψ) is defined as:

$$\psi = \frac{I}{I_M} \tag{4.24}$$

where $I_M = 5$ A is the maximum current allowed by the power supply. Note that I_M is not equal to I_{max}, i.e. the current needed to generate a ΔT_{max} across the module (see section 4.3). By substituting this expression into equation 4.23, a relation between ΔT and ψ was obtained:

$$\Delta T = \frac{\alpha T_h \psi - \frac{1}{2}\psi^2 I_M R}{\alpha \psi + K_t / I_M} \tag{4.25}$$

The values of α, R and K_t were computed from nominal data via equations 4.9, 4.10 and 4.11. However, the relation 4.25 was used to fit the same values at experimental conditions, thus deriving more accurate parameters. The fitting involved the regression of R and K_t values, fixing α to the value obtained from nominal data, to limit the number of adjustable parameters. The two sets of parameters obtained are reported in table 4.1.

Table 4.1: Seebeck coefficient, electrical resistance and thermal conductivity of peltier cell

	Nominal data	Experimental
α [V/K]	0.051	0.051
R [Ω]	1.99	1.08
K_t [W/K]	0.447	0.805

In cooling mode, the minimum temperature achievable on the cold side can be derived from equation 4.3, rearranged as:

$$\dot{Q}_c = (\alpha I + K_t)T_c - K_t T_h - \frac{1}{2}I^2 R \tag{4.26}$$

By defining a temperature:

$$T_c^{eq} = \frac{K_t T_h + \frac{1}{2}I^2 R}{\alpha I + K_t} \tag{4.27}$$

equation 4.26 becomes:

$$\dot{Q}_c = (\alpha I + K_t)(T_c - T_c^{eq}) \tag{4.28}$$

and the minimum achievable temperature (i.e. $\dot{Q}_c = 0$) is T_c^{eq}. Thus, the heat removed at the cold side can be expressed as a generally convective heat transfer following the Newton's law:

$$\dot{Q}_c = U A \Delta T \tag{4.29}$$

(a) Cooling

(b) Heating
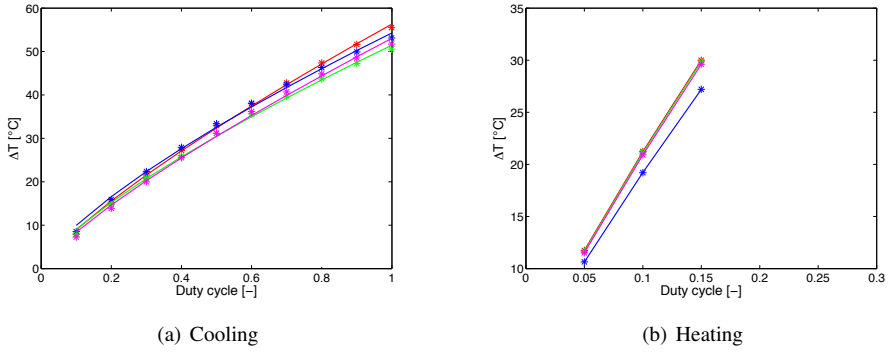
Figure 4.16: Experimental steady state ΔT vs duty cycle

(a) Cooling

(b) Heating
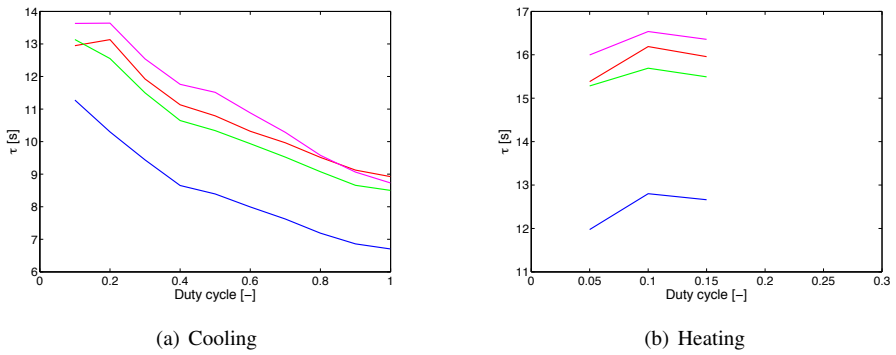
Figure 4.17: Characteristic peltier time vs duty cycle
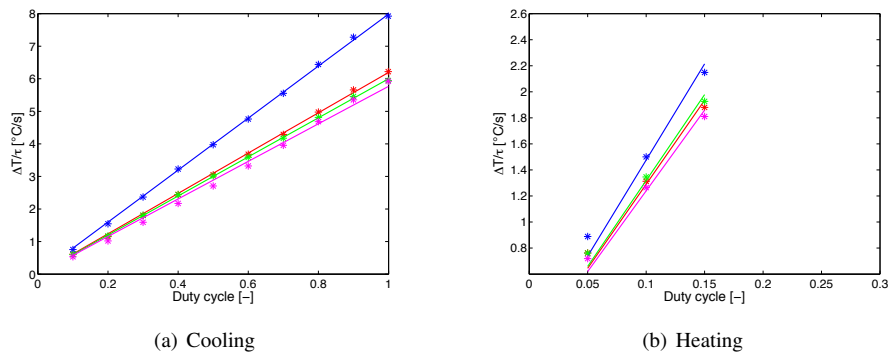

(a) Cooling

(b) Heating

Figure 4.18: Approximate cooling rate vs duty cycle

where $UA = \alpha I + K_t$ and $\Delta T = T_c - T_c^{eq}$.

From the relation between ΔT and duty cycle formulated in equation 4.25, the direct derivation of the required duty cycle value for inducing an assigned temperature difference on peltier cells is not possible. A function $\psi = f(\Delta T)$ would be extremely useful in terms of model assisted control. Therefore, a heuristic approach was followed, by defining the power law function:

$$\Delta T = a \cdot \psi^b \tag{4.30}$$

where a and b are fitting parameters. The comparison between experimental values and fitted curve is showed in figure 4.16.

The parameters a and b are different for cooling and heating operations. As a matter of fact, for all duty cycle values, when heating a higher ΔT is reached, due to the positive influence of Joule heating. When cooling, the complete range of duty cycle values (i.e. from 0 to 1) was explored; on the other hand, for heating only a small range of duty cycle was tested, to avoid overcoming the limit temperature of use for the peltier cells.

The characteristic time was derived by considering the system as a first order dynamics (see section 4.8.1). The as obtained times are plotted in figure 4.17. For cooling (figure 4.17a), the response time decreases with increasing the duty cycle.

Surprisingly, trying to obtain a relation among duty cycle, temperature difference and characteristic time, a linear relation was observed between duty cycle and average cooling rate (figure 4.18).

4.7 Modeling

A heat transfer analysis was carried out on the sample to better characterize the capabilities of the system. Two materials were considered for the sample vial: glass and sapphire, owing to their transparency. The properties of glass, sapphire and water relevant for heat transfer are resumed in table 4.2. As regards to sample, the physical properties of water were employed in calculations.

The system, treated as unidimensional, is schematized in figure 4.19. The peltier cell is considered as a heat source, where the heat transfer occurs by convection, following the Newton's law discussed in the previous section. The heat diffusion equation is:

$$\frac{\partial T}{\partial t} = \alpha \frac{\partial^2 T}{\partial x^2} \tag{4.31}$$

where α is the thermal diffusivity ($\frac{k}{\rho c_p}$). For each layer:

$$\frac{\partial \Theta_1}{\partial t_1} = \alpha_1 \frac{\partial^2 \Theta_1}{\partial x^2} \qquad \text{for } 0 \leq x \leq \delta_1 \tag{4.32}$$

$$\frac{\partial \Theta_2}{\partial t_2} = \alpha_2 \frac{\partial^2 \Theta_2}{\partial x^2} \qquad \text{for } \delta_1 < x \leq \delta_1 + \delta_2 \tag{4.33}$$

where $\Theta_i = \dfrac{T_i - T_w}{T_0 - T_w}$ is the dimensionless temperature. T_w is the temperature at the external wall (i.e. the temperature on the cold side of peltier cell, T_c^{eq}), which is assumed constant, and T_0 is the initial temperature (i.e. at $t = 0$).

Table 4.2: Material data relevant for heat transfer

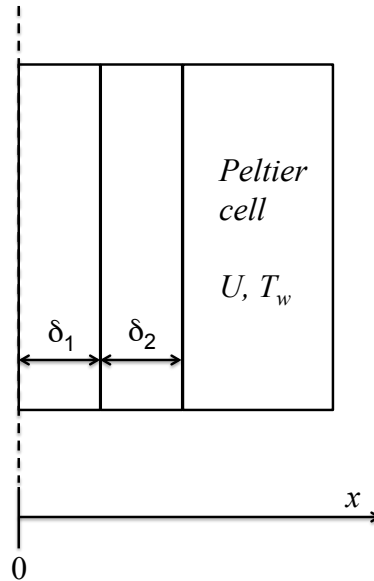|	Glass	Sapphire	Water
k_t [W/m K]	0.8	35	0.6
c_p [J/kg K]	2200	700	4184
ρ [kg/m^3]	800	3980	1000
α [m^2/s $\cdot 10^{-7}$]	4.55	126	1.43

Figure 4.19: Schematic representation of sample (1), sample vial (2) and peltier cell for 1D heat transfer modeling

To treat the system in a more convenient way, let us assume to substitute the layer 2 with a fictitious one composed by the material 1, in order to treat the diffusion in a single material. To do this, the heat diffusion dynamics must be the same in the two layers. From dimensional analysis, two dimensionless numbers must be equal for the two layers: the Biot number ($Bi = Ud/k$) and the Fourier number ($Fo = \alpha t/d^2$). The thickness of the fictitious layer is derived by equating the Biot numbers:

$$\delta_{1X} = \frac{k_1}{k_2}\delta_2 \tag{4.34}$$

where δ_{1X} is the thickness of the fictitious layer of material 1 which substitutes the material 2. Note that at this stage the layers are treated separately, i.e. the external heat transfer coefficient is the same.

At fixed δ_{1X}, the equality between Fourier numbers is ensured by introducing an (apparently) arbitrary coefficient ω:

$$\frac{\alpha_1}{\delta_{1X}^2}t = \frac{\alpha_2}{\delta_2^2}(\omega t) \tag{4.35}$$

The physical meaning of the ω parameter is easily explained. The Biot number is related to the heat transfer *regime* (i.e. concentrated or distributed parameters), and it is equal for the two layers. However, as the thermal diffusivities are different, the heat transfer *rate* is different. This means that the two materials experience the same thermal history (as Bi is equal) at different times, not contemporarily (as Fo is different). The coefficient ω represents the contraction/expansion of thermal history. Combining equations 4.34 and 4.35:

$$\omega = \frac{\alpha_1}{\alpha_2}\frac{k_2^2}{k_1^2} = \frac{(k\rho c_p)_2}{(k\rho c_p)_1} \tag{4.36}$$

i.e. at equal Bi number, the thermal history has the same rate if the product $k\rho c_p$ is equal for the two materials. In the case of $\omega \neq 1$, the temperature profile into materials 1 and 2 will be equal at different times related by:

$$t_1 = \frac{t_2}{\omega} \tag{4.37}$$

Now let go back to the initial problem, with the two layers in contact. To take into account the change in dimension (the thickness δ_2 is substituted by δ_{1X}) into equation 4.33, a change of coordinates is operated:

$$X = (x - \delta_1)\frac{\delta_{1X}}{\delta_2} + \delta_1 \tag{4.38}$$

thus obtaining:

$$\frac{\partial \Theta_2}{\partial t_2} = \alpha_2 \frac{\delta_{1X}^2}{\delta_2^2} \frac{\partial^2 \Theta_2}{\partial X^2} \qquad \text{for } \delta_1 < X \leq \delta_1 + \delta_{1X} \tag{4.39}$$

Substituting equation 4.35 into equation 4.39:

$$\frac{\partial \Theta_2}{\partial (t_2/\omega)} = \alpha_1 \frac{\partial^2 \Theta_2}{\partial X^2} \qquad \text{for } \delta_1 < X \leq \delta_1 + \delta_{1X} \tag{4.40}$$

and recalling the relation 4.37:

$$\frac{\partial \Theta_2}{\partial t_1} = \alpha_1 \frac{\partial^2 \Theta_2}{\partial X^2} \qquad \text{for } \delta_1 < X \leq \delta_1 + \delta_{1X} \tag{4.41}$$

A dimensionless length and time are defined:

$$\tilde{x} = \frac{x}{\delta_X} \qquad \tilde{X} = \frac{X}{\delta_X} \tag{4.42}$$

$$\tilde{t} = \frac{\alpha_1 t_1}{\delta_X^2} \tag{4.43}$$

where $\delta_X = \delta_1 + \delta_{1X}$. Substitution into equations 4.32 and 4.40 gives out:

$$\frac{\partial \Theta_1}{\partial \tilde{t}} = \frac{\partial^2 \Theta_1}{\partial \tilde{x}^2} \qquad \text{for } 0 \leq \tilde{x} \leq \frac{\delta_1}{\delta_{1X}} \tag{4.44}$$

$$\frac{\partial \Theta_2}{\partial \tilde{t}} = \frac{\partial^2 \Theta_2}{\partial \tilde{X}^2} \qquad \text{for } \frac{\delta_1}{\delta_{1X}} < \tilde{X} \leq 1 \tag{4.45}$$

These two equations can be condensed into a single expression:

$$\frac{\partial \Theta}{\partial \tilde{t}} = \frac{\partial^2 \Theta}{\partial \xi^2} \qquad \text{for } 0 \leq \xi \leq 1 \tag{4.46}$$

where

$$\xi = \begin{cases} \tilde{x} & \text{if } 0 \leq \xi \leq \dfrac{\delta_1}{\delta_{1X}} \\[2em] \tilde{X} & \text{if } \dfrac{\delta_1}{\delta_{1X}} < \xi \leq 1 \end{cases} \tag{4.47}$$

With the boundary condition of constant external heat transfer coefficient and temperature (i.e. given U and T_c^{eq} of equation 4.28), the solution of this differential equation is [Isachenko et al., 1987]:

$$\Theta = \sum_{n=1}^{\infty} \frac{2\sin\mu_n}{\mu_n + \sin\mu_n\cos\mu_n} \cos(\mu_n\xi)\exp(-\mu_n^2\tilde{t}) \tag{4.48}$$

where the μ_n values are a function of the Biot number:

$$\cot\mu = \frac{\mu}{\mathrm{Bi}} \tag{4.49}$$

and this latter equation holds for infinite solutions.

Examples of temperature profiles in composite slabs at various times are reported in figure 4.20. In both cases, the sample vial was assumed to be 1.2 mm thick, the half sample is 1.2 mm thick, and the initial temperature is 300 K. The electrical current was fixed to 2.5 A. In the case of water in contact with glass (figure 4.20a), the temperature profile is close to that of a single slab, owing to the similar heat transfer properties of the two materials. As a matter of fact, in this case the coefficient ω is equal to 0.56. When the sapphire is employed (figure 4.20b), the temperature in the external slab rapidly decays. The temperature evolution are highly different, as suggested by $\omega = 38.8$.

From this analysis it is easy to notice that the sample experiences temperature gradients, which should be avoided to perform a reliable cloud point measurement. As a matter of fact, if the sample temperature is not homogeneous, phase separation can start at different times, thus making difficult an accurate cloud point detection. Moreover, the sample could experience different cooling rates at various section, thus affecting measurement especially when testing relatively high cooling rates. The cooling rate can be calculated by computing the derivative of equation 4.48 with respect to $\tilde{t}$:

$$\frac{\partial\Theta}{\partial\tilde{t}} = -\sum_{n=1}^{\infty} \frac{2\mu_n^2\sin\mu_n}{\mu_n + \sin\mu_n\cos\mu_n} \cos(\mu_n\xi)\exp(-\mu_n^2\tilde{t}) \tag{4.50}$$

The cooling rate at different sample sections are presented in figure 4.21. The sapphire allows the reaching of higher cooling rates, but with an extreme inhomogeneity among sections. The glass, owing to its lower thermal diffusivity, allow a more homogeneous distribution of thermal history inside the sample. These results are obviously related to the considered sample dimension. As a matter of fact, the heat diffusion into the sample is controlled by its thermal diffusivity: the reduction of sample thickness will lower the inhomogeneities.

During a continuous cooling, the sample experiences a variable cooling rate, first increasing and then decreasing (see figure 4.21). This issue makes difficult the comparison of measurements carried out via continuous cooling protocols, as it is not easy to com-

pare different temperature histories. To overcome this issue, the reference parameter was assumed to be the *maximum cooling rate* experienced by the sample.

(a) Water-glass   (b) Water-sapphire
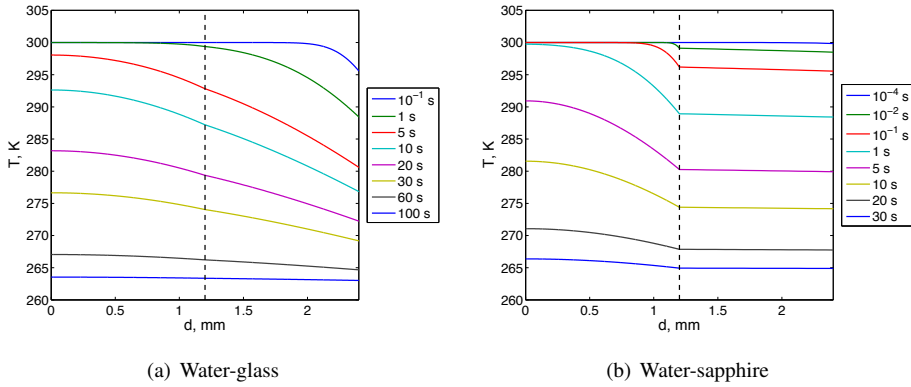
Figure 4.20: Calculated temperature profile in composite slabs. The dashed line represents the contact layer

(a) Water-glass   (b) Water-sapphire
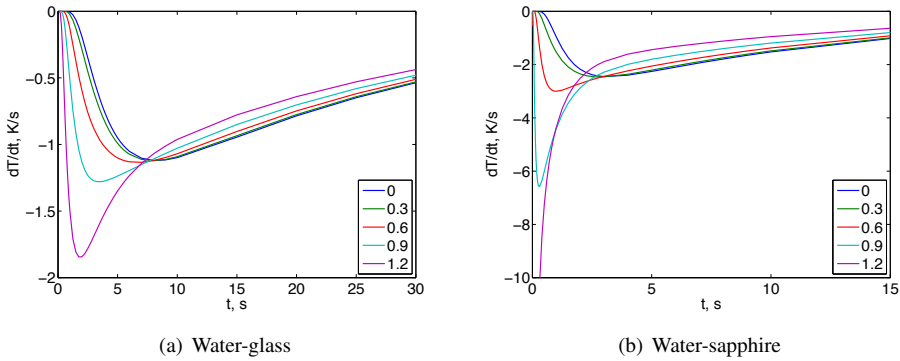
Figure 4.21: Calculated cooling rate evolution at different distance from the center (expressed in mm)

The modeling discussed here can be employed for deducing the required sample thickness for a homogeneous cooling. The half thickness of sample which ensures a very small cooling rate gradient was obtained via a trial-and-error procedure, giving a value of 0.01 mm; the resulting cooling rate profile is showed in figure 4.22.

The temperature evolution at the center, in the case of water in contact with sapphire and glass, is reported in figure 4.23. The results are compared in the same plot with those obtained via finite element analysis simulations (by means of COMSOL Multiphysics package), showing that the analytical solutions are comparable to the numerical ones (in the

case of glass are practically superimposed).

The characteristic times are computed as:

$$\tau_X = \frac{\delta_X^2}{\alpha_1} \tag{4.51}$$

and reported in table 4.3.

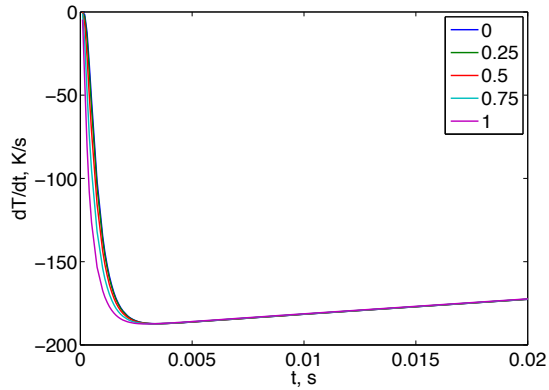**Figure 4.22:** Calculated cooling rate evolution at different distance from the center (expressed in 10^{-2} mm) for a sample half thickness of 10^{-2} mm
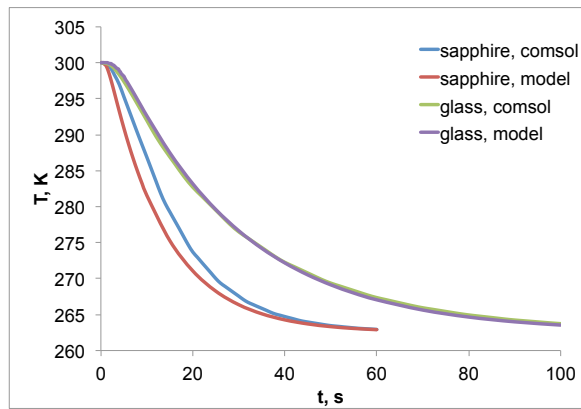
Figure 4.23: Calculated and simulated temperature evolution at the center of the slab

Table 4.3: Characteristic times for heat transfer

Material	τ_X [s]
water	10.1
glass slide	3.16
sapphire	0.11
glass slide + water	24.5
sapphire + water	12.3

4.8 Simulations

4.8.1 System dynamics

Peltier cells were assumed as a first order system, i.e. with a transfer function of the type:

$$G_p(s) = \frac{K_p}{\tau_p s + 1} \tag{4.52}$$

where K_p is the gain and τ_p is the time constant of the process. A transfer function represents the ratio between the output and the input: in this case, the output is the temperature difference between the two sides, and the input is the duty cycle:

$$G_p = \frac{\Delta T}{\psi} \tag{4.53}$$

As the gain is related to the steady state values, it can be directly derived from equation 4.30:

$$K_p = \frac{\Delta T_{ss}}{\psi_{ss}} = a\psi^{b-1} \tag{4.54}$$

where the subscript ss denotes the steady state values.

On the other hand, the time constant is not easy to be derived theoretically: it was derived experimentally, by fitting the step response with a first order function in the time domain:

$$\frac{\Delta T(t) - \Delta T_{ss}}{\Delta T_0 - \Delta T_{ss}} = e^{-t/\tau_p} \tag{4.55}$$

An example is showed in figure 4.24.

As regards for the sample, it is constituted by two distinct layers: the microscope slide and the solution itself. Each layer should be considered as a first order system with respect

131

(a) cooling   (b) heating
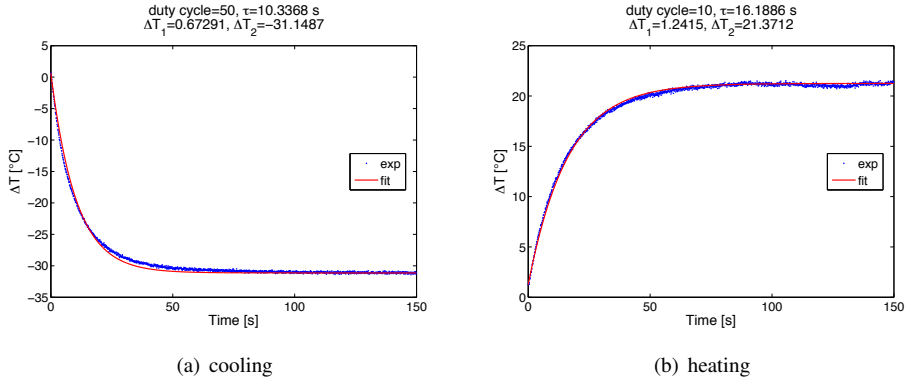
Figure 4.24: Step response of peltier cells

to heat transfer; however, on the basis of the modeling discussed in section 4.7, the two layers were treated as a single, first order system:

$$G_v(s) = \frac{K_v}{\tau_v s + 1} \tag{4.56}$$

which considered as in series with the peltier cell, gives out a second order relationship:

$$G_t(s) = \frac{K_t}{\tau_t^2 s^2 + 2\zeta\tau_t s + 1} \tag{4.57}$$

where K_t is the global gain $(= K_p K_v)$, τ_t is the global time constant and ζ is the damping factor. The time constant of peltier and sample can be calculated from the relations:

$$\tau_t^2 = \tau_p \cdot \tau_v \tag{4.58}$$

$$2\zeta\tau_t = \tau_p + \tau_v \tag{4.59}$$

The temperature evolution of the sample in the time domain is (valid for $\zeta > 1$):

$$\frac{T(t) - T_{ss}}{T_0 - T_{ss}} = e^{-\zeta t/\tau} \left[\cosh\left(\sqrt{\zeta^2 - 1}\frac{t}{\tau}\right) + \frac{\zeta}{\sqrt{\zeta^2 - 1}} \sinh\left(\sqrt{\zeta^2 - 1}\frac{t}{\tau}\right) \right] \tag{4.60}$$

By means of Simulink package, the complete system dynamics (peltier cell and sample vial) can be simulated via PC. An example of block diagram is reported in figure 4.25.
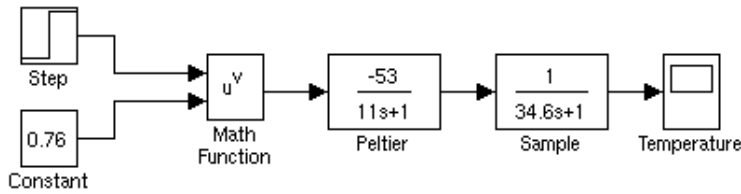
Figure 4.25: Simulink block diagram for open loop system simulation

This simplified modeling was double-checked with experimental measurements. The dynamic response of sample temperature to a step on duty cycle was recorded and compared with those predicted by equation 4.60. The values of τ and ζ were calculated from equations 4.58 and 4.59, by using $\tau_p = 11$ s and $\tau_v = 24.5$ s. Some examples are showed in figures 4.26, 4.27 and 4.28, denoting a very good agreement between experimental and predictions.
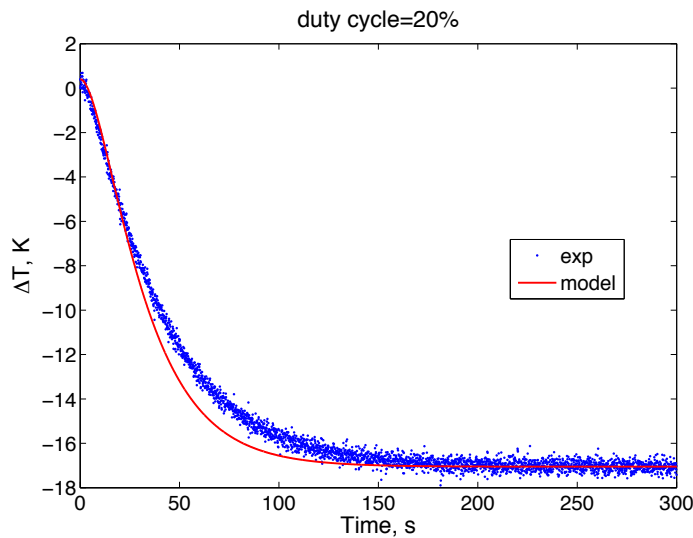
Figure 4.26: Step response of peltier cell and sample vial in series, 20% step amplitude

An additional experimental validation of the heat transfer dynamics was carried out on the glass slab. In this case, a thermocouple was located between two glass slides, which in their turn were inserted between peltier cells. The duty cycle was imposed to 99.9%, and the temperature history between the glass slabs was recorded. In this case, the characteristic time used in calculations were $\tau_p = 8.7$ s and $\tau_v = 3.16$ s. The comparison between

Figure 4.27: Step response of peltier cell and sample vial in series, 50% step amplitude
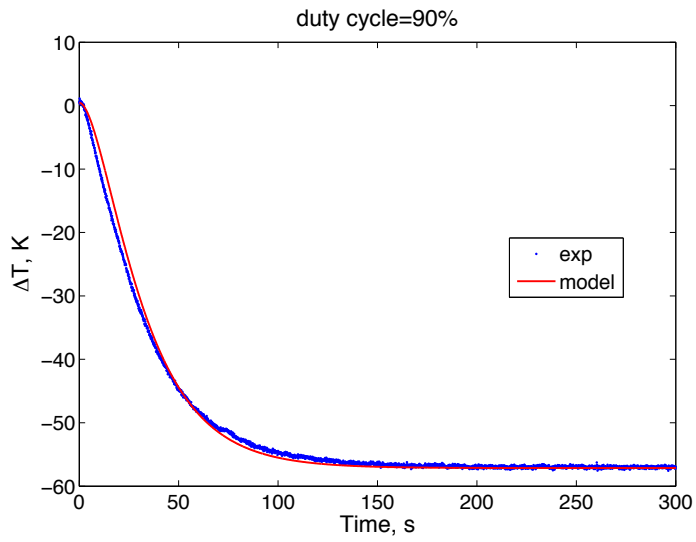
Figure 4.28: Step response of peltier cell and sample vial in series, 90% step amplitude

experimental and calculated values is reported in figure 4.29, showing a good agreement.
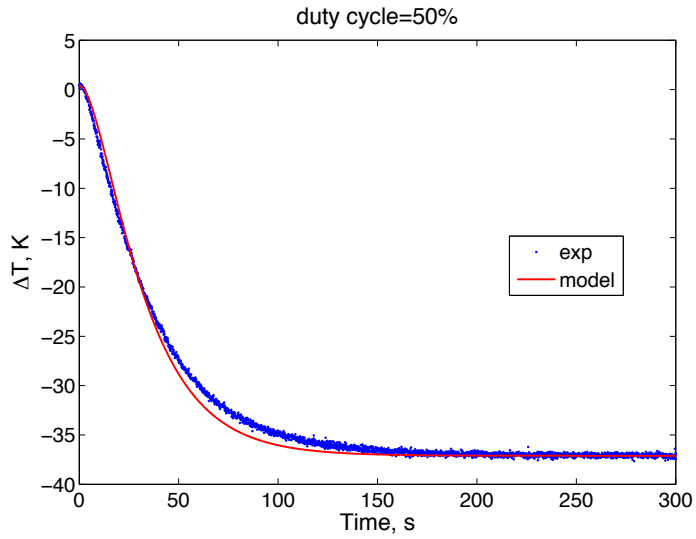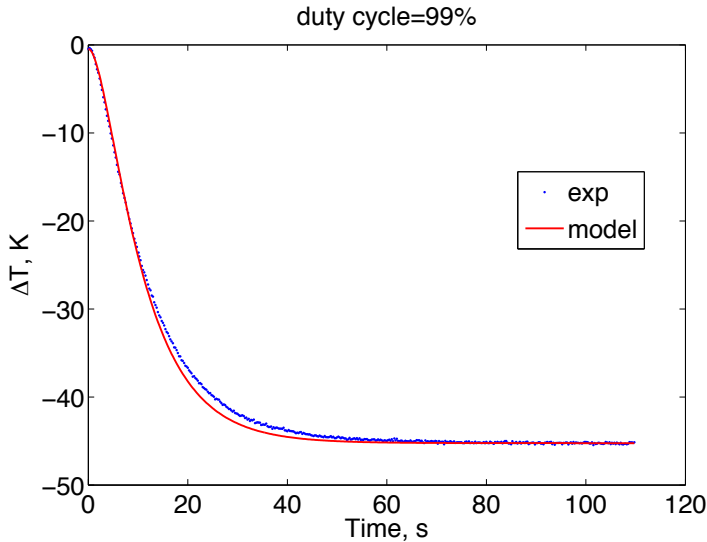

Figure 4.29: Step response of peltier cell and glass slab in series, 99.9% step amplitude

4.8.2 Finite element analysis

A finite element analysis of transient heat transfer was carried out with the software package COMSOL Multiphysics. In this way, additional information on the system can be worked out, e.g. two-dimensional temperature distribution, more accurate for a heat transfer analysis.

The system was treated as two-dimensional. The 2D representation of the system is sketched in figure 4.30, where the dimensions are the same of the real system: the glass slab and water thickness are 1.2 mm, the slab length is 76.2 mm and the distance between peltier cells is 3 mm. Note that the peltier modules are distanced to allow the laser beam pass through the sample. The model was simplified by taking the advantage from the symmetry of the system across an horizontal axis passing through the half section of the sample.

The thermal contact at the water/slab and peltier/slab interfaces was assumed to be ideal. All the remaining surfaces were considered as adiabatic. The initial condition is at constant temperature in both water and sample vial ($T_0 = 300K$). The peltier cells were assumed to be at the same initial temperature T_0, then cooled to a temperature T_c^{eq}, directly calculated

from a current value imposed (equation 4.27). The heat transfer coefficient was calculated as a function of current (see equation 4.28).
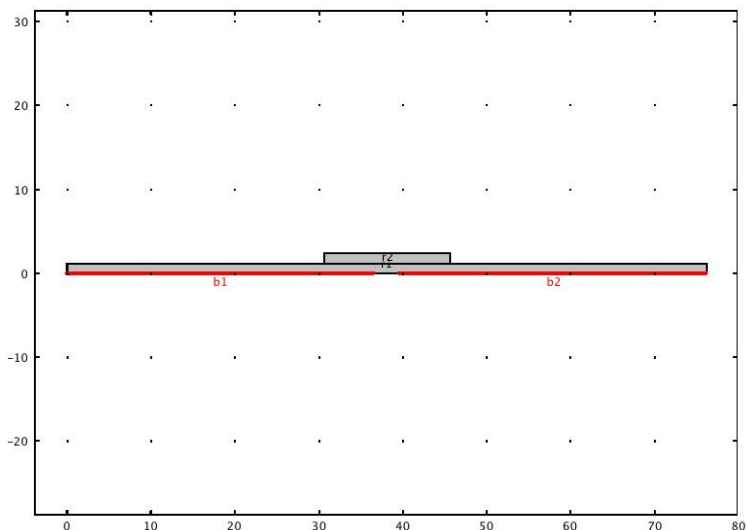
Figure 4.30: 2D model of glass slide and sample. The red lines represent the surfaces in contact with peltier cells

Results for the early stages of transient cooling are showed in figure 4.31. The glass sample vial results in a slower heat transfer rate (see figure 4.31a). From the results for late stages (figure 4.32) it can be noticed that the glass (figure 4.32a) is not able to give an uniform temperature distribution to the sample, which in the center is hotter. This may cause errors in the cloud point measurements, which are referred to the center of the sample. On the other hand, the sapphire (4.32b) is able to cool uniformly the sample, with a temperature gradient only in the vertical direction.

A complete simulation of the cooling was performed by adding the peltier cell dynamics to the model. To accomplish this feature, a 2D modeling of peltier cell was implemented to the simulation. The peltier module was schematized by considering the external ceramic plates and the internal semiconductor pellets (see figure 4.33). The ceramic plates thickness was measured to be around 1 mm, whereas the semiconductor pellets dimensions were approximately defined to be 1.5×2 mm (width $\times$ height). The copper tabs which weld the pellets to ceramic plates (see figure 4.7) were neglected in the proposed schematization, owing to the high thermal conductivity of copper with respect to the other materials concerned. The peltier modules utilized in the real system are composed by 128 pairs of P-N

136

pellets, disposed on a 8×16 array; each pair has dimension of $1.5 \times 4 \times 2$ mm (length $\times$ width $\times$ height), thus occupying a surface of 768 mm^2. As the surface of ceramic plates is 1600 mm^2, the active area of cooling is approximately the 50% of the total external surface. These aspects were taken into account in the development of the schematic model by considering a row of 16 semiconductor pellets, which occupy the 60% of the total external surface.

The material properties of ceramic plates and pellets are resumed in table 4.4. In absence of information on technical data-sheet provided by manufacturers, the semiconductors were assumed to be constituted of bismuth telluride (Bi$_2$Te$_3$), a material widely employed for the construction of peltier modules. This assumption was double-checked by comparing the module thermal conductance with that calculated from material properties. By considering the peltier cell as composed by three layer in series, two made by the ceramic plates and one by the pellets, the module thermal conductance can be calculated as:

$$K_t = \left(\frac{2\delta_c}{k_c A_c} + \frac{\delta_p}{k_p A_p} \right)^{-1} \tag{4.61}$$

where δ is the thickness, k is the thermal conductivity and A is the area; the subscripts c and p refer to ceramic plates and pellets, respectively. The as calculated thermal conductance was $K_t = 0.768$ W/K, whereas the experimental value was 0.805 W/K (see table 4.1). Being the difference between these two values lower than 5%, the assumption made on the constituent material of semiconductor pellets was considered acceptable.

Table 4.4: Physical properties of peltier module materials relevant for heat transfer

	Ceramic	Bi$_2$Te$_3$
k_t [W/m K]	24	2
c_p [J/kg K]	900	160
ρ [kg/m^3]	3980	7860
α [m^2/s $\cdot$ 10^{-7}]	70	20

The heat sources involved with the peltier module were deducted by referring to equation 4.3, thus the heat flow induced by Peltier effect and the Joule heating must be taken into account. The conductive heat flow is not an "external" heat source, as it is intrinsically related to the temperature gradients induced by heat flow. The semiconductor pellets were considered with a distributed heat source, where the heat generation is proportional to the square of the current. The heat removal induced by Peltier effect was assigned to the contact layer between the semiconductors and the upper ceramic plate. As a matter of fact,
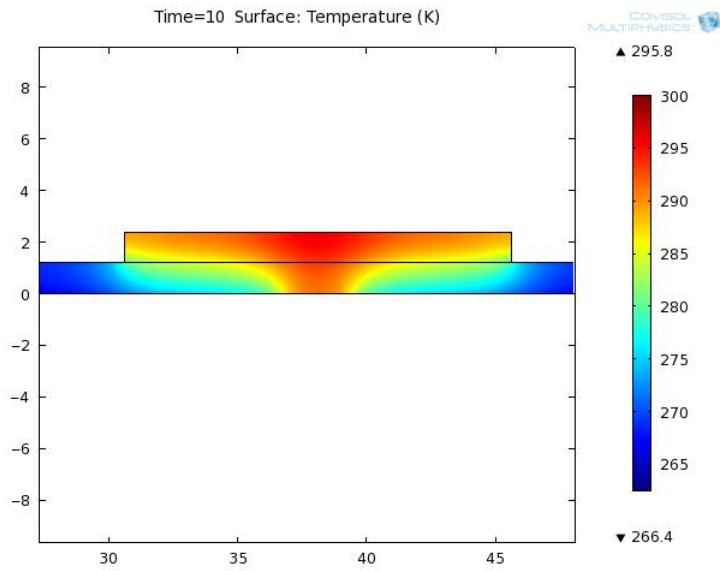
(a) Glass
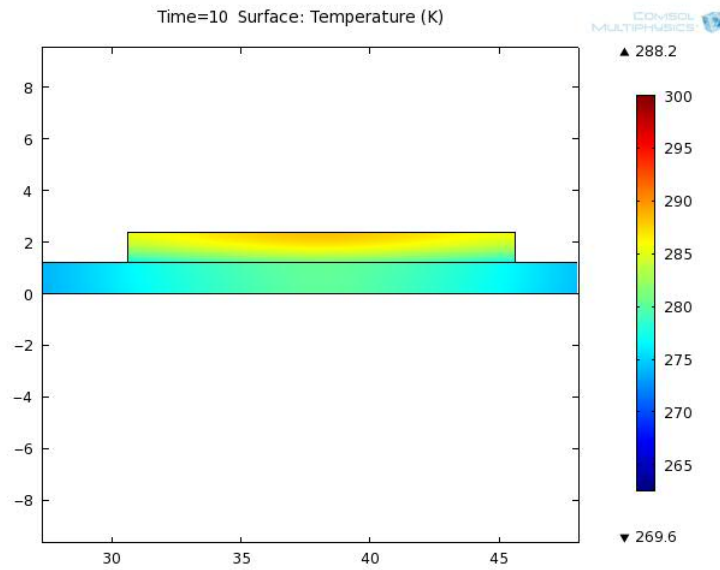
(b) Sapphire

Figure 4.31: Temperature distribution in a glass or sapphire slab in contact with water at t=10 s, simulated via COMSOL Multiphysics. The sapphire allows a faster cooling and the temperature distribution is approximately homogeneous for the horizontal sections
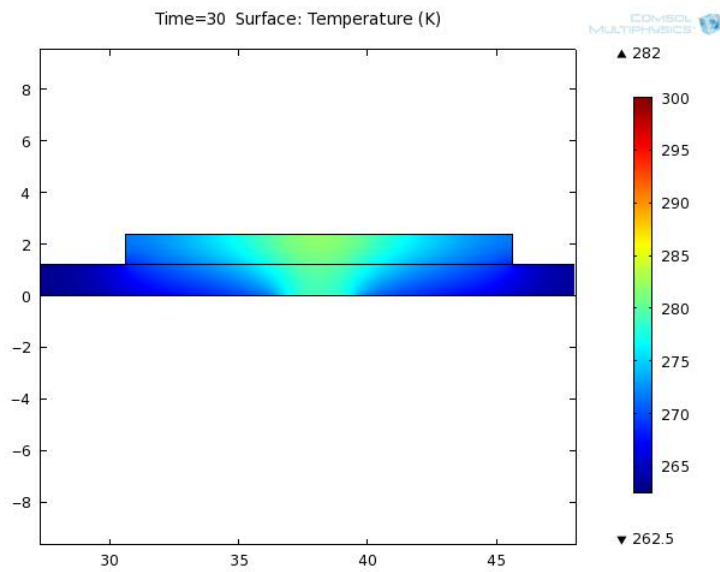
(a) Glass
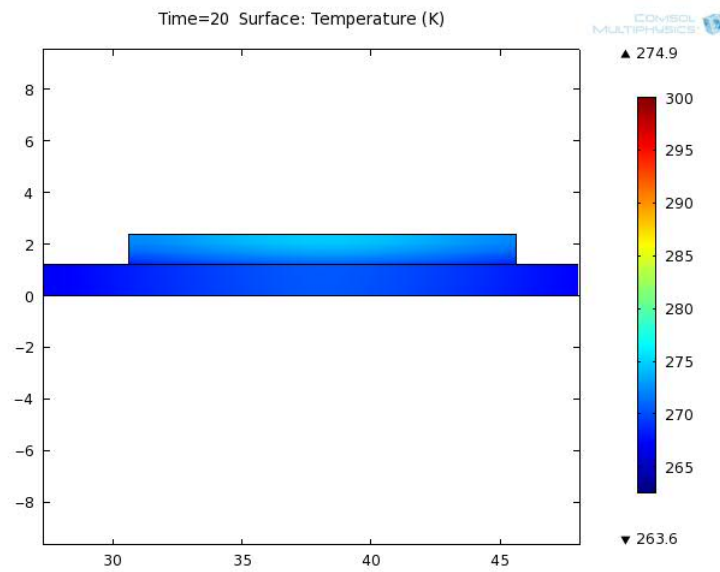
(b) Sapphire

Figure 4.32: Temperature distribution in a glass or sapphire slab in contact with water at late stages, simulated via COMSOL Multiphysics. The glass does not ensure a homogeneous cooling of the water: the central zone is hotter than external

Figure 4.33: Model of peltier cell

Figure 4.34: Model of complete system

the heat generation/removal occurs at the contact zone between P and N semiconductors, i.e. at the interface with the external plate. As regards to the lower ceramic plate, a heat generation should be taken into account: however, to simplify the model, a perfect heat sink was assumed, so that the boundary condition at the lower external surface is constant temperature, and the Peltier heat generation was neglected.
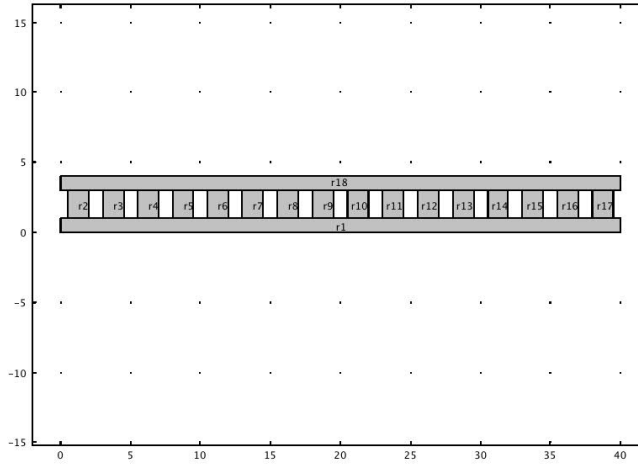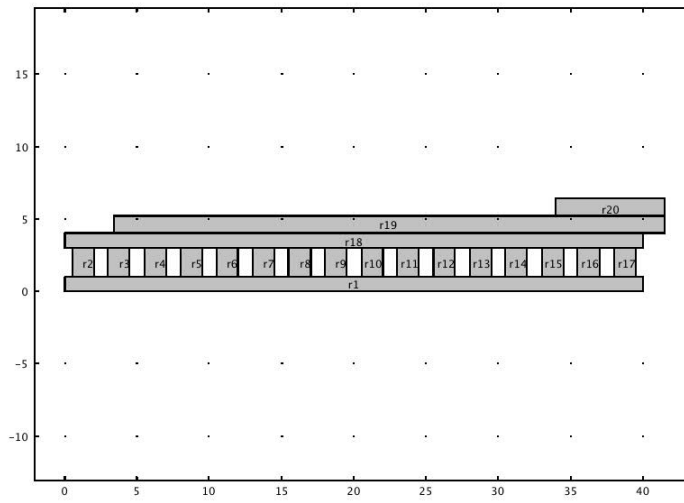
Due to the symmetry of the system, the simulation was carried out by considering only one peltier cell in contact with half glass slide and a quarter of sample (see figure 4.34). The results of the transient heat transfer simulation at three different times are showed in figures 4.35, 4.36 and 4.37.

After 5 s (figure 4.35), the main temperature reduction ($\sim 10-15$ K) concerns the upper peltier surface and the contacting glass slab, whereas inside the pellets a small temperature gradient is generated, due to the compensating effect of Joule heating. The sample temperature decreases only by a few degree K.

At $t = 10$ s (figure 4.36), the temperature gradient inside the pellets increases, whereas the upper peltier surface and the glass slabs are ~ 20 K below the initial temperature. The sample temperature decreases slower than glass, being ~ 5 K below the initial temperature.

At a relatively late stage ($t = 30$ s, figure 4.37) the peltier cell is approximately at its steady state condition, whereas the sample is still not fully cooled.

The simulation results were compared with experimental data. Figure 4.38 reports the simulated and measured temperature difference between two sample sections and the hot side of peltier cell. The center section coincides with the right sample edge in drawing, and it is the zone of interest for optical measurements. The edge section is the left side edge in drawing. These two sample zones experience a similar thermal history but at different times, thus the temperature measurement must take this issue into account. As a matter of fact, a thermocouple location too far from the center would give out erroneous measurement of temperature, especially when operating at high cooling rates. The experimental measure is quite superimposed at early times to the simulated center temperature, thus suggesting that an accurate temperature detection at the zone of interest is attained. The slight offset between steady values can be related to the difference between the actual and predicted equilibrium temperature; the deviations in the dynamics at intermediate times (i.e. from 40 to 120 s) could be due to a higher Joule effect heating in the real system. As a matter of fact, by supplying a square current wave to the module, the actual Joule heating effect is related to the maximum current flowing into the module, not to its time averaged value.

Figure 4.35: Temperature profile inside peltier cell and sample simulated via COMSOL Multiphysics, early stage
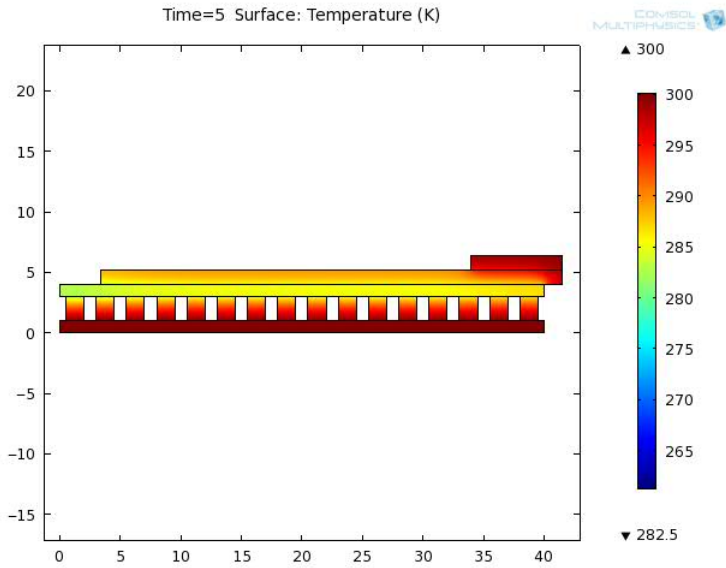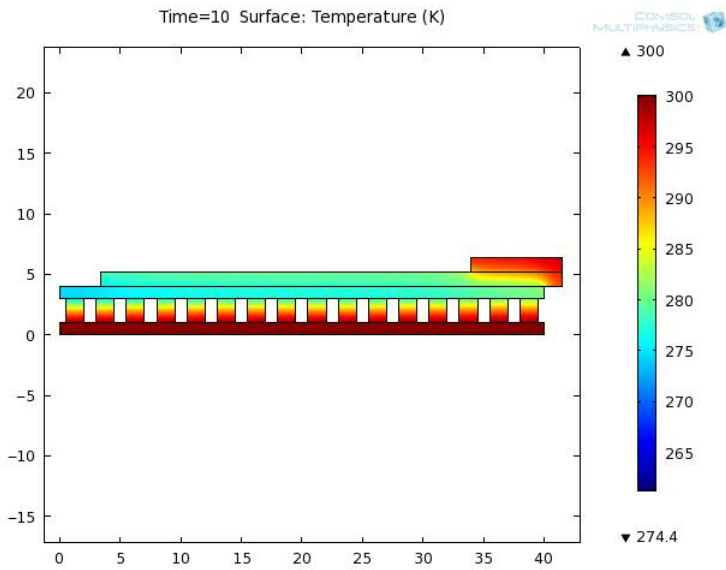

Figure 4.36: Temperature profile inside peltier cell and sample simulated via COMSOL Multiphysics, intermediate stage
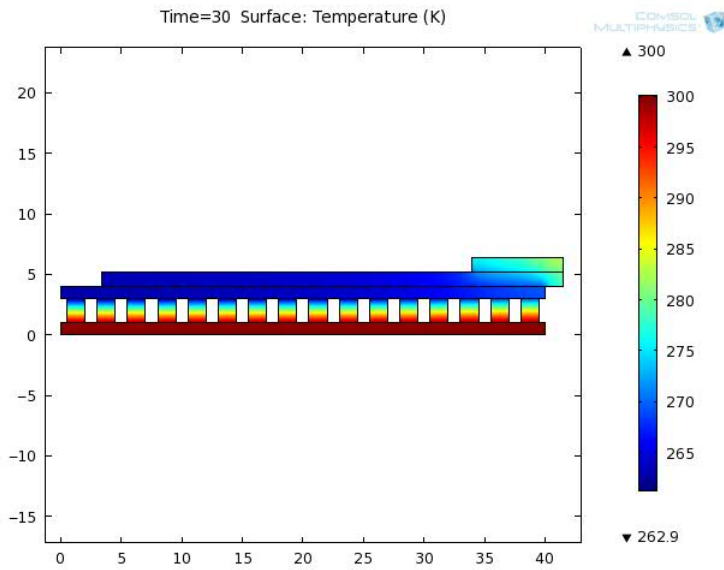
Figure 4.37: Temperature profile inside peltier cell and sample simulated via COMSOL Multiphysics, late stage
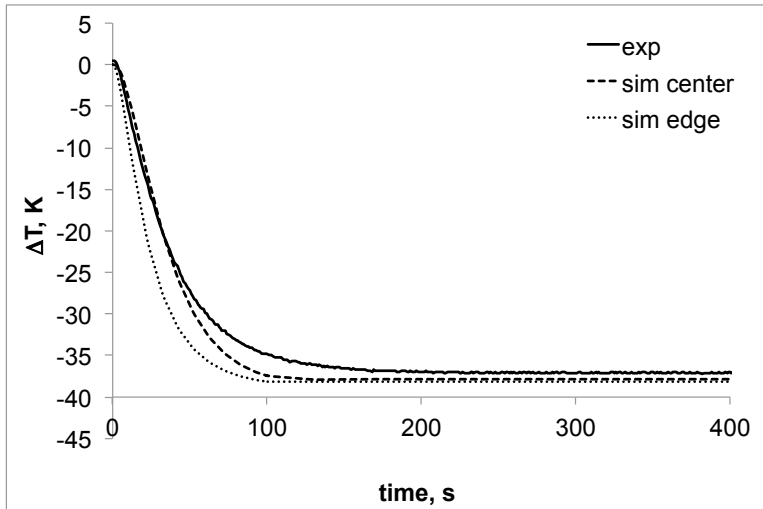
Figure 4.38: Comparison between experimental and simulated temperature difference between sample center and edge section and hot side of peltier cell

4.9 Controller

4.9.1 Estimation of parameters

A first estimate of controller parameters was carried out via Simulink simulations. The heuristic model of the system previously discussed (see Section 4.8.1) was employed. The closed-loop block diagram is reported in figure 4.39.
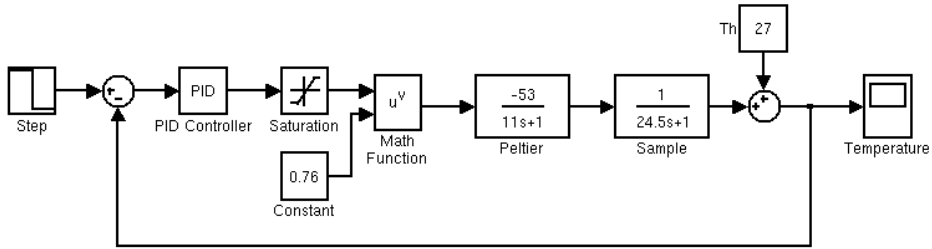
Figure 4.39: Simulink block diagram for closed loop system simulation

The Ziegler-Nichols method was adopted for a first estimate of PID controller parameters [Stephanopoulos, 1984]. The proportional gain which gave out constant oscillations, with period $P_u = 4.3$ s, was $K_u = 25$. The values obtained for the PID controller are $K_p = 15$, $\tau_i = 2.15$ s and $\tau_d = 0.54$ s. However, this set of parameters gave out an undershoot, which must be avoided in the present application, and the controlled temperature oscillates at steady state.

Another method adopted for tuning the controller parameters is the minimization of the Integral of Absolute Error (IAE) function [Stephanopoulos, 1984]:

$$IAE = \int_0^\infty |\epsilon(t)|\, dt \qquad (4.62)$$

The PID controller parameters were modified in order to reach the lowest IAE value. In this way, the parameters obtained were $K_p = 0.2$, $\tau_i = 1.5 \cdot 10^{-3}$ s and $\tau_d = 0.57$ s, with $IAE = 98.8$. However, this set of parameters gave out an undershoot with respect to the set point value (line C in figure 4.40). To overcome this issue, the parameters were changed in order to avoid an undershoot maintaining a low value of IAE. The new parameters adopted were $K_p = 0.05$, $\tau_i = 5 \cdot 10^{-4}$ s and $\tau_d = 0.5$ s, with $IAE = 283.3$ (line B in figure 4.40).

Obviously, the as obtained parameters do not ensure a satisfactory control, due to the intrinsic approximations on the model. To overcome this issue, the PID parameters were
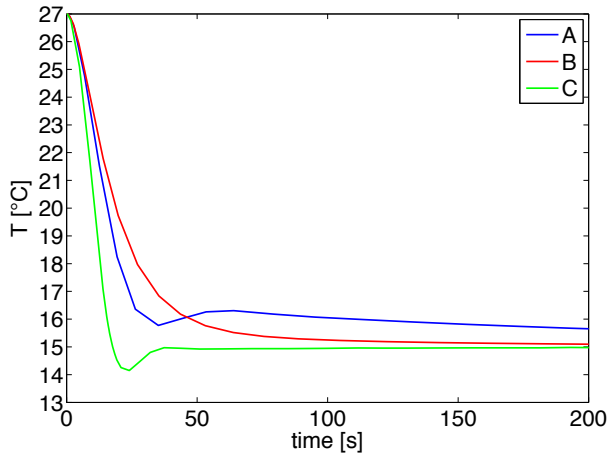
Figure 4.40: Simulated closed loop response. A: parameters used in real system; B: optimal parameters (no undershoot); C: minimum IAE

optimized experimentally by a trial-and-error procedure, using the values obtained via simulations as a first estimation value. The PID values adopted for the control system were $K_p = 0.05$, $\tau_i = 3 \cdot 10^{-4}$ s and $\tau_d = 0.1$ s, with $IAE = 469.2$ (line A in figure 4.40).

4.9.2 Mixed FF-FB controller

To enhance the quality and the speed of control, a mixed feedforward (FF) and feedback (FB) controller was used. The FF controller is based on the relation between duty cycle and ΔT (equation 4.30). In principle, to reach and maintain a certain temperature in the sample, it is sufficient to set a constant duty cycle from equation 4.30. However, errors may stem from the intrinsic approximations of fitting. To overcome this issue, a proportional-integral-derivative (PID) controller is coupled with the FF algorithm. In practice, the FF gives a fast approach to the set point, then the controller switch to FB mode and performs an accurate control avoiding undershoots.

This control configuration was firstly simulated via Simulink (figure 4.41), to check its applicability. An example of simulated step response is presented in figure 4.42. Then, it was implemented to the real system.

The PID was implemented with a discrete algorithm:

$$c(t_i) = P \cdot \epsilon(t_i) + I \sum_0^i \epsilon(t_i) + D \frac{\epsilon(t_i) - \epsilon(t_{i-1})}{\Delta t} \tag{4.63}$$
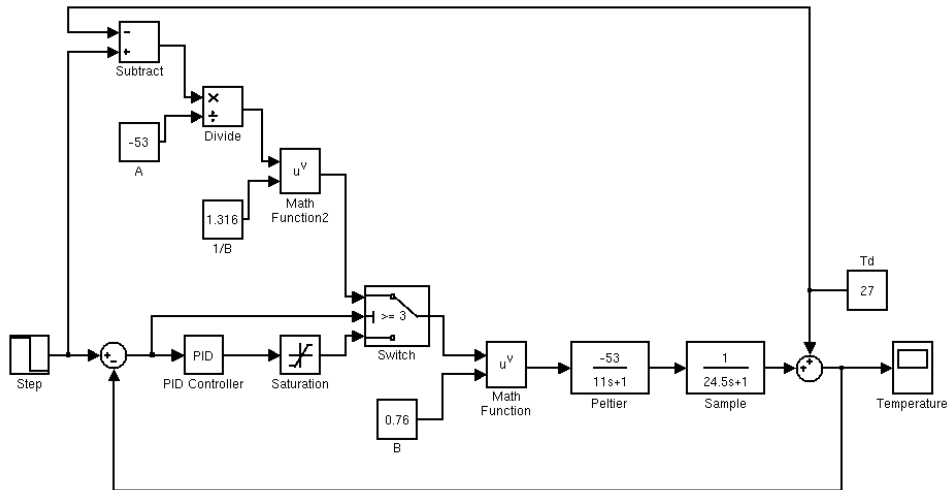
Figure 4.41: Simulink block diagram for closed loop mixed FF-FB control system simulation
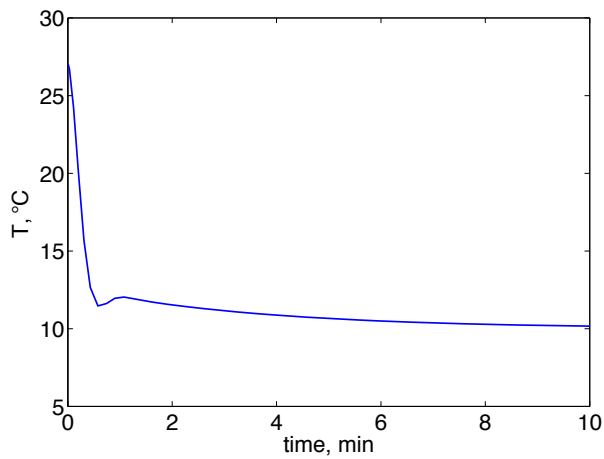
Figure 4.42: Step response simulated for the FF-FB control system

When the PID is activated, the integral and derivative contributions are zero. To achieve a faster control, the integral contribution is set to a finite initial value, related to the last FF action. A slightly oscillating measure affects negatively the derivative contribution: to make it more reliable, the slope of error is calculated taking into account the last 5 seconds.

An example of the control dynamics obtained is reported in figure 4.43. At first stages, the FF controller supply to peltier cells a current higher than the optimal value, to improve the speed of response. Afterward, when the measured sample temperature is close to the set point (i.e. $T_{sample} - T_{setpoint} < 3°C$), the control algorithm shifts to FB, to smoothly reach the imposed temperature.
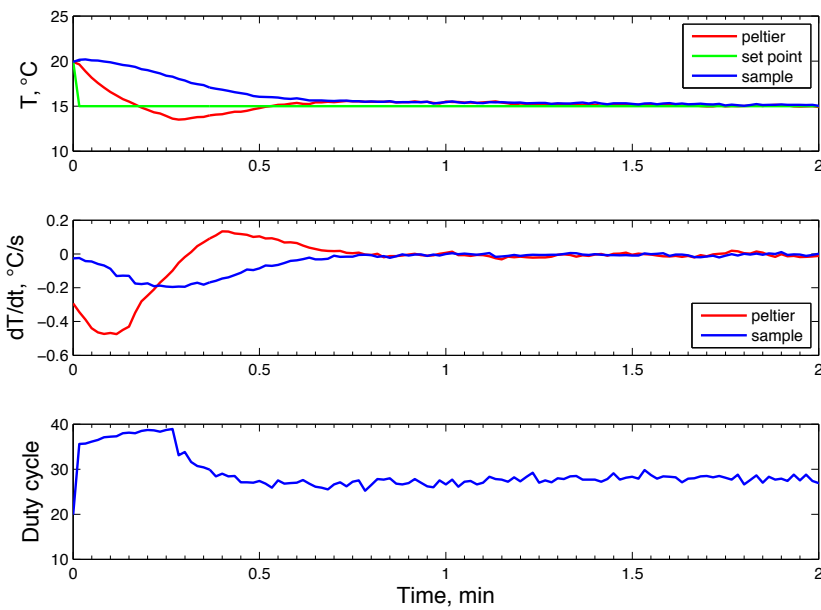
Figure 4.43: Example of FF-FB control for a $-5°C$ step on temperature. Top: measured temperatures and imposed set point; Middle: cooling rates achieved; Bottom: duty cycle imposed by the controller

Bibliography

V. Brucato, S. Piccarolo, and V. La Carrubba. An experimental methodology to study polymer crystallization under processing conditions. The influence of high cooling rates. *Chemical Engineering Science*, 57:4129–4143, 2002.

V. Brucato, Z. Kiflie, V. La Carrubba, and S. Piccarolo. The continuous cooling transformation (CCT) as a flexible tool to investigate polymer crystallization under processing conditions. *Advances in Polymer Technology*, 28(2):86–119, 2009.

V. P. Isachenko, V. A Osipova, and A. S. Sukomel. *Heat transfer*. MIR, 1987.

Y. Kraftmakher. Simple experiments with a thermoelectric module. *European Journal of Physics*, 26:959–967, 2005.

R. T. Martorana. Thermoelectric temperature control of instrumentation - A sample design. *IEEE Transactions on Industrial Electronics and Control Instrumentation*, 22(1):69–75, 1975.

D. Mitrani, J. A. Tome, J. Salazar, A. Turo, M. J. Garcia, and J. A. Chavez. Dynamic measurement system of thermoelectric module parameters. In 22nd *International Conference on Thermoelectrics*, pages 524–527, 2003.

R. Palacios, A. Arenas, R. R. Pecharroman, and F. L. Pagola. Analytical procedure to obtain internal parameters from performance curves of commercial thermoelectric modules. *Applied Thermal Engineering*, 29:3501–3505, 2009.

J. L. Perez-Aparicio, R. Palma, and R. L. Taylor. Finite element analysis and material sensitivity of peltier thermoelectric cells coolers. *International Journal of Heat and Mass Transfer*, 55:1363–1374, 2012.

D. M. Rowe. *CRC Handbook of Thermoelectrics*. CRC Press, 1995.

G. Stephanopoulos. *Chemical Process Control: An Introduction to Theory and Practice*. Prentice Hall, 1984.

5 Cloud point results

The turbidity measurement apparatus discussed in the previous chapter was employed for measuring cloud points of PLLA-dioxane-water solutions. The cloud points were detected following two different protocols: slow and fast cooling experiments.

The slow cooling experimental protocol allows one to measure a "quasi-equilibrium" or "isothermal" cloud point: the sample is cooled stepwise, with a step amplitude of $1°$C and with a step time during at least 1 minute, until a decrease in transmitted light is detected. After the onset of light transmittance decrease, the sample is reheated stepwise until the solution becomes completely homogeneous. Then, the cooling protocol is repeated twice or more, to ensure the results reproducibility.

The fast cooling produces a sort of "dynamic" cloud point. As a matter of fact, by imposing a relatively wide temperature step to the sample, the onset of light transmittance decrease occurs at a temperature lower than in the previous case (i.e. quasi-equilibrium transition temperature). The sample experiences a variable cooling rate, a condition similar to the common practice in membrane production, where a homogeneous solution sample is immersed into a thermostatic bath. As both temperature and turbidity vary with time, the cloud point must be univocally defined, to be derived from experimental data.

It should be however underlined that the data presented in this chapter are preliminary results only, to be further validated. The reason is related to some experimental issues concerning the interactions between the analyzed solutions and the sample vial, that still have not been fixed: presumably, a small amount of the plasticizers of the O-rings rubber diffused into the solution, thus affecting phase equilibria. As a matter of fact, after one experimental run, the sample often appeared visibly yellowing. The possible solutions of this issue are also argued.

Although the moderate solution contamination compromised an absolute determination of the cloud point, the general suitability of the experimental apparatus designed on purpose and of the protocols adopted are not prejudiced. This preliminary investigation campaign showed that the apparatus can detect accurately the cloud points and their dependence upon cooling rate and solution composition. Moreover, fast cooling conditions usually not explorable via other methods can be investigated.

5.1 Materials

The polymer examined in this study was the PLLA RESOMER® L 209 S, purchased from Boehringer-Ingelheim (inherent viscosity 3 dl/g). This polymer has been utilized in laboratory practice for a relatively long time, so that it was already characterized by other operators of the research group which hosted the present work. For the sake of completeness, a set of relevant data determined out of the present thesis are reported here.

By means of Differential Scanning Calorimetry (DSC), the glass transition and fusion temperature were determined. The heating curve of PLLA pellets is reported in figure 5.1. The glass transition temperature is about $T_g = 80°C$, whereas the melting temperature is $T_m = 188°C$.
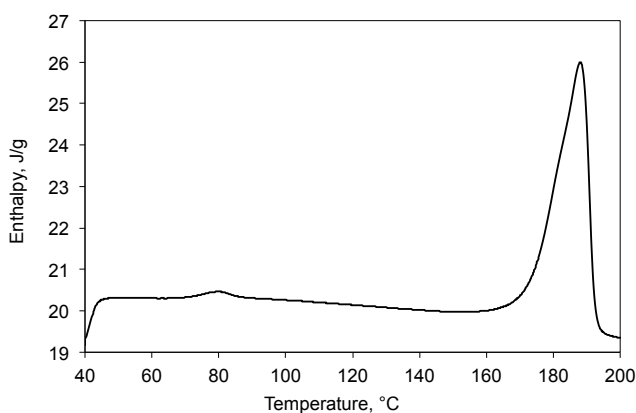
Figure 5.1: DSC heating curve of PLLA pellets

An estimate of weight-average molecular weight was attained via intrinsic viscosity measurements, by using Mark-Houwink parameters from [Garlotta, 2002]. The as-obtained M_w was 114500.

The solvents employed were deionized and osmotized water and 1-4 dioxane (used without further purifications).

The solutions analyzed were prepared by firstly dissolving the polymer in dioxane, and then adding the water. The amount of solvents and polymer to mix were fixed to obtain a certain polymer weight fraction and a known dioxane/water weight ratio (89/11 and 87/13). To double-check the polymer concentration, a quota of the solution was taken back and poured into an open vessel to promote solvents evaporation. The weight of dry polymer and of the starting solution were then compared to verify the actual polymer concentration in solution.

5.2 Detection of liquid solidification

A simple validation of the apparatus capabilities was carried out by analyzing the phenomenon of solidification of pure liquids. For those tests, the same molecular solvents, water and dioxane, were studied. When cooling a pure liquid, at the solidification point the temperature holds a constant value until the sample is fully solidified, whereas the light transmittance should exhibit a parallel decrease, owing to the light scattering induced by solid crystals.

Results for a continuous cooling of a water sample is reported in figure 5.2. The solidification temperature is 0°C, but the sample experiences an undercooling to overcome the energy barrier for the crystal formation. When crystals start to nucleate, the sample temperature jumps to the thermodynamic solidification temperature; then, the sample is rapidly fully crystallized and the temperature decreases further. Contemporarily to the solidification onset, the light transmittance jumps down abruptly, owing to the movement of the crystallization front in the sample volume.

The same considerations can be argued when referring to dioxane (see figure 5.3).
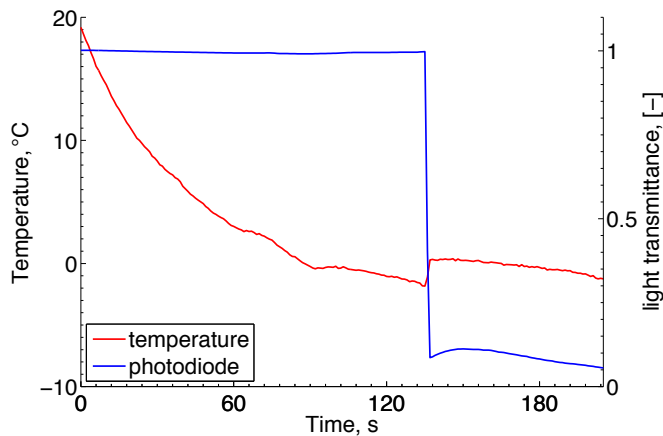
Figure 5.2: Detection of water solidification point via turbidimetry. The light transmittance abruptly decreases in correspondence to the liquid crystallization
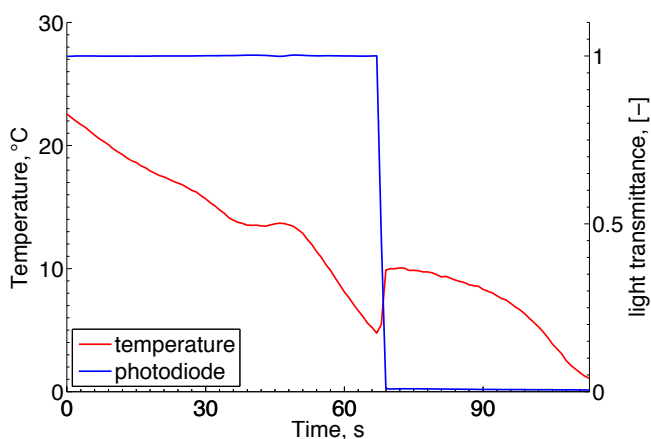
Figure 5.3: Detection of dioxane solidification point via turbidimetry. The light transmittance abruptly decreases in correspondence to the liquid crystallization

5.3 "Quasi-equilibrium" or "isothermal" cloud point

The "quasi-equilibrium" or "isothermal" cloud point was measured by cooling stepwise the polymer solution. An example of cloud point detection is shown in figure 5.4, where a stepwise diminution in temperature induces a simultaneous decrease in light transmittance.

If the solution is cooled farther, the light transmittance will decrease accordingly. Figure 5.5 shows an example of double-step cooling; the time instant $t = 0$ in figure 5.5 corresponds to $t = 60$ s of figure 5.4. During the second cooling, the transmitted light decreases faster than in the first step. This behavior is probably related to two different aspects: the increase of driving force for phase separation and the presence of already formed nuclei.

A multi-step cooling assay is showed in figure 5.6, where the step duration is 1 minute. The former two steps do not produce any detectable phase separation phenomenon. Afterwards, going from 43°C to 42°C, the transmitted light starts to decrease, suggesting that 42°C is the cloud point temperature for the considered solution. The successive step, at $t = 4$ min, produces a faster decrease of transmitted light, probably related to a faster phase separation kinetics. In successive coolings, the transmitted light decreases further, but gradually reducing in amplitude.

An open issue encountered in measurements was the reproducibility of detected cloud point temperatures. By carrying out multiple measurement runs on the same sample, or even by replacing the sample, slight differences on the measured cloud points (of the order
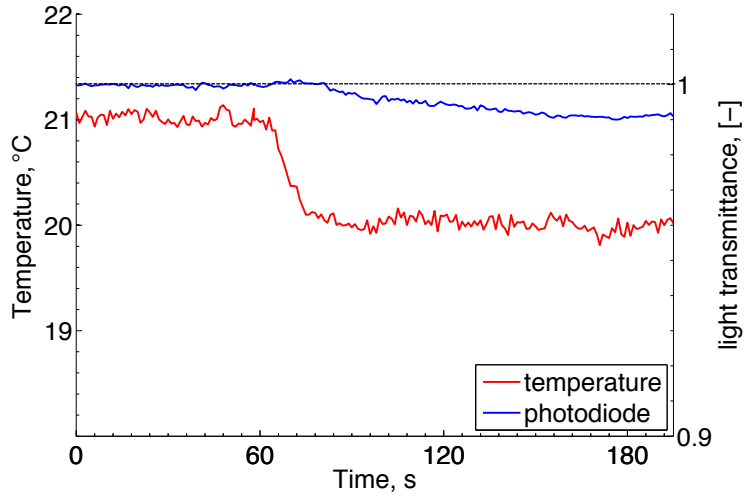
Figure 5.4: Temperature and light transmittance history in a PLLA-dioxane-water solution, showing the onset of turbidity. PLLA 4% wt, d/w=89/11
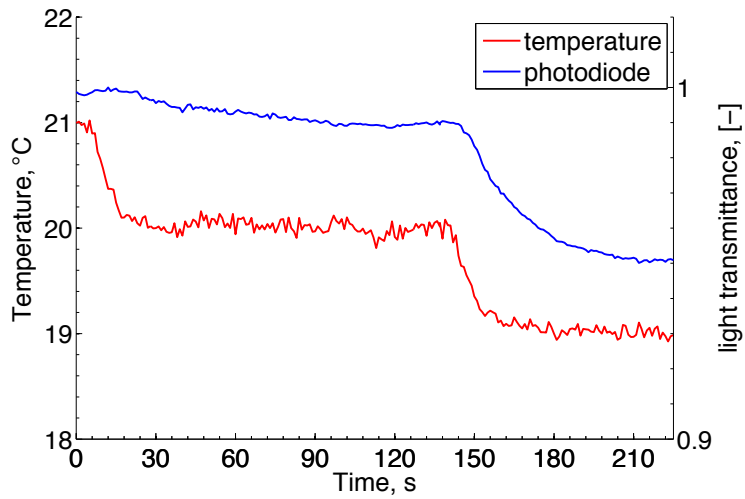
Figure 5.5: Temperature and light transmittance history in a PLLA-dioxane-water solution for a double-step cooling. PLLA 4% wt, d/w=89/11
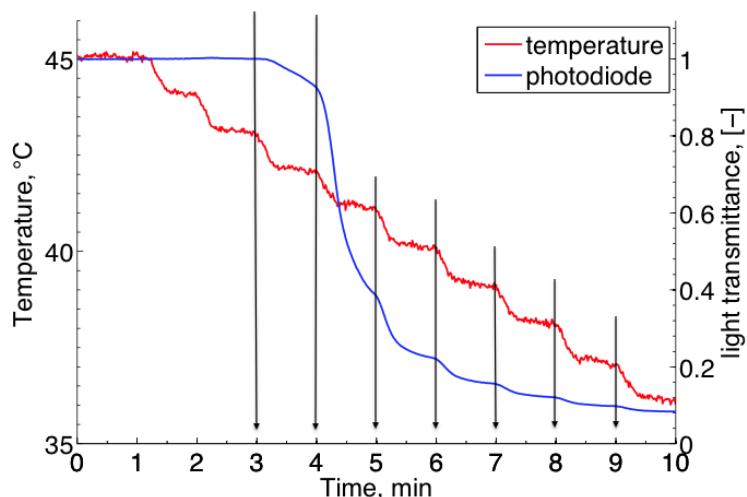
Figure 5.6: Temperature and light transmittance history in a PLLA-dioxane-water solution for a multi-step cooling. PLLA 4% wt, d/w=87/13

of few °C) were registered. Analyzing the system, it is reasonably to argue that the main uncertainty of the measurement apparatus is related to the possible interactions between the solution and the O-ring adopted as sample vial. Probably, the plasticizers contained into the O-ring rubber dissolve into the dioxane, and, conversely, the O-ring could take up dioxane.

This issue was firstly investigated by the immersion of an O-ring into pure dioxane. Two different O-ring materials were considered: the nitrile rubber (NBR), which is the most common material for sealing applications, and the fluorinate rubber (FKM, purchased from Teknofluor Srl). Each sample was inserted into a sealed flask together with the dioxane, and put into an oven at 60°C. After 30 minutes, the NBR O-ring caused a diffused and clearly visible yellow coloration of dioxane, whereas the FKM O-ring caused a slightly perceptible darkening of dioxane. Moreover, both O-rings were visibly swollen: the thickness increased and the inner diameter was comparable to the outer diameter of a pristine O-ring. All things considered, the O-rings can influence the solution composition, by absorbing dioxane and by releasing plasticizers into the solution.

To minimize these side effects, a pretreatment was adopted, consisting in the immersion of O-rings into a dioxane/water solution with the same concentration of the polymer solution to be analyzed, and heating into an oven at 60°C for 30 minutes. After this treatment, the O-ring was taken from the solution and assembled with the glass slides, without any

drying step. By considering the low polymer concentrations analyzed, the O-ring should be already close to equilibrium with the polymer solution, thus the dioxane uptake into the O-ring can be avoided. Moreover, the solution yellowing after the test run was not noticed. However, by applying this method, the measured cloud points were in the range of those measured without the O-rings pretreatment.

A summary of the cloud points measured is reported in figure 5.7. The results are in line with those reported in other works for the PLLA-dioxane-water system Tanaka et al. [2006], Tanaka and Lloyd [2004], Hua et al. [2002], van de Witte et al. [1996]: the cloud point increases when increasing the polymer or water concentration, and the measured temperatures are qualitatively in agreement. The differences in the quantitative values of cloud point temperatures are related to the average molecular weight and distributions of the considered polymer, which influence the phase equilibria, as discussed in the modeling part (Chapter 3).
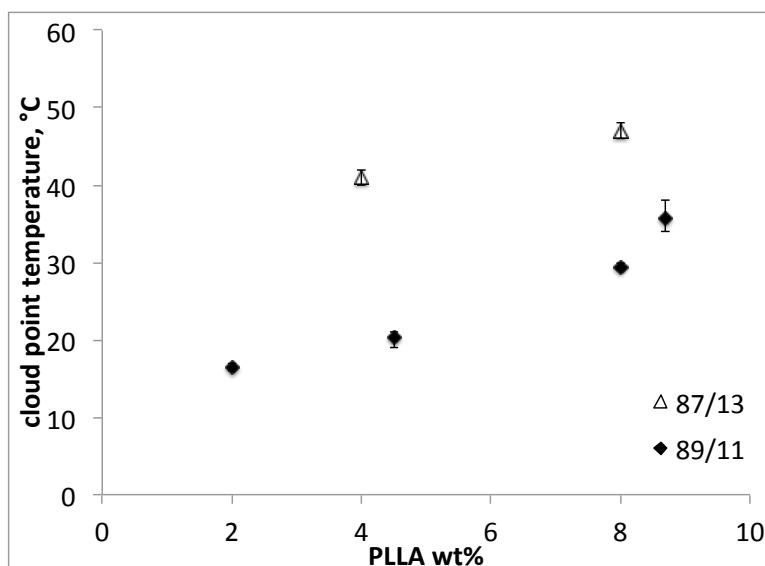
Figure 5.7: Cloud point temperatures measured for the PLLA-dioxane-water system at fixed dioxane/water concentration

5.4 "Dynamic" measure of cloud point

The turbidity measurement apparatus allows one to investigate the dependence of cloud point on cooling rate. When the solution was cooled rapidly (up to $1.7°C/s$), the measured

cloud point temperature was always lower than "isothermal" one. Polymeric systems are sensitive to the cooling rate, e.g. the crystallization from the melt gives out lower crystallinity values by increasing the cooling rate, owing to the time needed by the polymer chains to organize themselves into ordinate crystals. In the case of phase separation, a similar effect can be hypothesized.
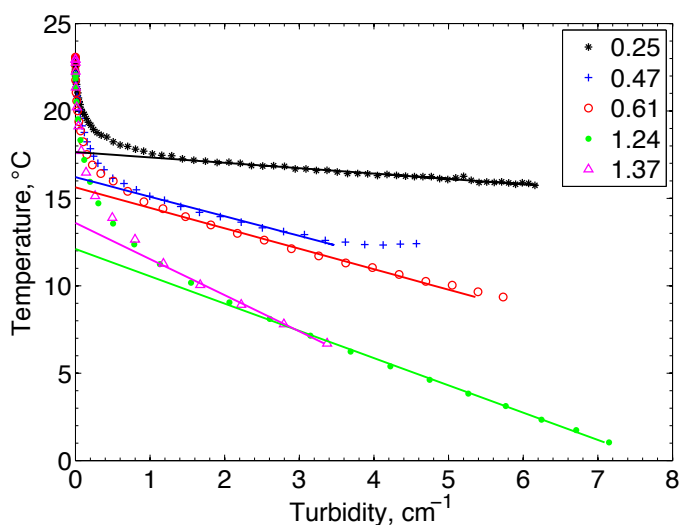
Figure 5.8: Measured turbidity and temperature at various maximum cooling rates (as defined in section 4.7, expressed in °C/s), PLLA 4% wt, d/w 89/11

In polymer science, the phase transitions are often dependent on the scanning rate. For example, the glass transition, melting and crystallization temperature of a polymer are strictly related to the time scale of the experimental (i.e. the rate). As regards to glass transition temperature (T_g), the cooling rate usually employed is $\dot{T} = 10°C/min$: obviously, it is not a quasi-static measurement, but the main aspect taken into account is the relation between the experimental time and the characteristic time of structure reorganization. On the other hand, crystallization (T_c) and melting (T_m) temperature are also related to the cooling/heating rate experienced by the sample. As a general rule, both T_c and T_m are influenced by the crystal size, and the equilibrium value (i.e. $T_c = T_m$) is usually extrapolated by means of Hoffman-Weeks plots [Gedde, 1995]. In the case of crystallization under fast cooling, the polymer density (or its logarithm) showed a linear dependence on the logarithm of cooling rate [Van der Beek et al., 2005, La Carrubba et al., 2004, 2000]. Even though liquid-liquid phase separation in polymer solutions and solid-liquid phase sep-

aration in polymer melts (i.e. crystallization) are two different and distinct processes, they are likely to show similar features in relation to the cooling rate influences. Both are phase separation processes, and the formation of a new phase involves characteristic energies and times for the set-in of the separated domains.

When a polymer solution is continuously cooled, the onset of turbidity is initially gradual (not stepwise), then soon afterwards the transmitted light decreases rapidly. In this case, the cloud point was not related to the onset of turbidity, as it is often difficult to be individuated, but drawn by data extrapolation (see figure 5.8). The zone where the turbidity increases rapidly can be fitted with a straight line: the intercept at zero turbidity is assumed to be the cloud point temperature. Obviously, the extrapolation depends on the number of data considered for fitting, thus this procedure must be improved to get precise estimates of cloud point.

The extrapolated cloud point temperature vs cooling rates is showed in figure 5.9, for a PLLA-dioxane-water solution at different compositions. The straight lines are least squares fittings: by plotting in linear scale (figure 5.9a), the intercepts at $dT/dt = 0$ are always lower than "isothermal" cloud point. Lee et al. [1992] reported similar results for binary solutions of isotactic polypropylene in various dialkyl phthalates: at a very low cooling rate ($0.5°C/min$) the measured cloud point temperature deviated from the linear relation drawn at higher cooling rates (2 and $10°C/min$). Although one can expect that when the cooling rate tends to zero the cloud point should attain the equilibrium value, in principle the two measurement routes are not comparable: the quasi-static measurement, where the sample is stepwise cooled and held for a certain time, is intrinsically different from the continuous cooling one.

A schematic of the temperature-composition history for both cooling protocols is showed in figure 5.10. In the case of stepwise cooling (figure 5.10a), the solution is brought to an unstable state and the composition of separated phases moves gradually towards the equilibrium values, i.e. on the binodal line. In this case, the nucleation and growth kinetics is related to the temperature of the system. On the other hand, if the solution is continuously cooled (figure 5.10b), the separated phases do not reach the equilibrium compositions, as the distance from the binodal line increases with time. The cloud point thus appears when the domain size is detectable, and it does not necessarily occurs when the equilibrium curve is just entered.

By plotting the cooling rate in a semi-logarithmic scale, the results are still well approximated by straight lines (figure 5.9b). The choice of a semilogarithmic scale is not arbitrary: the density of cooled melt is usually correlated by a linear relation with the logarithm of cooling rate [Van der Beek et al., 2005, La Carrubba et al., 2000]. Nevertheless, this data
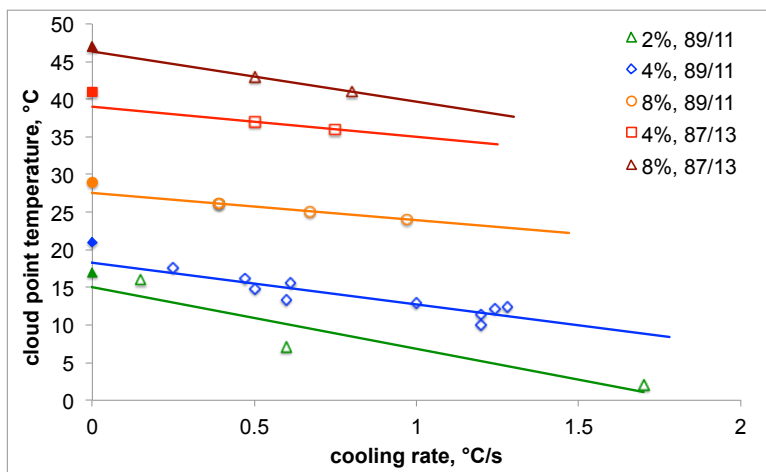
(a) Linear scale
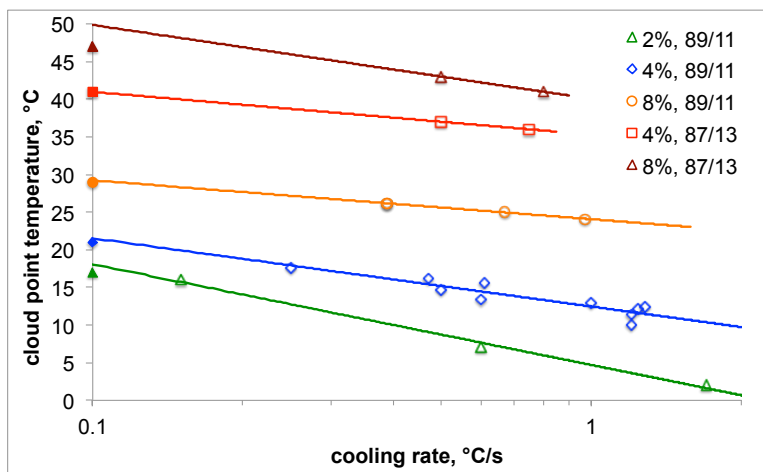
(b) Log scale

Figure 5.9: Measured cloud points in relation to the maximum cooling rate experienced by the sample, PLLA-dioxane-water system. Closed symbols are the "isothermal" cloud points

representation does not allow one to extrapolate the cloud point value at $\dot{T} = 0$: the maximum cooling rate reached in "quasi-equilibrium" measurements was about $\dot{T} = 0.1°C/s$, thus the intercept was assumed to be at that coordinate. With this data representation, the extrapolations at low cooling rate are in a good agreement to experimentals, for the examined system. A similar approach is followed in the description of polymer melt apparent viscosity as a function of shear rate ($\dot{\gamma}$): at high $\dot{\gamma}$ values, the apparent viscosity decreases linearly with $\log \dot{\gamma}$, whereas for low $\dot{\gamma}$ values the apparent viscosity is constant. In principle, the value of apparent viscosity for $\dot{\gamma} = 0$ cannot be extrapolated: however, the plateau value is taken as the zero shear data.

(a) Two cooling steps, from Song and Torkelson [1995]

(b) Continuous cooling, from Rullmann and Alig [2004]
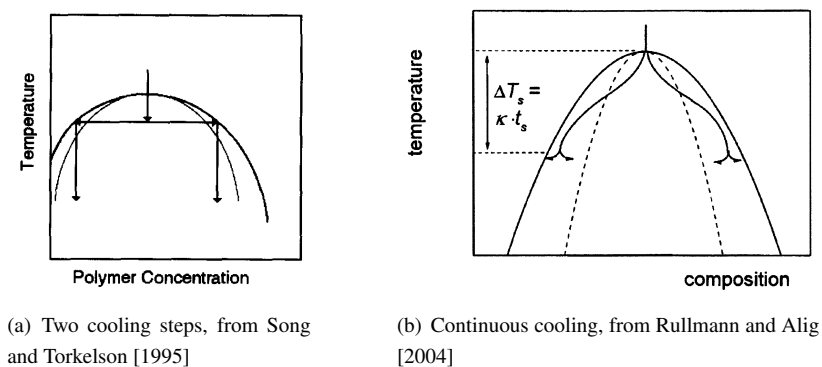
Figure 5.10: Schematic composition path of TIPS processes

Another kinetic effect recorded was the increase of cloud point upon heating. When heating a demixed solution, it became clear at a temperature higher than the cloud point detected upon cooling. Examples of this hysteresis-like phenomenon are reported in figure 5.11. These results are similar to the behavior of polymer melts (see figure 5.12), for which the crystallization temperature (measured upon cooling the molten sample) is usually lower than the melting temperature (measured upon heating the crystallized sample). The PVT curves (figure 5.12a) show a similar shape with those obtained via turbidimetry: a parallelism can be hypothesized for the pairs density-crystallinity and turbidity-demixing (liquid-liquid). The crystal nucleation and growth reduces the specific volume of the polymer, as the liquid domains nucleation and growth reduces the transmitted light through the solution. When considering DSC data (figure 5.12b), a qualitative similarity can be noticed between the heat released/absorbed and the variation of light transmittance with temperature (see figure 5.13). This analogy is only qualitative and has not been thoroughly examined from a theoretical point of view. However, the dynamic data of light transmittance showed in figure 5.13 allow an alternative way to recognize and extrapolate the cloud

point temperature in continuous cooling experiments. A similar result can be detected by using a dynamic light source, e.g. a sinusoidal wave.

(a) $\dot{T}_{max} = 0.4°\text{C/s}$

(b) $\dot{T}_{max} = 0.8°\text{C/s}$
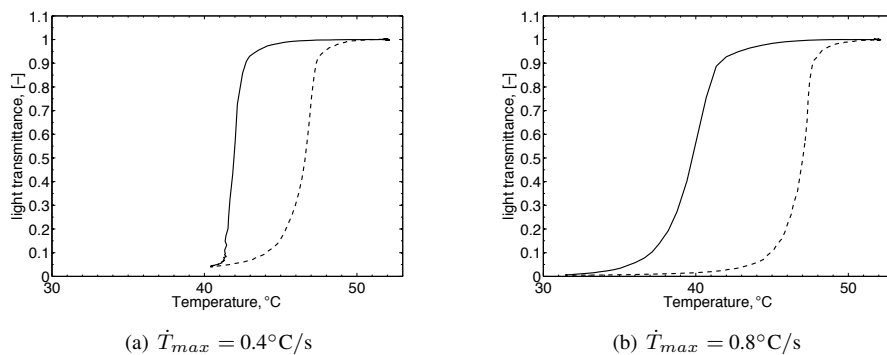
Figure 5.11: Light transmittance patterns for a sample cooled and then reheated. Bold line: cooling. Dashed line: heating. PLLA-dioxane-water solution, PLLA 8% wt, d/w 87/13
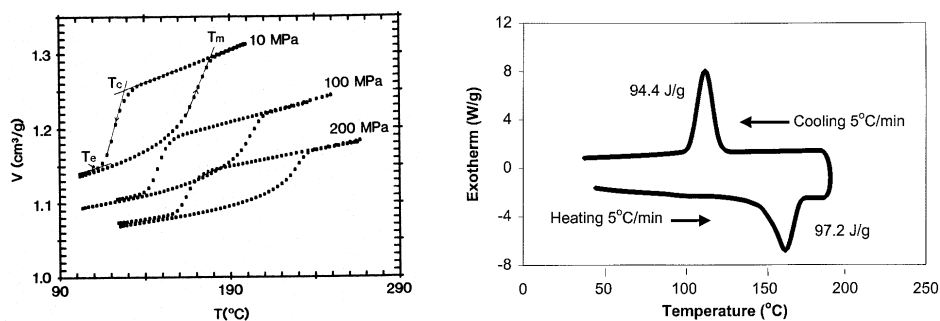
(a) PVT data, from He and Zoller [1994]. The heating/cooling rate is $2.5°C/min$

(b) DSC data, from Sperling [2006]

Figure 5.12: Crystallization an melting patterns of polypropylene

5.5 Conclusion

The preliminary results obtained with the self built experimental apparatus showed the versatility of measurement device for detecting cloud point temperatures in polymer solutions.

After assessing the experimental protocol, an accurate detection of cloud point curves can be carried out, with an adequate combination of compositions to be analyzed, e.g. at
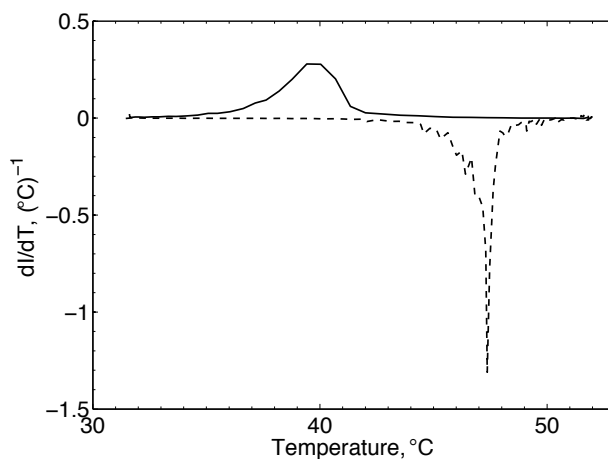
Figure 5.13: Derivative of light transmittance upon temperature for a sample cooled and then reheated ($\dot{T} = 0.8°\text{C/s}$). Bold line: cooling. Dashed line: heating. PLLA-dioxane-water solution, PLLA 8% wt, d/w 87/13

least three polymer concentrations (2, 4 and 8% wt) and three solvents weight ratios (85/15, 87/13 and 89/11). With a similar set of data, a tuning of model parameters can be worked out, on the basis of the procedure showed in Chapter 3, thus deriving a complete phase diagram of the system.

The influence of cooling rate on cloud point can be thoroughly investigated, as this aspect is of primary importance in practical TIPS applications. As a matter of fact, when preparing porous membranes via TIPS, the homogeneous solution is subjected to a cooling rate which can affect the onset of phase separation and thus the microstructure obtained. A better insight of the cooling rate influence on phase separation would be useful in the design of innovative TIPS protocols. Moreover, by reaching high cooling rates, a discrimination between binodal and spinodal zones could be likely attained.

The turbidity measurement apparatus can also be upgraded to enhance the characterization capabilities of the instrument. For example, the use of sapphire windows will improve the heat transfer issues, thus offering the possibility to explore higher cooling rates (i.e. $\dot{T} = 10 \div 100°\text{C/s}$). Moreover, the apparatus can be equipped with supplementary light detectors, in order to measure light scattering during phase separation. Light scattering data would improve the kinetic features characterization, e.g. the separation mechanisms (nucleation and growth, spinodal decomposition) and the domains growth rate.

Bibliography

D. Garlotta. A literature review of poly(lactic acid). *Journal of Polymers and the Environment*, 9(2): 63–82, 2002.

U. W. Gedde. *Polymer Physics*. Chapman & Hall, 1995.

J. He and P. Zoller. Crystallization of polypropylene, nylon-66 and poly(ethylene terephthalate) at pressures to 200 MPa: Kinetics and characterization of products. *Journal of Polymer Science Part B: Polymer Physics*, 32(6):1049–1067, 1994.

F. J. Hua, G. E. Kim, J. D. Lee, Y. K. Son, and D. S. Lee. Macroporous poly(L-lactide) scaffold 1. Preparation of a macroporous scaffold by liquid-liquid phase separation of a PLLA-dioxane-water system. *Journal of Biomedical Materials Research (Appl Biomater)*, 63:161–167, 2002.

V. La Carrubba, V. Brucato, and S. Piccarolo. lsotactic polypropylene solidification under pressure and high cooling rates. a master curve approach. *Polymer Engineering and Science*, 40(11):2430–2441, 2000.

V. La Carrubba, V. Brucato, and S. Piccarolo. The use of master curves to describe the simultaneous effect of cooling rate and pressure on polymer crystallization. *Polymer International*, 53:61–68, 2004.

H. K. Lee, A. S. Myerson, and K. Levon. Nonequilibrium liquid-liquid phase separation in crystallizable polymer solutions. *Macromolecules*, 25:4002–4010, 1992.

M. Rullmann and I. Alig. Scaling behavior of nonisothermal phase separation. *Journal of Chemical Physics*, 120(16):7801–7810, 2004.

S.-W. Song and J. M. Torkelson. Coarsening effects on the formation of microporous membranes produced via thermally induced phase separation of polystyrene-cyclohexanol solutions. *Journal of Membrane Science*, 98:209–222, 1995.

L. H. Sperling. *Introduction to Physical Polymer Science*. Wiley, NJ, 2006.

T. Tanaka and D. R. Lloyd. Formation of poly(L-lactic acid) microfiltration membranes via thermally induced phase separation. *Journal of Membrane Science*, 238:65–73, 2004.

T. Tanaka, T. Tsuchiya, H. Takahashi, M. Taniguchi, H. Ohara, and D. R. Lloyd. Formation of biodegradable polyesters membranes via thermally induced phase separation. *Journal of Chemical Engineering of Japan*, 39(2):144–153, 2006.

P. van de Witte, P. J. Dijkstra, J. W. A. van den Berg, and J. Feijen. Phase behavior of polylactides in solvent-nonsolvent mixtures. *Journal of Polymer Science: Part B: Polymer Physics*, 34:2553–2568, 1996.

M. H. E. Van der Beek, G. W. M. Peters, and H. E. H. Meyer. The influence of cooling rate on the specific volume of isotactic poly(propylene) at elevated pressures. *Macromolecular Materials and Engineering*, 290:443–455, 2005.

Part II

Characterization of membranes and definition of key features

The second part of the thesis is dedicated to a systematic investigation concerning some aspects of heat and mass transfer in a technological application of polymeric porous structures, such as the use of membrane in water purification.

More specifically, the application selected for a more detailed analysis was the desalination via *membrane distillation* (MD). It is a relatively new process, still under development. The literature studies concerning MD are mainly oriented to the optimization of the membrane modules and operating conditions. A small effort was spent so far regarding the production of membranes with properties compatible with the MD requirements in terms of mass and heat transfer performance. As a matter of fact, membranes used in MD application are mainly optimized for different membrane processes, e.g. microfiltration, whose choice is basically related to the pore size required for a valuable MD application.

Phase separation processes, as showed in the first part of the thesis, are employed for the production of microporous membranes: in principle, novel membranes for MD could be prepared via phase separation. Moreover, the properties of PLLA are to a large extent compatible with those demanded to polymeric membranes adopted in MD: a future application of polylactides as membrane materials could be thus plausibly envisaged in a not too far time horizon. By improving the control on the porous microstructure, e.g. achieving membranes with a narrow pore size distribution, with the desired pore dimensions, it is possible to increase the overall performance of the MD technology.

The studies presented in this second part concern an experimental characterization and a simplified modeling approach applied to membranes to be used in MD desalination process. Commercial membranes were selected, as a starting point to scrutinize different properties (such as material type, texture, pore size) and thus deducing the key features related to MD desalination technology. The set of preliminary results attained can be usefully recalled when designing and setting up innovative phase separation routes in the production of membranes for MD.

6 Membrane distillation

Membrane distillation (MD) is an emerging technology for seawater desalination at moderate temperatures and pressures [Li et al., 2008]. This field has been continuously growing in last 20 years, as it allows a lower energy consumption than reverse osmosis processes (RO), together with a higher heat recovery possibility.

MD consists schematically in contacting a hot solution with a hydrophobic membrane, which retains the liquid and allows the diffusion of water vapor through the pores (see figure 6.1). The membrane acts only as a physical interface between the two phases, the liquid solution and the vapor. The driving force for mass transfer is the difference in vapor pressure between the feed side and the permeate side [Schofield et al., 1987]. The feed temperature is usually $40 < T_f < 80°$C, thus a relatively low energy consumption can be achieved. As the processing solution is not boiling, a consistent energy saving is offered, and the heat released by permeate condensation can be recovered within the process. This feature makes MD very attractive in the purification of solutions affected by thermal instability, e.g. beverages and pharmaceuticals. MD was adopted for the concentration of fruit juices [Gunko et al., 2006, Jiao et al., 2004, Calabrò et al., 1994], bovine serum [De Zarate et al., 1998], non-volatile acid solutions [Tomaszewska et al., 1995], oil-water emulsions [Gryta and Karakulski, 1999] and sucrose solutions [Al-Asheh et al., 2006]. Another application of MD is the removal of volatile compounds from aqueous solution [Sarti et al., 1993], e.g. benzene [Banat and Simandl, 1996], benzene and toluene [Wu et al., 2005], chloroform [Urtiaga et al., 2000], ammonia [El-Bourawi et al., 2007, Ding et al., 2006], arsenic [Qu et al., 2009], isopropanol [Lee and Hong, 2001], propanone [Banat and Simandl, 2000], acetone-butanol-ethanol [Banat and Al-Shannag, 2000].

Another advantage of MD is the relatively low operating pressure: as a matter of fact, the evaporation and permeation are spontaneous processes and do not need any external pressure imposed; on the other hand, RO operations require very high pressure to drive the solvent flux. However, in some cases a vacuum pressure can be applied to permeate side, to enhance the vapor mass transfer.

Even though the technology involved in MD is relatively simple and low cost, the main disadvantage is the relatively low productivity of the process with respect to other mem-

brane operations (e.g. RO): in fact, first applications of MD gave out fluxes around 1 kg/m^{2}s [Weyl, 1967]. This aspect made MD of minor interest in its first 20 years of application (from Sixties to early Eighties), whereas nowadays, an increasing attention is payed to MD, as vapor fluxes up to 71 kg/m^{2}s were achieved [Li and Sirkar, 2005]. Moreover, the technology development offered a vaste latitude of methods for energy saving and recovery. For example, solar energy can be used to generate the heat needed for the process [Chang et al., 2010, Chen and Ho, 2010, Blanco Galvez et al., 2009, Al-Obaidani et al., 2008, Ding et al., 2005, Koschikowsky et al., 2003, Banat et al., 2002, Hogan et al., 1991].
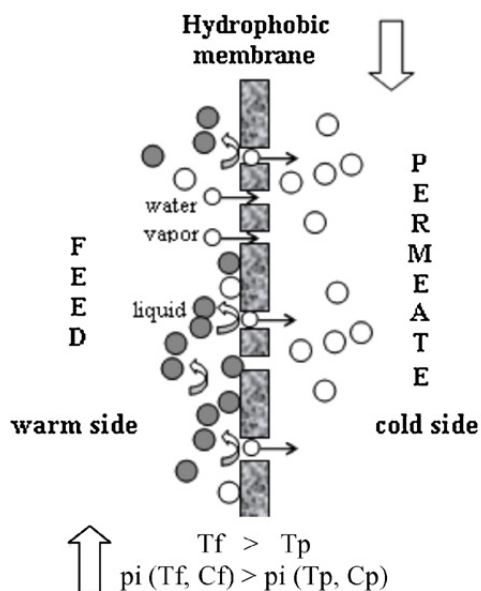
Figure 6.1: Schematic of membrane distillation principle, from Susanto [2011]

A promising application of MD is the water desalination. As the solution to be treated must not have strict properties, e.g. solute concentration, a wide range of not potable waters can be purified into drinking products: seawater [Al-Obaidani et al., 2008, Xu et al., 2006b, Hanemaaijer et al., 2006, El Amali et al., 2004, Hsu et al., 2002, Ohta et al., 1990, Kubota et al., 1988, Carlsson, 1983], brackish water [Termpiyakul et al., 2005], wastewater and industrial downstreams [Gryta et al., 2006, Calabrò et al., 1991] and also concentrated brines released by other desalination operations (e.g. RO) [Ji et al., 2010, Riziero Martinetti et al., 2009, Macedonio et al., 2007, Drioli et al., 2006, 1999, Godino et al., 1997].

Although studies on MD are increasing in time [Li et al., 2008], they are almost dedi-

cated to the determination of the best operating conditions for a determined configuration: more specifically, membranes used in MD are mainly optimized for other operations, e.g. microfiltration. Few studies focus the determination of membrane key features [Zhang et al., 2010] and the preparation of membranes *ad hoc* for MD processes [Tang et al., 2010, Bonyadi and Chung, 2007, Li and Sirkar, 2005, Bottino et al., 2005].

6.1 Configurations

For all MD applications, the hot solution is in direct contact with the membrane. Process performances are strongly affected by the vapor recovery technique, as it influences mass and heat transfer. Various technologies are available to arrange the vapor recovery from the permeate side: most used are the direct contact of the membrane with liquid distillate or an air gap between the membrane and a cooling liquid; other possibilities are the use of a sweeping gas or vacuum. Depending on the permeate recovery technique, membranes must have specific properties. An overview of main arrangements used is presented.

Direct Contact Membrane Distillation (DCMD)   In Direct Contact Membrane Distillation (DCMD) [Song et al., 2007, Cheng et al., 2008], cold liquid distillate is in contact with the membrane permeate side (figure 6.2). The temperature difference between hot feed and cold distillate generates the vapor pressure gradient, which drives the MD process. The permeate vapor condenses directly into the product stream. This configuration is the most widely studied [Li et al., 2008], as it is the easiest to be arranged. DCMD is the preferred configuration when the major permeate component is the solvent (e.g. water recovery from downstreams and aqueous solutions of non-volatile compounds).

However, the main disadvantage is the significant heat loss by the feed stream, owing to the high heat transfer coefficient of the flowing cold distillate.

Air Gap Membrane Distillation (AGMD)   In Air Gap Membrane Distillation (AGMD) [Feng et al., 2008], a condensing plate is placed close to the membrane (figure 6.3). The permeate vapor diffuses through the air gap, condensates on the cold surface and it is then collected. This application is best suited for the removal of volatile compounds, as the permeate fluid does not lap the membrane surface.

The AGMD was introduced to limit heat loss from feed to permeate side [Banat and Simandl, 1994, 1998, Liu et al., 1998]. However, the stagnant air film will lower the mass transfer, thus reducing vapor flux. A modified AGMD configuration was proposed

by Chouikh et al. [2005], consisting in inducing air movement into the gap by a temperature difference imposed externally. This configuration resulted in a slight enhancement of vapor flux.
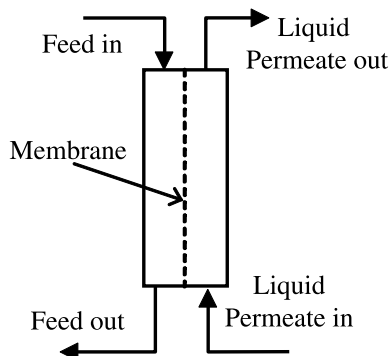
Figure 6.2: Schematic of Direct Contact Membrane Distillation (DCMD), from Li et al. [2008]
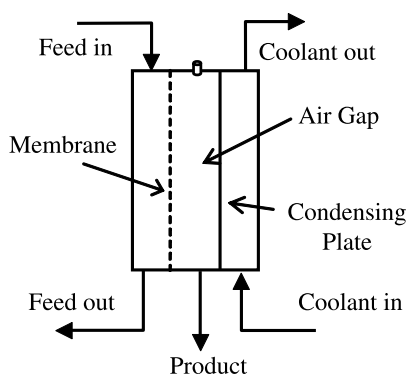
Figure 6.3: Schematic of Air Gap Membrane Distillation (AGMD), from Li et al. [2008]

Sweeping Gas Membrane Distillation (SGMD)   Sweeping Gas Membrane Distillation (SGMD) consists in removing vapor from permeate side with a non-condensing gas (e.g. dry air) [Khayet et al., 2000a,b, 2003]. In this case, vapor is condensed out of the MD module, in an external heat exchanger (figure 6.4). This configuration links the advantages of DCMD with those of AGMD: the sweeping gas enhances mass transfer and lowers the heat loss.

While this configuration gives higher vapor fluxes than those achieved with AGMD, the main disadvantage is the energetic load on the external heat exchanger.

The main parameters affecting vapor flux are the water temperature and the sweeping gas velocity, whereas the feed water velocity does not influence the process performances [Khayet et al., 2000a].
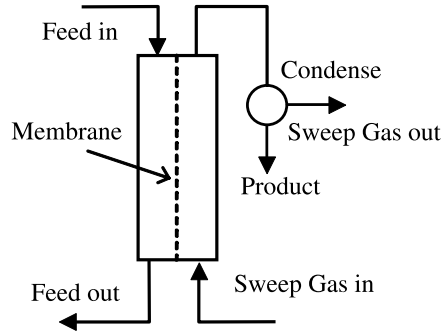
Figure 6.4: Schematic of Sweeping Gas Membrane Distillation (SGMD), from Li et al. [2008]
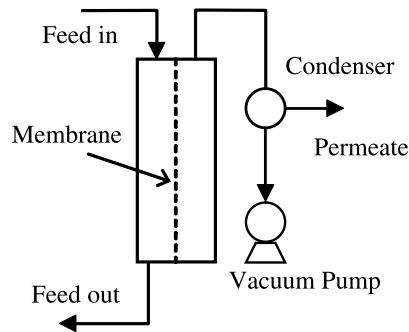
Figure 6.5: Schematic of Vacuum Membrane Distillation (VMD), from Li et al. [2008]

Vacuum Membrane Distillation (VMD)   In Vacuum Membrane Distillation (VMD), the permeate side is maintained at a pressure lower than water vapor pressure at the operating temperature [Bandini et al., 1992, 1997, Mengual et al., 2004, Safavi and Mohammadi, 2009, Mericq et al., 2009]. In this way, vapor is removed and can be condensed out of the MD module (figure 6.5).

In VMD, the main parameter affecting vapor flux is the vacuum pressure, whereas the least influent is the liquid flow rate [Mohammadi and Safavi, 2009]. Banat et al. [2003]

predicted a linear dependence of vapor flux upon permeate pressure, where the slope depends on the heat transfer coefficient of the liquid phase. Moreover, higher heat transfer coefficients gave out larger fluxes. Wu et al. [2007] measured a linear dependence of vapor flux on vacuum pressure, feeding pure water in a hollow fiber module.

Vacuum Sweeping Gas Membrane Distillation   Xu et al. [2006a] proposed a SGMD configuration where the air flux was induced by a sub ambient pressure in permeate side of the MD module. A tubular module was tested in this configuration, Vacuum Sweeping Gas Membrane Distillation (VSGMD), showing that one of the advantages is the no need of an external condenser for water recovery.

6.2 Modeling of mass transfer

Mass transfer in membrane distillation is affected by various factors: however, the main important features are membrane properties and process configuration. For all cases considered, the driving force for mass transfer is the vapor pressure difference between feed and permeate side, so that the vapor flux can be generally expressed as [Lawson and Lloyd, 1997]:

$$N = k_P \Delta P^0 \tag{6.1}$$

where ΔP^0 is the vapor pressure difference between feed and permeate side and k_P is the mass transfer coefficient. This latter is strictly related to membrane properties (e.g. pore size, porosity, tortuosity) and operating conditions (e.g. temperature and pressure).

The vapor permeation through a porous membrane can occur following three different mass transfer mechanisms [Li et al., 2008]:

1. Knudsen diffusion

2. molecular diffusion

3. viscous flow

Depending on operating conditions and membrane properties, one or more combined mechanisms must be considered. A way to determine if Knudsen or molecular diffusion take place is the estimate of Knudsen number:

$$\mathrm{Kn} = \frac{\lambda}{d} \tag{6.2}$$

where d is the (average) pore diameter and λ is the mean free-path of vapor molecules, calculated as:

$$\lambda = \frac{RT}{\sqrt{2}\pi\sigma^2 P_w^0 N_A} \tag{6.3}$$

where σ is the collision diameter, P_w^0 is the vapor pressure and N_A is the Avogadro number.

If Kn>1, Knudsen diffusion is the mass transfer mechanism. Conversely, if Kn<0.01, molecular diffusion is taken as mass transfer mechanism. For 0.01<Kn<1, both contributions must be considered, and the flow mechanism considered is named Knudsen-molecular diffusion transition.

Knudsen diffusion   When the mean free-path of molecules is higher than pore diameter, i.e. mass transfer is due to particle-wall collisions, the Knudsen diffusion model is used. The mass transfer coefficient can be estimated as [Lawson and Lloyd, 1997]:

$$k_P^k = \frac{2\epsilon r}{3\tau}\sqrt{\frac{8RT}{\pi M}}\frac{M}{RT}\frac{1}{\delta} \tag{6.4}$$

where ϵ is the membrane porosity, τ the pore tortuosity, δ the membrane thickness, r the pore radius, M the molecular weight of vapor molecules.

Molecular diffusion   Molecular diffusion is related to collisions between molecules, and mass transfer coefficient can be calculated as [Lawson and Lloyd, 1997]:

$$k_P^d = \frac{\epsilon}{\tau}\frac{P}{\bar{P}_a}D_{ij}\frac{M}{RT}\frac{1}{\delta} \tag{6.5}$$

where P is the pressure, $\bar{P}_a$ the mean air pressure and D_{ij} the water vapour diffusivity in air.

The PD_{ij} term, for the air-water system, can be estimated as [Li et al., 2008]:

$$PD_{ij} = 1.895 \cdot 10^{-5}\ T^{2.072} \tag{6.6}$$

where the resulting PD_{ij} is expressed in Pa·m^2/s.

Viscous flow   This model takes into account the effects of vapor viscosity on mass transfer, considered as continuum instead of diffusive. Usually this model depicts liquid flow, but in vacuum operations this mass transfer mechanism becomes important. The mass transfer coefficient is expressed as [Lawson and Lloyd, 1997]:

$$k_P^v = \frac{\epsilon r^2}{8\tau} \frac{\bar{P}_w}{\mu} \frac{M}{RT} \frac{1}{\delta} \tag{6.7}$$

where μ is the vapor viscosity and $\bar{P}_w$ the mean water vapor pressure inside the pores.

6.2.1 Mass transfer in DCMD, AGMD and SGMD

In DCMD, viscous flow is negligible with respect to Knudsen and molecular diffusion. Once given pore dimension of membrane and operating conditions (as temperature and pressure influence the mean free-path), Knudsen number can be estimated. Values of Knudsen number $0.01 < \text{Kn} < 1$ are related to transition region. In this case, these contributions to mass transfer are considered as series resistances:

$$k_P = \left(\frac{1}{k_P^k} + \frac{1}{k_P^d} \right)^{-1} \tag{6.8}$$

As membrane used in MD have pore dimension ranging from 0.1 to 1 μm, and operating temperatures are between 50 and 80°C, frequently $0.01 < \text{Kn} < 1$.

6.2.2 Mass transfer in VMD

When working at low pressures (usually less than 400 mbar), the molecular diffusion can be neglected with respect to Knudsen diffusion ($k_P^d \propto P$). However, the viscous contribution on flow must be considered. Three different transport regions can be defined, referring to Knudsen number [Li et al., 2008]:

1. Kn>10, only Knudsen diffusion;

2. Kn<0.01, only viscous flow;

3. 0.01<Kn<10, Knudsen-viscous transition.

In the latter case, the mass transfer coefficients are computed as parallel resistances:

$$k_P = k_P^k + k_P^v \tag{6.9}$$

A semi-empirical expression for mass transfer coefficient in Knudsen-Poiseuille transition was proposed by Schofield et al. [1990]:

$$k_P = a\tilde{P}^b \tag{6.10}$$

where a is the permeability divided by the membrane thickness, b is a fitting parameter ranging between 0 and 1 which indicates the extent of Poiseuille flow contribution and $\tilde{P}$ is the dimensionless pressure (P/P_{ref}). The b exponent is 0 in case of Knudsen diffusion, 1 in case of viscous flow and $0 < b < 1$ for Knudsen-viscous transition.

6.3 Membrane properties

The membrane features that mainly influence the MD process are:

- material type

- porosity

- pore dimension and tortuosity

- thickness

- liquid entry pressure (LEP)

A short discussion on their influence on MD performance is hereafter provided.

6.3.1 Materials and manufacture

The membrane for water purification via MD must be hydrophobic, to avoid the permeate contamination by the flow of the retentate solution through the membrane pores. By this reason, polymeric membranes used in MD are mainly made of polypropylene (PP), poly-tetrafluoroethylene (PTFE) or polyvinylidene fluoride (PVDF) [Curcio and Drioli, 2005]. Depending on the nature of the polymer, different fabrication techniques are employed to produce microporous membranes. For example, PVDF membranes are mainly made via phase inversion [Hou et al., 2009], whereas PTFE membranes are fabricated via stretching [Kitamura et al., 2000, Huang et al., 2004] or sintering. PP membranes are fabricated via phase inversion [Lin et al., 2009] or stretching.

The fabrication technology determines the resulting membrane morphology. For instance, membranes made via stretching show a fibrous morphology, where the pores are the open spaces between fibers. On the contrary, membranes produced via phase separation techniques show a network of interconnected pores. The performances of a membrane module for water purification are strictly related to the membrane microstructure. For instance, it has been demonstrated that membrane and support morphologies can affect both heat and mass transfer [Zhang et al., 2010].

Very often membranes are multilayer, to reduce thermal conduction and to enhance the mechanical stability. Different arrangements of membrane and support are used, depending on fabrication techniques. In their turn, different arrangements of membrane and support affect the process performances, in terms of heat and mass transfer. Examples are bi-layer membrane (support on membrane) or three-layer (support immersed into two membrane layers) [Mannella et al., 2010].

At present, membranes used in MD have mainly been optimized for microfiltration processes, owing to the relatively recent growth of MD technology. Design of membranes for MD processes can improve substantially the performance of separation and the energy recovery capabilities.

6.3.2 Porosity, pore dimension and tortuosity

Porosity is generally defined as the ratio between void volume (i.e. pores volume) and total membrane volume:

$$\epsilon = \frac{V_p}{V_t} \tag{6.11}$$

As a general rule, by increasing the porosity, the MD flux will increase for all MD configurations [El-Bourawi et al., 2006].

Porosity influences the overall thermal conductivity of the membrane: as a matter of fact, the amount of vapor entrapped inside the pores must be taken into account to estimate the overall thermal conductivity. Two models are mainly used for the determination of the global conductivity: the isostrain (i.e. parallel resistances) and the isostress model (i.e. series resistances). The mathematical expressions are respectively:

$$k_t = \epsilon k_g + (1 - \epsilon) k_m \tag{6.12}$$

$$k_t = \left(\frac{\epsilon}{k_g} + \frac{1 - \epsilon}{k_m} \right)^{-1} \tag{6.13}$$

where k_g and k_m are the thermal conductivities of the entrapped gas and the membrane material, respectively. Usually $k_g < k_m$, thus the overall thermal conductivity can be lowered by increasing the membrane porosity.

Pore dimension of membranes for MD applications ranges from 10^{-1} μm to 1 μm. The lower bound is related to an acceptable vapor flux, whereas the upper bound is related to membrane wetting, i.e. the liquid water flux through the membrane [Lawson and Lloyd, 1997]. This is an undesired phenomenon, as it reduces the separation efficiency.

Membranes usually show a pore size distribution, instead of a single value of pore dimensions. This aspect influences mass transfer: in fact, the mass transport mechanisms are affected by the pore size (see figure 6.6). As showed in section 6.2, depending on the Knudsen number (i.e. pore diameter), Knudsen or ordinary (molecular) diffusion can occur. When modeling, more accurate predictions can be achieved by taking into account the actual pore size distribution, and thus weighting the related mass transfer coefficients [Phattaranawik et al., 2003]. Pore size distribution showed an important influence in both DCMD and VMD processes [El-Bourawi et al., 2006].
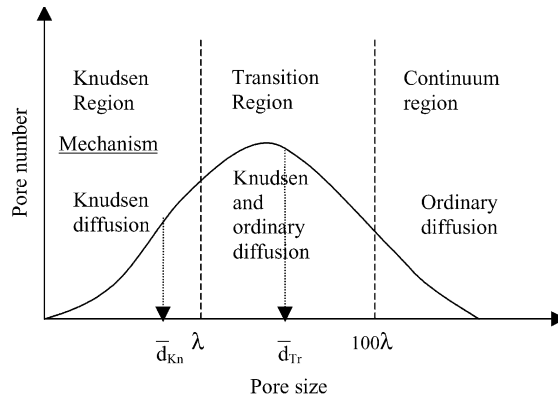
Figure 6.6: Example of pore size distribution covering multiple transport mechanisms, from Phattaranawik et al. [2003]

Pore tortuosity (τ) is defined as the ratio between effective pore length and membrane thickness. As the membrane pores are not cylindrical and straight, tortuosity quantifies the mass transfer reduction associated to the winding path traveled by molecules. Tortuosity can be estimated if experimental values of porosity (ϵ), effective porosity (ϵ/L_p) and membrane thickness (δ) are available:

$$\tau = \frac{\epsilon}{\delta(\epsilon/L_p)} \tag{6.14}$$

where L_p is the effective pore length. In common practice, if the tortuosity is not easy to be derived, a value of $\tau = 2$ is assumed [Schofield et al., 1987].

6.3.3 Thickness

Membrane thickness influences both mass and heat transfer. For example, by increasing the thickness, the mass transfer coefficients will lower (see equations 6.4, 6.5 and 6.7),

whereas the thermal conductivity will increase. From these conflincting conditions, an optimal membrane thickness could be derived: however, experimental studies showed that in general the vapor flux decreases with increasing membrane thickness; only in some DCMD case, a trade-off value was derived [El-Bourawi et al., 2006].

To overcome this issue, composite membranes can be employed. For example, the use of multilayer membranes made with a thin hydrophobic membrane supported on a highly porous layer can ensure an adequate mass flux, together with a low thermal conductivity.

6.3.4 Wetting and liquid entry pressure (LEP)

In MD process, an undesired phenomenon is the liquid penetration through the membrane, as it results in a permeate contamination. Even though hydrophobic membranes are used in MD practice, the liquid flow through the pores can occur, depending on the operating pressure. A general expression which relates the wetting pressure with the pore size is the Laplace-Young equation [Garcia-Payo et al., 2000]:

$$\Delta P_{entry} = -\frac{2\sigma_i \cos\theta}{r} \tag{6.15}$$

where ΔP_{entry} is the liquid entry pressure (LEP), σ_i is the water surface tension, θ is the contact angle and r is the pore radius. Surface tension depends on water temperature and solute concentration, whereas the contact angle is affected by the membrane material. For a highly hydrophobic material, a θ value of $0°$ can be assumed. If the membrane has a wide distribution of pore dimensions, the value of r to consider in ΔP_{entry} estimation is the highest of the smaller equivalent mean cross-section diameters along any possible pass-through path, instead of the average value. This aspect has not been thoroughly investigated in MD for desalination, that is, at water temperatures of 50-80°C and at different levels of salinity. LEP is usually measured at ambient temperature; an example of LEP measurement at different temperatures was carried out with water-alcohol solutions [Garcia-Payo et al., 2000].

Bibliography

S. Al-Asheh, F. Banat, M. Qtaishat, and M. Al-Khateeb. Concentration of sucrose solutions via vacuum membrane distillation. *Desalination*, 195:60–68, 2006.

S. Al-Obaidani, E. Curcio, F. Macedonio, G. Di Profio, H. Al-Hinai, and E. Drioli. Potential of membrane distillation in seawater desalination: Thermal efficiency, sensitivity study and cost estimation. *Journal of Membrane Science*, 323:85–98, 2008.

F. Banat, R. Jumah, and M. Garaibeh. Exploitation of solar energy collected by solar stills for desalination by membrane distillation. *Renewable Energy*, 25(2):293–305, 2002.

F. Banat, F. A. Al-Rub, and K. Bani-Melhem. Desalination by vacuum membrane distillation: sensitivity analysis. *Separation and Purification Technology*, 33:75–87, 2003.

F. A. Banat and M. Al-Shannag. Recovery of dilute acetone-butanol-ethanol (ABE) solvents from aqueous solutions via membrane distillation. *Bioprocess and Biosystem Engineering*, 23(6):643–649, 2000.

F. A. Banat and J. Simandl. Theoretical and experimental study in membrane distillation. *Desalination*, 95:39–52, 1994.

F. A. Banat and J. Simandl. Removal of benzene traces from contaminated water by vacuum membrane distillation. *Chemical Engineering Science*, 51(8):1257–1265, 1996.

F. A. Banat and J. Simandl. Desalination by membrane distillation: A parametric study. *Separation and Purification Technology*, 33:201–226, 1998.

F. A. Banat and J. Simandl. Membrane distillation for propanone removal from aqueous streams. *Journal of Chemical Technology and Biotechnology*, 75(2):168–178, 2000.

S. Bandini, C. Gostoli, and G. C. Sarti. Separation efficiency in vacuum membrane distillation. *Journal of Membrane Science*, 73:217–232, 1992.

S. Bandini, A. Saavedra, and G. C. Sarti. Vacuum membrane distillation: experiments and modeling. *AIChE Journal*, 43:398–415, 1997.

J. Blanco Galvez, L. Garcia-Rodriguez, and I. Martin-Mateos. Seawater desalination by an innovative solar-powered membrane distillation system: the MEDESOL project. *Desalination*, 246:567–576, 2009.

S. Bonyadi and T. S. Chung. Flux enhancement in membrane distillation by fabrication of dual layer hydrophilic-hydrophobic hollow fiber membranes. *Journal of Membrane Science*, 306:134–146, 2007.

A. Bottino, G. Capannelli, and A. Comite. Novel porous poly (vinylidene fluoride) membranes for membrane distillation. *Desalination*, 183:375–382, 2005.

V. Calabrò, E. Drioli, and F. Matera. Membrane distillation in the textile wastewater treatment. *Desalination*, 83:209–224, 1991.

V. Calabrò, B. L. Jiao, and E. Drioli. Theoretical and experimental study on membrane distillation in the concentration of orange juice. *Industrial Engineering and Chemical Research*, 33:1803–1808, 1994.

L. Carlsson. The new generation in sea water desalination SU membrane distillation system. *Desalination*, 45:221–222, 1983.

H. Chang, G.-B. Wang, Y.-H. Chen, C.-C. Li, and C.-L-Chang. Modeling and optimization of a solar driven membrane distillation desalination system. *Renewable Energy*, 35(12):2714–2722, 2010.

T.-C. Chen and C.-D. Ho. Immediate assisted solar direct contact membrane distillation in saline water desalination. *Journal of Membrane Science*, 358:122–130, 2010.

L.-H. Cheng, P.-C. Wu, and J. Chen. Modeling and optimization of hollow fiber DCMD module for desalination. *Journal of Membrane Science*, 318:154–166, 2008.

R. Chouikh, S. Bouguecha, and M. Dhahbi. Modelling of a modified air gap distillation membrane for the desalination of seawater. *Desalination*, 181:257–265, 2005.

E. Curcio and E. Drioli. Membrane distillation and related operations - A review. *Separation and Purification Reviews*, 34:35–86, 2005.

J. M. O. De Zarate, C. Rincon, and J. I. Mengual. Concentration of bovine serum albumin aqueous solutions by membrane distillation. *Separation Science and Technology*, 33(3):283–296, 1998.

Z. Ding, L. Liu, Z. Li, S. El-Bourawi, and R. Ma. Analysis of a solar-powered membrane distillation system. *Desalination*, 172:27–40, 2005.

Z. Ding, L. Liu, Z. Li, R. Ma, and Z. Yang. Experimental study of ammonia removal from water by membrane distillation (MD): The comparison of three configurations. *Journal of Membrane Science*, 286:93–103, 2006.

E. Drioli, F. Laganà, A. Criscuoli, and G. Barbieri. Integrated membrane operations in desalination processes. *Desalination*, 122:141–145, 1999.

E. Drioli, E. Curcio, G. Di Profio, F. Macedonio, and A. Criscuoli. Integrating membrane contactors technology and pressure-driven membrane operations for seawater desalination: Energy, exergy and costs analysis. *Chemical Engineering Research and Design*, 84(3):209–220, 2006.

A. El Amali, S. Bouguecha, and M. Maalej. Experimental study of air gap and direct contact membrane distillation configurations: application to geothermal and seawater desalination. *Desalination*, 168:357, 2004.

M. S. El-Bourawi, R. Ma, Z. Ding, and M. Khayet. A framework for better understanding membrane distillation separation process. *Journal of Membrane Science*, 285:4–29, 2006.

M. S. El-Bourawi, M. Khayet, R. Ma, Z. Ding, and X. Zhang. Application of vacuum membrane distillation for ammonia removal. *Journal of Membrane Science*, 301:200–209, 2007.

C. Feng, K. C. Khulbe, T. Matsuura, R. Gopal, S. Kaur, S. Ramakrishna, and M. Khayet. Production of drinking water from saline water by air-gap membrane distillation using polyvinylidene fluoride nanofiber membrane. *Journal of Membrane Science*, 311:1–6, 2008.

M. C. Garcia-Payo, M. A. Izquierdo-Gil, and C. Fernandez-Pineda. Wetting study of hydrophobic membranes via liquid entry pressure measurements with aqueous alcohol solutions. *Journal of Colloid and Interface Science*, 230:420–431, 2000.

M. P. Godino, L. Pena, C. Rincon, and J. I. Mengual. Water production from brines by membrane distillation. *Desalination*, 108:91–97, 1997.

M. Gryta and K. Karakulski. The application of membrane distillation for the concentration of oil-water emulsions. *Desalination*, 121(1):23–29, 1999.

M. Gryta, M. Tomaszewska, and K. Karakulshi. Wastewater treatment by membrane distillation. *Desalination*, 198:67–73, 2006.

S. Gunko, S. Verbych, M. Bryk, and N. Hilal. Concentration of apple juice using direct contact membrane distillation. *Desalination*, 190:117–124, 2006.

J. H. Hanemaaijer, J. van Medevoort, A. E. Jansen, C. Dotremont, E. van Sonsbeek, T. Yuan, and L. De Ryck. Memstill membrane distillation - A future desalination technology. *Desalination*, 199:175–176, 2006.

P. A. Hogan, Sudjito, A. G. Fane, and G. L. Morrison. Desalination by solar heated membrane distillation. *Desalination*, 81:81–90, 1991.

D. Hou, J. Wang, D. Qu, Z. Luan, and X. Ren. Fabrication and characterization of hydrophobic PVDF hollow fiber membranes for desalination through direct contact membrane distillation. *Separation and Purification Technology*, 69:78–86, 2009.

S. T. Hsu, K. T. Cheng, and J. S. Chiou. Seawater desalination by direct contact membrane distillation. *Desalination*, 143(3):279–287, 2002.

J. Huang, J. Zhang, and X. Haoand Y. Guo. Study of a new novel process for preparing and costretching ptfe membrane and its properties. *European Polymer Journal*, 40:667–671, 2004.

X. Ji, E. Curcio, S. Al Obaidani, G. Di Profio, E. Fontananova, and E. Drioli. Membrane distillation-crystallization of seawater reverse osmosis brines. *Separation and Purification Technology*, 71: 76–82, 2010.

B. Jiao, A. Cassano, and E. Drioli. Recent advances on membrane processes for the concentration of fruit juices: a review. *Journal of Food Engineering*, 63(3):303–324, 2004.

M. Khayet, P. Godino, and J. I. Mengual. Nature of flow on sweeping gas membrane distillation. *Journal of Membrane Science*, 170:243–255, 2000a.

M. Khayet, P. Godino, and J. I. Mengual. Theory and experiments on sweeping gas membrane distillation. *Journal of Membrane Science*, 165:261–272, 2000b.

M. Khayet, P. Godino, and J. I. Mengual. Theoretical and experimental studies on desalination using the sweeping gas membrane distillation method. *Desalination*, 157:297–305, 2003.

T. Kitamura, S. Okabe, M. Tanigaki, K. Kurumada, M. Ohshima, and S. Kanazawa. Morphology change in polytetrafluoroethylene (PTFE) porous membrane caused by heat treatment. *Polymer Engineering and Science*, 40(3):809–817, 2000.

J. Koschikowsky, M. Wieghaus, and M. Rommel. Solar thermal-driven desalination plants based on membrane distillation. *Desalination*, 156:295–304, 2003.

S. Kubota, K. Ohta, I. Hayano, M. Hirai, K. Kikuchi, and Y. Murayama. Experiments on seawater desalination by membrane distillation. *Desalination*, 69:19–26, 1988.

K. W. Lawson and D. R. Lloyd. Membrane distillation. *Journal of Membrane Science*, 124:1–25, 1997.

C. H. Lee and W. H. Hong. Effect of operating variables on the flux and selectivity in sweep gas membrane distillation for dilute aqueous isopropanol. *Journal of Membrane Science*, 188:79–86, 2001.

B. Li and K. K. Sirkar. Novel membrane and device for vacuum membrane distillation-based desalination process. *Journal of Membrane Science*, 257:60–75, 2005.

N. N. Li, A. G. Fane, W. S. W. Ho, and T. Matsuura. *Advanced membrane technology and applications*. John Wiley & Sons, Inc., Hoboken, New Jersey, 2008.

Y. K. Lin, G. Chen, J. Yang, and X. L. Wang. Formation of isotactic polypropylene membranes with bicontinuous structure and good strength via thermally induced phase separation method. *Desalination*, 236:8–15, 2009.

G. L. Liu, C. Zhu, C. S. Cheung, and C. W. Leung. Theoretical and experimental studies on air gap membrane distillation. *Heat and Mass Transfer*, 34:329–335, 1998.

F. Macedonio, E. Curcio, and E. Drioli. Integrated membrane systems for seawater desalination: energetic and exergetic analysis, economic evaluation, experimental study. *Desalination*, 203: 260–276, 2007.

G. A. Mannella, V. La Carrubba, and V. Brucato. Characterization of hydrophobic polymeric membranes for membrane distillation process. *International Journal of Material Forming*, 3 Suppl 1: 563–566, 2010.

J. I. Mengual, M. Khayet, and M. P. Godino. Heat and mass transfer in vacuum membrane distillation. *International Journal of Heat and Mass Transfer*, 47:865–875, 2004.

J.-P. Mericq, S. Laborie, and C. Cabassud. Vacuum membrane distillation for an integrated seawater desalination process. *Desalination and Water Treatment*, 9:293–302, 2009.

T. Mohammadi and M. A. Safavi. Application of Taguchi method in optimization of desalination by vacuum membrane distillation. *Desalination*, 249:83–89, 2009.

K. Ohta, K. Kikuchi, I. Hayano, T. Okabe, T. Goto, S. Kimura, and H. Ohya. Experiments on sea water desalination by membrane distillation. *Desalination*, 78(2):177–185, 1990.

J. Phattaranawik, R. Jiraratananon, and A. G. Fane. Effect of pore size distribution and air flux on mass transport in direct contact membrane distillation. *Journal of Membrane Science*, 215:75–85, 2003.

D. Qu, J. Wang, D. Hou, Z. Luan, B. Fan, and C. Zhao. Experimental study of arsenic removal by direct contact membrane distillation. *Journal of Hazardous Materials*, 163:874–879, 2009.

C. Riziero Martinetti, A. E. Childress, and T. Y. Cath. High recovery of concentrated RO brines using forward osmosis and membrane distillation. *Journal of Membrane Science*, 331:31–39, 2009.

M. A. Safavi and T. Mohammadi. High-salinity water desalination using VMD. *Chemical Engineering Journal*, 149:191–195, 2009.

G. C. Sarti, C. Gostoli, and S. Bandini. Extraction of organic components from aqueous streams by vacuum membrane distillation. *Journal of Membrane Science*, 80:21–33, 1993.

R. W. Schofield, A. G. Fane, and C. J. D. Fell. Heat and mass transfer in membrane distillation. *Journal of Membrane Science*, 33:299–313, 1987.

R. W. Schofield, A. G. Fane, and C. J. D. Fell. Gas and vapour transport through microporous membranes. I. Knudsen-Poiseuille transition. *Journal of Membrane Science*, 53:159–171, 1990.

L. Song, B. Li, K. K. Sirkar, and J. L. Gilron. Direct contact membrane distillation-based desalination: Novel membranes, devices, larger-scale studies, and a model. *Industrial Engineering Chemical Research*, 46:2307–2323, 2007.

H. Susanto. Towards practical implementations of membrane distillation. *Chemical Engineering and Processing: Process Intensification*, 50:139–150, 2011.

N. Tang, Q. Jia, H. Zhang, J. Li, and S. Cao. Preparation and morphological characterization of narrow pore size distributed polypropylene hydrophobic membranes for vacuum membrane distillation via thermally induced phase separation. *Desalination*, 256:27–36, 2010.

P. Termpiyakul, R. Jiraratananon, and S. Srisurichan. Heat and mass transfer characteristics of a direct contact membrane distillation process for desalination. *Desalination*, 177:133–141, 2005.

M. Tomaszewska, M. Gryta, and A. W. Morawski. Study on the concentration of acids by membrane distillation. *Journal of Membrane Science*, 102:113–122, 1995.

A. M. Urtiaga, G. Ruiz, and I. Ortiz. Kinetic analysis of the vacuum membrane distillation of chloroform from aqueous solutions. *Journal of Membrane Science*, 165:99–110, 2000.

P. K. Weyl. Recovery of demineralized water from saline waters. US Patent, 3340186, 1967.

B. Wu, X. Tandand W. K. Teo, and K. Li. Removal of benzene/toluene from water by vacuum membrane distillation in a PVDF hollow fiber membrane module. *Separation Science and Technology*, 40(13):2679–2695, 2005.

B. Wu, K. Li, and W. K. Teo. Preparation and characterization of poly(vinylidene fluoride) hollow fiber membranes for vacuum membrane distillation. *Journal of Applied Polymer Science*, 106: 1482–1495, 2007.

J. Xu, M. Furuswa, and A. Ito. Air-sweep vacuum membrane distillation using fine silicone, rubber, hollow-fiber membranes. *Desalination*, 191:223–231, 2006a.

Y. Xu, B. Zhu, and Y. Xu. Pilot test of vacuum membrane distillation for seawater desalination on a ship. *Desalination*, 189:165–169, 2006b.

J. Zhang, N. Dow, M. Duke, E. Ostarcevic, J. Li, and S. Gray. Identification of material and physical features of membrane distillation membranes for high performance desalination. *Journal of Membrane Science*, 349:295–303, 2010.

7 Membrane characterization: experimental and modeling

A set of commercial membranes were characterized to deduce the main features affecting MD performances. Two different measurements were carried out: vapor flux (permeability) and liquid entry pressure (LEP). Vapor flux is directly related to the process productivity; it was estimated by analyzing the system of vapor removal, i.e. by scrutinizing various MD configurations. On the other hand, LEP is relevant in separation efficiency.

Both characterizations involved the design and set up of various laboratory scale apparatuses, which are described in this chapter.

The apparatus for permeability measurement meets the need for a preliminary experimental characterization of membranes prior testing the membrane module. As a matter of fact, in common practice membranes used in MD operations are tested in an "assembled" module, thus making it very difficult to discriminate the relative influence of membrane properties on the module performance, as MD configuration can exert a strong influence on vapor flux.

The LEP measurement apparatus allows the detection of membrane wetting at controlled temperature. As the LEP is usually determined at room temperature, thanks to the proposed apparatus it is possible to obtain more reliable data for the design of MD modules and for a guided selection of the corrected operating conditions.

A further characterization was carried out by Scanning Electron Microscopy (SEM), with the aim of visualizing membrane microstructure and texture, and to relate them to MD performance.

The membranes tested in this work are reported in table 7.1, together with relevant nom-

inal data. A summary of the tests performed for each membrane is showed in table 7.2.

Table 7.1: Membrane properties

Manufacturer	Material	Support	NPS [μm]	Thickness [μm]	LEP [bar]
Gore	PTFE	Spunbonded PP	1	140-340	0.34-0.55†
Gore	PTFE	Spunbonded PP	0.45	180-360	0.62-0.91†
Gore	PTFE	Spunbonded PP	0.2	130-380	0.88-1.59†
GVS	PVDF	Non-woven polyester	0.2	190-247	2.4-3*
PALL	AC	Non-woven nylon	0.2	130-320	1.43*
PALL	PTFE	Non-woven polyester	0.2	203-330	1.1-1.79†

NPS: nominal pore size. AC: acrylic copolymer.

$\dagger$, isopropyl alcohol; $*$, water.

Table 7.2: Membrane sample codes and tests performed (as indicated by an X)

Manufacturer	Sample code	Material	NPS [μm]	SEM	Vapor flux	LEP
Gore	1	PTFE	1	X		
Gore	2	PTFE	0.45	X	X	X
Gore	3	PTFE	0.2	X	X	
GVS	-	PVDF	0.2	X	X	
PALL	1	AC	0.2	X		
PALL	2	PTFE	0.2	X		

7.1 Design of a permeability measurement apparatus

A versatile apparatus for testing membrane permeability would be useful for preliminary design of a MD unit. In common practice, the membranes are tested within the module (e.g. plate and frame, spiral winded), thus providing data related also to the module characteristics (e.g. geometry and flow arrangement). The main features of the designed-on-purpose apparatus are the ease of membrane substitution and the possibility of changing conditions in permeate side, i.e. to try different MD configurations.

The measurement were carried out in a batch system. This choice was related to the ease of preparation and operation for a laboratory scale apparatus.

7.1.1 Description

The batch MD apparatus designed on-purpose is schematized in figure 7.1. It consisted in a cylindrical vessel ($V \simeq 1$ l) equipped with an electrical heater ($P_{max} = 1200$ W). One

end is open, to allow the membrane positioning and sealing via O-rings. Depending on the MD configuration chosen, membrane can be exposed to atmosphere or closed in a chamber, thus using two different screwed tops:

1. open to atmosphere (figure 7.2a);

2. closed and equipped with two inlet-outlet channels (figure 7.2b).

(a) membrane exposed to atmosphere   (b) membrane closed in a chamber
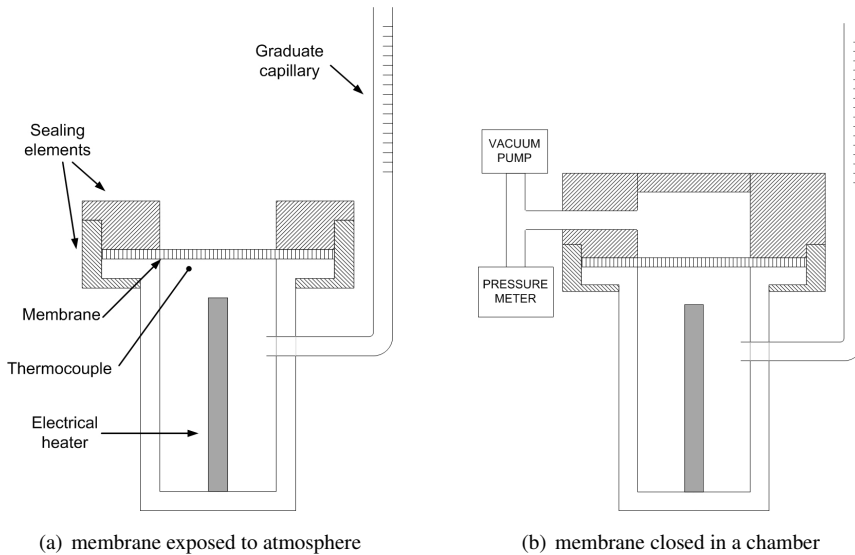
Figure 7.1: Schematic of permeability measurement apparatus

A capillary tube was inserted on the lateral surface: the water level variation in the tube was recorded and related to the vapor flux across the membrane. The capillary tube position ensures the contact of water with the membrane during the whole experiment. The possible vapor flux out of the capillary was inhibited by reducing its open section; furthermore, the water temperature in the capillary was significantly lower than into the vessel, thus making the vapor loss negligible. Temperature was controlled with a PID controller CAL 3200 (CAL Controls, Inc.), and experiments were carried out at a water temperature in the range 20-80°C. A thermocouple for temperature measurement was located near the membrane surface.

When the membrane was exposed to the atmosphere, two configurations were experimentally reproduced:

1. air gap membrane distillation (AGMD), i.e. the vapor is removed by natural air convection;

(a) Open top

(b) Closed top

Figure 7.2: Screwed tops used

2. sweeping gas membrane distillation (SGMD), i.e. vapor removal by forced convection induced by a fan.
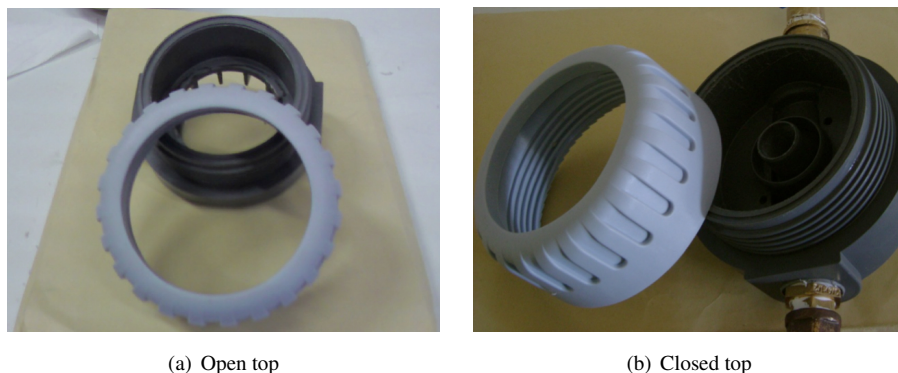
With the membrane sealed into a chamber, two configurations were experimentally reproduced, both by using a vacuum pump:

1. vacuum membrane distillation (VMD);

2. vacuum sweeping gas membrane distillation (VSGMD), i.e. vacuum with air loss along the sealing around.

In VMD experiments there is no convective mass transfer in permeate side, as the chamber is sealed and a low pressure is maintained. In VSGMD experiments, air can enter into the chamber, maintained at a pressure lower than atmospheric, thus inducing a convective mass transfer in the permeate side. In those latter cases, a zinc-coated grid was used to prevent the membrane deformation due to pressure gap. Moreover, the chamber was connected to a Venturi vacuum pump (VP20-100H, VACCON) and a pressure meter (TP704-20BAI, DeltaOhm).

Distilled water was used to avoid the complications induced by the influence of salt concentration on the process [Safavi and Mohammadi, 2009, Mericq et al., 2009, Qtaishat et al., 2008]. The net effect of using salty water is only a linear reduction of permeate flux with increasing salt concentration; moreover, the main influence of solute is the reduction of driving force, with no influence on mass transfer coefficient [Martinez and Rodriguez-Maroto, 2007]. Water was boiled before tests to eliminate dissolved gas. Indeed, bubble formation during heating was observed with aerated water and obviously bubbles disturb significantly liquid volume measurements.

Under all the configurations, the vapor permeation through the membrane was recorded by reading the level in the capillary tube. The slope of permeate volume vs time curve (approximately a straight line) was used to determine the vapor flow rate throughout the membrane. Experiments were repeated twice or more times to ensure the reproducibility.

7.1.2 Modeling

The vapor flux for the MD process is given by [Lawson and Lloyd, 1997]:

$$N = k_P \left(P_f^0 - P_p^0 \right) \tag{7.1}$$

where k_P is the global mass transfer coefficient, P_f^0 and P_p^0 are the vapor pressure at the feed and permeate side, respectively.

Mass transfer coefficients were estimated for both natural and forced convection conditions and for three possible mass transfer mechanisms through the membrane: Knudsen diffusion, coupled Knudsen-molecular diffusion (the most reliable for forced convection [Khayet et al., 2000, 2002]) and viscous flow (to be considered in VMD, [Lawson and Lloyd, 1997]). As regards to feed side, the mass transport resistance was assumed to be negligible.

The expressions of mass transfer coefficient in the membrane for viscous flow, Knudsen and molecular diffusion are respectively [Lawson and Lloyd, 1997]:

$$k_P^v = \frac{\epsilon r^2}{8\tau} \frac{\bar{P}_w}{\mu} \frac{M}{RT} \frac{1}{\delta} \tag{7.2}$$

$$k_P^k = \frac{2\epsilon r}{3\tau} \sqrt{\frac{8RT}{\pi M}} \frac{M}{RT} \frac{1}{\delta} \tag{7.3}$$

$$k_P^d = \frac{\epsilon}{\tau} \frac{P}{\bar{P}_a} D_{ij} \frac{M}{RT} \frac{1}{\delta} \tag{7.4}$$

where ϵ is the membrane porosity, τ the pore tortuosity, δ the membrane thickness, r the (mean) pore radius, μ the vapor viscosity, D_{ij} the water vapor diffusivity in air, P the pressure, $\bar{P}_a$ the mean air pressure, $\bar{P}_w$ the mean water pressure and M the molecular weight of vapor molecules. Owing to the lack of data, the porosity (ϵ) and the tortuosity (τ) were assumed to be 0.8 and 2, respectively, in line with other works available in literature [Phattaranawik et al., 2003, Schofield et al., 1990]. The membrane thickness was taken as the average value of the range reported in table 7.1.

The external mass transfer coefficients were evaluated by empirical correlations for Nusselt number (Nu) [Gates, 1980], both in the case of natural and forced convection:

$$\mathrm{Nu} = 0.523(\mathrm{Pr} \cdot \mathrm{Gr})^{0.25} \quad \text{(natural convection)} \tag{7.5}$$

$$\mathrm{Nu} = 0.595 \cdot \mathrm{Re}^{0.5} \quad \text{(forced convection)} \tag{7.6}$$

where the dimensionless Nusselt, Prandtl (Pr), Grashof (Gr) and Reynolds (Re) numbers are defined as follows:

$$\mathrm{Nu} = \frac{hd}{k_t} \tag{7.7}$$

$$\mathrm{Pr} = \frac{\mu c_p}{k_t} \tag{7.8}$$

$$\mathrm{Gr} = \frac{d^3 g \rho \Delta \rho}{\mu^2} \tag{7.9}$$

$$\mathrm{Re} = \frac{\rho v d}{\mu} \tag{7.10}$$

where h is the heat transfer coefficient, d the characteristic dimension, k_t the thermal conductivity, c_p the specific heat, g the gravitational acceleration and ρ the density. Grashof number was evaluated considering the density difference between "pure" air and the water-air mixture lying on the membrane surface (see appendix B).

The Chilton-Colburn analogy [Geankoplis, 2003] was applied:

$$\frac{\mathrm{Nu}}{\mathrm{RePr}^{\frac{1}{3}}} = \frac{\mathrm{Sh}}{\mathrm{ReSc}^{\frac{1}{3}}} \tag{7.11}$$

and the values of k_P^{nc} (natural convection) and k_P^{fc} (forced convection) were evaluated. The dimensionless Sherwood (Sh) and Schmidt (Sc) numbers are defined as:

$$\mathrm{Sh} = \frac{k_C d}{D_{ij}} \tag{7.12}$$

$$\mathrm{Sc} = \frac{\mu}{\rho D_{ij}} \tag{7.13}$$

where k_C is the mass transfer coefficient.

The as-calculated mass transfer coefficients were combined both as series or parallel resistances, on the basis of the "Dusty Gas Model" [Mason and Malinauskas, 1983]. The mass transfer resistances are represented with the electric analogy in figure 7.3.

Appropriate contributions to mass transfer coefficient are deducted from Knudsen number analysis:

$$\text{Kn} = \frac{\lambda}{d} \tag{7.14}$$

where λ is the mean free path of molecules and d the pore diameter. The values of Knudsen number calculated are reported in table 7.3.

Table 7.3: Calculated mean free path (λ) and Knudsen number (Kn)

T [°C]	λ [μm]	Kn ($d = 0.45\ \mu m$)	Kn ($d = 0.2\ \mu m$)
60	0.746	1.66	3.73
70	0.451	1.00	2.26
80	0.333	0.74	1.66

Three different transport regions can be defined, referring to Knudsen number:

1. if $\text{Kn} > 1$, Knudsen diffusion is the mass transfer mechanism;

2. conversely, if $\text{Kn} < 0.01$ molecular diffusion is taken as mass transfer mechanism;

3. for $0.01 < \text{Kn} < 1$, both contribution must be considered, and the flow mechanism considered is named Knudsen-molecular diffusion transition.
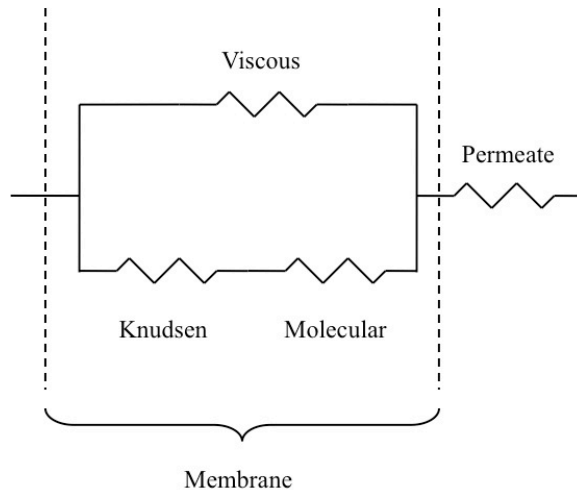

Figure 7.3: Electric analogy for mass transfer resistance

In AGMD and SGMD the viscous mass transfer does not occur. In all cases considered Kn $\simeq$ 1, thus both Knudsen and molecular diffusion mechanisms must be taken into account. The membrane and permeate side resistance were considered as series. The air velocity induced by the fan was approximately 2 m/s. In VSGMD experiments, air velocity was unknown. Therefore, air velocity was traced back from experimental mass transfer coefficient (equation 7.1), by solving equations 7.6 and 7.11 for unknown Reynolds number values.

As regards to VMD, the molecular diffusion can be neglected, owing to the low pressure of the process. In addition, the viscous contribution to mass transfer must be taken into account. As $0.01 <$ Kn < 10, Knudsen-viscous transition is the selected mass transport mechanism: the mass transfer coefficients are computed as parallel resistances [Mason and Malinauskas, 1983]. The permeate side resistance was assumed negligible [Lawson and Lloyd, 1997], as temperature and pressure are practically constant in the permeate chamber.

The resulting expressions of the global k_P are resumed in table 7.4.

Table 7.4: Expression of global mass transfer coefficients

Configuration	Membrane, k_P^m	Permeate, k_P^p	Global coefficient, k_P
AGMD	$\left(\dfrac{1}{k_P^k} + \dfrac{1}{k_P^d}\right)^{-1}$	k_P^{nc}	$\left(\dfrac{1}{k_P^m} + \dfrac{1}{k_P^p}\right)^{-1}$
SGMD, VSGMD	$\left(\dfrac{1}{k_P^k} + \dfrac{1}{k_P^d}\right)^{-1}$	k_P^{fc}	$\left(\dfrac{1}{k_P^m} + \dfrac{1}{k_P^p}\right)^{-1}$
VMD	$k_P^k + k_P^v$	/	k_P^m

7.2 Design of a LEP measurement apparatus

In MD operations membrane wetting has to be always avoided, as it would lower the permeate quality. Therefore, the LEP measurement is mandatory in a preliminary experimental characterization of membranes to be used in a MD module.

7.2.1 Description

The liquid entry pressure (LEP) was measured through the self-built dedicated apparatus schematized in figure 7.4. It is constituted of a cylindrical vessel (with diameter D=10 cm) containing hot water continuously recirculated from a thermostatic bath. The membrane was placed on one end of the vessel, in contact with the liquid hot water, whereas the other face of the membrane was exposed to the atmosphere. A brass disk diaphragm was used

to reduce the area of the membrane exposed to pressure and to minimize the membrane deformation due to the pressure gap. The membrane area exposed to atmosphere was a circle of diameter D=2 cm. Moreover, a zinc-coated grid was inserted on the dry face of the membrane to limit the border concentration of stresses, which were potentially responsible for the microstructure modifications. The pressure in the vessel was controlled by a manual valve and measured with a pressure meter (TP704-20BAI, DeltaOHM). A thermocouple was inserted inside the vessel to measure the liquid temperature close to the membrane surface.

A small amount of methylene blue was added to water as a dyeing agent to allow an easy visual detection of liquid membrane pass-through. LEP was detected visually, as small colored water droplets started to appear at a given (reproducible) pressure level (see figure 7.5). The very low dye concentration did not significantly influence the liquid properties.

The LEP was recorded after it reached a constant stationary value. As a matter of fact, when a water pressure was applied on the membrane, the LEP value measured was always higher than after a few cycle of operations. This fact could be explained by the inference that water intrusion into the pores, even in nonwetting cases, modified the membrane microstructure; for example, it caused an enlargement of the pores [Barbe et al., 2000]. For this reason, LEP values were taken only after stationary and reproducible results were observed.
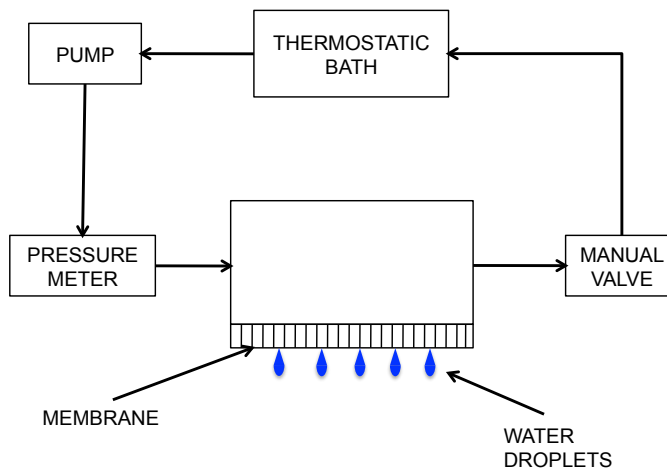

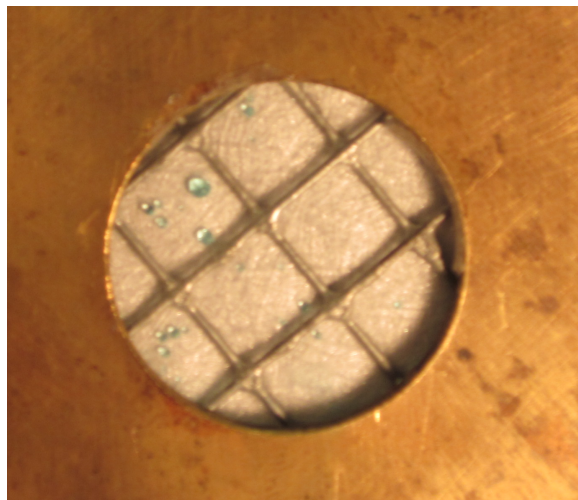**Figure 7.4:** Schematic of the LEP measurement apparatus

Figure 7.5: Example of visual detection of LEP by the appearance of liquid droplets

7.3 SEM imaging

Membrane morphology was visualized by scanning electron microscopy (SEM) with a Philips 505 Microscope. Micrographs of the membrane surface and cross sections were taken. With reference to the sample cross-section preparation before observation, the usually adopted procedure of inducing brittle fracture at liquid nitrogen temperature was not easy to obtain because of the very small membrane thickness. Alternatively, membrane cutting at liquid nitrogen temperature was then applied to preserve its bulk structure.

The pore size distribution of the PALL 1 membrane was determined from the analysis of the SEM micrographs. With regard to the other membranes studied, the visual discrimination of pores was very difficult: strictly speaking; the fibrous structure did not allow the recognition of distinct pores, which are the free space among a high number of fibers. In this latter case, gas-liquid porometry offered a way to measure the pore size distribution independently of the membrane microstructure. From the as-obtained distribution, the numerical and weighed average pore sizes were derived [Kreyszig, 1988], and the first- and second-order momentum of the distribution were calculated, that is:

$$D_n = \sum x_i D_i \tag{7.15}$$

$$D_w = \frac{\sum x_i D_i^2}{D_n} \tag{7.16}$$

where D_n is the numerical average diameter, x_i is the fraction of pores with diameter D_i, and D_w is the weighted average diameter. The first-order momentum represents the numerical average of the pore diameter; the second-order momentum, divided by the numerical average, is the area-weighted average and it is more appropriate to denote the membrane permeability.

Bibliography

A. M. Barbe, P. A. Hogan, and R.A. Johnson. Surface morphology changes during initial usage of hydrophobic, microporous polypropylene membranes. *Journal of Membrane Science*, 172:149–156, 2000.

D. M. Gates. *Biophysical ecology*. Springer-Verlag New York, 1980.

C. J. Geankoplis. *Transport Processes and Separation Process Principles*. Prentice Hall, Upper Saddle River, NJ, 2003.

M. Khayet, P. Godino, and J. I. Mengual. Nature of flow on sweeping gas membrane distillation. *Journal of Membrane Science*, 170:243–255, 2000.

M. Khayet, P. Godino, and J. I. Mengual. Thermal boundary layers in sweeping gas membrane distillation processes. *AIChE Journal*, 48(7):1488–1497, 2002.

E. Kreyszig. *Advanced Engineering Mathematics;*. John Wiley & Sons, Inc., New York, 1988.

K. W. Lawson and D. R. Lloyd. Membrane distillation. *Journal of Membrane Science*, 124:1–25, 1997.

L. Martinez and J. M. Rodriguez-Maroto. On transport resistances in direct contact membrane distillation. *Journal of Membrane Science*, 295:28–39, 2007.

E. A. Mason and A. P. Malinauskas. *Gas Transport in Porous Media: The Dusty-Gas Model*. Elsevier, Amsterdam, 1983.

J.-P. Mericq, S. Laborie, and C. Cabassud. Vacuum membrane distillation for an integrated seawater desalination process. *Desalination and Water Treatment*, 9:293–302, 2009.

J. Phattaranawik, R. Jiraratananon, and A. G. Fane. Effect of pore size distribution and air flux on mass transport in direct contact membrane distillation. *Journal of Membrane Science*, 215:75–85, 2003.

M. Qtaishat, T. Matsuura, B. Kruczek, and M. Khayet. Heat and mass transfer analysis in direct contact membrane distillation. *Desalination*, 219:272–292, 2008.

M. A. Safavi and T. Mohammadi. High-salinity water desalination using VMD. *Chemical Engineering Journal*, 149:191–195, 2009.

R. W. Schofield, A. G. Fane, and C. J. D. Fell. Gas and vapour transport through microporous membranes. I. Knudsen-Poiseuille transition. *Journal of Membrane Science*, 53:159–171, 1990.

8 Membrane characterization: results

8.1 SEM images

SEM images (figures 8.1 and 8.2) show the microstructures of the membranes studied so far. The membrane morphologies recorded via SEM imaging were ascribable to two different fabrication technologies:

1. fibrous morphology: monoaxial stretching (figure 8.1a) and biaxial stretching (figure 8.1b-d);

2. porous morphology: phase separation (figure 8.2).

As a matter of fact, the random structure of PTFE membranes with nominal pore size of 0.45 and 0.2 μm (figure 8.1b-d) should be related to a biaxial stretching technique [Huang et al., 2004], whereas the Gore 1 (figure 8.1a) morphology inferred a fabrication via uniaxial stretching [Kitamura et al., 2000] because of the ordered and parallel arrangement of the fibers. The PALL 2 membrane exhibited the same structure but a different arrangement of the support. Gore membranes were composed of two clearly distinct layers (figure 8.3a), whereas PALL 2 membrane showed the support embedded into two membrane layers (figure 8.3b). The PALL and GVS membranes exhibited a similar membrane-support arrangement.

The pore size distribution of PALL 1 membrane, obtained via image analysis, is shown in figure 8.4. As can be readily observed, most of the pores exhibited a diameter larger than the nominal pore size (0.2 μm), and the most frequent dimension was about 0.5 μm. On the other hand, the average pore sizes derived via equations 7.15 and 7.16 were 0.85 and 1.20

(a) Gore 1

(b) Gore 2

(c) Gore 3

(d) PALL 2

Figure 8.1: SEM images of membranes fabricated via stretching

(a) GVS

(b) PALL 1

Figure 8.2: SEM images of membranes fabricated via phase separation
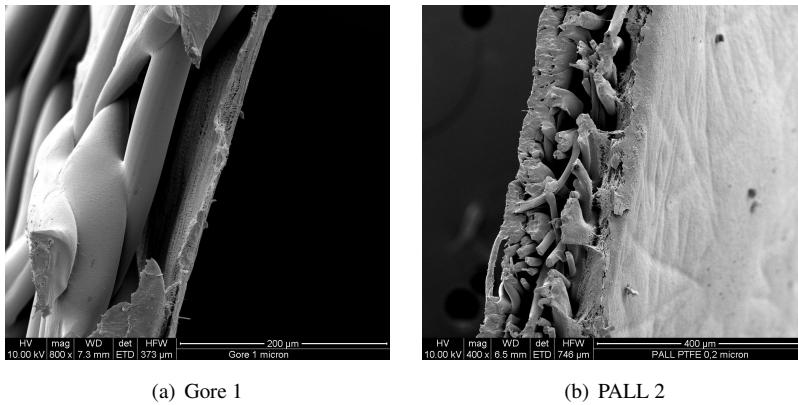
(a) Gore 1

(b) PALL 2

Figure 8.3: SEM images of PTFE membranes, transversal section
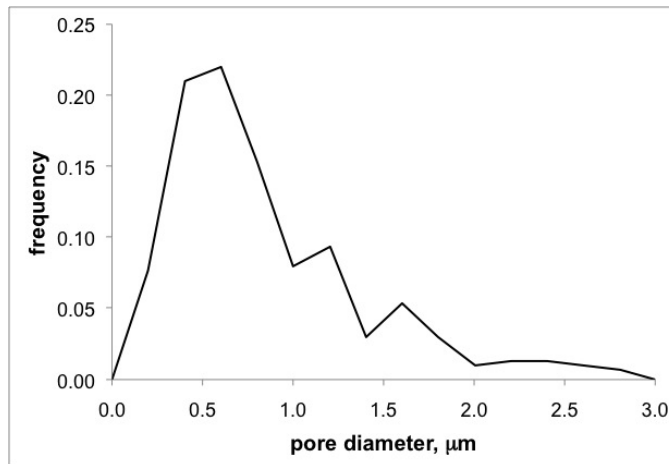

Figure 8.4: SEM based pore size distribution, PALL 2 membrane

μm, respectively. By calculating the area of all pores, the surface porosity was estimated; for the examined membrane, the porosity value was on the order of 60%.

The presented data refer only to the membrane surface. Although a complete characterization must include the measurement of the pore size and porosity of the whole membrane, for example, via gas-liquid porometry and mercury porosimetry, the information obtained was of some relevance in relation to the MD process. In fact, the surface properties of the membrane influenced the water flux and membrane fouling [Gryta, 2007]. The water flux was directly proportional to the surface porosity: a large area for evaporation increased the vapor flux across the membrane. On the other hand, a small surface porosity (or a small pore size on the surface) reduced the risk of crystal growth into the membrane, that is, fouling.

These results show how nominal pore size is a datum to be carefully handled. An experimental study aimed at determining the actual pore size distribution of the membrane is thus mandatory for addressing the design of membrane modules and to select the appropriate operating conditions. Moreover, the true pore size distribution is a useful tool for interpreting and modeling the vapor flux and wetting measurements. It is worth noticing that the LEP is referred to the largest pores, which could be wetted under a lower pressure than the smaller pores (see equation 6.15).

8.2 Vapor flux measurements

8.2.1 Natural and forced convection (AGMD and SGMD)

Measured fluxes (figure 8.5) show an exponential-like increase with temperature, in agreement with other works in literature [Schofield et al., 1987]. This dependence has been explained by considering that the driving force for mass transfer, i.e. the vapor pressure difference (see equation 7.1) exhibits an exponential-like dependence on temperature.

For NC conditions, results for the different membranes are very close to each other: this fact can be explained by inferring that natural convection is the controlling resistance of the global mass transfer process.

For FC conditions, a difference between membranes stems out. As showed in figure 8.5, fluxes through Gore membranes (made of PTFE) are slightly higher than GVS (made of PVDF), in spite of the same nominal pore size for both membranes, as declared by the producers (see table 7.1). This circumstance induces to infer that mass transfer is also governed by membrane microstructure (pore size and distribution, interaction of the material with water vapor molecules). As a matter of fact, it has been showed in the previous

section that the "true" average pore size determined from the pore size distribution can be extremely different from the nominal pore size; in addition, the shape of distribution can affect the mechanism of mass transport, e.g. favoring the Knudsen or the molecular diffusion. For the membranes tested in this study, data of pore size distributions were not provided by the manufacturers.
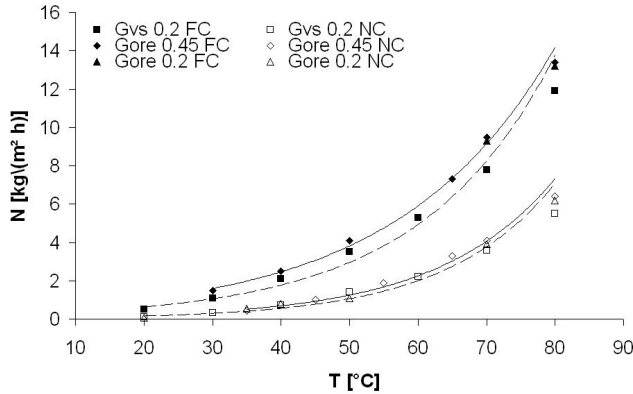
Figure 8.5: Experimental vapor fluxes for natural (NC) and forced (FC) convection. Lines are exponential least-square fitting
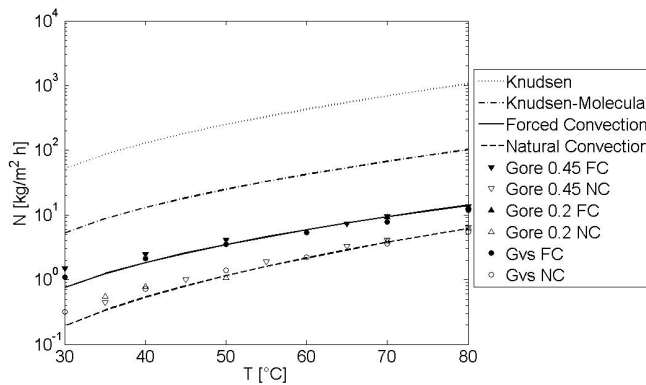
Figure 8.6: Experimental vapor fluxes (dots) compared with predictions (lines)

Vapor flux predictions according to the various models (figure 8.6) show that the main resistance to mass transfer is related to permeate side conditions. In other words, membranes should give rise to fluxes of 1-2 orders of magnitude higher than experimentally recorded

ones, if by Knudsen or Knudsen-Molecular diffusion coefficients are applied. Therefore, process effectiveness could be improved by enhancing mass transport in the permeate side.

8.2.2 Vacuum sweeping gas MD

This configuration is similar to SGMD, as air flow is tangential to the membrane surface. The difference consists in the way the air flow is induced: in VSGMD, air is entrained in the permeate chamber as it is maintained at a pressure $P < P_{atm}$.

The temperature dependence of flux is still exponential-like (see figure 8.7), as seen for the forced convection case. The main advantage of this configuration is the tangential air flow on the membrane surface, which enhances mass transfer coefficient. Moreover, the water vapor contained in the permeate stream can be simply recovered with a flash or a barometric condenser.
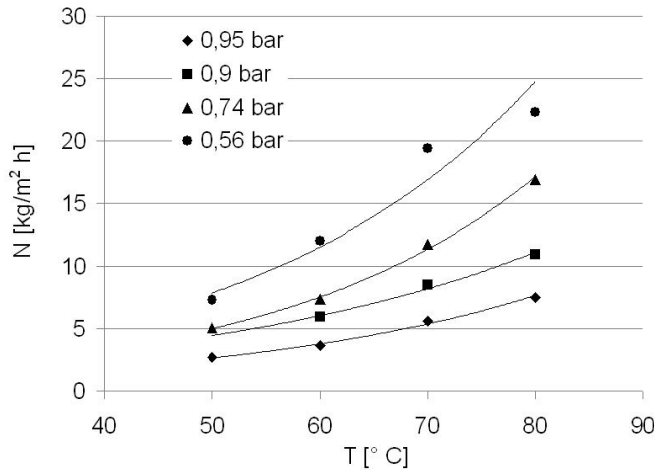

Figure 8.7: Experimental VSGMD vapor fluxes, Gore 0.2 μm membrane. Lines are exponential least-square fitting

Air velocities predicted through equations 7.6 and 7.11 were plotted as a function of pressure difference between atmosphere and the permeate chamber (figure 8.8). A linear relation between air velocity and ΔP was detected: the same relation is derivable from a momentum balance. Although air velocities were drawn by fitting experimental results with equations 7.6 and 7.11, and not experimentally measured, they show a dependence on pressure coherent with the process dynamics. By increasing air velocity, vapor flux rises with $v^{0.5}$ (figure 8.9). A similar trend was recorded by Xu et al. [2006].

Figure 8.8: Calculated air velocity vs pressure difference between atmosphere and permeate chamber

Figure 8.9: Experimental VSGMD (filled symbols) and SGMD (open symbols) vapor fluxes compared with predictions (eq. 7.6 and 7.11, lines), Gore 0.2 μm membrane

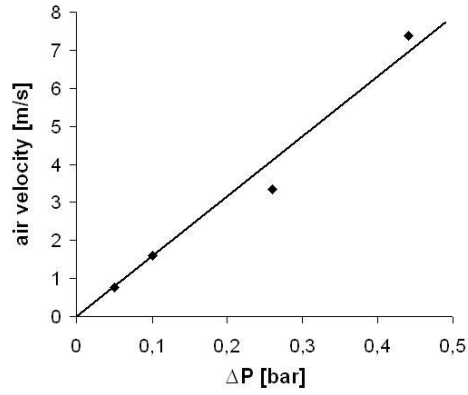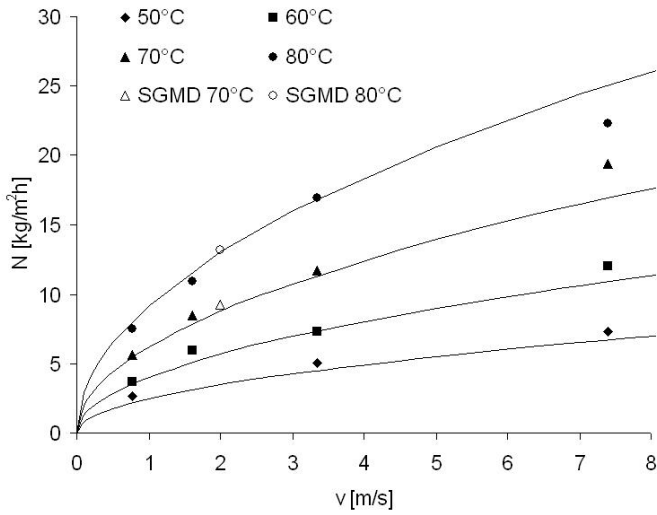Another confirmation of the reasonable assumptions made (i.e. permeate mass transfer is the controlling resistance and vacuum pressure only drives air flux, not vapor flux as VMD) stems from the comparison of VSGMD and SGMD results (figure 8.9), which are very close to each other. This means the VSGMD process is equivalent to SGMD: the only difference being the way the sweeping gas flow is induced.

8.2.3 Vacuum MD

Vacuum conditions in the permeate side induced a vapor flux proportional to (partial) pressure difference between feed and permeate side (see figures 8.10 and 8.11). All fluxes tend to zero at a permeate pressure close to water vapor pressure at the given experimental temperatures, as suggested by equation 7.1.

Figure 8.10: Experimental VMD fluxes vs permeate chamber pressure, Gore membranes. Filled points at $N = 0$ are the water vapor pressures at experimental temperatures

Gore membranes (figure 8.10), although different in pore size, showed similar fluxes under the same conditions. This result can be related to the similar fibrous morphology of Gore membranes, thus affecting in the same way the heat and mass transfer [Zhang et al., 2010].

Also in this configuration GVS membrane (figure 8.11) exhibited fluxes lower than Gore membranes under the same conditions. As previously mentioned, this difference can be
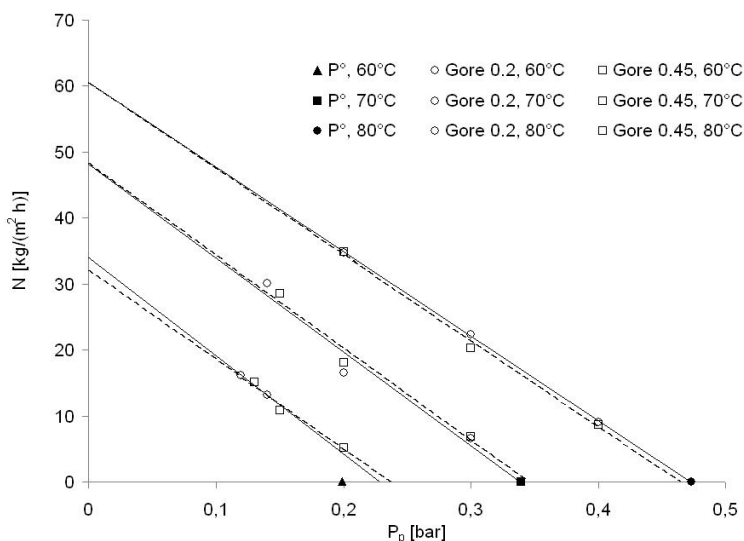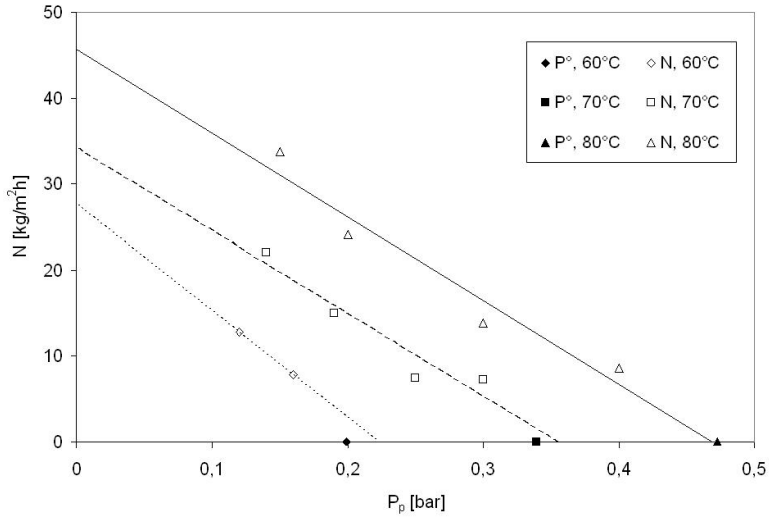
Figure 8.11: Experimental VMD fluxes vs permeate chamber pressure, GVS membrane. Filled points at $N = 0$ are the water vapor pressures at experimental temperatures

related to the different nature of the membrane, exhibiting a different morphology (see section 8.1), which presumably affects vapor mass transfer.

Experimental values of mass transfer coefficients were calculated from equation 7.1 and compared with predictions (equations 7.2 and 7.3). Results are reported in table 8.1.

In all cases (with only one exception), the predicted mass transfer coefficients are higher than experimental ones (up to three times). All the Gore membranes, in spite of their different nominal pore size (which strongly affects model predictions), showed very similar flux values. This apparently anomalous behavior can be related to membrane material intrinsic features and/or to the real pore size distribution. As a matter of fact, the pore size affects not only the mass transfer coefficient, but it determines also the mass transfer mechanism: for example, a certain pore size distribution can have a portion falling in the Knudsen region, whereas other pore sizes can favor a viscous transport mechanism. However, most of experimental k_P fall between predicted k_P^k and k_P^v values. Also in this case, a possible explanation refers to membrane pore size distribution: likely, the mean free-path of water vapor molecule falls into the pore size distribution, thus denoting two different transport mechanism zones [Phattaranawik et al., 2003], e.g. for $r < \lambda$ only k_P^k must be considered, whereas for $r > \lambda$, viscous flow or a Knudsen-viscous transition depict better the mass transfer mechanism.

Table 8.1: Experimental and predicted mass transfer coefficients [kmol/m^{2}Pa s $\times 10^8$], VMD

Membrane	T [°C]	k_P^k	k_P^v	k_P	k_P^{exp}
Gore 0.2	60	2.36	0.088	2.45	3.27
Gore 0.2	70	2.33	0.117	2.45	2.19
Gore 0.2	80	2.30	0.132	2.43	1.97
Gore 0.45	60	5.02	0.422	5.45	3.39
Gore 0.45	70	4.95	0.558	5.51	2.23
Gore 0.45	80	4.88	0.630	5.51	1.92
GVS 0.2	60	2.76	0.103	2.86	1.92
GVS 0.2	70	2.72	0.136	2.86	1.62
GVS 0.2	80	2.68	0.154	2.83	1.47

8.2.4 Results overview

In all tests performed, the only processing variable in the feed side was the water temperature. As a general result, when increasing water temperature, the vapor flux increases. At a constant water temperature, differences between configurations are ascribable to permeate side resistances only (for a given membrane). The highest fluxes recorded for each MD configuration with Gore 0.2 μm membranes are compared in figure 8.12.
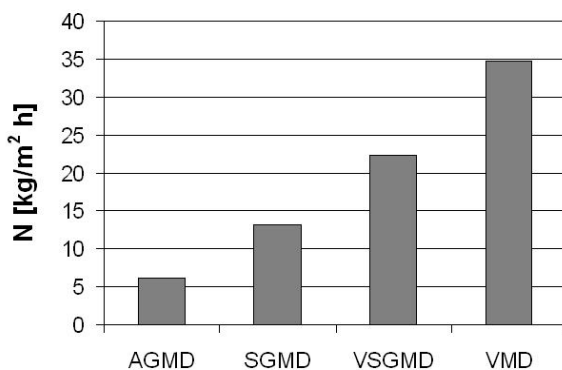
Figure 8.12: Highest fluxes obtained in various MD configurations, T=80 °C, Gore 0.2 μm membrane

The VMD configuration, owing to its low permeate side resistance (due to negligible heat and driving force loss), allowed the highest flux to be obtained. On the other side, the AGMD resulted in lowest vapor flux, ascribable to the high resistance offered by natural

convection. Sweeping gas operations lays in an intermediate range: the differences between SGMD and VSGMD are ascribable to air velocity reached in the experiments, 2 m/s in SGMD and about 7.4 m/s in VSGMD.

8.3 Liquid entry pressure

Results of liquid entry pressure (LEP) measurements for Gore 0.45 μm membrane are displayed in figure 8.13. The LEP value decreased with increasing temperature: this result can be explained by recalling the depression of the surface tension with increasing temperature (see equation 6.15). As discussed previously (see Section 7.2.1), these values were obtained after a few of operation cycles to reach a steady state with a stabilized pore size.
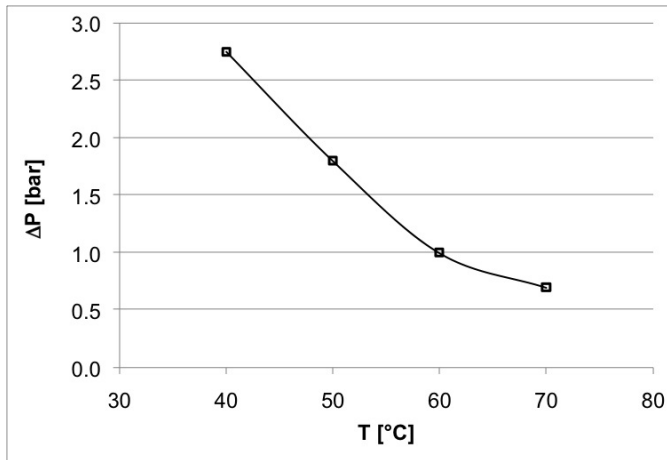
Figure 8.13: Liquid entry pressure ($\Delta P = P_{feed} - P_{permeate}$) versus temperature, Gore 0.45 μm membrane

In general, for a fresh membrane, LEP decreased during the early test cycles, and then, it reached a stationary value. In the first stages of operation, the intrusion of hot water into the pores modified the membrane microstructure. This circumstance must be carefully considered when one performs wetting experiments, as the results can be significantly overestimated, and this will globally lower the process efficiency.

8.4 Conclusion

The batch measurement apparatus designed on-purpose resulted versatile for membrane characterization in various MD configurations.

The NC conditions showed a higher mass transfer resistance, which makes it the MD process independent of the type of membrane used. For FC conditions, membrane properties, namely material type and morphology, affect the vapor flux, whereas the nominal pore size (as declared by manufacturers) seems not to influence the mass transfer through the membrane.

VSGMD turned out to be a valuable configuration, reaching satisfactory fluxes and allowing a less expensive permeate recovery than SGMD. However, VMD resulted the best configuration, mainly due to low transport resistance in permeate side. The highest vapor flux reached was about 35 kg/m^{2}h, in line with the best performances reported in literature [Li and Sirkar, 2005, Mericq et al., 2009].

The modeling proposed showed a satisfactory accord with experimental measures, with some exceptions for VMD, suggesting that the effective pore size distribution must be considered to refine the modeling results. In other words, knowing the pore size distribution, one could determine a parallel distribution of mass transfer coefficients related to different mass transfer mechanisms occurring simultaneously. The global mass transfer coefficient could be calculated via weighting the mass transfer coefficients by the fraction of pores where vapor flux follows a certain mechanism.

For all the MD configurations studied, significant influence of permeate side conditions was found. Therefore, a further progress in MD performances can be achieved by addressing studies on enhancing mass transfer in the permeate side.

First of all, as the microstructure of the membrane (and also of the support) exerts a sensible influence on the mass and heat transfer, the most suitable morphology for a given application target must be selected, and one must choose among the various membrane production technologies (phase separation and uniaxial and biaxial stretching). As shown by the vapor flux measurements, the PTFE membranes showed better performance than the PVDF membranes; the main reason, although not deeply investigated, should be related to the membrane morphology and texture. As a matter of fact, both materials are hydrophobic, and the material hydrophobicity did not exert a consistent influence on the vapor flux. On the other hand, the membrane preparation techniques, strictly related to the material properties, determined the membrane microstructure. A fibrous morphology has a pore tortuosity lower than that of a network of interconnected pores: this could be the key value of the PTFE membranes. To double-check this hypothesis, a comparison between membranes made of the same material and fabricated with different techniques could be addressed. To accomplish this study, PP is likely the most promising polymer, as PP membranes can be fabricated with both phase separation and stretching.

The LEP measurements showed that with increasing temperature, the liquid pass-through

became more probable; this circumstance confirmed the usefulness of LEP reliable data at high temperatures (whereas the data sheets included at most the LEP at room temperature), especially for VMD, where the pressure difference across the membrane could be considerably larger than in the other MD configurations.

Bibliography

M. Gryta. Influence of polypropylene membrane surface porosity on the performance of membrane distillation process. *Journal of Membrane Science*, 287:67–78, 2007.

J. Huang, J. Zhang, and X. Haoand Y. Guo. Study of a new novel process for preparing and costretching ptfe membrane and its properties. *European Polymer Journal*, 40:667–671, 2004.

T. Kitamura, S. Okabe, M. Tanigaki, K. Kurumada, M. Ohshima, and S. Kanazawa. Morphology change in polytetrafluoroethylene (PTFE) porous membrane caused by heat treatment. *Polymer Engineering and Science*, 40(3):809–817, 2000.

B. Li and K. K. Sirkar. Novel membrane and device for vacuum membrane distillation-based desalination process. *Journal of Membrane Science*, 257:60–75, 2005.

J.-P. Mericq, S. Laborie, and C. Cabassud. Vacuum membrane distillation for an integrated seawater desalination process. *Desalination and Water Treatment*, 9:293–302, 2009.

J. Phattaranawik, R. Jiraratananon, and A. G. Fane. Effect of pore size distribution and air flux on mass transport in direct contact membrane distillation. *Journal of Membrane Science*, 215:75–85, 2003.

R. W. Schofield, A. G. Fane, and C. J. D. Fell. Heat and mass transfer in membrane distillation. *Journal of Membrane Science*, 33:299–313, 1987.

J. Xu, M. Furuswa, and A. Ito. Air-sweep vacuum membrane distillation using fine silicone, rubber, hollow-fiber membranes. *Desalination*, 191:223–231, 2006.

J. Zhang, N. Dow, M. Duke, E. Ostarcevic, J. Li, and S. Gray. Identification of material and physical features of membrane distillation membranes for high performance desalination. *Journal of Membrane Science*, 349:295–303, 2010.

9 Conclusion

The preparation of polymeric porous structures via phase separation was investigated by means of thermodynamic modeling and experimental measurement of phase boundaries. In addition, a characterization of commercial membranes was carried out to deduce the main features required to a porous structure for an effective employment in a separation process.

Various models for the calculation of thermodynamic phase diagram for the PLLA-dioxane-water system were explored. Among these, the lattice fluid model extended to specific interactions gave out the best results: a phase diagram was obtained by taking into account the proper physical properties and features of the real system, i.e. the influence of specific interactions. The model parameters were fitted on the basis of experimental cloud point curves available in literature. The appropriate interaction parameters can be selected by scrutinizing Hansen solubility parameters values and with the help of empirical observations, thus reducing the number of adjustable parameters from six to three. The adopted procedure reduces the need for experimental information, offering a tool able to easily and reliably describe the phase behavior of scaffold forming systems.

A temperature-controlled turbidity measurement apparatus was designed and set up. The device allows one to carry out simultaneous measurements of temperature and light transmittance on a polymer solution, and to cover a wide span of cooling rates. The temperature control was realized by employing peltier cells, i.e. thermoelectric devices allowing both heating and cooling by imposing a direct current.

The heat transfer issues of the system were analyzed, modeled and discussed, to achieve a complete picture of the system capabilities. The transient temperature distribution into the sample was calculated for two different sample vial materials: glass and sapphire. At this stage, only a sample vial constituted of glass was used; the sapphire, which allows one to reach higher cooling rates and to reduce the temperature gradients inside the sample, will be implemented in future upgrades of the apparatus. Moreover, the transient heat transfer inside the peltier cell and the sample was simulated via a finite element analysis software package. A heuristic model of peltier cells was developed and utilized for the simulation of system dynamics and the tuning of controller parameters.

On the other hand, a set of cloud point curves for the PLLA-dioxane-water system at different compositions was measured, and the influence of cooling rate on the onset of phase separation was also detected and discussed. The preliminary results obtained through the self built experimental apparatus showed the versatility of measurement device while detecting cloud point temperatures in polymer solutions.

All things considered, the turbidity measurement apparatus can be used for the derivation of cloud point data, which in their turn are the input for the tuning of thermodynamic model parameters. In this way, a complete characterization of the phase behavior for a given polymer solution can be achieved. This set of information is useful for the design of TIPS protocol, aimed to obtain a porous structure with a certain morphology, depending on the peculiar application. With this respect, the characterization of membranes for MD application gave out a set of relevant features for guiding the membrane production.

As regards for commercial membranes characterization, the batch measurement apparatus designed on-purpose resulted versatile for membrane characterization in various membrane distillation (MD) configurations. The performances of membrane distillation process are mainly influenced by the permeate recovery technique, whereas the influence of membrane properties is mainly related to the microstructure of both selective layer and support. The membranes made by PTFE showed better performance than those made by PVDF. The main reason, although not deeply investigated, should be related to the membrane morphology. The membrane preparation techniques, strictly related to the material properties, determine the membrane microstructure: a fibrous morphology had a pore tortuosity lower than that of a network of interconnected pores, thus probably constituting the key value of the PTFE membranes.

The most performant configuration explored is the Vacuum MD (VMD), were the permeate vapor is recovered by a vacuum pump. The highest vapor flux reached was about 35 kg/m^{2}h. The mass transfer modeling showed a satisfactory accord with experimental measure, with some exceptions related to the actual pore size distribution of membranes. In fact, the pore dimension determines the mass transfer mechanisms, and a relatively wide pore size distribution generates multiple parallel mass transfer dynamics inside the membrane. This aspect must be taken into account for a more accurate modeling of mass transfer in membranes.

The liquid entry pressure (LEP) measurements showed that the liquid pass-through became more probable with increasing the liquid temperature. This circumstance confirms the usefulness of LEP reliable data at high temperatures (whereas the data sheets included at most the LEP at room temperature), especially for VMD, where the pressure difference across the membrane could be considerably larger than in the other MD configurations.

Future work

The studies presented in this thesis address the directions for a future work, as each result can be seen as a starting point for further investigations. Moreover, the individual sections are strictly interconnected, thus a complementary and unified approach can be envisaged.

First of all, the model parameters of compressible lattice fluid model with specific interactions can be tuned on the basis of few experimental cloud point data obtained via the turbidity measurement apparatus. For example, nine cloud point temperatures, evaluated at three different polymer concentration and three dioxane/water ratios would be adequate. Moreover, the model could be extended to polydisperse system, thus obtaining predictions more adherent to the features of real system. To do this, the system can be considered as multicomponent, with several polymeric components having different molecular weight. A preliminary study on binary polymer solutions, constituted by one solvent and two polymers with different chain length, was carried out (even if not shown in the thesis) by applying the compressible model extended to specific interactions. The main aim was to test the sensitivity of calculated phase equilibria on polydispersity, before starting a deeper computational campaign. By using only two different polymer chain lengths, the model resulted highly sensitive to the average molecular weight and their individual values. In principle, this modeling approach can be applied the ternary system focused in this thesis, and hopefully it will clarify the influence of polydispersity on cloud point temperature. Moreover, the effect of polydispersity can be experimentally verified with "model" polymers, characterized by the same average molecular weight and significantly different distributions.

The turbidity measurement apparatus can be employed for the characterization of other polymer solutions of relevant interest in the production of porous membranes and scaffolds. The device will be upgraded to raise the number of experimental information achievable on phase separation dynamics. The two short time horizons are the improvement of heat transfer issues, for reaching and analyzing higher cooling rates (i.e. $\dot{T} = 10 \div 100°C/s$), and the enclosure of additional detectors to the apparatus, in order to measure light scattering and/or other radiation probes during phase separation. Light scattering data would improve the characterization of kinetic features, e.g. the separation mechanisms (nucleation and growth, spinodal decomposition) and the domains growth rate. A better insight

on phase separation kinetics, derived at various cooling rates, could be achieved. Additionally, cloud point curves for polymers with different molecular weight distributions will be measured and compared with modeling outcomes, thus optimizing the information flow between modeling and experimentals.

A complete phase diagram can help the design of TIPS protocols. In principle, the membrane morphology (in terms of pore size, pore size distribution and interconnection) can be controlled by tuning the time spent by the solution in the binodal and spinodal zones. Membranes with peculiar features for a given application could be produced, e.g. for membrane distillation.

A systematic approach for clarifying the influence of membrane morphology on MD performance could be pursued with a comparison between membranes made of the same material and fabricated with different techniques. To accomplish this study, polypropylene (PP) is the most promising polymer, as PP membranes can be fabricated by both phase separation processes and stretching.

A Free energy derivatives

A.1 Compressible LF model

A.1.1 Binary system

$$g_{11} = kT \left(\frac{1}{r_1 v_1^* \phi_1} + \frac{1}{r_2 v_2^* \phi_2} - 2\chi\tilde{\rho} \right) \tag{A.1}$$

$$g_{vv} = P^* \left\{ -2\tilde{\rho}^3 + \tilde{T}\tilde{\rho}^2 \left[\frac{1}{1-\tilde{\rho}} - \left(1 - \frac{1}{r} \right) \right] \right\} \tag{A.2}$$

$$\begin{aligned} g_{1v} &= \tilde{\rho}^2 (\phi_1 - \phi_2) kT\chi \\ &\quad + P_1^* \left\{ \tilde{\rho}^2 + \tilde{T}_1 \left[\ln(1-\tilde{\rho}) + \left(1 - \frac{1}{r_1} \right) \tilde{\rho} \right] \right\} \\ &\quad - P_2^* \left\{ \tilde{\rho}^2 + \tilde{T}_2 \left[\ln(1-\tilde{\rho}) + \left(1 - \frac{1}{r_2} \right) \tilde{\rho} \right] \right\} \end{aligned} \tag{A.3}$$

A.1.2 Ternary system

$$g_{11} = kT \left(\frac{1}{r_1 v_1^* \phi_1} + \frac{1}{r_3 v_3^* \phi_3} - 2\tilde{\rho}\chi_{13} \right) \tag{A.4}$$

$$g_{22} = kT \left(\frac{1}{r_2 v_2^* \phi_2} + \frac{1}{r_3 v_3^* \phi_3} - 2\tilde{\rho}\chi_{23} \right) \tag{A.5}$$

$$g_{vv} = P^* \left\{ -2\tilde{\rho}^3 + \tilde{T}\tilde{\rho}^2 \left[\frac{1}{1-\tilde{\rho}} - \left(1 - \frac{1}{r} \right) \right] \right\} \tag{A.6}$$

$$g_{12} = kT \left[\frac{1}{r_3 v_3^* \phi_3} - \tilde{\rho}(\chi_{13} + \chi_{23} - \chi_{12}) \right] \tag{A.7}$$

$$g_{1v} = kT\tilde{\rho}^2 \left[\phi_2(\chi_{23} - \chi_{12}) + \chi_{13}(\phi_1 - \phi_3) \right]$$
$$+ P_1^* \left\{ \tilde{\rho}^2 + \tilde{T}_1 \left[\ln(1 - \tilde{\rho}) + \left(1 - \frac{1}{r_1} \right) \tilde{\rho} \right] \right\}$$
$$- P_3^* \left\{ \tilde{\rho}^2 + \tilde{T}_3 \left[\ln(1 - \tilde{\rho}) + \left(1 - \frac{1}{r_3} \right) \tilde{\rho} \right] \right\} \tag{A.8}$$

$$g_{2v} = kT\tilde{\rho}^2 \left[\phi_1(\chi_{13} - \chi_{12}) + \chi_{23}(\phi_2 - \phi_3) \right]$$
$$+ P_2^* \left\{ \tilde{\rho}^2 + \tilde{T}_2 \left[\ln(1 - \tilde{\rho}) + \left(1 - \frac{1}{r_2} \right) \tilde{\rho} \right] \right\}$$
$$- P_3^* \left\{ \tilde{\rho}^2 + \tilde{T}_3 \left[\ln(1 - \tilde{\rho}) + \left(1 - \frac{1}{r_3} \right) \tilde{\rho} \right] \right\} \tag{A.9}$$

A.2 Compressible LF model with specific interactions

A.2.1 Ternary system

$$g_{11} = -\frac{2\tilde{\rho}}{kT}(\epsilon_{11}^* + \epsilon_{33}^* - 2f_{13}^*) + \left[\frac{1}{r_1\phi_1} + \frac{1}{r_3\phi_3} \right] \tag{A.10}$$

$$g_{22} = -\frac{2\tilde{\rho}}{kT}(\epsilon_{22}^* + \epsilon_{33}^* - 2f_{23}^*) + \left[\frac{1}{r_2\phi_2} + \frac{1}{r_3\phi_3} \right] \tag{A.11}$$

$$g_{\tilde{\rho}\tilde{\rho}} = \frac{1}{\tilde{\rho}} \left[\left(\frac{1}{r\tilde{\rho}} + \frac{1}{1 - \tilde{\rho}} \right) + \frac{2}{kT} \left(\frac{Pv^*}{\tilde{\rho}^2} - \epsilon_T^* \right) \right] \tag{A.12}$$

$$g_{12} = -\frac{2\tilde{\rho}}{kT}(\epsilon_{33}^* + f_{12}^* - f_{13}^* - f_{23}^*) + \frac{1}{r_3\phi_3} \tag{A.13}$$

$$g_{1\tilde{\rho}} = -\frac{2}{kT} \left[\phi_1(\epsilon_{11}^* - f_{13}^*) + \phi_2(f_{12}^* - f_{23}^*) - \phi_3(\epsilon_{33}^* - f_{13}^*) + \frac{Pv_1^*}{2\tilde{\rho}} \right]$$
$$+ \frac{1}{\tilde{\rho}} \left(\frac{1}{r_1} - \frac{1}{r_3} \right) \tag{A.14}$$

$$g_{2\tilde{\rho}} = -\frac{2}{kT} \left[\phi_1(f_{12}^* - f_{13}^*) + \phi_2(\epsilon_{22}^* - f_{23}^*) - \phi_3(\epsilon_{33}^* - f_{23}^*) + \frac{Pv_2^*}{2\tilde{\rho}} \right]$$
$$+ \frac{1}{\tilde{\rho}} \left(\frac{1}{r_2} - \frac{1}{r_3} \right) \tag{A.15}$$

B Grashof number evaluation in natural convection

The expression used for Grashof number evaluation is:

$$\mathrm{Gr} = \frac{d^3 g \rho_m}{\mu^2}(\rho_a - \rho_{aw}) \tag{B.1}$$

where d is a characteristic dimension, g the gravitational acceleration, μ is the air viscosity and ρ is the density. The subscripts a, aw and m refers respectively to air, air-water mixture and mean values.

The density of air-vapour mixture is:

$$\rho_{aw} = x_w \rho_w + (1 - x_w)\rho_a \tag{B.2}$$

where the mole fraction of water vapour in air is:

$$x_w = \frac{P_w^0}{P} \tag{B.3}$$

The average density is:

$$\rho_m = \frac{\rho_a + \rho_{aw}}{2} \tag{B.4}$$